IMPRESSION CREEP AND FATIGUE CRACK GROWTH BEHAVIOUR OF ALUMINIUM ALLOY FRICTION STIR WELDMENTS

JAYASHREE DAS
(Roll No. 146103012)

Department of Mechanical Engineering
Indian Institute of Technology Guwahati
Guwahati 781039, Assam, India
2023

IMPRESSION CREEP AND FATIGUE CRACK GROWTH BEHAVIOUR OF ALUMINIUM ALLOY FRICTION STIR WELDMENTS

Thesis submitted to
Indian Institute of Technology Guwahati
for the award of the degree

Doctor of Philosophy

By

JAYASHREE DAS

(Roll No. 146103012)

Department of Mechanical Engineering
Indian Institute of Technology Guwahati
Guwahati 781039, Assam, India
May 2023


भारतीय प्रौद्योगिकी संस्थान गुवाहाटी
Indian Institute of Technology Guwahati

Department of Mechanical Engineering
Indian Institute of Technology Guwahati
Guwahati-781039,
INDIA

CERTIFICATE

It is certified that the work contained in the thesis entitled "**Impression Creep and Fatigue Crack Growth behaviour of Aluminium alloy Friction Stir Weldments**" submitted by **Ms. Jayashree Das** (Reg. No. **146103012**) to the Indian Institute of Technology Guwahati for the award of degree of Doctor of Philosophy has been carried out under my supervision in the Department of Mechanical Engineering, Indian Institute of Technology Guwahati. This work has not been submitted elsewhere for the award of any other degree or diploma.

The thesis, in my opinion, has reached the standard fulfilling the requirements for the award of degree of Doctor of Philosophy in accordance with the regulations of the institute.

8th May, 2023

Professor K.S.R.K. Murthy
HOD
Department of Mechanical Engineering
Indian Institute of Technology Guwahati
Guwahati-781039
INDIA

Professor P. S. Robi
Department of Mechanical Engineering
Indian Institute of Technology Guwahati
Guwahati-781039
INDIA

DECLARATION

I declare that,

a. The work contained in this thesis is original and has been done by me under the guidance of my supervisor.

b. The work has not been submitted to any other institute for any degree or diploma

c. I have followed the guidelines provided by the institute in preparing the thesis.

d. I have confirmed to the norms and guidelines given in the Ethical code of Conduct of the Institute.

e. Whenever I have used materials (data, theoretical analysis, figures and text) from other sources I have given due credit to them by citing them in the text of the thesis and giving their details in the references. Further, I have taken permission from the copyright owners of the sources, whenever necessary.

Signature of the Student
(JAYASHREE DAS)

Acknowledgement

I start this by thanking The Almighty for keeping me healthy and giving patience throughout my thesis work. I wish to express my deep gratitude to all those who have helped me in various ways directly and indirectly during the tenure of my PhD work at IIT Guwahati. In each step, the PhD work was supported by many people and each one has played important role. I am grateful to all of them.

I express my sincere gratitude and appreciation to my supervisor, **Professor P.S Robi**, **Department of Mechanical Engineering, IIT Guwahati**, for his valuable advises, expert guidance, patience and encouragement, and for all the support he has given me from the day one and throughout the PhD work. Without his support, advice, and motivation, it would have just been an impossible task for me to carry out this research work. Regardless of his work load, he always found time to discuss with me for the PhD work and also so many suggestions for betterment of my personal life. I really feel privileged for having the opportunity to work under him and as my PhD supervisor.

I sincerely appreciate **Prof. S. Senthilvelan, Prof. Santosha K. Dwivedy Prof. Anoop K. Dass**, the present and former Head of the department, for extending all essential facilities of the department. I would like to be thankful to my doctoral committee chairman **Prof. S. Kanagaraja,** Professor, Department of Mechanical Engineering for his priceless suggestions and encouragement throughout the PhD work. Also, I would like to be grateful to my doctoral committee members **Prof. S. Senthilvelan,** Professor, Department of Mechanical Engineering and **Prof. D. Pamu,** Professor, Department of Physics for their assistive suggestions and shaping criticisms which made the research work improved. A heart-felt thanks to all the faculty members of the department not only for their technical suggestions at times but for their cordial interactions also that create a pleasurable working environment.

I would like to express my sincere acknowledgement to Mr. S. Sharma and Mr. S. Ahmed for their assistance in various experimentation. I am also grateful to HOC, CIF, staff and TA of FESEM for their assistance. I would like to express my sense of gratitude to Mr. N. K. Das, workshop superintendent and impressive helping staff, Mr. M. Sharma, Mr. M. Medhi, Mr. J. K. Saikia, Mr. D. Khaklary, Mr. C. Banikya, Mr. M. Baishya, Mr. N. Saikia and Mr. U. Gohain for their helping hand for the experimentation.

A heart felt thanks to my seniors and friends Dr. Rashmi Ranjan Behera, Dr. Purnendu Kumar Mondal, Dr. Soumya Ranjan Dash, Abhishek, Uttam, Sujit, Saibal, Ajit, Bikash and Vivek for their help, support and advice in different occasions of my PhD work.

The most important persons to support this work and I shall always be grateful to them are my parents **Mrs. Sabitri Das** and **Mr. Sudhir Kumar Das** for their great encouragement, guidance, love, affection, motivation and warm blessings. The blessings I got from my mother-in-law Late **Mrs. Sumati Sahu** and father-in-law **Mr. Sudhasindhu Sahu** are highly impelling and influencing. I am also thankful to my siblings for their moral support to complete this work. I express my special gratitude to my husband **Dr. Prakash Kumar Sahu** who acted as a guide, guardian, philosopher, friend and the one who stands near me in each and every hurdle during the time periods of this research work. His persistent support, encouragement, patience and motivation gives me strength to complete this work. Love and warmness of our beloved daughter **Sindhu Shreya** are the source of inspiration during my entire PhD work. I will always remain grateful to my teachers who have shown me a path to move on in my life. I may have missed out a few names in the above list; my sincere apologies are due for any such inadvertent oversight.

This Thesis is Dedicated
To

My Loving Parents

&

My Family

Abstract

Abstract: Joining Aluminium alloys by Friction stir welding (FSW) results in different weld zones viz, nugget zone (NZ), thermos-mechanically affected zone (TMAZ), heat affected zone (HAZ) and the base metal (BM). Each zone exhibits different microstructures and mechanical properties across the weld leading to poor mechanical attributes for the weldment. An insight in to the creep deformation and fatigue crack growth through these weld zones will enlighten the research community with the usage of these materials for elevated temperature applications as well as for conditions of dynamic loading. The present work was therefore taken up with the objective of joining defect free joints of Aluminium alloys by FSW and investigating the (i) creep behaviour of different weld zones at elevated temperatures by impression creep (IC) tests and (ii) fatigue crack growth (FCG) behaviour through different weld zones of the weldments. The materials chosen for the study are commercial Aluminium alloys viz, AA2014 and AA6061-T6. For obtaining the best quality joints of the two Aluminium alloys based on the mechanical properties the process parameters selected were low tool rotational speed, low welding speed, low plunge depth and moderate shoulder diameter of square pin (SQ) tool profile. The effect of process parameters on the mechanical properties viz, ultimate tensile strength (UTS), yield strength (YS), % elongation, Flexural strength (FS) and bend angles of the weldments were studied. The best AA6061-T6 weldments exhibited 97%, 98% and 98% of the UTS, YS and FS of the base metal respectively. In the case of AA2014 alloy the corresponding properties were 86%, 80% and 90% of the base metal. The results of the microstructure and fractography under field emission scanning electron microscope (FESEM) are studied and discussed.

The creep deformation behavior of different weld zones is investigated by IC tests. IC tests were performed at NZ, TMAZ, HAZ and BM with combination of temperatures 310, 330 and 350 ºC and stresses 21, 24 and 27 MPa. From the experimental data the steady state creep rate (SSCR) for each weld zones were estimated and their respective creep rates $\dot{\varepsilon} = f(T, \sigma, t)$ were established using a power law relationship. The creep rate was the highest for the NZ and decreased in the order of TMAZ, HAZ and BM. The constants in the power law equation such as stress exponents *(n)* and apparent activation energy for the IC deformation (Q_{ic}) for each weld zone were determined. The power law

constitutive equation for creep deformation at each weld zone was developed. Microstructure of the different weld zones were invested after the IC tests and the creep deformation behavior was discussed with the support of the microstructure.

The fatigue crack growth rate experiments of the best weldment were performed by allowing the crack growth along each particular weld zones using compact tension (CT) specimen. For each weld zone, experiments were performed with three stress ratios, R = 0.10, 0.33 and 0.60. From the FCGR plots, the constants C and m of Paris equation were determined for the steady state crack growth region and compared with the BM. The fracture surfaces of the failed specimen after FCGR tests were investigated using FESEM and correlated to the microstructure and the crack growth behaviour. It is found that fatigue cracks propagated faster at NZ in compared to the other zones due to the finer grain size that was mainly due to the dynamic recrystallization as a result of the stirring action during the FSW process. Though the mechanical properties of the friction stir weldment was lower than the BM, a post weld heat treatment (PWHT) leads to the release of the stored internal energy at the weld zones and restored almost all the mechanical properties back to the BM. The FCGR at NZ was also improved and comparable to the BM after PWHT.

To summarize, the present work highlights the combination of process parameters for FSW of AA2014 Al alloy and AA6061-T6 Al alloy for obtaining the best mechanical properties and discusses the microstructure, hardness, impression creep behaviour and fatigue crack growth behaviour of the four weld zones, viz NZ, TMAZ, HAZ and BM in the two Aluminium alloy weldments.

List of Acronyms

% Elong.	Percentage of elongation
AA	Aluminium alloy
AHNZ	Average hardness at the nugget zone
Al	Aluminium
AS	Advancing side
ASTM	American Society for Testing and Materials
BA	Bending angle
BM	Base material
CNC	Computer numerical controlled
COD	Crack opening displacement
CS	Compressive strength
CT	Compact tension
D	Diameter
EDS	Energy dispersive X-ray spectroscope
EDX	Energy dispersive X-ray
FCGR	Fatigue crack growth rate
FCP	Fatigue crack propagation
FESEM	Field emission scanning electron microscope
FS	Flexural strength
FSP	Friction stir processed
FSSW	Friction stir spot welding
FSW	Friction stir welding
FSWed	Friction stir welded
H	Hardness
H	High
HAZ	Heat affected zone
HT	Heat treatment
HTed	Heat treated
HV	Hardness values
IC	Impression creep

IMCs	Intermetallic compounds
I_nC	Indentation creep
LBW	Laser beam welding
LVDT	Linear variable differential transducer
NZ	Weld nugget zone
OM	Optical microscope
PD	Plunge depth
PWHT	Post weld heat treatment
R	Stress ratio
RPM	Tool rotational speed
RS	Retreating side
SD	Shoulder diameter
SEM	Scanning electron microscope
SIF	Stress intensity factor
SQ	Square
SSCR	Steady state creep rate
STC	Straight cylindrical
SZ	Stir zone
TAC	Tapered cylindrical
TCs	Thermocouples
TEM	Transmission electron microscope
THC	Threaded cylindrical
TMAZ	Thermo-mechanical affected zone
TO	Tool offset
TWI	The Welding Institute
UTM	Universal testing machine
UTS	Ultimate tensile strength
WBT	Weld bead thickness
WC	Tungsten carbide
WS	Welding speed
XRD	X-ray diffraction
YS	Yield strength

Nomenclature

σ	Equivalent compressive stress
P	Compressive load
D	Indenter diameter
d	Impression depth
T_m	Absolute melting point temperature
$\dot{\varepsilon}$	Steady-state creep rate
A	Constant
σ	Equivalent stress
n	Stress exponent
Q	Activation energy
R	Universal gas constant
T	Temperature in K
Q_{ic}	Activation energy for the IC deformation
h_m	Maximum impression depth
h	Impression depth
t	Impression time
V_{imp}	Minimum impression velocity
C_1	Conversion factor
C_2	Conversion factor
Q_d	Activation energy for self-diffusion
E	Elastic modulus
R^2	Coefficient of correlation
Q_{IC}	Activation energy for the IC process
a	Crack length
N	Number of cycles
ΔK	Stress intensity factor range
$\Delta \mathrm{K}_{\mathrm{eff}}$	Effective stress intensity factor range
R	Stress ratio
P_{min}	Maximum load
P_{max}	Minimum load

ΔP	Applied tensile load range
da/dN	Fatigue crack growth rate
C	Material constants
m	Paris index
ΔK	Stress intensity factor range
ΔK_{th}	Threshold stress intensity factor range
K_{max}	Maximum stress intensity
B	Net thickness of CT-specimen
W	Width of the CT-specimen from load line
a	Initial crack length
a_c	Critical crack length
σ_y	Yield strength
σ_f	Flexural stress
F	Maximum applied load
L	Support span length
b	Width of beam
d	Thickness of beam

List of Figures

List of Tables

Contents

Welded AA6061-T6 Aluminium Alloy

Chapter 1

Introduction

1.1 Overview of Friction Stir Welding

Friction stir welding (FSW) is a recently developed solid state joining process invented at The Welding Institute (TWI) UK (Thomas et al., 1991). Application of FSW expedited with joining of aluminium (Al) and its alloys which are difficult to weld by conventional fusion welding techniques. Aluminium alloys (AA) are the best choice structural alloys for strategic applications like defense, aircraft, automobiles, etc., where high strength to weight ratio and low cost to weight ratio are of overriding importance. Among different grades of Al-alloys, the precipitation hardenable AA2014 and AA6061-T6 alloys find extensive use for structural applications. However, joining Al-alloys by fusion welding encounters several difficulties like severe oxidation, gas entrapment in the molten weld pool, hot cracking, high spatter formation, dissolution of hardening precipitates, etc., resulting in structure exhibiting inferior properties.

In FSW process a cylindrical non-consumable shoulder tool with a profiled probe is rotated and slowly plunged into the joint line between the two pieces to be joined together. Due to friction, heat is generated to plasticize the metal without melting and allows traversing the tool along the weld line. The stirring action of the tool pin and forging action of the tool shoulder makes the specimen facilitate the weld joint. A schematic diagram of the FSW process is represented in Fig.1.1. Before welding, the work-pieces were placed on a backing plate and rigidly clamped to a fixture. The tool pin-center was positioned at the middle of the joint line of the two plates as in (Fig. 1.1a). The next step was the rotation of the tool either clockwise or anticlockwise and the pin is plunged into the work-piece (Fig. 1.1b). The tool pin rotation plasticizes and mixes the material from the two pieces to get joined (Fig. 1.1c). After the completion of welding the pin is retracted (Fig. 1.1d). Out of the three parts of the tool namely shank, shoulder and pin (Fig. 1.1e), shank holds the shoulder and pin generates heat of friction on the work-piece. The diameter and height of the pin depends on the thickness of work-piece.

The quality of FSW process is controlled by various parameters like, shoulder diameter, tool rotational speed, welding speed, downward force by the tool, plunge depth, tool tilt angle and tool geometry that includes, pin profile, tool shoulder diameter (D), pin diameter (d), D/d ratio of tool, pin length etc. Proper selection of these parameters has a major role in achieving a good joint quality. Due to the peculiar nature of the FSW process, the weldment exhibits various heterogeneous microstructural zones like nugget zone (NZ), thermo-mechanical affected zone (TMAZ), heat affected zone (HAZ), and the base metal (BM) as shown in Fig.1.2. This heterogeneous microstructure results in non-homogeneous mechanical properties across the weld bead. For example, the creep deformation behaviour at elevated temperatures and the fatigue crack growth behaviour during cyclic loading at each of these zones are different. Information regarding the creep deformation and fatigue crack growth along the distinct weld zones are required *a posteriori* for improving the properties of the friction stir welded (FSWed) material as well as from designing point of view of the component. The main aim of the present work is to investigate the microstructural features and mechanical attributes of FSWed **AA2014** as well as **AA6061-T6** alloy weldments processed at different conditions.

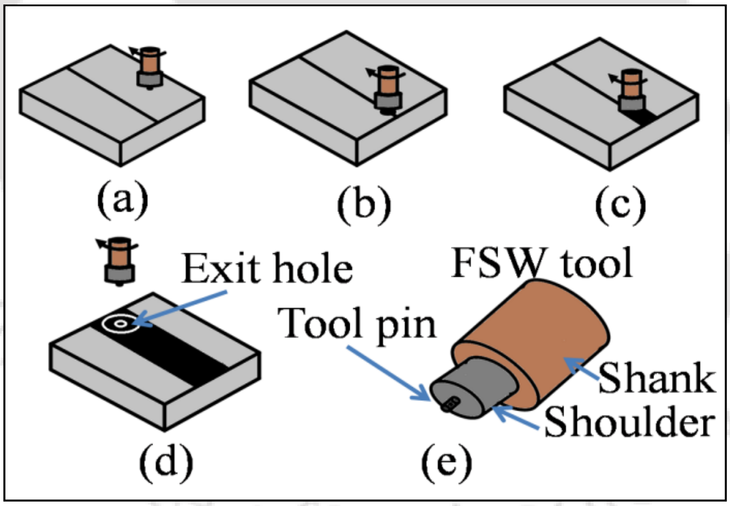

Fig. 1.1. Schematic representation of FSW process (a) Positioning plates and tool before plunging, (b) Plunge of the tool pin, (c) Tool traversing along the joint, (d) Pin removal and (e) Schematic of a FSW tool

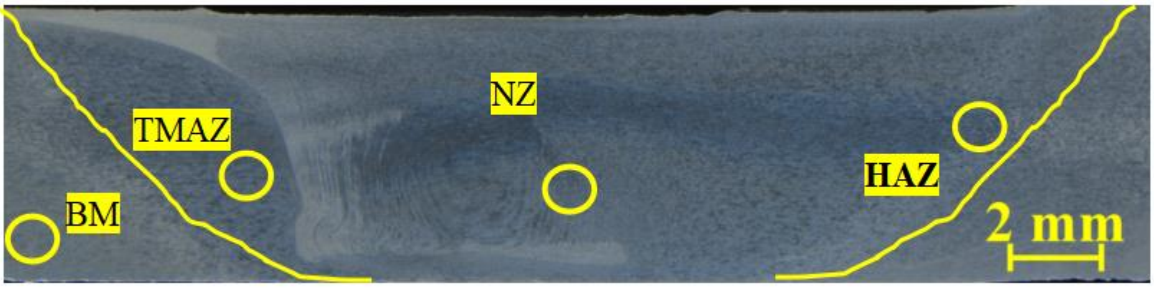

Fig. 1.2. Macro-graph of friction stir welded Al alloy showing various zones

1.2 Motivation

Structural components for application in aviation industries and energy sectors are exposed to (i) elevated temperatures for prolonged period and (ii) non-steady loading conditions. A large number of FSWed components are applied in these energy sectors. Before being put in to use they require stringent quality control to avoid catastrophic failures and ensure safe service life. In welded components that are subjected to extended periods of service at elevated temperatures, the main cause of failure is by creep deformation. Investigating the creep deformation behaviour of structural materials is a time-consuming process. Hence, researchers are developing new techniques for faster evaluation of the creep deformation behaviour of welded components for the safe and productive application in the relevant sectors. Study of creep deformation behaviour of welded material was carried out by many researchers by conventional way that has many drawbacks. Recently impression creep (IC) technique has come in to limelight as a tool for faster investigation of creep deformation of engineering materials. IC technique has several advantages compared to conventional creep tests viz., (i) simple instrumentation, (ii) easy and fast experimental procedures, (c) very small specimen requirement, (d) ability to test the creep deformation behaviour at localized regions and (e) cost effective. The newly developed technique resolved all the drawbacks meets the requirements of the testings.

The high strength AA2014 alloy is extensively used in aircraft structures. During conventional fusion welding of these alloys, they are prone to solidification cracking, void generation and dissolution of hardening precipitates resulting in degradation of the properties of the weldments. To achieve the desired weld qualities AA2014 plates are joined by FSW due to its inherent advantages over fusion welding. In this technique all the drawbacks mentioned above are removed as it is a solid-state metal joining process. AA6061-T6 alloy has extensive applications in sectors like automobile, aerospace, marine and medical industries. Recently FSW of AA6061 alloys are used as fluid coupler application in aircraft industry. High corrosion resistance as well as high strength-to-weight ratio finds AA6061-T6 alloy useful for a wide range of structural applications and replaces other materials like steel, copper and titanium. Considering the above points, it was decided to use AA2014 and AA6061-T6 alloys as the material of choice for the present work.

Studies has been carried out regarding the creep behavior and fatigue crack growth behavior of FSWed aluminium alloys. The creep deformation and fatigue crack growth of the weldments are always along the weaker zones of the weldments. So far investigation regarding the fatigue crack growth and creep deformation behavior through various weld zones of the FSWed components has not been reported. Hence, the present work was taken up to investigate the IC behaviour of Al-alloy friction stir weldment along various particular weld zones. The creep deformation properties are estimated minutely at each particular regions of the welded area. It is expected that that the results of the investigation would benefit the material scientists in identifying failure regions and take precautionary measures for extending the life of the FSWed structural components.

Fatigue crack growth rate (FCGR) behaviour of the material is required for the safe and reliable design of FSWed products subjected to cyclic loading. The FSWed region comprises of heterogeneous microstructural zones each having its own characteristics. The actual site of the origin failure during the cyclic loading is still not revealed due to the heterogeneity. FCGR studies of FSWed Al alloys have been carried out by investigators. However, no attempt has been made to investigate the FCGR behaviour along the individual zones of the welded area of FSWed materials. Hence, it was also decided to investigate the FCGR behaviour along each weld zones of FSWed aluminium alloys. The effect of heat treatment on the microstructure and the fatigue crack growth behaviour of FSWed AA2014 Al-alloy as well as AA6061-T6 Al-alloy was also investigated.

To conclude, the main objectives of the present work is to join AA2014 Al-alloy as well as AA6061-T6 Al-alloy by FSW process under various conditions and investigate the IC and FCGR behaviour along the different weld zones.

1.3 Research Objectives

Based on the research gaps from the published research work, the present work was taken up with the following major objectives:

- Experimental investigation, microstructural and mechanical properties evaluation of FSWed AA2014 Al alloy.
- Evaluation of deformation behaviour at different weld zones of FSWed AA2014 through IC technique.

- To investigate the FCGR behaviour at various weld regions of FSWed AA2014 Al alloy weldment before and after heat treatment (HT).
- Process parameter's effect on mechanical and microstructural properties of FSWed AA6061-T6 Al alloy.
- To investigate the IC deformation behavior at different weld zones of FSWed AA6061-T6 Al-alloy weldment.
- Analysis of FCGR behaviour at different weld zones of FSWed AA6061-T6 Al alloy weldment before and after HT.

1.4 The Most Important Contributions of the Thesis

The important contributions of this research work are summarized as follows:

- Influence of process parameters viz. plunge depth, tool pin profile, etc., on the weld quality of FSWed (i) AA2014 and (ii) AA6061-T6 alloys have been established.
- Considering power law creep deformation, the properties like minimum creep rate, stress exponent and the apparent activation energy for the IC process for different friction stir weld zones has been determined.
- Nugget zone has been identified as the weakest region of the weldment in terms of creep deformation and FCGR.
- Solution heat treatment improved the tensile properties and increased the resistance to FCGR of FSWed Al alloy weldments at NZ.

1.5 Outlines of the Thesis

The thesis comprises of ten chapters and highlight of each chapter are as follows:

Chapter 1 starts with the overview of FSW followed by motivation behind the present work, brief objectives, important contribution and organization of the thesis.

Chapter 2 presents brief summary of the research work carried out by other researchers in the area of FSW, impression creep deformation and FCGR of FSWed aluminium alloys. This includes the effect of various process parameters on the microstructure, mechanical properties, weld quality, minimum creep rate, FCGR behaviour of FSWed aluminium alloy weldments with special thrust on AA2014 and AA6061-T6 alloys. The chapter ends by highlighting the research gaps and detailed objectives of the thesis work.

Chapter 3 presents the details of the experimental procedures followed for achieving the research objectives and different testing techniques considered for conducting FSW experiments. This chapter also outlines different test techniques used for the considered sample and characterization technique for different sets of experiments.

Chapter 4 presents optimization of the process parameters and its effects on mechanical and microstructural properties of FSWed AA2014 Al alloy to get defect free joint.

Chapter 5 deals with the creep analysis at localized weld zones of the selected defect free joint as optimized from the previous parametric analysis of AA2014 Al alloy through IC technique.

Chapter 6 deals with FCGR analysis at selected weld zones of defect free AA2014 Al alloy weld obtained from the parametric analysis.

Chapter 7 starts with the effects of individual process parameters on microstructure and mechanical properties of FSWed AA6061-T6 Al alloy.

Chapter 8 represents the detail analysis on the IC test performed at various weld zones of defect free weld joint obtained from previous parametric analysis of FSWed AA6061-T6 Al alloy.

Chapter 9 presents the FCGR behaviour study at localized weld zones of defect free FSWed AA6061-T6 Al alloy sample obtained from the parametric analysis.

Chapter 10 casts the brief conclusions of the present research work with related future scope of the work.

This is followed by references.

A methodology flow diagram relating to all the chapters of the thesis is presented as a flow diagram for the easy and quick understanding of the thesis work. This flow diagram may add value.

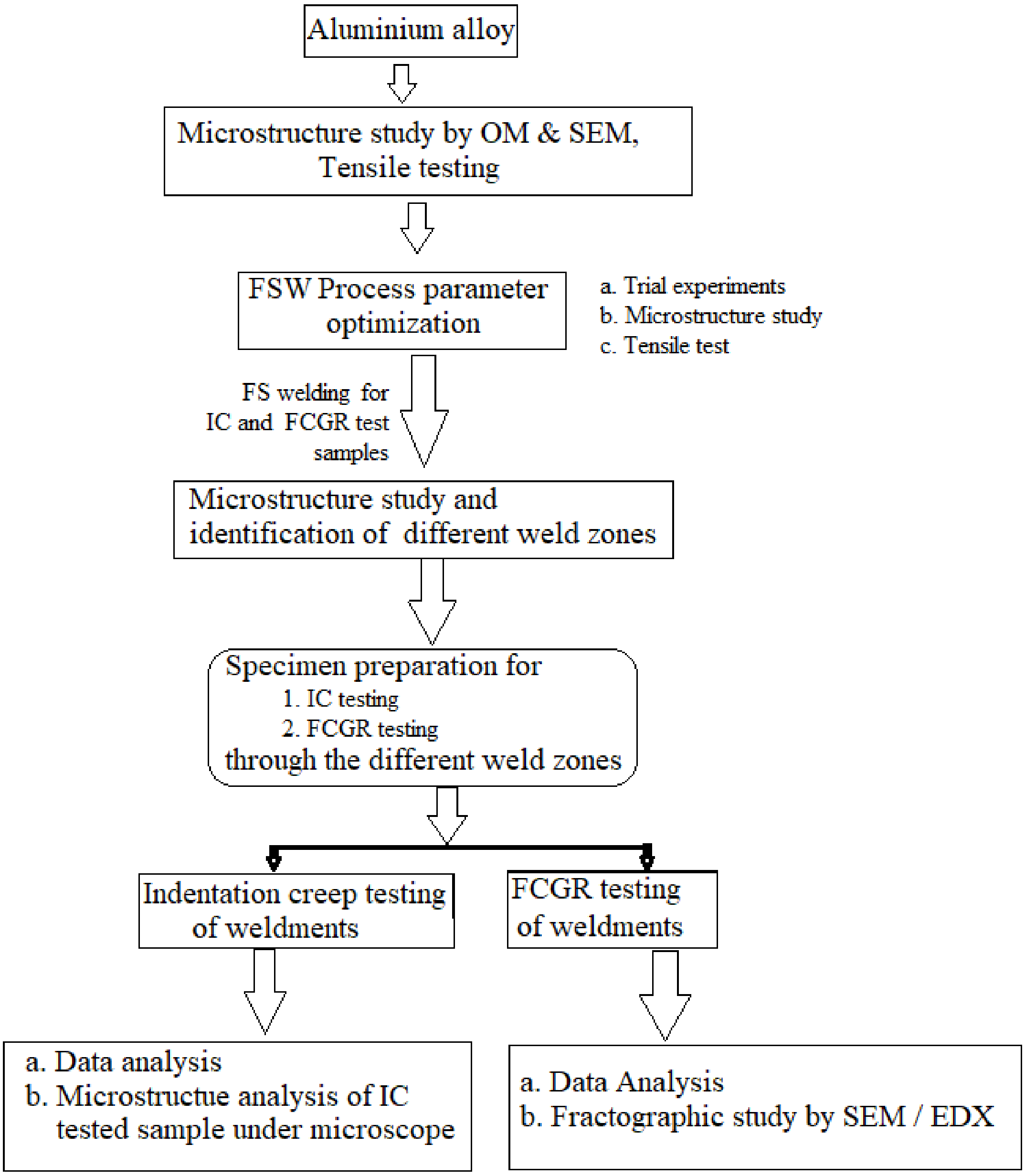

Fig. 1.3. Flow diagram of the thesis

Chapter 2

Literature Review

2.1 Introduction

FSW possesses a number of advantages over the other welding processes. It uses a non-consumable tool that can be used repeatedly to weld the materials without any arc or flame, any shielding gas and flux that do not generate any spatter and fumes. The process is relatively easier to perform and environmentally friendly. FSW process does not need the material to be melted as the temperature involved is below the melting point temperature of the material. The material is only brought to a plasticized state and hence the difficulties of shrinkage after solidification is absent. It is an energy efficient process with minimum residual stresses and distortion in the weldment compared to the other welding processes. Superior quality welds are obtained with better mechanical attribute and finer microstructure with respect to the fusion welding process. FSW process is proved to be very useful for the alloys those are found to be difficult to weld with fusion welding processes.

The shipbuilding and marine industries are the initial two industrial sectors that implemented FSW procedure for commercial purposes. Other sectors are land transportation, railway industry, aerospace industry and land transportation industry. Shipbuilding and marine industrial sectors use superstructures, decks panels, bulkheads, sides, floors, marine and transport structures, offshore accommodation etc. Presently the aerospace industry accommodates the FSW process to weld different prototype parts. A successful implementation of FSW process on Al cryogenic fuel tanks for space vehicles is found. The aerospace companies namely Boeing, Eclipse and Airbus etc. are successfully applying FSW process to produce the individual parts. FSW process has brought revolution in Railway industry by producing high speed trains with Al extrusions. It incorporates container bodies, railway rolling stock, trams, underground carriages, railway tankers and goods wagons. FSW is widely used in Land transportation sectors for the welding of wheel rims, chassis cradles, tailored blanks, attachments to hydro formed tubes, tail lifts for lorries, tail light panels, fuel tankers, buses and airfield transportation vehicles as well as motorcycle and bicycle frames.

Extended researches are carried out to explore the application of FSW process on various materials and sectors all over the globe. The literature reveals selection and effect of process parameters on weld quality, quality estimation of the joint through different procedures. Since this research work is focused on the FSW of AA2014 and AA6061. The relevant literature related to the viz, process parameters and their effects on mechanical and microstructural properties, high temperature deformation behaviour and fatigue crack growth behaviour of the FSWed Weldments. The literature study includes six separate sections.

- **Section 2.2** discusses the available work related to the effect of various process parameters on the mechanical properties and microstructure properties of FSWed Al alloy joints.
- **Section 2.3** presents the work performed in the field of creep deformation of weldments. In this section special attention is made to highlight the literature related to the impression creep (IC) of FSWed Al weldments.
- **Section 2.4** reviews on the literature related to FCGR behaviour study of FSWed Al alloys.

2.2 Effect of process parameters on microstructure and mechanical properties of FSWed Joints

The microstructure and mechanical properties of the FSW joints depend on the selection of various process parameters. The input parameters for the welding and the output qualities of the welds are interdependent, nonlinear and complex. The correlation between the parameters and the output attributes are studied in many FSWed weldments. The welding parameters viz; the tool rotation and welding speeds with the mechanical attributes are correlated in FSWed joints of AA2139-T8 and AA7020-T651 (Bertrand et al., 2019). They found that the joint hardly failed at the NZ and most of the specimens failed at the HAZ which was the region of low hardness due to the faster coarsening of η-precipitates present in the matrix (Bertrand et al., 2019). The tensile behaviour and corrosion resistance of AA2014 aluminium alloy FSWed at seven different speeds revealed that the highest temperature was achieved at higher tool rotation speed and lower welding speed. Microhardness and corrosion resistance of the weldment were found to be the best at low rotation speed and high traverse speed (Sinhmar et. al., 2019). The influences of various tools with a high ratio of depth-to-width on weld quality, hardness, grain structure, as well as crystallographic texture in the FSW process were also studied (Ahmed et al., 2019 and Huang et al., 2018). In the FSW of AA2198/AA2024, it is realized that as the tool traverse speed was increased the over-all hardness of the joint increased and kissing bond defects are formed (Khalilabad et al., 2018). In the FSW of AA2219-T6, it is possible to fabricate higher quality weld at higher speeds using hybrid tool pin profile without any harm to the tool pin than the conventional conical threaded tool (Mastanaiah et al., 2018). The mechanical and microstructural characteristics of both similar and dissimilar FSWed sheets of AA2219 and AA7475 were investigated at process parameters of rotation speed, welding speed and tool tilt angle and found that grain refinement occurs at the NZ. The dissimilar metal FSWed joint exhibited poor tensile strength due to improper metal transfer during welding. The retreating side of the thermo-mechanical affected zone (TMAZ) showed the lowest microhardness due to thermal softening (Khan et al., 2017). During the FSW process heat generated by the tool due to friction has a remarkable effect in reducing the (i) minimum hardness, (ii) heat affected area and (iii) its distance from the weld centre (Sun et al., 2017 and Wu et al., 2015). Investigation on the effect of process parameters viz: tool rotation speed, welding speed, axial load and the shoulder to pin diameter ratio (D/d) for AA2024-T6 and AA7075-T6 in dissimilar FSW was carried out and found that D/d ratio has the maximum effect on the microstructure and mechanical properties (Saravanan et al., 2016). The hardness variation at constant tool rotation speed and different welding speed of FSWed dissimilar joints of Mg–Zn–Gd and Mg–Al–Zn alloys carried out revealed that the tensile properties of the joints are significantly influenced by the material's positions, grain size and crystallographic orientation. Defects formed at lower heat input conditions due to insufficient metal plasticization (Luo et al., 2016). FSWed AA2024 produced excellent quality weld by scroll shoulder and tri-flute pin at high welding speed. The welds achieved were defect-free and with a good ductility (Trimble et al., 2015). The influence of different process parameters along with the tool pin design chosen for the experiment on the mechanical aspects of AA2014-T6 was studied and found that the quality of weld achieved by hexagonal tool pin profile was superior compared to the conical one (Kadaganchi et al., 2015). Investigation on the effect of tool rotational speed on the mechanism of bonding at the interface of FSWed dissimilar Ti-6Al-4V/AA6061 revealed that the tensile properties and micro-hardness were increased due to recrystallization. The tool rotational speed causes the formation of the intermetallics at the joint line (Rajesh et al., 2018).

The effect of various process parameters namely, tool rotational speeds, tool forces, and welding speeds on the weld strength of FSWed AA2219-T87 were investigated by (Sahu et al., 2020). The rotational speed, welding speed, diameter of the shoulder as well as tool pin were considered as process parameters for the and their influence on joint strength was realized (Arora et al., 2010). The variation in microstructure and mechanical properties with the tool rotation speed and welding speed in the case of FSWed AA6060 were investigated (Kucukrendeci, 2015). The grain structure at NZ and tensile properties were studied relating to the chosen process parameters in FSWed AA7075-T6 (Rajakumar and Balasubramanian, 2012). The authors have studied the relationship between various process parameters and the microstructural behaviour of the FSWed Al alloy (Padhy et al., 2018). The study of the process parameters like rotational speed, welding speed and the axial force on the tensile properties of A356 and C355 aluminium alloys joint were carried out and the best welding parameters were decided by response surface methodology (Dwivedi, 2014). Extensive study is carried out on the effect of various tool pin geometries on the microstructure and mechanical properties of FSWed AA5086-H34 (Rambabu et al., 2015). Investigation on the effect of alloying element Zn during Friction stir welding of Al/Cu was revealed that Zn enhances the weld qualities (Sahu et al., 2019). Effect of tool pin geometry at constant tool rotational speed on the FSW joint quality of AA6061 and realized revealed that the hexagonal pin yielded the best joint quality (Prasanna et al., 2013). The influence of tool pin profiles and power consumption during FSW were studied and modeled by the finite element method (Ahmed et al., 2019). In dissimilar FSW of AA6061 to AA5086 the effect of process parameters on the joint quality was evaluated with respect to the tensile and microstructure (Ilangovan et al., 2015).

More insight is required for FSW of different grades of high strength material like AA6061 alloy. Jayabalakrishnan and Balasubramanin (2017) investigated the effect of different process parameters and tool path pattern on the mechanical properties and microstructure of AA6061 alloy. Kadian and Biswas (2017) studied the material flow pattern of during FSW of AA6061 alloy and observed that the material movement was due to tool shoulder and pin profile. Das et al. (2018) worked on the similar and dissimilar FSW of AA6101-T6 and AA6351-T6 alloy and studied the microstructure and mechanical properties for the weldments. observed Investigation of the fatigue behavior of AA6061 alloy weldment by Uematsu et al. (2006) indicated that the fatigue strength of the welded joint is lower than the base material (BM). Haldar et al. (2018) observed the effect of tool material on the mechanical and microstructural properties of AA6061 alloy joint and found that the tool was not affected by plastic deformation. Huang et al. (2019) used tool probe profile with a disc at the top of the tool for the FSW of AA6061 alloy which resulted in defect free weld. Kumar and Patel (2020) studied the effect of SiC/Si_3N_4 micro-reinforcement at the weld joint and observed enhanced mechanical and wear properties of AA6061 alloy weldment. Zhang et al. (2020) studied the fatigue crack growth behaviour of AA6061 alloy and found that the nugget zone exhibited finer grain size with lower hardness and impact absorbing energy compared to base material and heat affected zone. Tao at al. (2016) observed special grain boundary at the nugget zone (NZ) of FSWed AA6061 alloy at different weld parameters. Kalinenko et al. (2020) detected the microstructure and strength relationship in FSWed AA6061 alloy. Trueba et al. (2015) observed the effect of tool shoulder features on defect free weld and its effect on the tensile properties of the FSWed AA6061 alloy.

2.3 Study of creep deformation behaviour in weldments

In this section literature regarding the high temperature creep deformation in the welded materials are discussed with a special attention given to the IC behaviour of the FSWed joints. Researchers have evaluated the FSWed joint quality in terms of mechanical attributes through several methods. Rao et al. (2010) suggested evaluating the joints by uniaxial tensile tests. The authors have used hardness measurement and investigated the variation of strength across the weld area, as hardness measurements can be able to provide approximate information related to the variation in the stress-strain behaviour. Ceyhan and Papierflieger (2007) discovered a sophisticated method for the measurement of the local stress-strain behaviour in welded materials by micro tensile specimen taken out from the welds. Their research has also been concentrated on the proficiency of the indentation creep (IC) test to afford the tensile properties of the welded material. Phani and Oliver (2016) pointed out that IC process is a popular method to study the high-temperature deformation properties for its simplicity in the instrumental arrangement and simplicity in carrying out the experiments. Liu et al. (2007) reported that the process can be applied in many fields due to its numerous advantages as it requires only a tiny test area, comparatively less testing time than the conventional creep testing method and cheap. Torre et al. (1991) cited the IC test as a non-destructive process which decreases the properties variation from sample to sample. Chu et al. (1977) stated that the IC test is a localized creep testing method. In this a flat end straight cylinder-shaped indenter of diameter '*d*' is pressed with a constant load '*p*' on the surface of the specimen. The creep sample and the indenter are embedded in the vertical furnace kept at the same temperature and environment throughout the whole experiment. A linear variable differential transducer (LVDT) measures and record the time dependent penetration depth of the indenter into the sample. IC tests are applied to the FSW joint to estimate the joint quality through analyzing the local stress strain behaviour. Haeberle et al. (2007) inspected the creep resistance as well as other mechanical properties such as tensile strength and compressive strength through micro indentation technique. Wang et al. (2014) carried out compression creep test on FSWed oxide dispersion strengthed Ni-Cr alloys as well as on as-received material at different temperatures conditions and estimated the the creep parameters like stress exponents of the power law creep. They observed that the creep resistance of FSWed material was lower than the BM and an after-weld heat treatment at 1598 K for 1 hour had significantly improved the creep strength due to the coarse-grained microstructure. Rao et al. (2010) by a new technique determined the local stress–strain properties of FSWed AA 5083 sheet based on instrumented indentation testing and found that the results were compatible with that obtained from micro-tensile testing. Spigarelli et al. (2011) studied the effect of FSW on the minimum creep rates of magnesium alloys and also determined the minimum creep rate of the BM at different temperatures. They compared the results and found that the variation in the creep properties was due to the changes in the solid solutions and microstructural features. Except for FSWed specimen, the IC test method is also applied in other welded materials. Vijayanand et al. (2014) studied the IC behaviour of the high Nitrogen grade 316LN SS manual metal arc welded joint at weld area, BM and heat-affected zone (HAZ) and found that the creep deformation characteristics were not identical at each selected zones. The variation was due to the variation in the microstructure and morphology of the joint. They were able to correlate the IC data with the uniaxial creep data and established a good relation. Prasanna et al. (2016) correlated the mechanical properties of the stainless-steel welded joints derived from IC studies at different test temperatures with the ultimate tensile strength of the welded sample and developed useful correlation equations. Yanga et al. (2018) carried out in-situ creep test at the subzones in a CrMoV weldment at HAZ. The creep strength was highest at the weld pass metal in the welding direction decreased in the order of multiple welds passes through the thickness direction and HAZ and showed an inverse trend with that of the creep ductility. IC test differs from the conventional creep testing as: (i) it is less destructive, quick to perform and a small quantity of testing material is sufficient. (ii)a constant stress can be obtained with a constant load. (iii) the temperature and stress dependence of the steady-state (or minimum) creep rate can be obtained on a single specimen so the sample-to-sample property variation is less and (iv) absence of the tertiary stage of IC test unlike the conventional creep makes the deformation more stable and hence the test is better suitable for investigating near brittle materials.

As the IC test can accommodate very small area of load application, the test can be conducted at a localized zone requiring only very small sample size across which the properties change, requires only less time and is cost effective (Das et al., 2018). Constant load creep tests are carried out on the FSWed magnesium alloy (Mg Alloy) joint along with the BM and the creep rates at different temperatures were compared, the microstructural evolution during the high temperature creep deformation was studied (Spigarelli et al., 2011). The IC behaviour at constant loading conditions of FSWed polyethylene plate welded with different process parameters was studied and found that the creep resistance increased after FSW process (Hoseinlaghab et al. 2015). Heat treated oxide dispersion strengthened Ni-Cr alloy joined by FSW process exhibited superior creep properties than the as welded sample and BM. The threshold stress was found to be dependent on grain size and temperature (Wang et al. 2014). Creep properties were reported to be reduced after the friction stir processing of AA2024 -T3 than the BM. The authors have developed a modified constitutive model of the creep deformation considering the variation in the microstructure and mechanical properties of the processed alloy (Santecchia et al., 2020).

Except FSWed specimen IC technique was also employed to estimate the deformation behaviour at high temperature on fusion welded specimen. IC behaviour of P9 steel at individual zones of the weld carried out with different conventional welding processes was investigated and result was correlated with the uniaxial creep parameters (Surya et al., 2019). Automated ball indentation creep method was employed at different temperatures to realize the tensile properties of the weld zones of fusion welded 316LN stainless steel. The weld metal represented the best tensile properties and the BM and the HAZ showed improved work hardening behaviour than the welded metal (Ganesh Kumar and Laha 2015). IC test method was applied to high nitrogen grade of 316LN SS manual metal arc welded joint to evaluate the local creep behavior of different weld regions. The variation in the creep properties were correlated to the dissimilar microstructural features of the welded area (Vijayanand et al. 2014). The localized mechanical properties of the modified indirect electric arc welded AA6061 at BM, weld metal and HAZ were estimated by indentation creep technique and the evolution of weld zones with respect to the heat input of the welding method was realized (Ambriz et al., 2011).

Except IC test, creep properties of the FSWed material were also evaluated by instrumented creep testing process. By instrumented creep test method, the creep resistance of FSWed 9% Chromium martensitic-ferritic steel which is dependent on the precipitate evolution at the micro grain boundaries were studied and found out that the precipitated lave phase particles deteriorate the creep strength of the welded material than the BM (Cui et al., 2019). The effect of heterogeneity in the microstructure of the HAZ in the FSWed joint of 9Cr 1.5W RAFM steel was studied. The particle coarsening after the FSW process decreased the creep resistance of the welded sample (Zhang et al.,2019). The creep deformation properties of the FSWed pipes of poly-methyl methacrylate along with the BM at constant loading conditions with different initial stress and temperatures were studied. The creep life of FSWed pipes subjected to the effect of both internal pressure and rotation were found to be lower than the BM. Modeling for creep deformation by constitutive models were also carried out (Vakili-Tahami et al., 2019). Instrumented IC testing method was employed to FSWed AA5083 to figure out the variation in the localized stress strain properties. A neural network method was employed to validate the change in the mechanical properties as well (Rao et al., 2010).

2.4 Fatigue crack growth rate (FCGR) studies of FSWed Al Alloys

Friction stir welding of plates results in non-homogenous microstructures resulting in different weld zones viz, NZ, TMAZ, HAZ and the BM. The non-uniformity in the microstructure is mainly due to the variation in grain size and orientation and is of high concern among researchers with regard to the fatigue performance of the components.

Investigation by Jata et al. (2000) revealed that the non-homogeneity in the microstructure of weldment resulting from the FSW process decreased the resistance to fatigue crack growth rate (FCGR) of the material. Pouget et al. (2008) investigated the effect of weld microstructure and the residual stress developed during the FSW process on the fatigue behavior of AA2050. The fatigue crack propagated along both parallel and perpendicular directions of the weld. During crack propagation parallel to the weld direction, FCGR was faster through the NZ compared to the base alloy. However, considering FCGR in the direction perpendicular to the weld direction, considering the correlation between effective stress intensity factor Δk_{eff} and crack propagation rate da/dN and microstructure changes at various weld zones, the authors observed higher FCGR in the NZ, which was characterized by fine grain size, compared to other weld zones. Zhang et al. (2020) studied the fatigue crack propagation (FCP) characteristics of Al alloy FSWed and found that the resistance of NZ was inferior to the HAZ and BM due to the finer grain structure at NZ. D'Urso et al. (2014) investigated the effect of welding parameters on the FCGR of FSWed AA6060 and found that NZ exhibited lower FCGR than the other zones at low ΔK values. They also investigated the rate of FCG at different weld zones of FSWed AA6060 and reported the slower crack growth in the weld NZ than the BM.

Tra et al. (2012) investigated that residual stress and hardness of the FSWed AA6063-T5 had negligible effect on the FCGR in SZ, rather the recrystallized microstructure played a more essential role in this case. Gavras et al. (2010) found that in the absence of weld residual stress, microstructural features have a great impact on the FCGR in FSWed AA6061-T61 as well as other light weight metals. The threshold value for the FCG in ultra-fine grains lowered due to the crack deflection. To identify the origin of the fatigue crack in the FSWed joint, researches carried out further investigations considering different factors. Lemmen et al. (2011) studied crack origins, examining the TMAZ and HAZ and the effect of the weld line angle on fatigue life. Basel et al. (2016) evaluated the location of the fatigue origin of FSW joints for different welding conditions. Sharma and Mishra (2008) studied the origin of FCG in friction stir processed Al alloy and investigated the effect of precipitate distribution in fatigue crack origin. The effect of stress ratio (R) has a great role on the FCGR. Okada et al. (2017) considered three 'R' ratios of 0.1, 0.4, and 0.7 to study the FCP behavior of FSWed Al alloy and found that with the increase in the stress ratios, the FCGR of the FSWed specimen followed the similar trend as the BM. Also the BM showed a better FCG resistance than the FSWed sample with a decrease in R value. On contrary, Ma et al. (2013) did not notice any effective difference in FCGR at the NZ and BM of FSWed specimen with R ratios. However, Tanaka et al. (2013) evaluated the influence of stress ratio on FCG in friction stir Al alloy weldments.

In FSW process, the metal gets plasticized and the temperature may rise to more than 400 °C due to which the strengthening second phase precipitates are either coarsened or dissolved in the matrix thereby degrading the tensile properties. To restore the properties, a heat treatment (HT) process after FSW was carried out and the effect of post weld heat treatment (PWHT) on the FCGR was studied. Sivaraj et al. (2014) reported that FCGR at NZ improved and was comparable to BM after PWHT. HT process followed by aging after FSW results in re-precipitation of the strengthening precipitates that improves the mechanical attributes. Kafali and Ay (2014) performed PWHT on FSWed Al alloy and found a decrease in the FCG properties but increase in the hardness. The decrease in the fatigue properties was due to the defects like porosity in the weld joint. Tra et al. (2012) conducted a post weld solutionising HT to FSWed Al alloy to restore the softened hardness at and around the weld zones that improved the mechanical properties and FCP behaviour of the joint.

Yadav et al. (2020) studied the microstructural effect of FSWed AA2024 on fatigue crack growth rate (FCGR) at constant load ratio and found that the threshold stress intensity factor increases after treatment (HT). Ilman et al. (2013) studied the FCP behavior of FSWed AA2024-T3 and reported that at low stress intensity factor range the FCGR at nugget zone (NZ) was lower than the others. Zhang et al. (2020) studied the FCP characteristics of FSWed AA6061 along with other mechanical properties like microstructure and hardness and found that the FCG resistance of NZ was inferior to the heat affected zone (HAZ) and base material (BM). Moghadam and Farhangdoost (2016) estimated the dependency of FCP properties of the FSWed AA2024-T351 at NZ on the tool rotational and traverse speeds and found that the fracture toughness of the joints was lower at both lower and higher traverse speeds. The FCP rate at NZ was lower than the BM at low values of stress intensity factor range and faster at high values of stress intensity factor range. Urso et al. (2014) investigated FCGR at different weld zones of FSWed AA6060 and reported the slower crack growth in the weld NZ than BM.

Fatigue crack growth rate are also known to be sensitive to the stress ratio i.e., R ratio ($\sigma_{min}/\sigma_{max}$). Okada et al. (2010) studied the FCP behavior of FSWed Al alloy at three different 'R' ratios of 0.1, 0.4, and 0.7 and found that at higher stress ratio the FCP rate of the FSWed specimen was same as the BM. With the decrease in the stress ratio, BM shows better FCP rate than the FSWed sample. Moreira et al. (2008) studied the effect of stress ratios on FCGR and reported that for both BM and NZ the FCGR was higher for high stress ratios. In contrast, Ma et al. (2013) inspected the effect of stress ratios on the FCP rates and found that the rate of fatigue crack propagation is not much sensitive to the R ratio in the NZ as compared to that in BM.

Mishra et al. (2005) reported that during FSW process temperatures may rise up to 400–500 °C at the NZ and other zones as a result of which the strengthening precipitates in the alloy matrix are either coarsened or dissolves in the matrix. These precipitates play a major role during the FCGR in the weld. Thus, HT process after FSW is opted to produce the desired change in the mechanical attributes due to re-precipitation of the strengthening precipitates by aging. The effect of HT after FSW on the FCGR was studied. Sivaraj et al. (2014) stated that the FCGR of FSWed Al alloy was more than the BM due to the dissolution of the strengthening precipitates in the weld NZ. After HT of the welded component, the FCG resistance improved and was almost equal to the BM. Kafali and Ay (2009) performed the solutionizing HT at 550 ºC followed by artificial aging on FSWed Al alloy specimen and observed an increase in the hardness but a reduction in fatigue strength due to the weld defect like porosity in the joint. Costa et al. (2017) compared the effect of HT after FSW under cyclic and monotonic loading and concluded that FSWed joint shows better mechanical attributes in monotonic loading in compared to cyclic. Tra et al. (2012) conducted a post weld solutionising treatment and HT followed by aging on FSWed Al alloy to improve the mechanical properties and FCG behaviour.

2.5 Major Gaps from the Literature

From the literature survey, several research gaps are evident where research intervention is required. Few of the research gas are as follows:

- The material deposition and microstructural evolution at NZ of the FSWed AA2014 and the impact of plunge depth and tool pin profile on the weld is not understood clearly.

- No studies have so far been reported regarding the creep deformation behavior at different weld zones of FSWed AA2014. This can be investigated by IC testing
- Limited studies are present on the investigation of FCGR along various weld zones of FSWed AA2014 Al alloys. Also, only few reports are available regarding the study of FCGR of FSWed weldments after post weld heat treatment.
- Detailed investigation is required regarding the effect of process parameters especially the effects of tool pin profile, welding speed, rotational speed and plunge depth on microstructural and mechanical properties of FSWed AA6061-T6 aluminium alloy joint.
- Very less studies have so far been reported regarding the impression creep deformation process at localized weld zones in FSWed AA6061-T6 Al-alloys.
- Almost no information is available regarding the fatigue crack growth rate along different weld zones in FSWed AA6061-T6 Al-alloys. Study in this line can identify the weakest region during fatigue loading.

2.6 Objectives of the present work

The main objectives of the present work are as follows:

- Carry out welding experiments to identify the best combination of process parameters for FSW of AA2014 alloy.
- Study the high temperature creep deformation behaviour at different weld zones of FSWed AA2014 through IC technique.
- Study the FCG behaviour through different weld zones of FSWed AA2014 Al alloy weldment before and after HT.
- Study the effect of process parameters on strength, microstructure and fatigue properties of FSWed AA6061-T6 Al alloy weldments.
- Investigate the impression creep deformation behavior at localized weld zones of FSWed AA6061-T6 Al alloy weldment.
- Analysis of FCGR behaviour at selected weld zones of FSWed AA6061-T6 Al-alloy weldment before and after HT.

The methodology adapted to complete the stated objectives, observations and summary of the present work are discussed in detail in the subsequent chapters.

Chapter 3

Experimental Procedures

3.1 Introduction

This chapter describes in detail the experimental procedures and techniques followed for achieving the objectives of the work. The different experimental set up used for the FSW, the post welding processes, the equipment used and the techniques adopted for the characterization have been presented. The post welding processes carried out *viz.*, sample preparation, heat treatment, mechanical test procedure and macro/ microstructural characterization, etc., have been presented in detail in the subsequent sections.

3.2 Material Preparation

The base materials for the FSW were obtained in the form of plates. The two mating edges of the plates to be welded were milled to get better surface alignment which were further smoothed by filing. Subsequent polishing using SiC polishing paper was done in order to avoid any gap between the adjacent plate edges. Prior to the FSW process, the workpiece surfaces to be welded, tool pin and the shoulder surface which will be in contact with the plates were cleaned by acetone to remove any dirt, grease or oil that might have been present at the edges. After FSW, samples of the required dimensions were machined using a wire cut EDM machine and band saw followed by milling operation.

3.3 Experimental Methodologies

Two different types of Al alloys, namely AA2014 and AA6061-T6 were considered for the experiments. For each alloy similar sets of experiments are performed. Three sets of experimental analysis were performed by using AA2014 Al alloy and similarly another three sets by using AA6061-T6 Al alloy. The whole experiment was divided into few sub-groups depending on the type of process adopted and grade of Al alloy considered. The following sections represent the sub-groups as mentioned.

3.3.1(a) Optimization of Process Parameters for the FSW of AA2014 Al.

It was necessary to identify the optimum combination of process parameters for obtaining the best quality weldment. After optimized process conditions further experiments like the impression creep studies and fatigue crack growth rate studies can be carried out. Experiments were carried out to optimize the process parameters to get the best defect-free weldment and the effect of process parameters on the mechanical properties were investigated. In this case a total set of 16 experiments were performed by considering 5 individual process parameters. The base material (BM) used is AA2014 Al alloy plates of 6 mm thickness. As per the standards, the chemical composition (wt.%) of this alloy is Cu: 3.9-5%, Fe: 0.7%, Mn: 0.4-1.2%, Mg: 0.2-0.8%, Cr: 0.1%, Si: 0.5-1.2%, Ti: 0.15%, Zn: 0.25% and balance Al. The composition of the alloy, determined by EDX analysis is shown in Table 3.1 and indicates that the alloy is AA2014. Mechanical properties of the AA2014 alloy as per the ASTM standard are shown in Table 3.2.

Table 3.1 The chemical composition (weight %) of AA 2014

Cu	Si	Mn	Mg	Fe	Zn	Al
4.7	1.2	0.5	0.4	0.3	0.2	Balance

Table 3.2. Mechanical attributes of the base material

YS (MPa)	UTS (MPa)	Elongation (%)	FS (MPa)	Bend angle (°)	Hardness (HV)
350	460	13	545	140	105

A knee-type vertical milling machine (Fig. 3.1) was used for the FSW of the AA2014 alloy plates. The machine has provision for different spindle rotational speeds ranging from 50 to 1500 rev/min in 12 steps and different welding speeds ranging from 22 to 550 mm/min in 8 steps. FSW tools of H13 tool steel with a pin length of 5.6 mm (decided according to the plate thickness) designed with 4 different tool pin profiles were used for this process. Figure 3.2 shows the photographs of 4 tool pin profiles: (a) straight cylindrical (STC), (b) tapered cylindrical (TAC), (c) threaded cylindrical (THC) and (d) square (SQ). The 100 mm×100 mm×6 mm dimension plates were welded by using FSW set up in the rolling direction in a single pass butt joint configuration. As mentioned in Section 3.2, the plates were edge prepared to obtain nearly zero gaps and the surface was cleaned by acetone to avoid any chance of defect in the welds due to foreign particle. FSW was done by varying the five process parameters presented in Table 3.3. For each considered process parameter, three experiments were performed for repeatability. The results of the repeated experiments indicate very negligible variation.

Subsequent to the FSW process, specimens were prepared from the weldments for carrying out tensile test, flexural test, three-point bending test, micro-hardness test and metallographic analysis. Figure 3.3 shows the photograph of the test specimens machined from the weldment. The tests were carried out to assess the weld quality. The average values of ultimate tensile strength (UTS), yield strength (YS), percentage elongation (%E), bending angle, flexural strength (FS), hardness at different zones (HV) were determined and microstructure of the welded region was also investigated. Tensile tests were carried out following the ASTM E8M-04 standard using a hydraulically operated servo-controlled dynamic universal testing machine (UTM) (Make: INSTRON; Model: 8801). The elongation during the tensile test was measured by using 50 mm gauge length extensometer attached to the specimen. The bending test was carried out to determine the FS and bending angle using a 3-point bending test set up compatible with the UTM. The hardness of the HAZ, TMAZ, NZ as well as BM was measured using a Vickers micro hardness tester by applying a load of 500 gmf for a dwell time of 10 seconds.

Fig. 3.1. The FSW setup used for the experiments

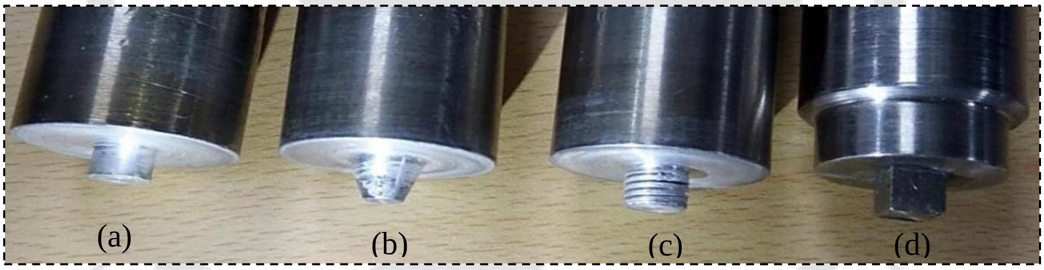

Fig. 3.2. Tools used for FSW process (a) Straight Cylindrical (STC) (b) Tapered Cylindrical (TAC) (c) Threaded Cylindrical (THC) (d) Square (SQ)

The macro/microstructure of the weldment was studied using an optical microscope (OM) (make: Carl Ziess, model: Axiotech). The specimen was mounted in cold setting resin. This was then dry polished using different grades of abrasive papers (grit sizes in the order of 300, 600, 800, 1000, 1200, 1500, 2000 and 2400) and subsequently cloth polished using alumina suspension in water following the standard metallographic sample preparation procedure. In order to observe bead geometry, grain distribution and variation in the grain size of the different weld zones, the specimen were etched using modified Keller's reagent. After etching, the microstructure was investigated using the OM. The failure surfaces of the tensile tested samples were investigated using a field emission scanning electron microscope (FESEM).

Table 3.3 Experiments conducted with different process parameter combinations

Exp. No	Shoulder Diameter (mm)	Plunge Depth (mm)	Tool Pin Profile	Tool Rotation Speed (rev/min)	Welding Speed (mm/min)
E1	16	0.03	Straight cylindrical	600	22
E2	20				
E3	**24**				
E4	28				
E5	24	**0.06**	Straight cylindrical	600	22
E6		0.09			
E7		0.12			
E8	24	0.06	Tapered Cylindrical	600	22
E9			Threaded Cylindrical		
E10			**Square**		
E11	24	0.06	Square	**815**	22
E12				1100	
E13				1500	
E14	24	0.06	Square	815	36
E15					**63**
E16					98

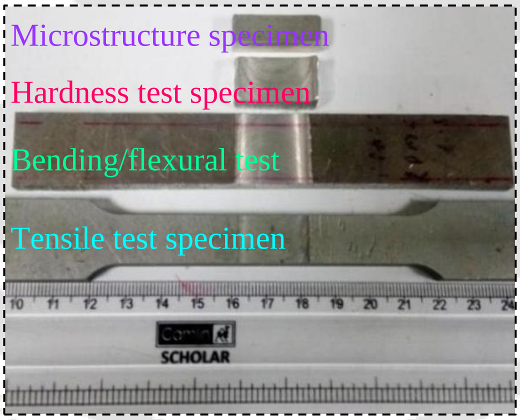

Fig. 3.3. Photographs of different test specimens extracted from the welded plates.

3.3.1(b) Optimization of Process Parameters for FSW of AA6061-T6 Al

The FSW experiments of AA6061-T6 Al alloy were carried out for various process parameters and their effect on mechanical and microstructural properties were also evaluated. A total of 10 experiments were conducted with 4 process parameters with the objective of obtaining joints with best mechanical attributes. The alloy used for this investigation was commercially purchased AA6061-T6 alloy plates of dimension 200×100×6 mm with chemical composition (in weight percentage) of Mg: 0.8%-1.2%, Si: 0.4%-0.8%, Cu: 0.15%-0.4%, Cr: 0.04%-0.35%, Fe: 0.7%, Mn: 0.15%, Ti: 0.15%, Zn:

0.25% and balance Al. The composition was also analyzed by EDX. The plates were FSWed in single pass butt configuration. The mechanical properties of the as-received BM plates, determined from the tensile test, are presented in Table 3.4. The parameters considered for the present study are tool pin profile, plunge depth, tool shoulder diameter and tool tilt angle at different levels. However, from the trial experiments and our previous research work the welding speed of 60 mm/min and the rotational speed of 875 rev/min are kept constant for all the experiments. The range and values of each process parameter are presented in Table 3.5. FSW tools of H13 tool steel with different tool pin profiles as shown in Fig. 3.2 were used for this investigation with the only difference that the pin length, as determined from the plate thickness, was fixed as 5.6 mm for all experiments. FSW experiment was carried out on the same machine setup as shown in the Fig.3.1.

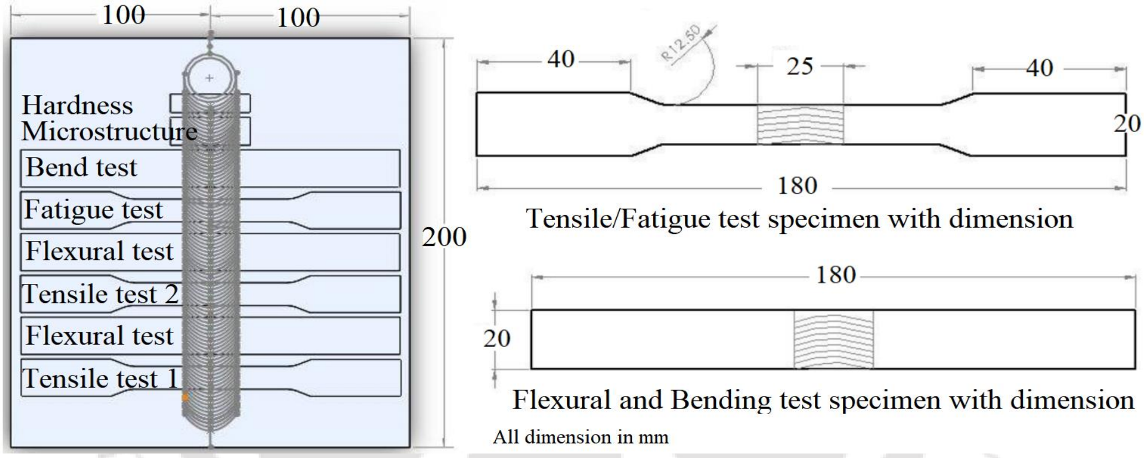

Fig. 3.4. Schematics of extraction of different test specimens from the welded plates and specimen geometry

Table 3.4. The mechanical properties of the as-received AA6061-T6 alloy plate

Ultimate Tensile Strength (MPa)	Yield Strength (MPa)	Elongation (%)	Flexural Strength (MPa)	Bending Angle (°)	Grain Size (μm)	Hardness (HV)
310	270	11	505	140	85	105

The quality of the weld processed under the conditions mentioned in Table 3.5 was evaluated following the similar tests procedures mentioned in Section 3.3.1(a). Figure 3.4 shows the details regarding the specimen geometry and the locations of various specimens which were extracted from the welded plates. Joint quality attributes such as UTS, YS, %E, bending angle, compressive strength as well as HV at different weld areas viz. NZ, TMAZ and HAZ were determined along with the macro-microstructural analysis for each test specimen.

Table 3.5 Considered process parameters for the present work

Exp. No	Shoulder Diameter of Tool (mm)	Plunge Depth (mm)	Tool Tilt Angle (°)	Tool Pin Profile
E1	18	0.03	1	Straight Cylindrical (STC)
E2	**21**			
E3	24			
E4	21	**0.06**	1	Straight Cylindrical (STC)
E5		0.09		
E6	21	0.06	**2**	Straight Cylindrical (STC)
E7			3	
E8	21	0.06	2	Tapered Cylindrical (TAC)
E9				**Square (SQ)**
E10				Threaded Cylindrical (THC)

* Tool rotational speed 875 rev/min and welding speed 60 mm/min are fixed

3.3.2 Impression Creep Testing

Impression creep (IC) test is carried out as an alternative and fast technique to obtain the creep deformation behavior-of the weldments. The general principle of the IC testing is shown schematically in Fig. 3.5. A cylindrical flat end indenter having diameter ‘D’ is pressed on the work piece at a constant temperature and compressive loading *‘P’*. The time dependent flow of material under the indenter is understood by recording the impression depth (*d*) which is a function of lapsed time. The equivalent compressive stress (σ) which is the mean pressure beneath the indenter for the IC process was found to be

$$\sigma = \frac{4P}{\pi D^2} \tag{3.1}$$

IC tests were carried out in an indentation creep testing setup (Make: Spranktronix). Figure 3.6 shows the photograph of the IC testing set up used for the present study. The set up consists of the following basic units: (i) a loading frame for load application, (ii) dead weights, (iii) extension rods to transfer the load from the loading frame to the sample, (iv) indenter holder fitted at the end of the extension, (v) sample holder, (vi) thermocouple, (viii) PID controller for temperature control, (vii) resistance heated furnace for heating the test sample (ix) linear variable differential transducer (LVDT) for measurement of indenter displacement and (x) data acquisition system (DAQ) for measurement and acquiring the temperatures, load and indenter displacement data.

During IC test, the load was applied through the tension rod on to the indenter and was measured through the load cell. The sample and the indenter assembly were surrounded by a vertical furnace. The displacement of the indenter was measured through LVDT. The correctness of the displacement and the thermal control were up to 0.1 mm and ±1ºC respectively. The creep curves were acquired and recorded by the DAQ. Creep curves were obtained only for the primary and secondary creep regions since in IC tests, tertiary creep region is generally not obtained. IC tests were stopped after achieving a steady-state creep stage. Assuming power law equation, the creep parameters for the different weld zones are determined at the secondary creep.

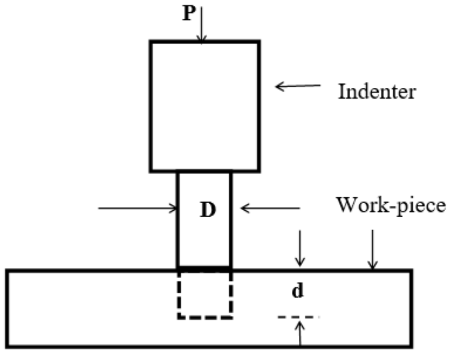

Fig. 3.5. Schematic diagram illustrating the IC test

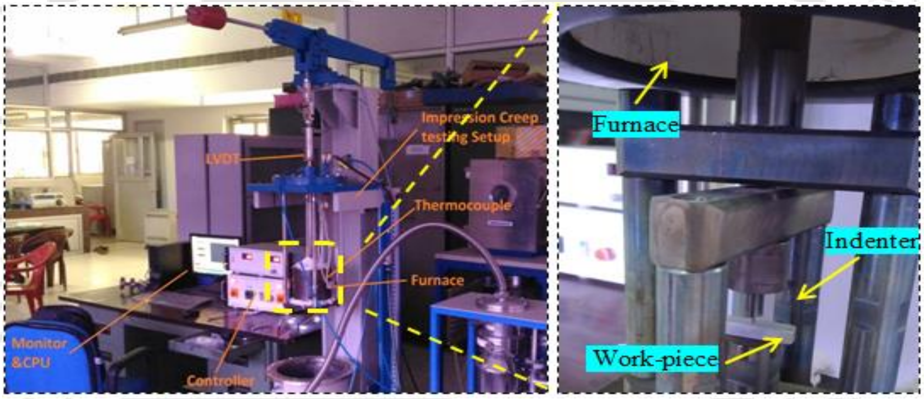

Fig. 3.6. Impression creep test setup and indenter-work piece assembly of the furnace.

IC tests were carried out at temperatures greater than $0.5T_m$ where, T_m is the absolute melting point temperature. The applied constant stresses were in the range of (40 – 90) % of the measured yield strengths at the respective temperatures. The creep equation considered in the present study was of a power law creep expressed as

$$\dot{\varepsilon} = A\sigma^n e^{\left(-\frac{Q}{RT}\right)} \qquad (3.2)$$

Where $\dot{\varepsilon}$ is the steady-state creep rate, n is stress exponent, A is a constant, Q is activation energy for the process, R is the universal gas constant, T is the temperature in K and σ is equivalent stress. The equivalent stress for the IC test is calculated using equation 3.1 with the value of D = 1 mm

The steady state creep rate $\dot{\varepsilon}$ is calculated as the lowest creep rate value found from the strain rate vs. time curve for each experimental condition. The value of stress exponent n is determined from the slope of the linear fits of the log-log plots presented as the function of $\dot{\varepsilon}$ with respect to the equivalent stress (σ). The apparent activation energy for the IC deformation processes (Q_{ic}) is evaluated from the slope (slope $=\frac{Q_{ic}}{2.3R}$) of the semi logarithmic plot ln($\dot{\varepsilon}$) vs (1/T) at constant stress, where T is in K.

3.3.2 (a) Impression Creep Testing of FSWed AA2014 Al Weldments

One of the objectives of the present work is to understand the high temperature deformation of different weld zones by IC test. The present section describes the procedures followed for the IC testing of FSWed AA2014 Al alloy weldments. From the results of the experiments mentioned in Section 3.2.1(a), the welding of plates was carried out using the process parameters obtained for the best welding conditions thereby obtaining defect free weldment.

The process parameters for obtaining the best weldment were square tool pin, 24 mm shoulder diameter, tool rotation speed 815 rev/min, welding speed 63 mm/min and single pass butt FSW. Sufficient number of plates necessary for carrying out all experiments were welded under the above conditions. Samples with dimensions 24 mm x 6 mm x 6 mm from the welded region (Fig. 3.7(a)) shown in Fig. 3.7(b) were machined for the IC tests. The machined samples were initially dry polished using SiC polishing papers and subsequently cloth polished using colloidal silica as medium to achieve a very smooth surface. Light etching was carried out using modified Keller's reagent of 2ml HF (48%), 3 ml HCL (conc.), 5 ml HNO_3 (conc.), 190 ml H_2O for revealing the NZ, TMAZ, HAZ and BM by macroscopic observation. Once various weld zones are identified, IC experiments were carried by placing the indenter on the specific weld zone. Tungsten carbide (WC) indenter with 1 mm diameter and 3 mm height fixed to the holder shown in Fig. 3.7(c) was used for carrying out the IC test at NZ, TMAZ, HAZ and BM.

The IC experiments were carried out at temperatures above 0.5 T_m (T_m = 620 ºC) where T_m is the melting temperature of alloy in Kelvin. For AA2014 alloy, T_m corresponds to 620 ºC. Test temperatures chosen corresponding to 0.5 T_m, 0.53 T_m, 0.56 T_m. ie., 310, 330 and 350 ºC respectively. Experiments were carried out at three stress levels for each test temperatures. The IC experimental test matrix are shown in Table 3.6 for each combination of temperature and stress. IC tests were carried out by placing the indenter at NZ, TMAZ, HAZ and BM of the weldment using the equipment shown in Fig. 3.6. In each zone, experiments were carried out for all the nine conditions specified in Table 3.6. The detailed procedure of the IC test is mentioned in Section 3.3.2.

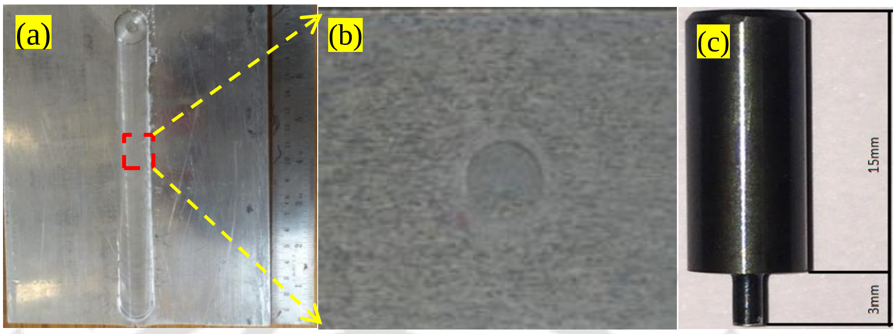

Fig. 3.7. photographs showing (a) FSWed plate with the weld location (b) IC tested sample with the impression of indenter and (c) WC indenter

Table 3.6 Experimental matrix for the impression creep test

Exp. No.	Temperature Range (°C)	Stress Range (MPa)	Creep Test Zones
E1	310	21	BM, NZ, TMAZ, HAZ
E2		24	
E3		27	
E4	330	21	BM, NZ, TMAZ, HAZ
E5		24	
E6		27	
E7	350	21	BM, NZ, TMAZ, HAZ
E8		24	
E9		27	

In order to study the microstructure, the IC tested sample was sectioned transverse to the load axis (i.e., parallel and along the impression mark). Proper care was taken during the sectioning as well as polishing. The sectioned surface was mirror polished, metallographically etched and the microstructure below the indenter in each localized zone was investigated under the OM. The hardness after the IC test was determined using a micro-hardness tester. The detailed microstructure of the IC tested samples were investigated using FESEM. EDX analysis of the second phase particle was performed to determine the chemical composition of the second phases precipitated during the IC test.

3.3.2(b) Impression Creep Testing of FSWed AA6061-T6 Al Alloy

The objective of this section is to highlight the procedure of IC testing and microstructure studies of IC tested AA6061-T6 weldment. Samples are taken from the best welded plates of AA6061 Al alloy of Section 3.3.1(b). The plates were FSWed using a square pin tool of 21 mm shoulder diameter at tool rotation speed 875 rev/min and welding speed 60 mm/min, plunge depth of 0.06 mm and 2º tool tilt angle in a single pass butt FSW. For the extraction of IC test samples from the welded plate the same preparation method was adopted as in previous case (Section 3.3.2(a)). The IC experiments were performed on BM and NZ, TMAZ and HAZ of the FSWed samples using the same IC test set up mentioned in Section 3.3.2. A set of 9 experiments were carried out with the combinations of temperature and stress for each selected zone as given in Table 3.7. The procedure of carrying out the experiments were similar to that followed for the AA2014 alloy. Macro/microstructural evolution and characterization of IC tested sample was carried out and the sample was prepared according to the method as mentioned in Section 3.3.2(a).

Table 3.7 Experimental matrix of IC testing for AA6061-T6 weldment

Expt. No.	Temperature (ºC)	Stress (MPa)	IC test zones
E1	326	24	BM, NZ, TMAZ, HAZ
E2		28	
E3		32	
E4	359	24	BM, NZ, TMAZ, HAZ
E5		28	
E6		32	
E7	378	24	BM, NZ, TMAZ, HAZ
E8		28	
E9		32	

3.3.3 FCGR Studies along Different Weld Zones of FSWed Al Alloy

The procedure of carrying out the fatigue crack growth rate (FCGR) experiments of FSWed weldments is presented in this section. For this purpose, compact tension (CT) specimen were machined out from the best weldments in both as-welded defect free as well as post weld heat treated (PWHT) samples. The welded samples for metallographic observation were initially rough polished and etched with modified Keller's reagent to reveal the specified zones; viz. NZ, TMAZ and HAZ under OM. Once the weld zones were identified and properly labelled, the CT specimens were machined such that the machined notch tip of the CT specimen is positioned in the particular weld zone and the machined notch is aligned parallel to the weld direction. This is mainly to ensure that the crack propagation is along the particular weld zone. CT specimens were prepared as per the ASTM E-647 standards having width *(w)* of 50 mm and thickness *(t)* of 6 mm and surfaces were polished with 600 grit polishing papers. The orientation of notches during the sample preparation of the CT specimen is illustrated in Fig. 3.8. The geometry and photographs of the CT specimens are shown in Fig. 3.9(a-b) respectively. Photograph of the CT specimen attached to the testing setup, the crack growth direction and few fractured surfaces are presented in Fig. 3.10(a-c).

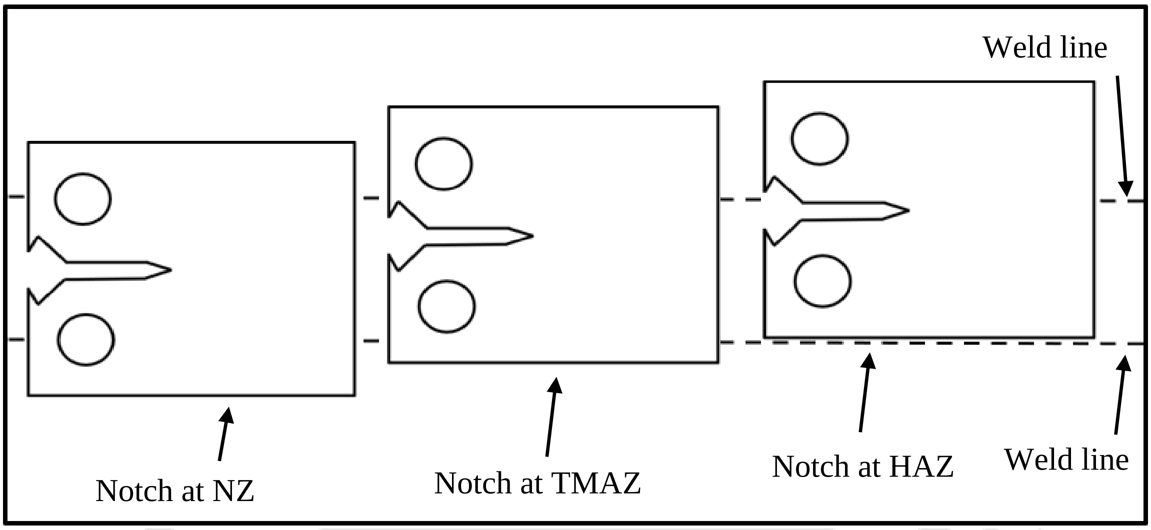

Fig. 3.8. Schematic extraction of CT samples from welded plate with initial notches at NZ, TMAZ and HAZ

FCGR experiments were carried out in the closed loop servo hydraulic controlled universal testing machine (UTM; Make INSTRON; Model: 8801) following ASTM E-647(1) and ISO 12108 (2) test procedures. Initially pre-cracking of the machined notch was carried out as per the standard. This was mainly to achieve a very sharp crack at the crack tip. After the pre-cracking, all the experiments were carried out at room temperatures at a constant P_{max} at a sinusoidal frequency. For the FCGR studies through each weld zone, experiments were done at three *R* values of with a constant amplitude cyclic loading. The crack length is measured by the crack opening distance (COD) gauge according to the concept of unloading compliance technique. The test is stopped when COD travel reaches the desired limit or crack becomes unstable.

The crack length vs. number of cycles (*a* vs. *N*) and ΔK vs. *N* data were recorded during the entire period of the experiment. The *a* vs. *N* data was smoothed by seven-point incremental method. From this, the *da/dN* vs. ΔK plot was evaluated and plotted. Stress intensity factors for each experimental condition are calculated by following the ASTM E647 guidelines. Using ΔK_{eff}, the effective stress intensity factor range for the FCGR testing, fatigue crack growth rate curves are obtained. Figure 3.11 shows schematically a da/dN vs. ΔK plot for general ductile alloys. For analysis of the data, especially for determining the constants of the *Paris law* for crack propagation through each zone for the three *R* values.

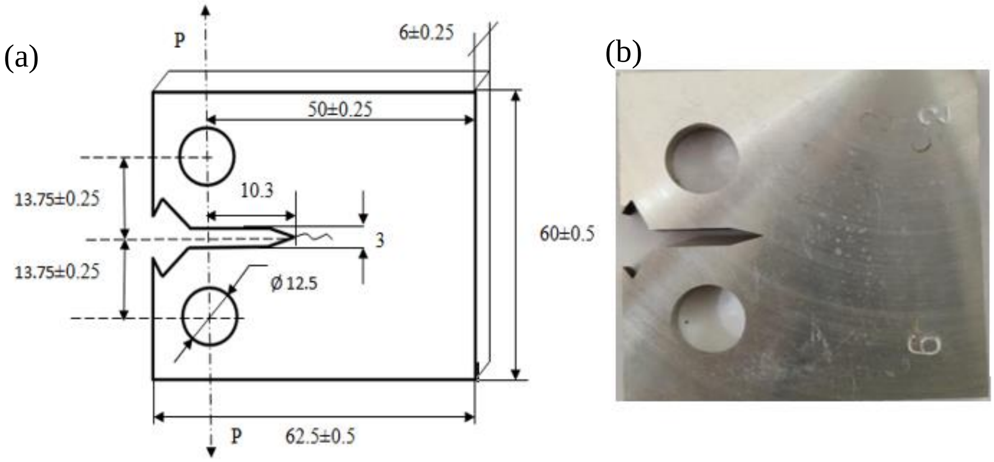

Fig. 3.9. Shows the (a) schematic drawing, and (b) photograph of a machined CT specimen

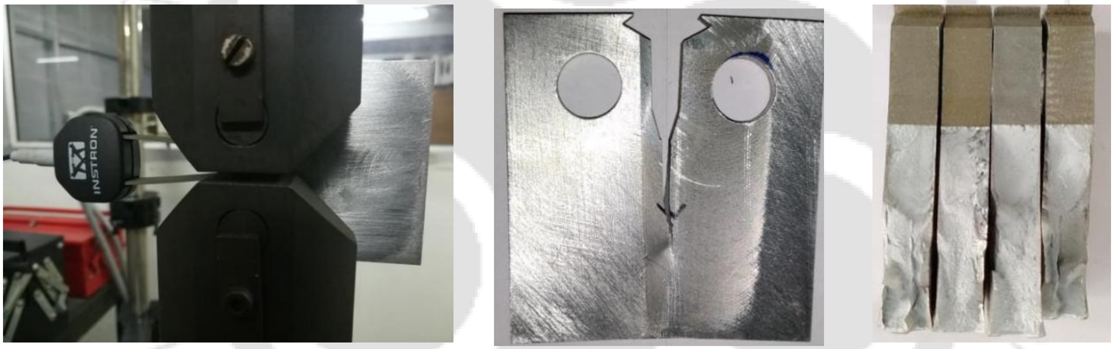

(a) (b) (c)

Fig. 3.10. Photographs showing (a) FCGR testing set up, (b) FCGR specimen crack line, (c) fracture surface after FCGR testing

Stage I as shown in the figure is called as threshold (ΔK_{th}) crack growth region where the FCG rate is considered to be almost zero, i.e., 10^{-10} m/cycle. Microstructural features affect the FCP rate at this region. In the stable crack growth region or *stage II*, for most of the metallic materials the FCGR generally lies in the range of 10^{-9} to 10^{-6} m/cycle.

Stage III is the unstable crack growth region that involves rapid crack growth of nearly10^{-6} m/cycle and the curve approaches the critical stress intensity factor (SIF) (K_{Ic}) of the material. The Paris law, da/dN vs ΔK is applicable only in uniform crack growth region *(stage II*). The Paris constants *C* and *m* are determined by curve fitting by the linear regression analysis, where *m* and *C* corresponds to the slope and intercept of the best fitted line. The maximum and minimum load values for the load ratios are selected as per the ASTM standard and is governed by the following relations,

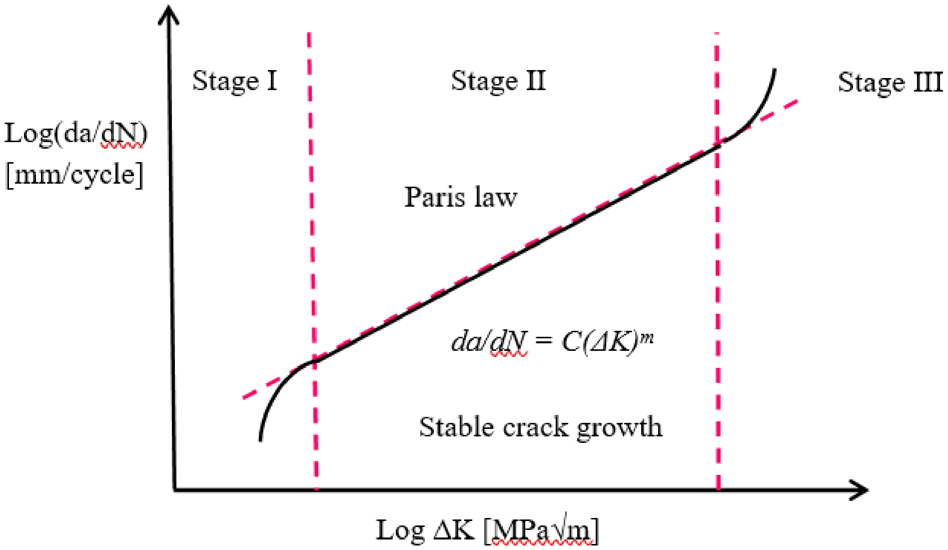

Fig. 3.11. Log-log plot of the da/dN vs ΔK regions during the FCGR test

$R=P_{min}/P_{max}$ (3.3)

$P_{max}=\Delta P/1-R$ (3.4)

$P_{min} = \Delta P/\ (1/R - 1)$ (3.5)

To get the FCGR, *Paris model* is implemented as follows:

$Da/dN=C(\Delta K)^m \quad for\ \Delta K > \Delta Kth$ (3.6)

Where *C* and *m* are material constants, ΔK_{th} is the threshold stress intensity factor range. The expression for ΔK for the CT specimen is given as:

$\Delta K=(\Delta P/B\sqrt{W})\ f(a/W)$ (3.7)

Where ΔP is the applied tensile load range, *B* the specimen thickness, *W* is width of the CT-specimen from load line, *a* is the initial crack length, and the function *f(a/W)* is:

$f(a/W) = [(2+\beta)/(1-\beta)^{3/2}]\ (0.886+4.64\beta-13.32\beta^2+14.72\beta^3-5.60\beta^4)$ (3.8)

Where $\beta = a/W$.

In order to achieve a uniform microstructure thereby avoiding the non-homogeneity in the properties across the weld, a post weld heat treatment (PWHT) of the welded samples were also carried out. The FCGR studies of the post weld heat treated samples were also carried out. Since, it was found that the heat treatment resulted in a homogenous microstructure across the weld, the studies were carried out only through the

NZ. Tensile tests and Vicker's micro-hardness tests were performed on the samples after HT and the results were compared to the results without HT. Metallographic study by OM was also carried out after the FCGR test. Fractographic study of the surfaces of the fatigue ruptured and tensile fractured specimen before and after HT was carried out by FESEM.

3.3.3 (a) FCGR Studies of Different Weld Zones in FSWed AA2014

The section is about the FCGR analysis at specified weld regions of the best FSWed AA2014 Al alloy sample in the as welded conditions and after PWHT. For the FCGR analysis, specimens were extracted from the defect-free best quality welds in terms of the mechanical and metallurgical properties achieved from Section 3.3.1(a). The samples are extracted from the FSWed plates welded with 24 mm shoulder diameter with squared pin, 0.06 mm plunge depth, tool rotational speed and welding speeds of 815 rev/min and 63 mm/min respectively with a single pass butt geometry. The dimensions and method of extraction of CT specimens for the FCGR study were as per that mentioned in Section 3.3.3. Figure 3.12 shows the photograph of CT samples extracted from FSWed plates. FCGR tests were performed at room temperatures at a constant P_{max} = 3.5 *kN* and sinusoidal frequency of 20 *Hz*. The studies are done at each weld zone at three *R* values of 0.1, 0.33 and 0.6 with initial notches at NZ, TMAZ, HAZ and BM. *Paris law* was employed in the crack propagation region and from the linear fits of the double logarithmic plot between the da/dN vs. ΔK, *C* and *m* values were calculated.

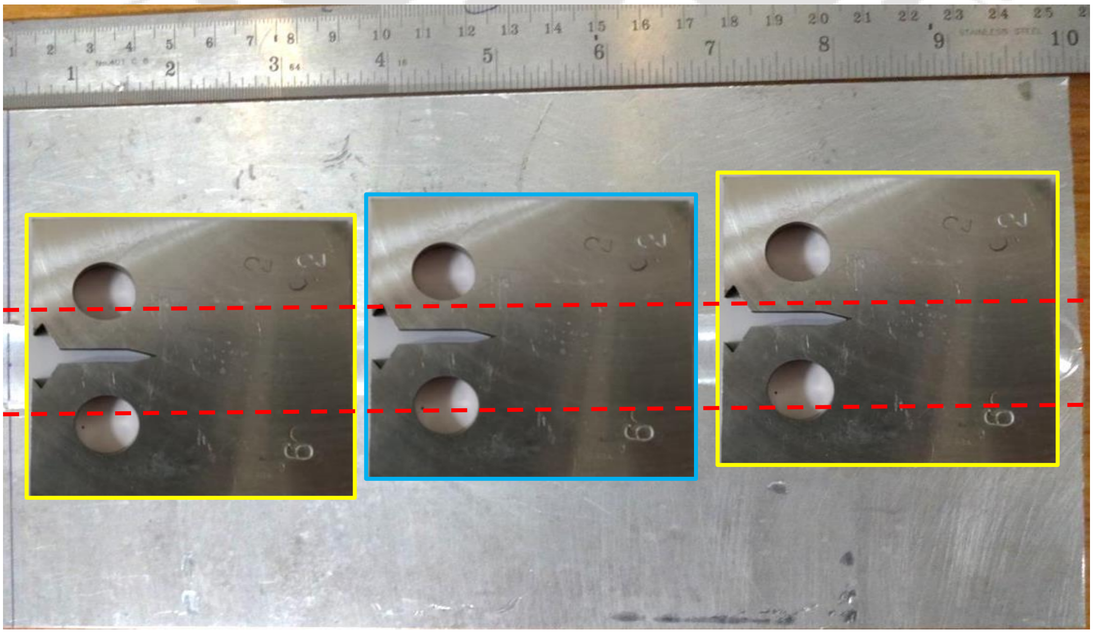

Fig. 3.12. shows the CT specimen location for different weld zones. Dashed line corresponds to the weld bead width

The samples were PWHT at 530˚C for 1hr then water quenched and then subjected to a precipitation heat treatment at 175 ºC for 18 hr. FCGR tests were performed at NZ with R=0.1 on the PWHTed sample. Tensile tests and Vickers micro-hardness tests were performed on the samples after HT and the results were compared to the results without HT. Metallographic study by OM was performed to visualize the microstructural characteristics. Fractography of the fatigue fractured and tensile tested sample after HT was carried out by FESEM.

3.3.3 (b) FCGR Studies of Different Weld Zones in FSWed AA6061-T6

The procedure followed for the FCGR studies of AA6061 Al alloy is presented in this section. As per the results obtained from the experiments mentioned in Section 3.3.1(b), the defect free and best welded samples were obtained when FSWed using a square pin tool having 21 mm shoulder diameter, a tool rotation speed 875 rev/min, welding speed 60 mm/min, plunge depth of 0.06 mm, 2º tool tilt angle and with a single pass butt FSW. The UTS, YS and flexural strength of the best considered sample was 97%, 98% and 98% of the BM respectively. The extraction of CT samples, geometry of the specimen used and preparation method of the FCGR sample is similar to that mentioned in Section 3.3.3(a). Crack growth studies through the BM, NZ, TMAZ and HAZ were done at the same P_{max} and the three R values opted for AA2014 Al alloy. The data recorded during the testing and post processing and analysis of data were carried out by the same procedure mentioned in Section 3.3.3(a).

In order to achieve a homogeneity in the microstructure and properties of the weld region, a PWHT was given to the welded sample. This was solutionising at 515 ºC for 1hr., followed by quenching in water and subsequently age hardening at 175 ºC for 18hr. The results obtained for the as welded and heat treated (HTed) samples were compared with the BM. Hardness values at various weld zones after HT was determined and the results were compared with the sample without HT. Tensile properties of the welded sample were estimated after HT. Microstructure and fractographic studies of the failed samples were carried out by similar procedure adopted for AA2014 Al weldments.

3.4 Tensile Test

Tensile tests were carried out per ASTM standards E8M-04, using the UTM in which the FCGR tests were carried out. Figure 3.13 depicts the schematic geometry of the tensile test specimen. A 50 mm gauge length extensometer was used to measure the elongation across the gauge length during the tests. Tensile specimens were machined from the as-welded and post weld HTed plates. For each experimental conditions two samples were tested and the average of the readings is reported in the present work. The UTS, YS and percentage of elongation are measured determined for the as-welded as well as post-weld heat treated samples.

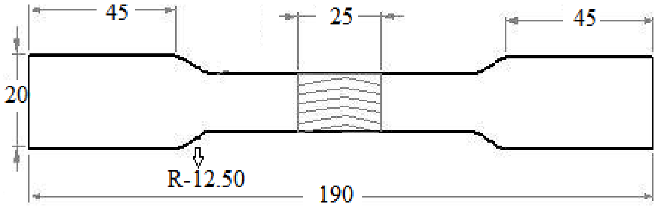

Fig.3.13. Schematic diagram of the tensile test specimen

3.5 Hardness Test

The hardness across the weld zone was measured using a Vickers micro-hardness tester as per ASTM standards E384 (Make: Buehler; Model: Micromet-2101). Figure 3.14 shows the photograph of the hardness testing equipment. The specimens for the hardness testing were sliced from the welded plates, normal to the welding direction. The sliced surfaces were metallographically polished dry using different grades of polishing papers in the order of grit sizes 200, 400, 600, 800, 1000 and 1500. The location at which the hardness measurement was carried out is illustrated in Fig. 3.15. Hardness was measured along three layers: near to the top, middle and bottom of the cross section. Each specimen consisted of 60 total considered points (20 points in one layer) at a regular spacing of 1 mm in the NZ and 2 mm in other zones. Hardness testing was carried out using a diamond pyramid indenter by applying a load of 500 gmf for a dwell time of 10s. Hardness was measured on the specimen after IC test just below the impression mark.

Fig. 3.14. Vickers micro-hardness measuring machine

Fig. 3.15. Hardness specimen with indentation marks

3.6 Flexural and Bend Test

Flexural strength of the welded samples was evaluated by bend test. Flexural test was carried out on the UTM machine according to ASTM E9-09 guidelines. A 3-point bending test fixture was used for flexural stress. A photograph showing the three-point bend bending test is presented in Fig. 3.16. The bending angle was measured for all sets of experiments through the bending test. The dimension and geometry of the test specimens employed to measure the flexural strength is given in Fig. 3.17. The specimen was placed in the 3-point bend test fixture and the load was applied at the centre. The load vs. ram displacement data was recorded and plotted. The flexural stress (σ_f) is determined from the maximum load before rupture using the relationship.

$$\sigma_f = \frac{3FL}{2bd^2} \tag{3.9}$$

where, F is the maximum applied load (N), L is the support span length (mm), that is 90 mm for the existing setup, b is taken as width of the considered beam (mm), that is 20 mm for all considered samples, d is the thickness (mm), which is 6 mm.

Fig. 3.16. Flexural/bending test setup connected to UTM

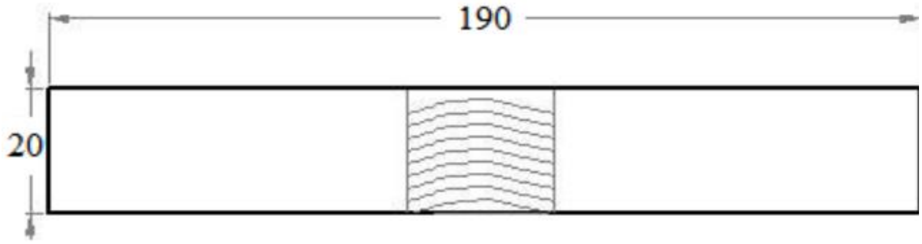

Fig. 3.17. Schematic of flexural and bending test specimen.

3.7 Macro/Microstructure Study by Optical Microscope

The weld bead geometry was studied using an optical microscope (Make: Carl Zeiss; Model: Axiotech-100HD). Figure 3.18 shows the photograph of the OM used for studying the microstructure of the joints after (i) FSW, (ii) Post weld heat treatment, (iii) IC test. All the welded sample's microstructure are compared with the BM. The specimen was sliced normal to the welding direction and polished with different grades of emery papers (400, 600, 800, 1000, 1200, 1500, 2000, 2500 grade). Final polishing was carried out by cloth polishing using alumina suspension as the abrasive medium. The specimens were then etched with modified Keller's reagent to reveal the microstructure and then investigated under the OM. Grain size at each weld zone along with BM are measured by Heyn Line Intercept method.

Fig. 3.18. Photograph of the optical microscope

3.8 Field Emission Scanning Electron Microscope (FESEM) Study

The micro structure of the weldments at higher magnification were investigated using a field-emission scanning electron microscope (FESEM) attached with an energy dispersive X-ray spectroscope (EDS) system. The photograph of the FESEM (Make: Zeiss; Model: sigma) used is shown in Fig. 3.19. For microstructure investigation, the specimen preparation was same as followed for OM. The fracture surface of the tensile tested and FCGR samples are examined by FESEM to analyze the fracture behaviour of the joints. Microstructure of the IC tested samples were also studied using the FESEM/EDS system.

Fig. 3.19. Field emission scanning electron microscope

Chapter 4

Mechanical and Microstructural Property Analysis of FSWed AA2014 Joints

4.1 Introduction

The experimental procedures followed in this work has been discussed in detail in Chapter 3. The results obtained during optimization of process parameters of FSW of AA2014 alloy are analyzed and the weld quality attributes are correlated to the process parameters and presented in this chapter. The chapter starts with the presentation of the mechanical properties of the joints under different processing conditions. The impact of the tool shoulder diameter, plunge depth, tool pin profile, tool rotational speed, welding speed, etc. on the mechanical attributes are discussed in detail. This is followed by discussion on the microstructure of the welded joints. A detailed discussion on the effect of process parameters on the grain size and mechanical properties are included. The results of the fracture surface investigation carried out under FESEM is discussed. At the end, the findings of the study are summarized.

4.2 Mechanical Properties of AA2014 Al Alloy Weldments

4.2.1 Tensile Properties

The tensile properties of the weldments for the considered parameter settings are presented in Table 4.1. In all the cases, the UTS, YS and % elongation of the weldment was lower than the BM. The best mechanical properties were obtained for experiment no. 15 followed by experiment nos. E14, E11 and E10. The process parameters (Table 3.3) presented in Chapter 3 is reproduced here for the easy recapitulation. The stress vs. strain plots of few weldments along with the BM is depicted in Fig.4.1. The UTS, YS and % elongation is the highest for the BM. The UTS and YS of the best specimen are 394 MPa and 282 MPa and corresponds to 86% and 80% of the BM respectively. The welded specimen shows lower amount of work hardening. During the tensile straining of BM, the stress continuously increased with strain till fracture, exhibiting a large work hardening region whereas for the sample welded as per E15, the stress increased up to a strain of 4.2% and remained constant at this value with further deformation till failure.

Table 3.3 Experiments conducted with different process parameter combinations

Exp. No.	Shoulder Diameter (SD) (mm)	Plunge Depth (PD) (mm)	Tool Pin Profile	Tool Rotation Speed (RPM) (rev/min)	Welding Speed (WS) (mm/min)
E1	16	0.03	Straight cylindrical	600	22
E2	20				
E3	**24**				
E4	28				
E5	24	**0.06**	Straight cylindrical	600	22
E6		0.09			
E7		0.12			
E8	24	0.06	Tapered Cylindrical	600	22
E9			Threaded Cylindrical		
E10			**Square**		
E11	24	0.06	Square	**815**	22
E12				1100	
E13				1500	
E14	24	0.06	Square	815	36
E15					**63**
E16					98

Table 4.1 Mechanical properties of joints with various process parameters

Exp. no	UTS (MPa)	YS (MPa)	%E
BM	**460**	**350**	**13**
E1	280	166	7.08
E2	320	200	7.95
E3	355	236	8.86
E4	330	210	7.98
E5	370	250	9.03
E6	360	230	8.00
E7	343	221	7.71
E8	372	256	9.07
E9	375	261	9.20
E10	380	265	9.91
E11	389	277	10.58
E12	377	270	9.20
E13	359	260	8.89
E14	391	279	10.86
E15	394	282	11.75
E16	380	265	10.08

Variation of UTS, YS and % elongation vs. shoulder diameter (SD) for the specimen welded at a constant plunge depth, tool rotational speed and welding speed using a straight cylindrical tool pin is shown in Fig.4.2. During the initial trial experiments, proper welding was not achieved while attempting to join the metal using tools having shoulder diameters less than 16 mm. The mechanical attributes increase with increase in shoulder diameter up to 24 mm. With further increase in shoulder diameter, the mechanical attributes show a decreasing trend. As the shoulder diameter increases from 16 mm to 24 mm, the UTS, YS, and % elongation increased by around 27%, 42% and 25%, respectively.

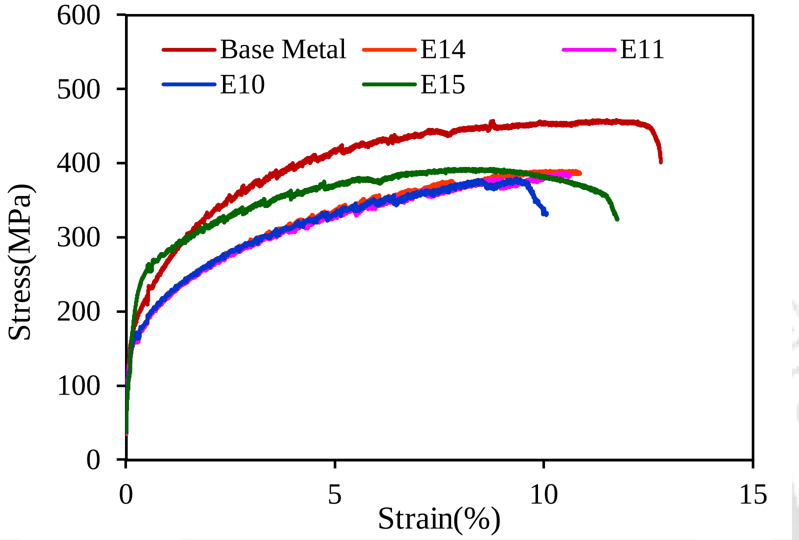

Fig. 4.1. Stress vs. strain curve of E10, E11, E14 and E15 obtained from experiment with base metal

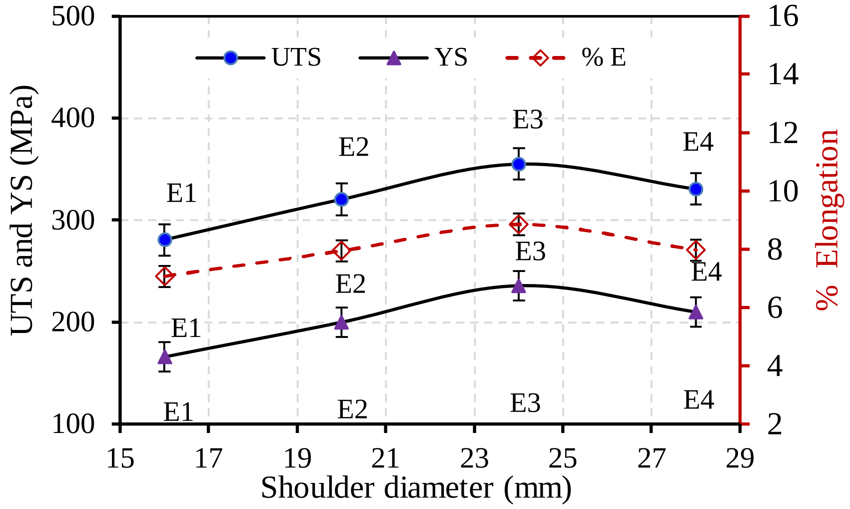

Fig. 4.2. Plot of UTS, YS and % Elongation vs. tool shoulder diameter

Variation of UTS, YS and % elongation vs. plunge depth for the specimen welded at a constant shoulder diameter (24 mm), tool rotational speed (600 rpm) and welding speed (22 mm/min) using a square tool pin is shown in Fig 4.3. The properties increased marginally (<4.2%) with increase in plunge depth up to 0.06 mm and decreased continuously with further increase in plunge depth.

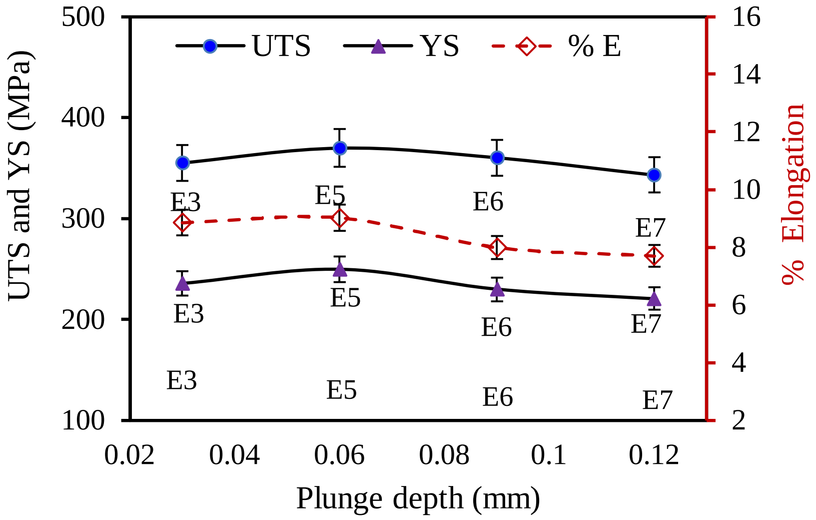

Fig. 4.3. Plot of UTS, YS and % Elongation vs. plunge depth.

The values of UTS, YS and % elongation of the weldment processed using different tool pin profile at constant shoulder diameter, plunge depth, tool rotational speed and welding speed is shown in Fig. 4.4. Specimen welded with square tool profile exhibited the highest mechanical attributes. By changing the tool profile, the mechanical attributes changed only marginally (by < 2.5%).

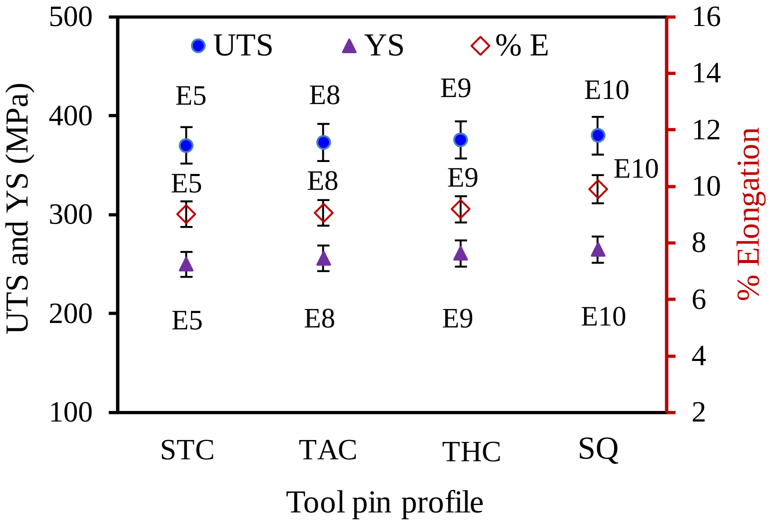

Fig. 4.4. Plot of UTS, YS and % Elongation vs. tool pin profile

Figure 4.5 illustrates the plot of UTS, YS and % elongation vs. tool rotational speed by keeping all other parameters constant. A marginal increase in tensile property attributes is observed when the tool rotational speed was increased from 600 to 815 rpm. The attributes showed a decreasing trend with further increase in the speed.

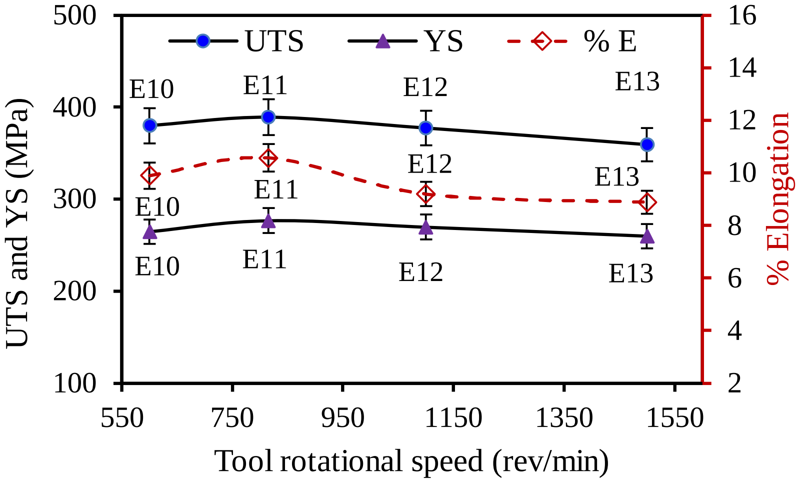

Fig. 4.5. Plot of UTS, YS and % Elongation vs. tool rotational speed.

The variation of UTS, YS and % elongation vs. welding speed keeping other parameters constant is shown in Fig.4.6. The figure indicates that the tensile attributes remain almost constant (variation < 1%) up to a welding speed of 63 mm / min. Further increase in the welding speed up to 98 mm/min showed a decreasing trend for the mechanical attributes.

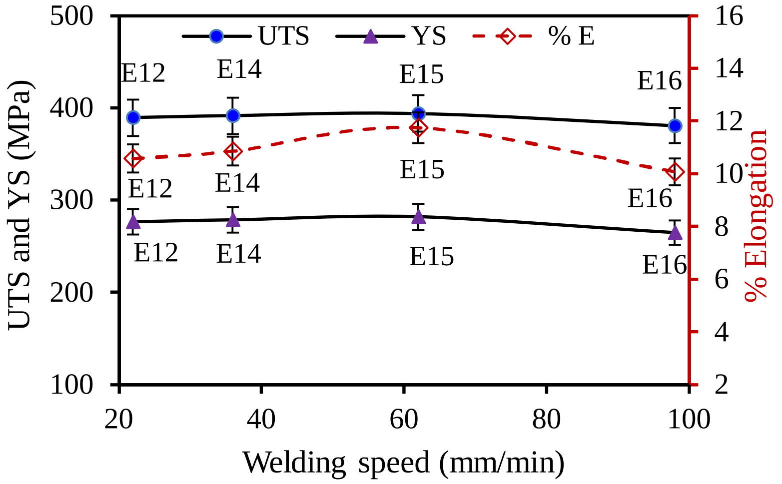

Fig. 4.6. Plot of UTS, YS and % Elongation vs. welding speed.

4.2.2 Flexural Strength

The results obtained from the flexural test for the samples welded with various process parameters are presented in Table 4.2. The variation of FS of the weldments vs. process parameters is plotted in Fig. 4.7.(a-e). The values shown in the figures are the case where experiments were carried out by varying one parameter at a time keeping all the remaining parameters constant. As the shoulder diameter increases from 16 to 24 mm, FS increases from 271 MPa to 408 MPa (Fig. 4.7(a)) indicating an increase of 51%. Further increase in the tool shoulder diameter indicates a deceasing trend. Effect of plunge depth on FS shown in Fig 4.7(b) indicates lower FS for the weldments compared to that of the BM. Maximum FS of 420 MPa for the weldment was achieved while welding with a plunge depth of 0.06 mm. This value was 77% of the BM value. It may be noted that the variation of the FS with plunge depth (plunge depth in the range 0.03 mm to .12 mm) was only marginal.

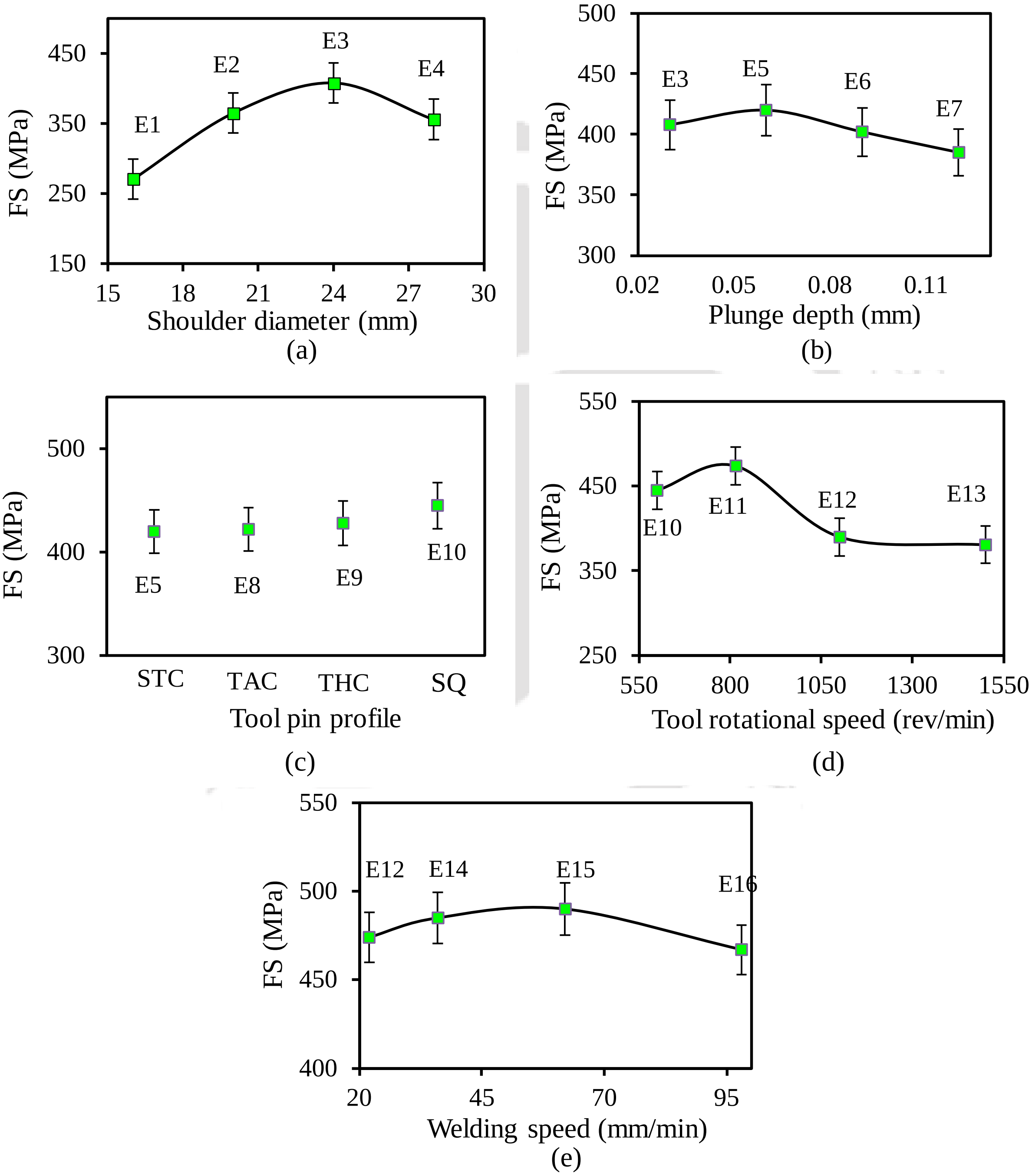

Fig. 4.7. Variation of FS with respect to (a) shoulder diameter, (b) plunge depth, (c) tool pin profile, (d) tool rotational speed and (e) welding speed

Figure 4.7 (c) depicts the FS for different tool pin profiles. The results indicate minimum FS (420 MPa) with STC profile and maximum (445 MPa) with the SQ profile. Though the % increase in the value is marginal, 81.65 % of BM value is achieved for the joint while using the SQ pin tool. The FS vs. tool rotational speed is plotted in Fig. 4.7 (d). The plot shows an increase in the FS value (6%) as the tool rotational speed increased from 600 rev/min to 815 rev/min followed by a decrease in the trend. The increase in the FS value with respect to the BM is 87 %. The welding speed vs. FS is represented in Fig. 4.7 (e). The trend shows an increase in the FS value for 22 mm/min to 63 mm/min welding speed from 474 MPa to 490 MPa. The achieved FS is 90% of BM.

Table 4.2 Flexural strength of joints with various process parameters

Exp. no	E1	E2	E3	E4	E5	E6	E7	E8
FS (MPa)	271	365	408	356	420	402	385	422
Exp. no	E9	E10	E11	E12	E13	E14	E15	E16
FS (MPa)	428	445	474	390	381	485	490	467

*Flexural strength of BM is 545 MPa

4.2.3 Bend Test

The photographs of the specimen after the bend test are shown in Fig. 4.8. The results of the bend test for the specimens welded with considered process parameters are shown in Table 4.3. The BM sample could be bent to a bending angle of 140°. The bend angle that could be achieved for the weldments were either equal to or less than that exhibited by the BM. The weldment obtained using the cylindrical tool pin showed the lowest bend angle while the bend angle of 140 ° could be achieved using the square tool pin, though the same could be achieved in one case each with threaded and taper tool pins.

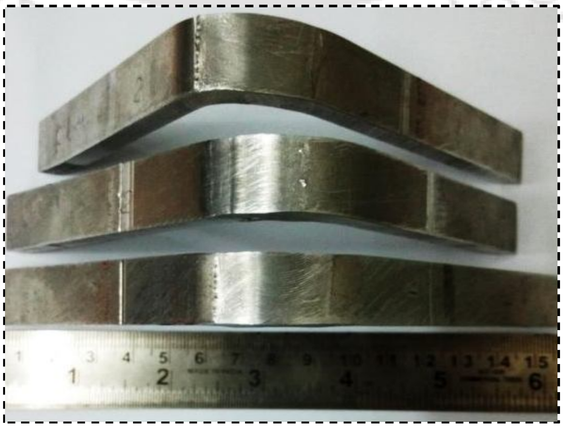

Fig. 4.8. Bending tested specimen

Table 4.3 Bending properties of joints with various process parameters

Exp. no	E1	E2	E3	E4	E5	E6	E7	E8
Bend angle (°)	120	130	135	130	135	120	115	130
Exp. no	E9	E10	E11	E12	E13	E14	E15	E16
Bend angle (°)	135	140	140	130	120	140	140	130

*Base material bend angle is 140^{0}

4.2.4 Micro-hardness

The hardness of the weldment in every case was higher than the hardness of the base metal. The maximum hardness is obtained at the NZ of sample E15. This hardness is 56% higher than that of the hardness of the BM. Vickers hardness values (HV) of the welded specimen measured along the thickness direction at the top, middle and bottom of the section as shown in Fig. 4.9 (a) are plotted in Fig. 4.9 (b). At NZ the hardness was measured at 1 mm distances apart and in other zones at 2 mm distances. The microhardness profile of the specimen E15 (welded with tool shoulder diameter of 24mm, plunge depth of 0.03 mm, square tool pin at a tool rpm of 815, welding speed of 63 mm/min) is shown in Fig. 4.9 (b). The hardness at the upper portion of the weldment is higher than the middle and lower sections. The highest hardness is obtained for the NZ followed by TMAZ, HAZ and BM respectively.

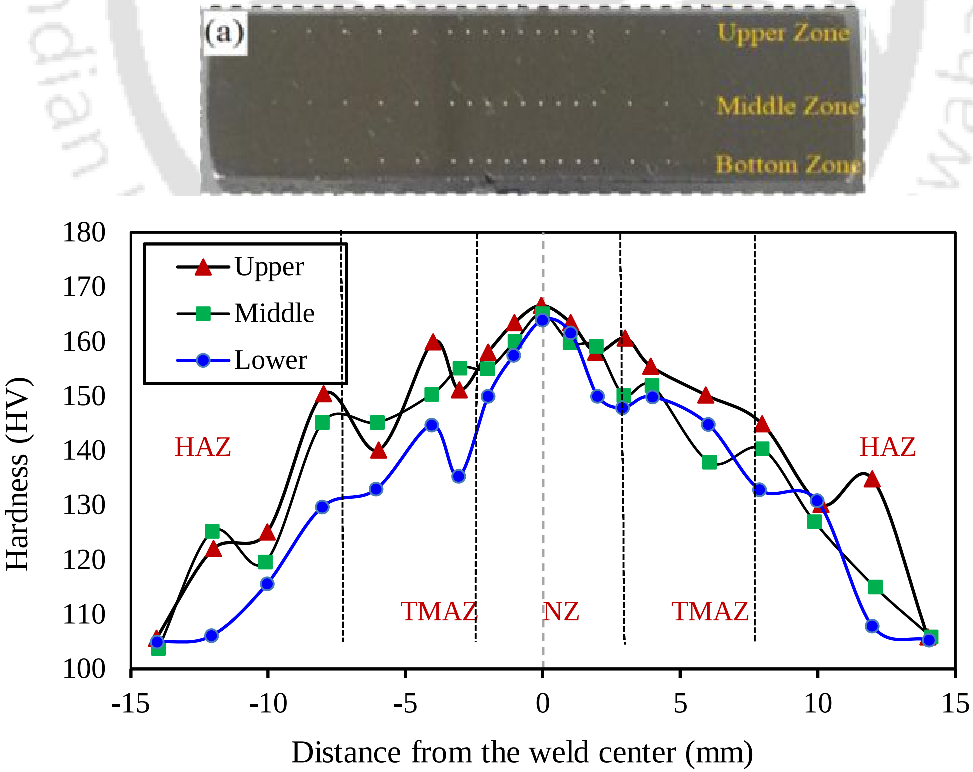

(b)

Fig.4.9. (a) Location of the hardness tests across the joint (b) variation of Vicker's hardness along the upper, middle and lower part across the joint

The variation of micro-hardness vs. shoulder diameter for the specimen welded at a constant plunge depth, tool rotational speed and welding speed using a SQ tool is shown in Fig 4.10 (a). The plot depicts 7% increase in hardness value as the shoulder diameter was increased from 16 to 24 mm. The maximum hardness achieved at 24 mm shoulder diameter is 39 % of the BM. Figure 4.10(b) illustrates the change in the HV value with change in the plunge depth. The plot shows a marginal increase in the hardness value (< 2%) with increase in the plunge depth from 0.03 mm to 0.06 mm. As the plunge depth was further increased to 0.09 mm, the hardness decreases by 5%. The maximum HV was attained at 0.06 mm plunge depth is 39% of the BM.

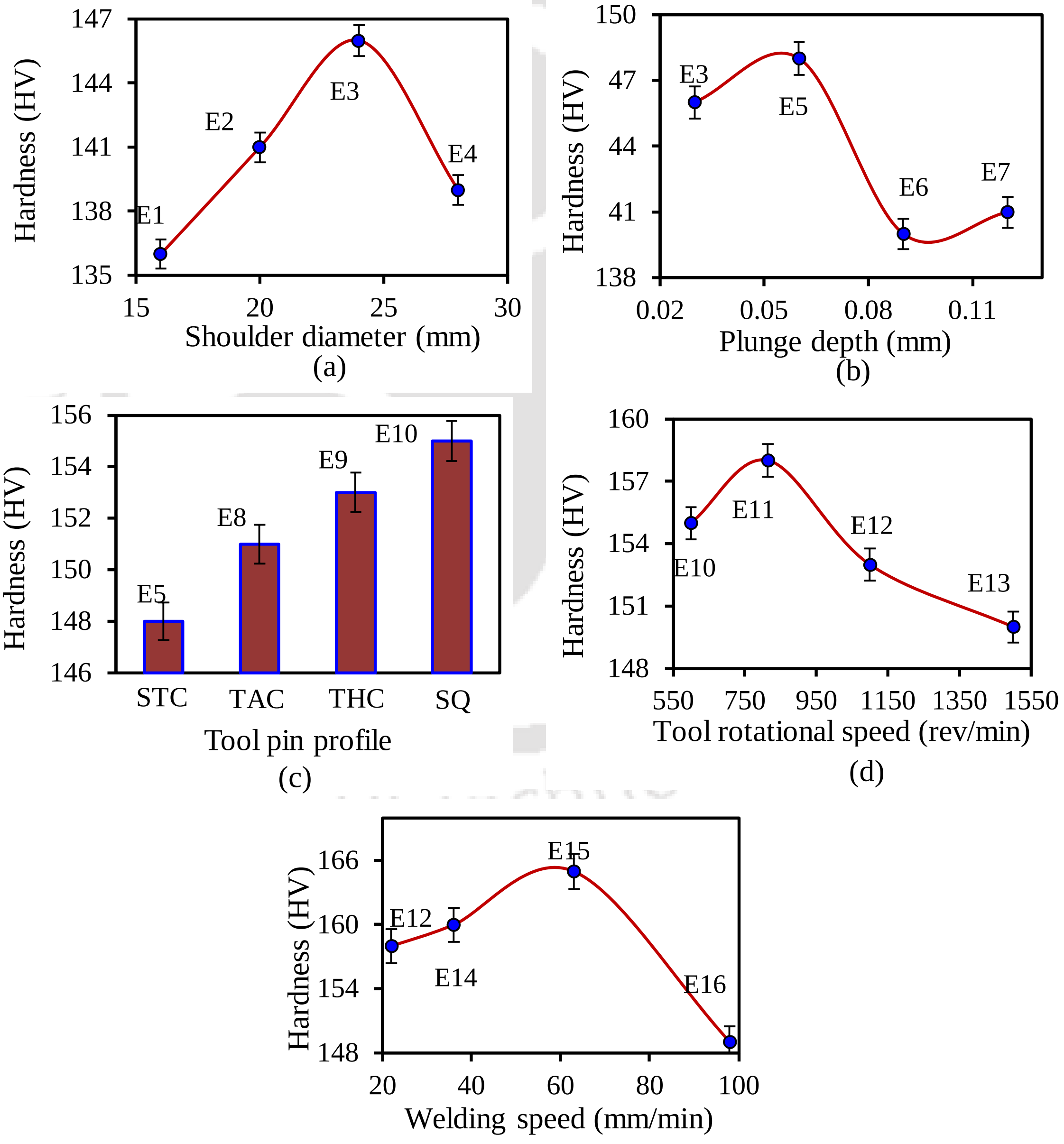

(a)

(b)

(c)

(d)

(e)

Fig. 4.10. Plot of HV vs. (a) shoulder diameter, (b) plunge depth, (c) tool pin profile, (d) tool rotational speed and (e) welding speed

The plots of HV vs. tool pin profile is shown in Fig. 4.10(c). Maximum HV value for the weld was achieved while using the tool with SQ pin profile. The hardness value achieved for the weldment using the SQ pin profile was 4.7 % higher than that of the STC tool. The variation in HV vs. tool rotational speed for the FSWed specimen is plotted in Fig. 4.10 (d). As the tool rotational speed is increased from 600 rpm to 815 rpm, the hardness increases marginally. The hardness decreases continuously with further increase in the speed up to 1500 rpm. The maximum hardness is achieved at tool rotational speed of 815 rev/min which is 49% of the BM. The plot of HV vs. welding speed is shown Fig. 4.10 (e). As the welding speed increases from 22 mm/min to 63 mm/min the hardness increases by 4.5%. However, with further increase in the welding speed from 63 mm /min to 98 mm/min resulted in a decrease in the hardness by 10.7%. The maximum hardness achieved by varying the welding speed is 55% of the BM.

Photographs of few tensile tested specimen is shown in Fig. 4.11. The failure of the tensile samples was not confined to any particular location. For examples specimen labeled in Fig. 4.11(a-c) (corresponding to Expt. No. E10, E11 and E 15 respectively) are the case where the failure occurred outside the weld zone. Specimen labeled in Fig. 4.11d (Expt. No. E3) is the case where failure occurred at the HAZ and specimen labeled in Fig. 4.11(e-f) (Expt. No. E1 and E2) corresponds to the case where failure occurs at the NZ. Most of the specimens failed at the retreating side of the joint.

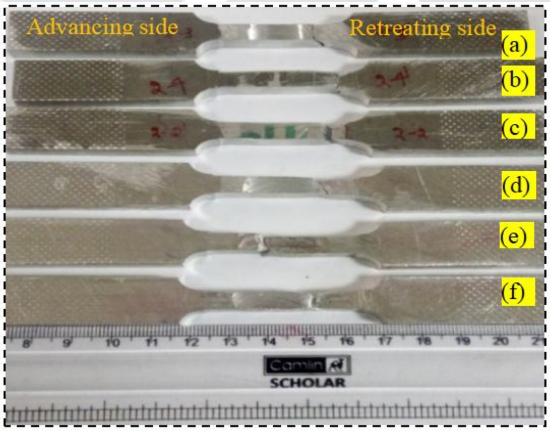

Fig. 4.11. Tensile tested specimen

4.3 Metallographic Study

Microstructure of the welded joints was investigated using the optical microscope (OM). The grain morphology and its size at various zones of the weld and the significance of variation in process parameters on the grain size at NZ are analyzed and presented below.

4.3.1 Weld Bead Analysis

Figure 4.12(a-d) shows the optical micrographs of few weldments. The features reveal the following: (i) improper mixing of metals at low shoulder diameter (ii) tunnel defects while welding using straight and tapered cylindrical tool pin (iii) porosity associated with threaded cylindrical pins (iv) features indicating good flow of metal when welded using threaded cylindrical tool pin or square tool pin (v) no evidence of microscopic defects was there while joining using square tool pins. Observation of the microstructure of the weldment under OM at low magnifications reveals tunnel defects (Fig. 4.12 (a) & (b)) when welded using the straight cylindrical or tapered cylindrical tool pins. This was evident for specimen nos. E1 to E8. The tunnel defects were present along the full weld length. Though tunnel defect was observed in the specimen welded using threaded cylindrical tool pin, the size of the defect was very small compared to that found in samples welded using straight or tapered cylindrical tool pin and very fine sized porosities are evident as in Fig. 4.12(c). Neither tunnel defect nor porosities were observed in the specimen welded using square tool pins as shown in Fig 4. 12(d).

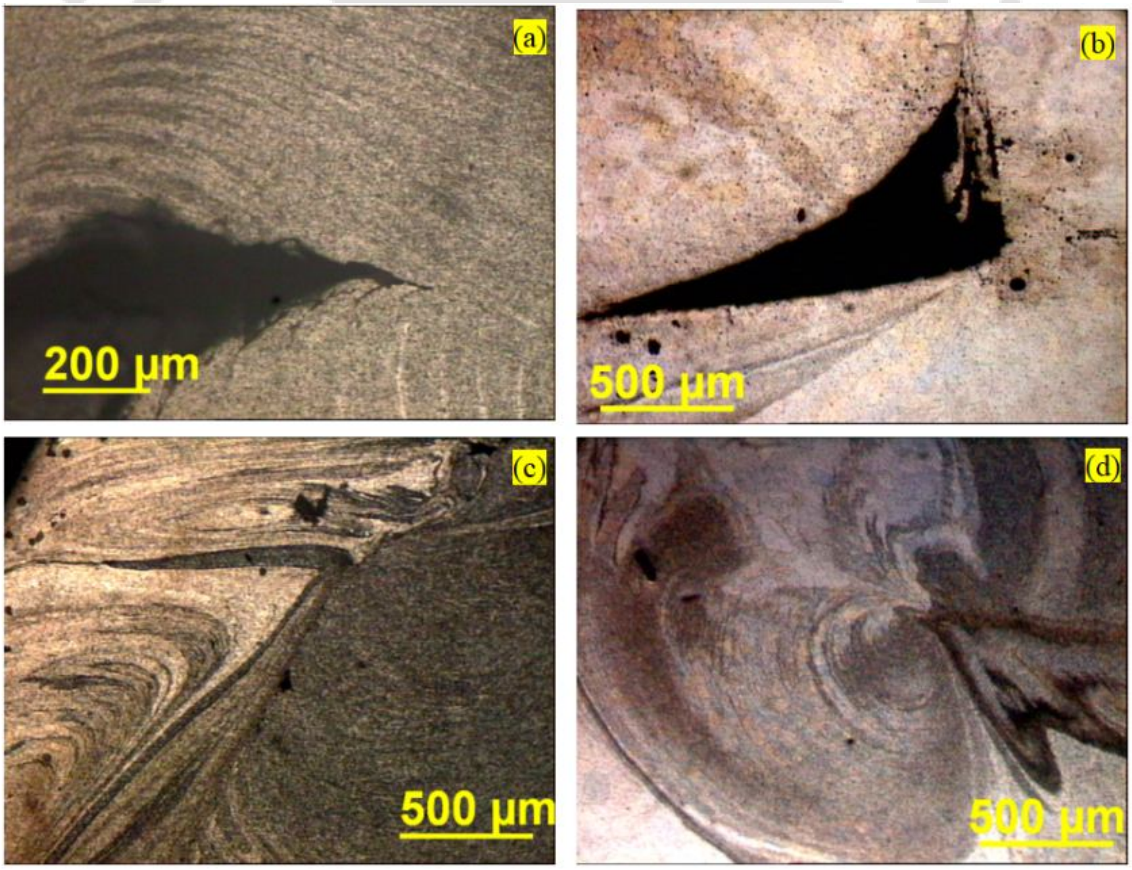

Fig.4.12. Tunnel defect in (a) STC (E1-E7) (b) TAC (E8) (c) minute pores in THC (E9) (d) defect free in SQ (E10-E16)

The optical micrographs of various weld zones of the best weldment (sample E15), based on mechanical properties, is shown in Fig. 4.13(a). The variation in grains size at the weld zones viz. top and bottom of NZ, TMAZ and HAZ are evident from the figure. The two dashed lines drawn in the figure represents the transition between the NZ/TMAZ as well as TMAZ/HAZ. The microstructure of BM as well as advancing side and retreating side of TMAZ are presented in Figs. 4.13(b-c-d) respectively. The microstructure indicates very fine equi-axed recrystallized grain having an average diameter of 15 μm at the top region of the NZ, as revealed by line intercept method. Compared to the top region of the NZ, the grains at the bottom region are marginally coarser. The grain diameter marginally increases as we move away from the center of the NZ towards the TMAZ. At the TMAZ, very coarse and non-equiaxed grins are visible. The average grain size of the TMAZ region is 33 μm (Fig. 4.13(c)) at the advancing side, whereas it is 35 μm (Fig 4.13(d)) at the retreating side. The average grain size at the HAZ is determined as 63 μm. The BM is characterized by coarse and almost equiaxed grains with an average grain diameter of 93 μm.

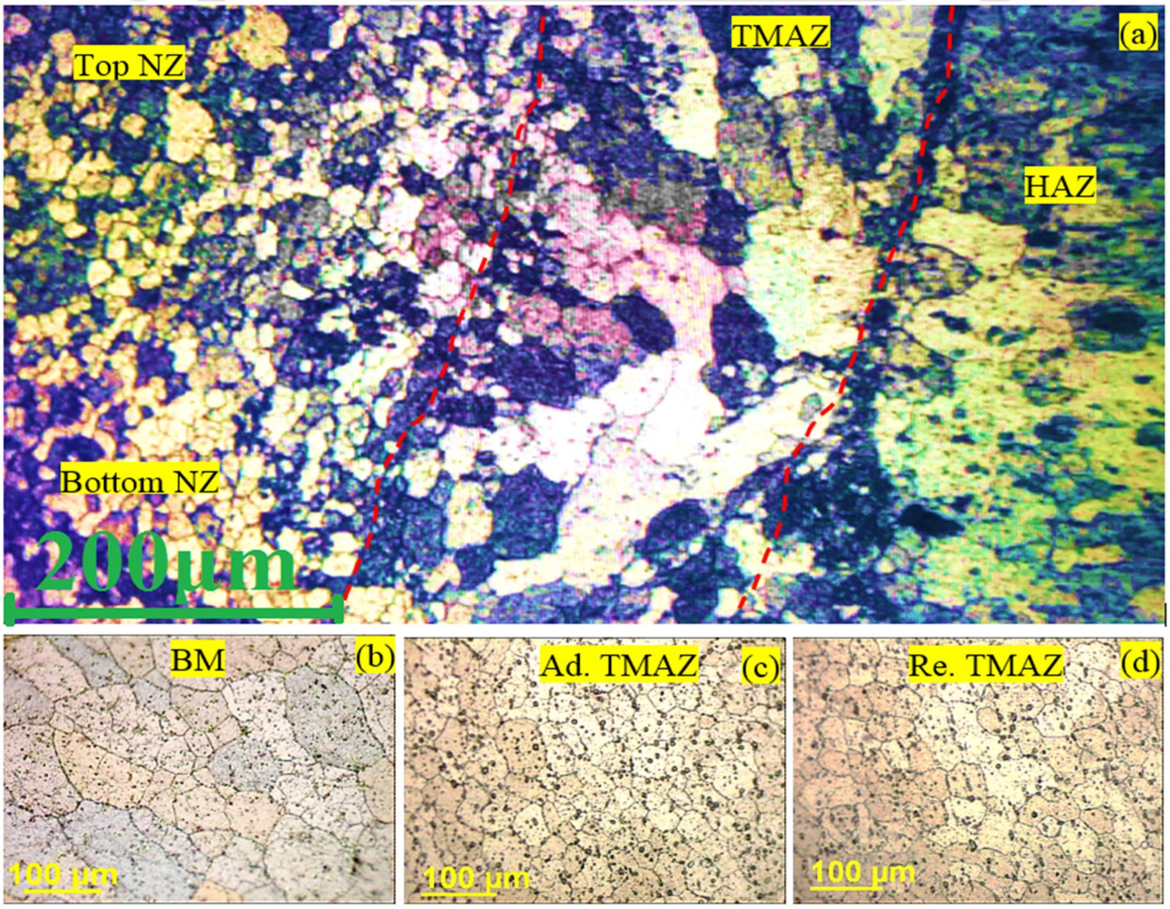

Fig. 4.13. (a) Weld bead micrograph with different weld zones, (b) base material (c) advancing side TMAZ, (d) retreating side TMAZ

4.3.2 Grains Size Variation at NZ with respect to Process Parameters

The average grain diameter at NZ with the process parameters is depicted in Table-4.4. The micrographs revealing the grain size for different shoulder diameter are shown in Figs. 4.14 (a-d). Analysis indicates that shoulder diameter 24 mm results in finer grains of 23 μm at the NZ in compared to the grain sizes of 37 μm and 28 μm at 16 and 20 mm of shoulder diameter respectively. At higher shoulder diameter, i.e., at 28 mm, size of grains observed is 45 μm and hence no further grain refinement was observed with further increase in shoulder diameter. The photo-micrographs of Fig 4.15 (a) to (d) shows the variation in the grain size with variation in plunge depth while keeping all other parameters constant during the FSW process. The average grain size obtained for the NZ of the weldment when welded with a plunge depth of 0.03 mm is 23 μm. The grain size analysis indicates a reduction in the grain diameter as the plunge depth was increased to 0.06 mm. However, the average grain diameter increased to 27 μm and 30 μm as the plunge depth is increased to 0.09 mm and 0.12 mm, respectively.

Table 4.4 Variation of average grain size at NZ with different experimental conditions

Exp. No	E1	E2	E3	E4	E5	E6	E7	E8
Grain Size (μm)	27	26	23	32	21	24	30	25
Exp. No	E9	E10	E11	E12	E13	E14	E15	E16
Grain Size (μm)	20	18	17	28	31	16	15	25

Figure 4.16 shows the optical photo-micrographs of the NZ of the weldments using different tool pin profiles. The grain size obtained for the weldments processed using the straight cylindrical tool is 21 μm (Fig 4.16(a)) whereas the grain sized obtained while using the square tool pin profile is 18 μm (Fig 4.16(d)). Figure 4.17(a) to (d) shows the photo-micrographs of the NZ of the weldments showing the average grain diameter when welded at different tool rotational speeds. At low rotational speed of 600 rev/min, fine grains were achieved whereas the grain size increased with increase in the tool rotational speed. In addition, the grain morphology changed from almost equiaxed grain at 600 rev /min to elongated grains by increasing the tool rotational speed to 1500 rev/min. Figure 4.1 (a) to (d) indicates that the variation in the welding speed under the conditions investigated did not have much effect on the average grain size. The grain size obtained at WS of 22 mm/min is 17 μm where as it is 15 μm at 63 mm/min. Grains were slightly coarse when welded at 98 mm/min. However, features of fine recrystallized grains can be observed at the grain boundary regions as the WS is increased from 22 mm /min to 63 mm/min.

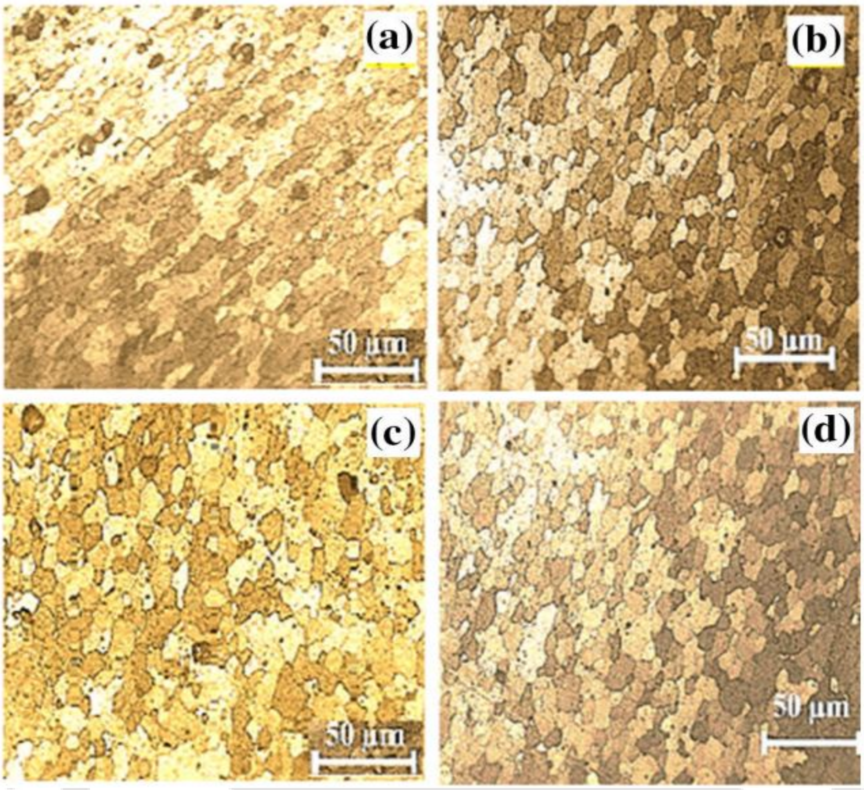

Fig. 4.14. Grain size variation with respect to shoulder diameter (a) 16 mm, (b) 20 mm, (c) 24 mm, (d) 28 mm

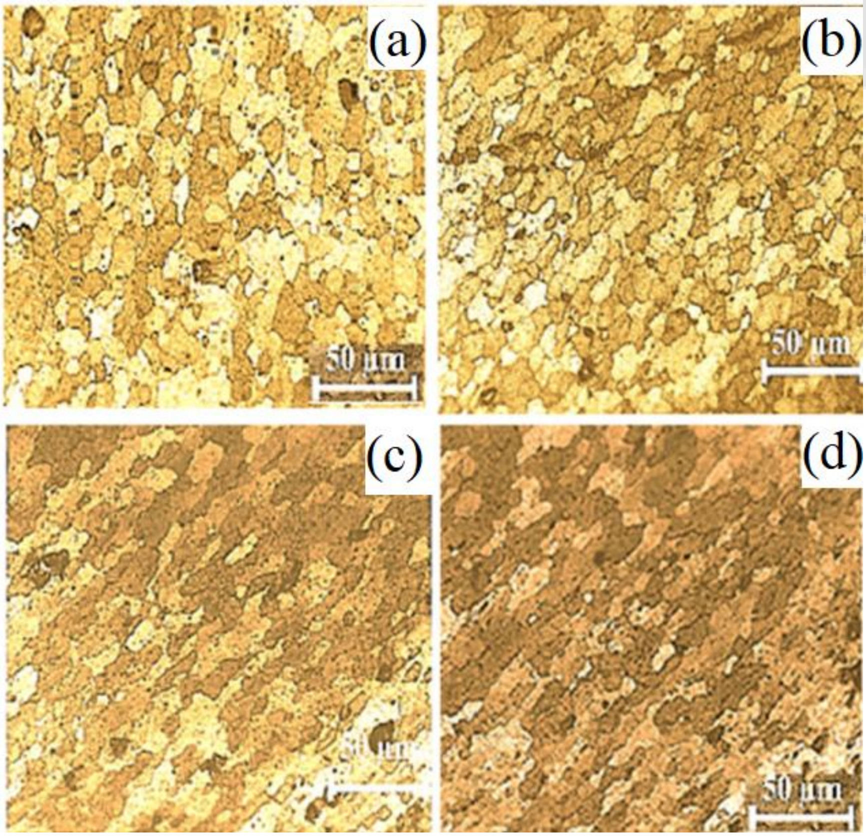

Fig. 4.15. Grain size variation with respect to plunge depth (a) 0.03 mm, (b) 0.06 mm, (c) 0.09 mm, (d) 0.12 mm

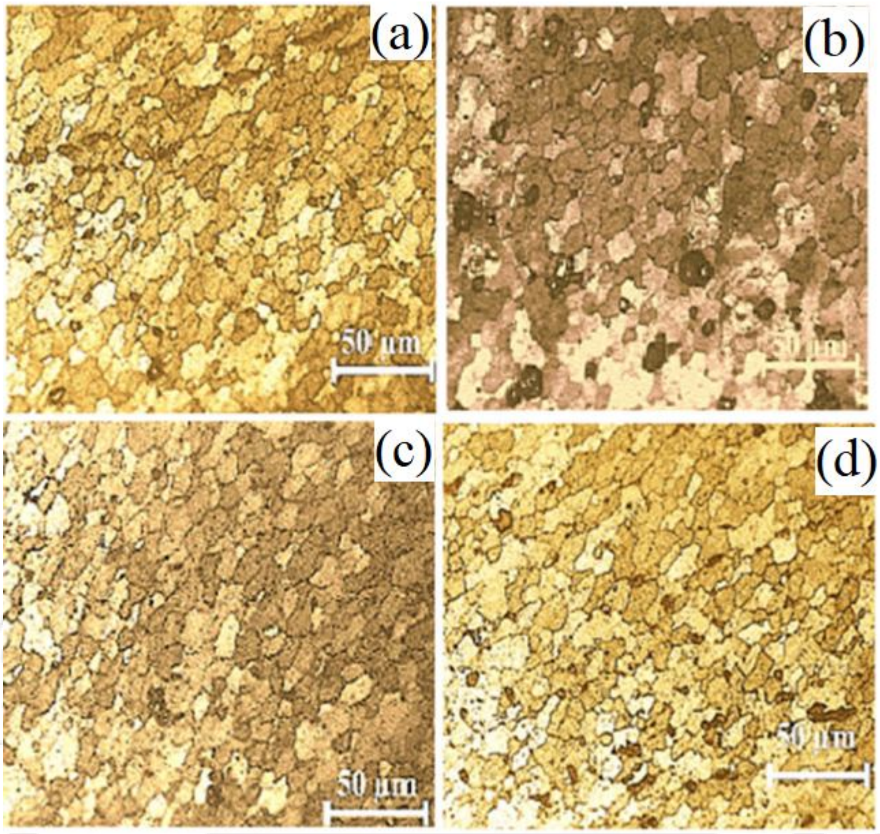

Fig. 4.16 Grain size variation with respect to tool pin profile (a) Straight Cylindrical (b) Tapered Cylindrical (c) Threaded Cylindrical (d) Square

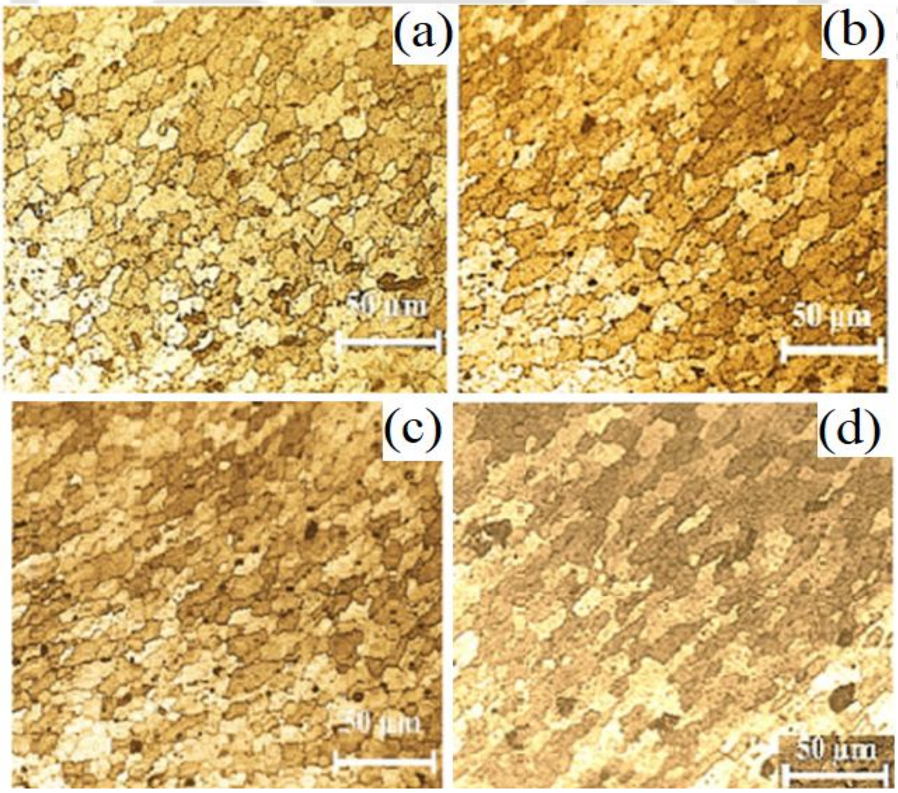

Fig. 4.17. Grain size variation with respect to rotational speed (a)600 rev/min, (b) 815 rev/min, (c) 1100 rev/min, (d) 1500 rev/min

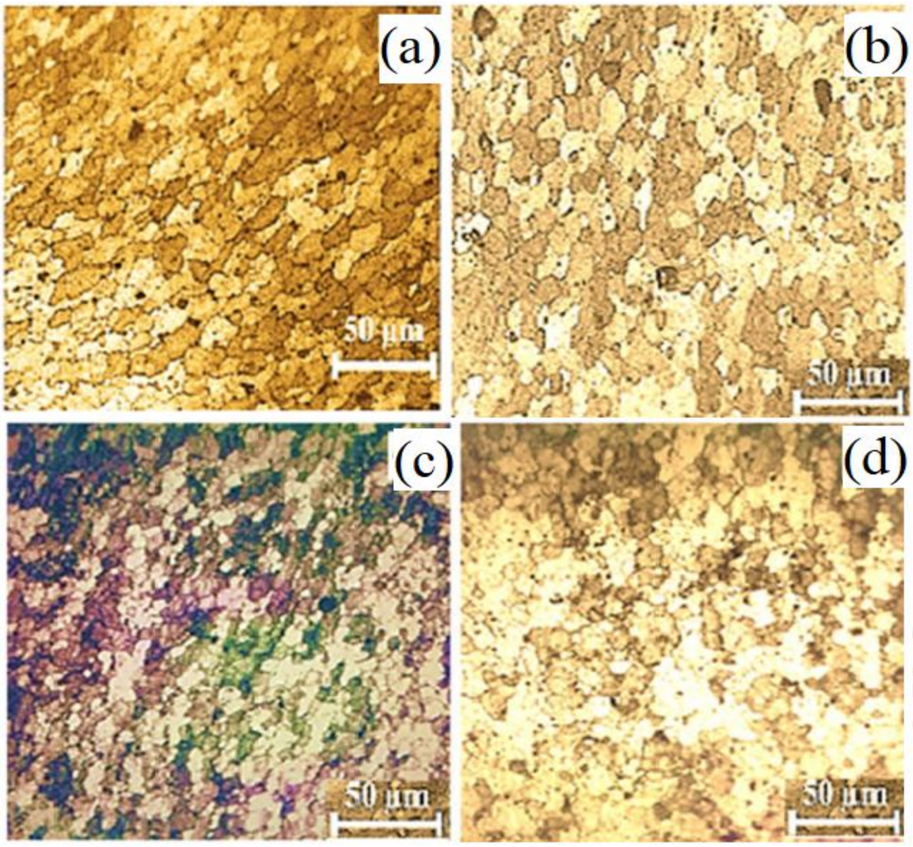

Fig. 4.18. Grain size variation with respect to welding speed (a) 22 mm/min, (b) 36 mm/min, (c) 63 mm/min, (d) 98 mm/min

4.4 Fracture Surface Studies

Fractograph of few tensile tested fractured surfaces are presented in Fig. 4.19. The fracture location varies according to the quality of the welds which is a function of the process parameters chosen as described in the previous section. The fracture located outside the weld zone for the best quality welds is presented in Figs. 4.19 (a-d). The fracture features observed under FESEM of the specimen E15 is similar to the BM as shown in Fig. 4.19(a) and (b) respectively. The figure depicts dimple feature indicating pure ductile mode of fracture and is also evidenced from the mechanical test result. This is typical of the alloys since the material is face centered cubic (FCC) lattice where the number of active close packed slip systems are large. However, the tensile fractograph of specimen E3 shown in Fig. 4.19(c) reveals cleavage and micro-cracks which are typical of brittle fracture, along with ductile features. Due to some amount of brittle fracture, the ductility of specimen E3 is lower compared to E15. The fracture in E3 occurred at the interface (transition region) of TMAZ/HAZ. The lower ductility for E3 compared to E15 is due to the influence of the stirring by the tool pin.

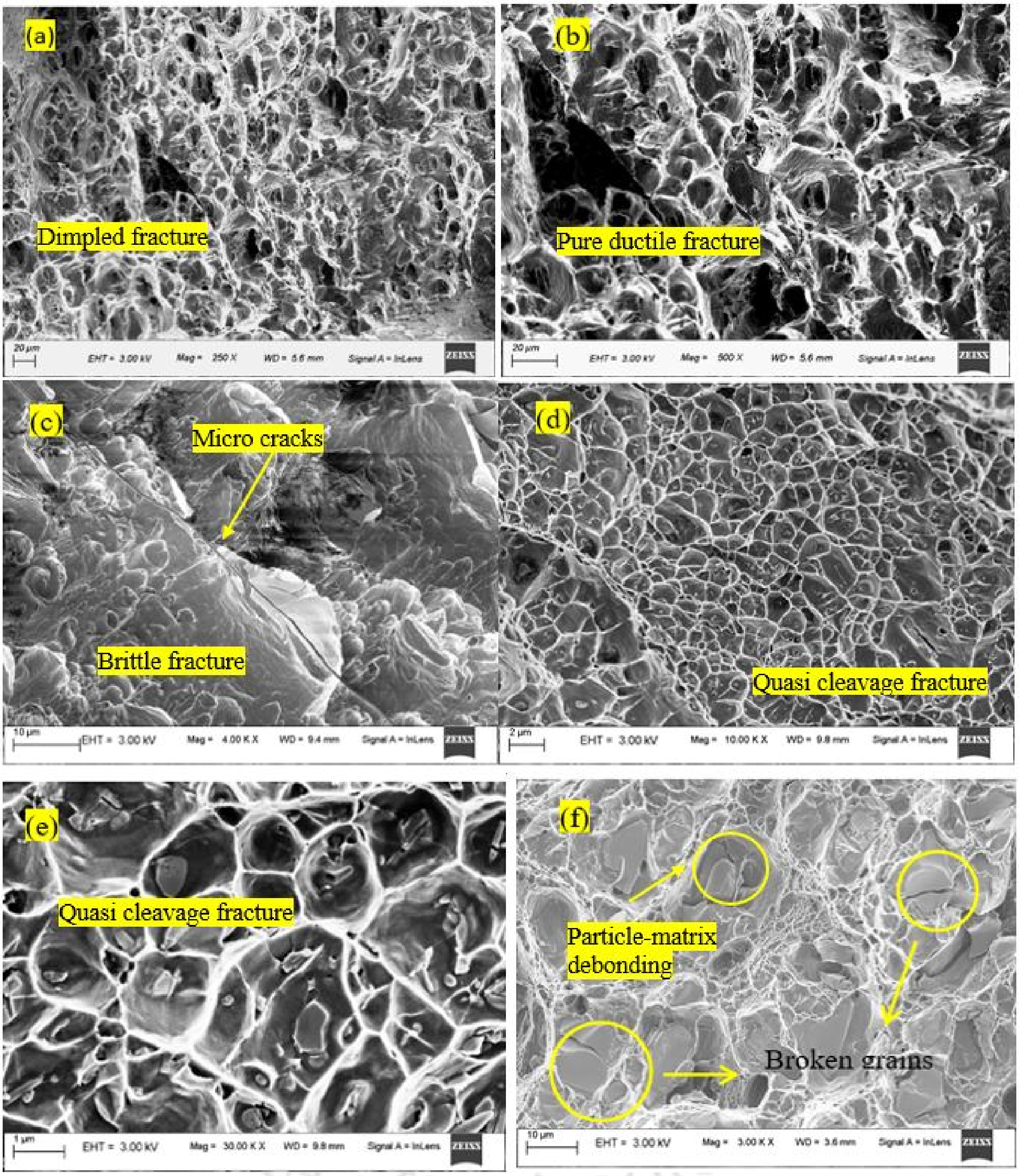

Fig. 4.19. FESEM image of different tensile tested fractured surfaces (a) specimen E15, (b) BM, (c) specimen E3, (d) specimen E1, (e) enlarged view of specimen E1, (f) specimen E12

The fracture surfaces of specimen E1, E2, E6 and E7 also revealed features similar to E3 is quasi ductile features, which is a combination of ductile and brittle features. However, the dominant features were dimples as is evident from Fig. 4.19 (d) and (e). The fracture features in most of the specimen exhibiting lower tensile strength are characterized by quasi-cleavage fracture. In the case of E12 and E13, second phase particle breakage and debonding at the particle matrix interface are also observed (Fig. 4.19(f). These features were also reported by others (Sahu and Pal 2017). It may be noted that in these specimens the fracture occurred at TMAZ and is attributed to the variation in grain size at this region.

4.5 Discussions

The Mechanical test results reveal the FSWed specimen using square tool pin having tool shoulder diameter 24 mm, plunge depth of 0.06 mm at a tool rotational speed of 815 rev/min and welding speed of 63 mm/min gave the best quality of joint. The stress strain diagram shown in Fig. 4.1 reveals higher UTS, YS and % elongation for the base metal. However, mechanical properties of the joint in the as welded condition were lower than that of the BM. This is expected for any FSWed joint due to either or a combination of the following: (i) the recrystallization of the alloy during processing as a result of heat generated, leading to softening (ii) the 2014 Al alloy is a precipitation hardenable alloy. The as-received alloy was subjected to thermo-mechanical treatment resulting in the precipitation of hard intermetallic particles of $CuAl_2$ in the Al matrix which contributes to the strengthening of the alloy. During FSW, the high heat generated results in dissolution of these hard second phase particles in the matrix thereby the effect of precipitation strengthening is nullified (Liu et al., 2003) and (iii) formation of various weld zones viz, NZ, TMAZ, HAZ, etc. during the FSW. The microstructure evolved across these zones are different and hence the mechanical properties are different. This results in non- uniform material behavior during load application resulting in early failure of the weldment and (iv) FSW with process parameters outside the parameter window leads to formation of defects at the weld zone resulting in deterioration in the mechanical properties.

From Fig.4.11 and Table-4.1, it is found that failure of the specimen during tensile loading was not confined to any particular location. Samples where failure occurred outside the weld zone exhibited better UTS, US and % elongation compared to the cases where failure occurred in the weld zone. As tunnel defect was observed in the weld regions in samples E1 to E7 hence failure occurred at the weld region in these samples. Presence of defects at the weld zone results poor ductility and lowering of UTS and YS. Presence of recrystallized grain at the NZ and absence of defects result in higher ductility thereby achieving high bend angles for the samples E10, E11 and E15 whereas the presence of defects in samples E1-E7 results in lower bend angles. Like mechanical properties, the same trend was also reflected in the flexural strength of the weldments as seen from Table

4.3. Weldments exhibiting higher tensile strength, ductility, flexural strength and bend angle (sample E10, E 11, E14, E15) did not reveal any defects under the OM. Presence of defects formed during FSW was the main cause of deterioration in the mechanical properties of the weldments.

The process parameters during FSW have a strong influence on the defect formation and hence on the mechanical properties of the weldments. During FSW, major part of the heat is generated due to friction at the tool shoulder - work piece interface. The frictional heat generated can increase with increase in tool pin diameter, or increase in the tool rotational speed (RPM). A major part of the heat generated is used for softening the work piece resulting in the material becoming plastic thereby favoring the proper flow of metal and subsequent mixing. During the initial experimental trials, proper welding could not be achieved using the tools with shoulder diameter less than 16 mm. This is due to the fact that at very low tool shoulder diameters, the heat generated is highly inadequate for the material to plasticize, hence could not achieve proper welding. Figure 4.2 indicates that the tensile properties increase with an increase in shoulder diameter from 16 mm to 24 mm and then decreased for a shoulder diameter of 28 mm. The best tensile properties were achieved at a shoulder diameter of 24 mm. Higher shoulder diameter results in higher shoulder-work piece interface area which generate higher frictional heat during the tool rotation. Hence with increase in the shoulder diameter in the range 16 to 24 mm, the heat generation is adequate to heat the workpiece to the temperature required for plasticizing the metal to the desired level thereby facilitating proper mixing and interlocking resulting in a superior joint (Khan et al., 2017). The strength of the weldment was reduced as the tool shoulder was increased from 24 mm to 28 mm. The reason behind this is that heat generated at a shoulder diameter of 28 mm was higher resulting in high fluidity of the plasticized metal at the stir zone. This leads to (i) removal of material from the weld region in the form of flash thereby local thinning of the metal, (ii) formation of tear line defect at the weld region and (iii) formation of wider TMAZ and HAZ, and (iv) grain coarsening at the NZ due to higher heat input. All these results in lowering of UTS and YS of the weldment (Saravanan et al., 2016; Peel et al., 2003).

The effect of the shoulder diameter on flexural strength (FS) revealed that the trend is similar to that followed by the tensile properties and shown in Fig. 4.7(a). FS increased to 408 MPa, which is around 74% that of the BM, as the shoulder diameter was increased to 24 mm due to the proper heat generation and recrystallization of the grains at NZ. Further increase in the shoulder diameter lowered the FS due to the grain coarsening for the unnecessary heat generation and grain growth (Peel et al., 2003).

Plunge depth is a parameter which controls the final quality of the weld. The plunge depth maintains the work piece in contact with the tool shoulder and the base plate and thereby facilitate transfer the frictional heat generated by friction between the rotating tool shoulder and the work piece (Jamalian et al., 2016). Figure 4.3 indicates the best tensile properties is achieved with plunge depth of 0.06 mm. The UTS, YS, % E as in Fig. 4.3 and FS as shown in Fig. 4.7(b) attained for the considered plunge depth are 370. MPa, 250 MPa, 9.03, and 420 MPa respectively, which are 80.45 %, 71.40 %, 69.50 %, and 77 % of the BM respectively. The lower strength and ductility at a plunge depth of 0.03 mm is due to the improper contact between the tool shoulder and the work piece. Under this condition, sufficient heat is not generated to soften the material, thus hinder the mechanical intermixing of the two metal pieces. The strength and ductility of the weldment decreases continuously with increase in plunge depth from 0.06 mm to 0.12 mm. This is attributed to the fact that with higher plunge depth, higher amount of insertion of the tool shoulder in to the work piece takes accompanied by trimming off some amount of the work piece material. This results in reduction in thickness of the weld zone and at the same induces stress concentration at the NZ (Sahu et al., 2016).

Figure 4.4 depicts the weld quality in terms of tensile properties and FS in Fig. 4.7 (c) obtained while welding using four different tool pins such as STC, TAC, THC and SQ. The tool pin profile affects the heat generation and plastic flow of material. The material filling effect during FSW due to the various tool pin profile is represented in Fig. 4.12 (a-d). Volumetric tunnel defects are evident at the NZ (Fig.12 (a-b)) at the lower corner of the tool pins regions, when welding is carried out with STC and TAC tool profiles. The defects prevent the plastic metal filling during the joining process and induces high levels of stress intensity during external loading resulting in the deterioration of mechanical properties (Liu et al., 2013). Very small pores are evident in the welded zone while joining using THC pin profile as shown in Fig. 4. 12(c) which affects the microstructural evolution and hence the quality of the FSW joints. The welds obtained were defect free in case of SQ tool pin profile as shown in Fig. 4.4 (d) due to its unique pulsating action on the plastic metal (Liu et al., 2013) and a superior metal interlocking during welding.

The SQ pin tool is found to yield the best tensile results as compared to the others. The % E and FS of the joint are also improved. The UTS, YS, % E and FS achieved with square pin profiles are 380.22 MPa, 265 MPa, 9.91, and 445 MPa respectively, and are 82.65%, 75.71%, 76.23% and 81.65 % of BM respectively. The flat edge surface of the tool pin profile generates more frictional heat relative to the other tool pin with the same input energy. The plasticized metal gets swirled beneath the tool pin and the edges of the SQ pin tool pulsate the material in a regular manner due to which an imposed plastic flow of metal occurs across the two work-piece interface. The high heat and plastic flow of metal also results in dynamic recrystallization of very fine crystal grains at the NZ (Jamalian et al., 2016). The fine grain size leads to improvement in the tensile, flexural and bending properties of the weldment (Liu et al., 2013).

The effect of tool rotational speed (RPM) on the tensile properties, as shown in Fig. 4.5 and on FS as in shown in Fig. 4.7 (d) reveals that the best weld quality is achieved at a tool rotation speed of 815 rev/min. The UTS, YS, %E and FS achieved at this sped are 389.34 MPa, 277 MPa, 10.58, and 474 MPa respectively, and are 84.63 %, 79.14 %, 81.38 %, and 87 % of the BM respectively. Further increase in RPM to 1100 rev/min and 1500 rev/min results in a decrease in the mechanical properties. At high tool rotation speed, excessive frictional heat is generated which favors the metal becoming more plastic causes excessive grain growth at the NZ (Malika et al., 2014). The high temperature and the stirring of the plasticized metal also results in dissolution of the strengthening hard second phase precipitates in the matrix (Moradi et al., 2018). The coarse-grained structure as well as the dissolution of strengthening particles formed at tool rotational speeds of 1000 rev/min and more decreases the yield strength, UTS and % elongation

Welding speed is another process parameter controlling the weld quality. At higher welding speed there is less contact time between the tool and the work piece material due to which heat input per unit length necessary for plasticizing the material is not achieved. Hence poor material stirring and inferior filling across the two parts do not occur resulting in poor weld quality. Improper plasticization and material transfer result in presence of weld defects like microvoids thereby reducing the mechanical properties. At lower welding speed, the tool pitch travel distance is less. Therefore, the heat generated per unit length increases and may be adequate for plasticizing the material and favour the mixing of the plasticized material. This also results in refined grain sizes. At the conditions of very low welding speed, the heat input is very large, cooling rates low and grain growth occurs at the NZ and results in lowering of the mechanical properties (Salari et al. 2014 and Sahu et al. 2017). For the present experimental condition, the welding speed of 63 mm/min yields the best mechanical properties as evident Fig. 4.6 and FS as shown in Fig. 4.7(e). The UTS, YS, % E and FS achieved are 393.87 MPa, 282 MPa, 11.75, and 490 MPa respectively, and are 86%, 80.57%, 90.4%, and 90% of the BM respectively. From the bend tests, the best bend angle obtained is 140°. The bending angle for the best combination of process parameters without any visible crack is E15. The bend angle without formation of defect may be higher than 140° since the limitation in obtaining the bend angle with the present setup is 140°. From the above tests carried out, the best combination of mechanical properties is achieved when FSWed at a plunge depth of 0.06 mm, at a tool rotational speed of 815 rev/min and welding speed of 63 mm/min using SQ tool pin profile having 24 mm shoulder diameter.

4.6 Summary

From the obtained results the conclusions extracted are summarized as below

- FSW process is a suitable method to join AA2014 of 6 mm thickness plate with a modified vertical milling machine with full penetration which yielded zero-defect joints by a 24 mm shoulder diameter SQ tool with 0.06 mm plunge depth at 815 rev/min tool rotational speed and 63 mm/min welding speed.
- The excellency of the joint is justified by the UTS and FS values which are 86% and 90% of the BM respectively. The microstructural feature is found to be the best with outstanding metallurgical characteristics contributed by the grains which are 84% finer than the BM.
- Hardness profile of the FSWed specimen along the thickness represents an inverted V shape with the maximum value at NZ and the lowest at HAZ. The hardness measured at the upper zone of the joint is the highest among the middle and lower zones.
- The metallurgical transformation at the NZ was revealed individually with respect to the considered process parameters by studying the grain size variation.

Chapter 5

Creep Behavior of Weld Zones of FSWed AA2014 Alloy by Impression Creep Testing

5.1 Introduction

Understanding the creep response from impression creep (IC) has been of great interest to researchers in the last two decades. Structural components of Aluminium alloy joined by FSW process for application in aviation industries and energy sectors are subjected to elevated temperatures and non-steady loading conditions. A large number of components require stringent quality control before being put in to use. In welded components that subjected to extended periods of service at elevated temperatures, the main failure is by creep deformation. The FSWed joints observed under OM revealed different zones viz. NZ, TMAZ, HAZ and BM. The metallurgical features at these regions are different from each other. Hence the creep properties at these regions are different with failure occurring at the weakest regions. Hence it is necessary to establish the creep behaviour of each weld zones.

The process parameters for obtaining the best weldment are arrived based on the mechanical property attributes. The results of the tensile properties, flexural strength, hardness of the FSWed AA2014 alloy weldments is presented in Chapter 4. The creep deformation behavior at different weld zones of the best FSWed Aluminium alloy weldment is studied at temperatures in the range 310-350 °C and at stresses 21–27 MPa by impression creep (IC) test. In this chapter, the IC deformation phenomena of different individual weld zones of FSWed AA2014 is investigated and the results are compared with the BM. The deformation characteristics are correlated to the microstructural changes throughout the FSW process and at different zones. The hardness and the microstructural evolution of the creep tested samples are investigated using OM and FESEM. The precipitated particles and dislocation structures are studied by transmission electron microscope (TEM). The composition of the intermetallic particles is ascertained through an EDX which provides an insight in to the metallurgy relating to the creep behaviour. The results obtained is presented in the subsequent sections. This is followed by discussion of the results and finally the chapter ends by summarizing the findings.

5.2 Mechanical Properties

The weld qualities were judged based on the mechanical properties: tensile tests, flexural and bend tests and the properties of the weldments chosen for the IC study are reproduced in Table 5.1. The UTS and YS of the best FSWed samples are 394 MPa and 282 MPa which corresponds to 86% and 80% of the BM respectively. The bending angle of this weldment is same as that for the BM. Vickers microhardness at NZ is the maximum followed by TMAZ and HAZ. The mechanical properties at the upper surface of the weld cross section are higher compared to the lower and middle sections.

Table 5.1 Mechanical properties of the best FSWed sample (sample No. E15)

UTS (MPa)	YS (MPa)	% Elong.	Flexural stress (MPa)	Bending angle (°)	Hardness at NZ (HV)	Hardness at TMAZ (HV)	Hardness at HAZ (HV)
394	282	11.75	490	140	165	160	150

5.3 Microstructural Features of the FSWed Joint before IC Test

Figure 5.1 shows the optical photo-micrographs of different weld zones of FSWed specimen along with the BM. Figure 5.1(a) is a very low magnification image indicating the NZ, TMAZ and HAZ while the high magnification images of these zones are presented in Fig. 5.1 (b-e) respectively. The microstructure of the HAZ (Fig. 5.1e) in FSWed material is similar to that of the BM shown in Fig. 5.1 (b) and do not reveal any feature representing either plastic deformation or recrystallization (Sahu et al. 2016). However, the grain size measurement by line intercept method revealed that the average grain diameter at the HAZ (Fig 51(d)) is 63 μm which is almost 68% of that of the BM (93 μm) (Fig. 5.1(b)). It is also observed that the average grain diameter at NZ is around 23 μm which is 25% of the BM**.** The finer grain structure improves the mechanical properties which are the outcomes of the process parameters chosen for the FSW process.

5.4 Creep Analysis of Base and Welded Material

The plots of impression depth *vs.* time for the BM as well as for the welded sample at NZ, TMAZ and HAZ at 310 °C for three different applied stresses are presented Fig.5.2(a-d) respectively. The plots show two stages of creep: (a) an instantaneous strain at the instant of load application followed by the transient creep called primary creep stage which is characterized by an increase in strain but at a decreasing rate with time and (b) a secondary creep stage or the viscous creep in which the rate of indenter penetration remains constant. This creep rate is known as the steady state creep rate or minimum creep rate. During impression creep tests, the tertiary creep stage is generally not observed since after a certain amount of indenter depth, the frictional forces at the indenter-work piece interface impede further penetration.

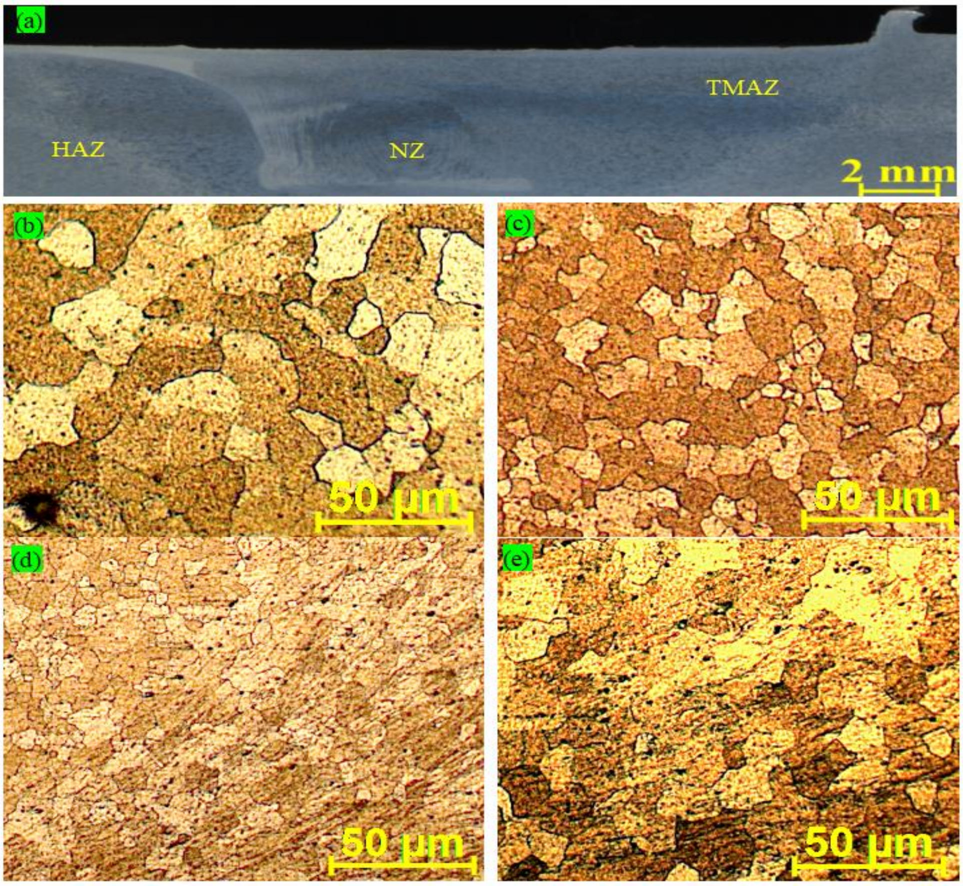

Fig. 5.1. (a) Low magnification OM photographs of weld bead of FSWed sample, high magnification micrographs at (b) BM (c) NZ (d) TMAZ and (e) HAZ

The impression depth *h*, at a stress of 27 MPa for the BM, as illustrated in Fig.5.2 (a), increases continuously up to 0.23 mm during a period of 600 minutes. At 24 MPa stress, *h* increases continuously up to around 0.17 during a period of 400 minutes and almost remain constant with further increase in time. At a stress of 21 MPa, the impression depth of 0.12 mm is reached within around 200 minutes. With further increase in the impression time, the change in strain is found to be negligible. Investigation of the deformation in the HAZ shown in Fig.5.2 (b) reveals that *h* value increases with time and after a certain time, no further increase in penetration depth was visible. However, the maximum strain that could be achieved in the HAZ was lower than that of BM. The impression depth vs. time plot for the TMAZ shown in Fig.5.2(c) indicates trend similar to that of the HAZ. However, the maximum penetration that could be achieved was less compared to the HAZ for the similar stress levels.

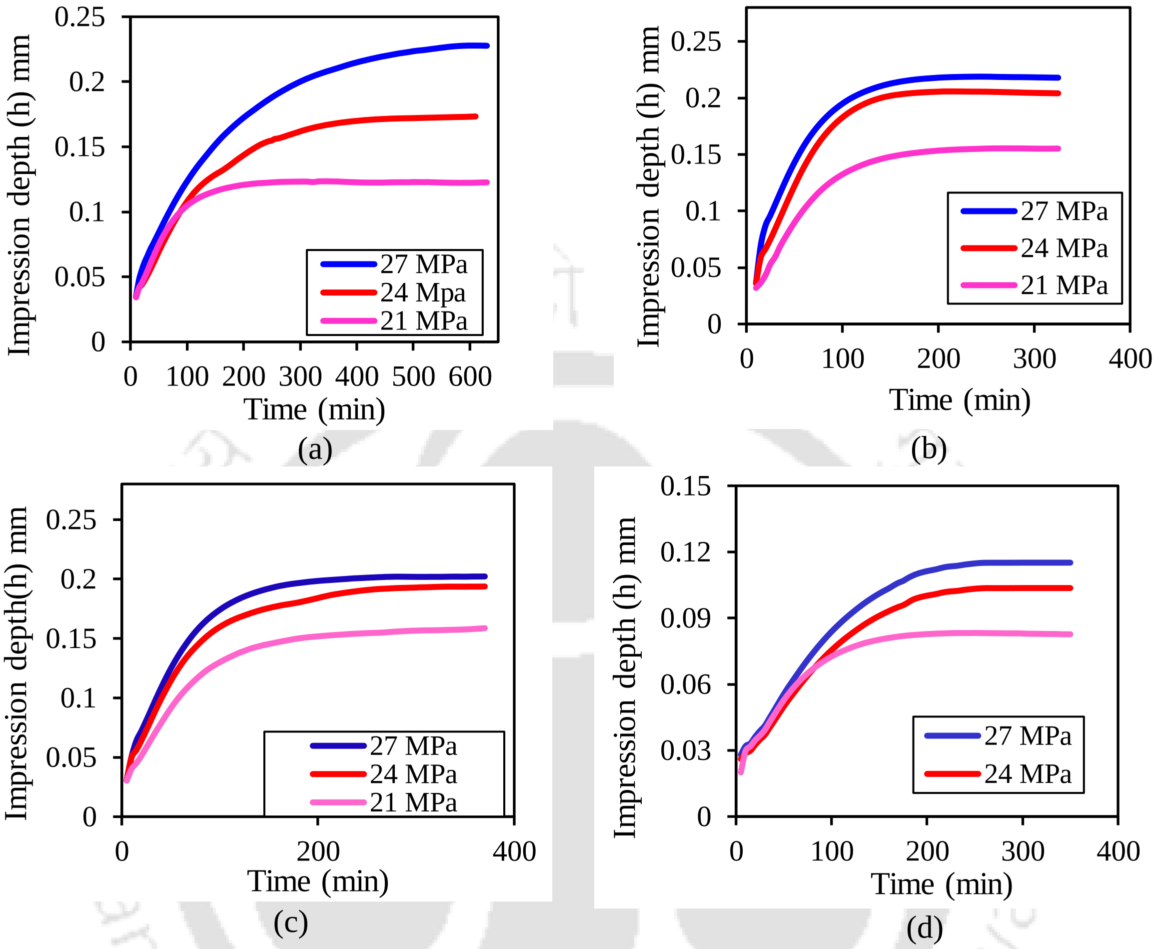

Fig. 5.2. Creep curves at 310 °C for (a) BM and welded samples at (b) HAZ, (c) TMAZ and (d) NZ at different loading conditions.

For the NZ as in Fig. 5.2 (d), the penetration depth that could be achieved was the least with the least time duration among the four weld zones i.e the secondary creep stage is achieved earlier than the other zones. The variation in *h* vs. time plot reveals the trend similar to that of the trend in the TMAZ. The plots of impression depth vs. time for the different individual weld zones when tested at 330 °C and 350 °C are presented Fig. 5.3 and Fig. 5.4 respectively. From the figures, the following are the observations of IC tests: (i) at a particular test temperature, the maximum impression depth (h_m) increases with increase in applied stress, (ii) at a particular stress, h_m increases as the test temperature increases from 310 to 330 °C (Fig. 5.5) and decreases with further increase in test temperature and (iii) as the test temperature increases, the rate of change of h_m w.r.t the stress applied increases linearly (Fig 5.6).

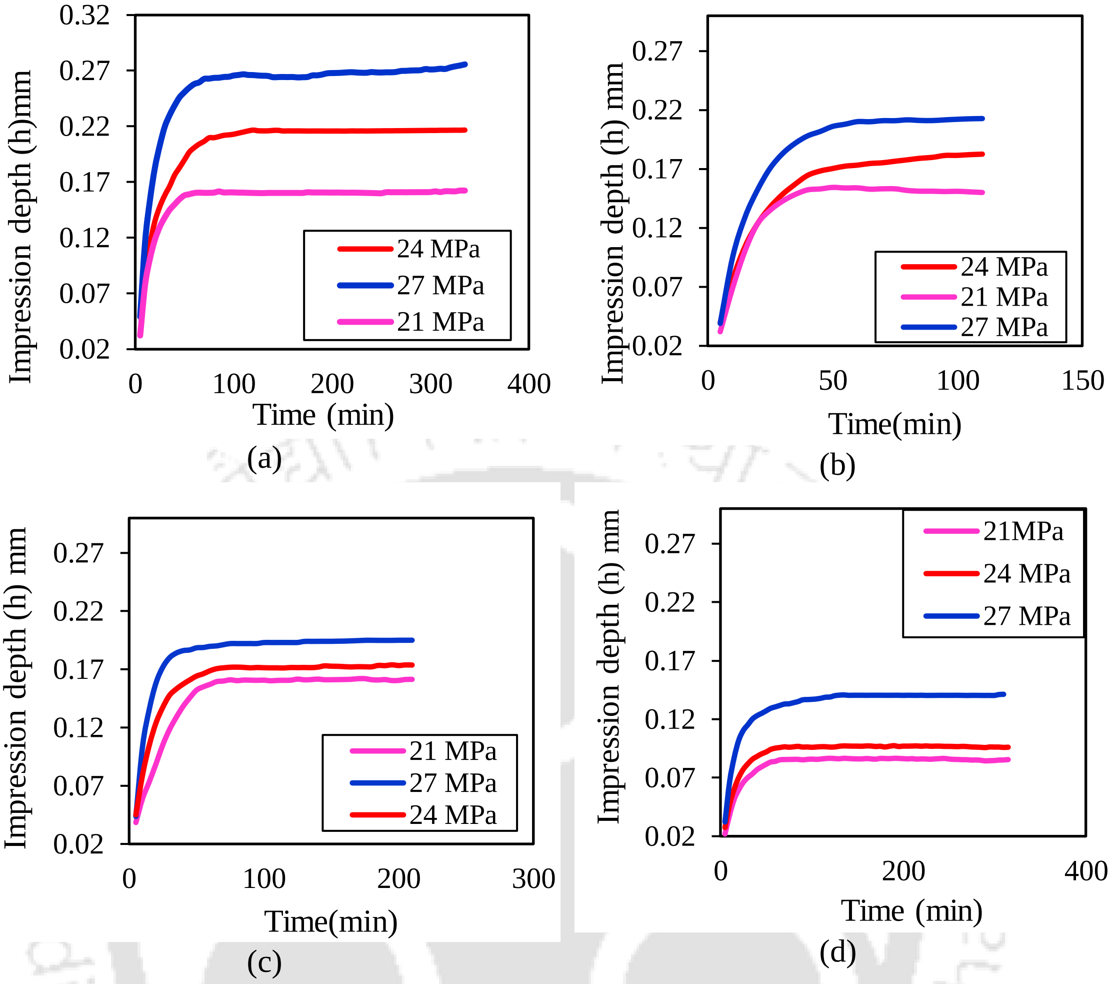

Fig. 5.3. Creep curves at 330 °C for (a) BM and welded samples at (b) HAZ, (c) TMAZ and (d) NZ at different loading conditions.

Figure 5.7 shows typical plots of the creep rate vs. time ($\frac{dh}{dt}$ $vs\ t$). As mentioned earlier, the creep rate decreases with time, reaches a minimum value and remains almost constant for some time and then starts increasing with time. At this stage the experiments were interrupted. The value of minimum creep rate (referred to as steady state creep rate, SSCR) was determined from the plot. The values of SSCR obtained from the tests for all the weld zones for various test temperatures and stresses are presented in Table 5.2.

The penetration of the indenter into the test material is controlled by the deformation of the material beneath the indenter and hence the overall creep deformation process is controlled. From the graphs (Fig. 5.2 – Fig. 5.4), it is evident that the indenter velocity is the maximum in NZ followed by TMAZ, HAZ and the lowest in BM zone. The variation in the indenter velocity at different zones is attributed to the heterogeneity in the microstructure i.e., mainly the variation in grain size (Vijayanand et al., 2014). Tertiary creep stage which is commonly detected in uniaxial creep curves is usually not present in

IC curve since necking does not take place under compressive loading (Wang et al., 2014). Under this condition, fracture of the creep specimen do not take place unlike in the case of tensile loading.

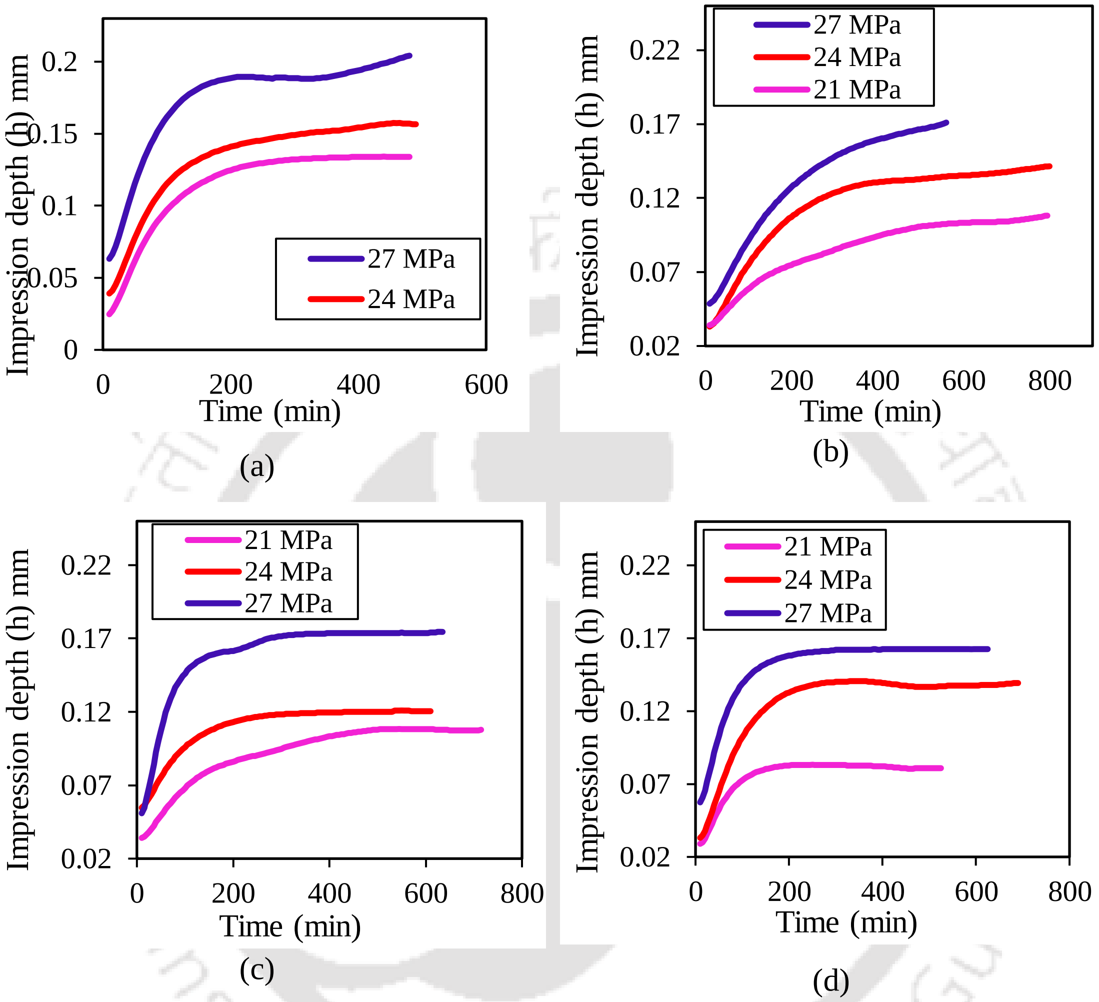

Fig. 5.4. Creep curves at 350 °C for (a) BM and welded samples at (b) HAZ, (c) TMAZ and (d) NZ at different loading conditions.

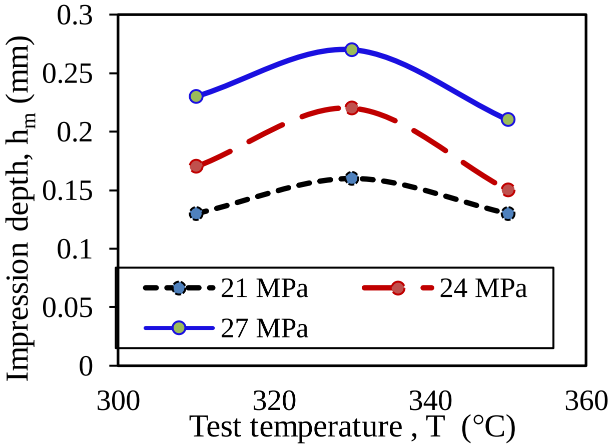

Fig. 5.5. Plot of impression depth (h_m,) vs. test temperature (T)

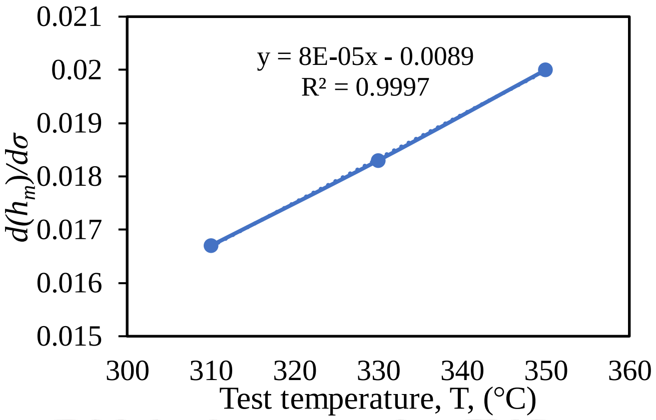

Fig. 5.6. Plot of rate of change of penetration depth w.r.t stress applied $\frac{d}{d\sigma}(h_m)$ vs. T

Table 5.2 SSCR at various weld zones with different stress and temperature

Zone	Stress (MPa)	SSCR, $\dot{\varepsilon}$ (mm / sec)		
		310 °C	330 °C	350 °C
BM	21	4.35×10^{-5}	1.33×10^{-4}	1.00×10^{-3}
	24	6.06×10^{-5}	2.50×10^{-4}	1.28×10^{-3}
	27	1.38×10^{-4}	3.51×10^{-4}	2.30×10^{-3}
NZ	21	1.0×10^{-4}	3.18×10^{-4}	4.42×10^{-4}
	24	3.0×10^{-4}	3.99×10^{-4}	6.32×10^{-4}
	27	4.0×10^{-4}	6.31×10^{-4}	7.94×10^{-4}
TMAZ	21	9.20×10^{-5}	2.81×10^{-4}	2.94×10^{-4}
	24	1.56×10^{-4}	2.69×10^{-4}	3.24×10^{-4}
	27	2.33×10^{-4}	2.53×10^{-4}	5.18×10^{-4}
HAZ	21	1.34×10^{-4}	2.01×10^{-4}	2.13×10^{-3}
	24	2.33×10^{-4}	5.98×10^{-4}	4.17×10^{-3}
	27	3.39×10^{-4}	1.00×10^{-3}	4.76×10^{-3}

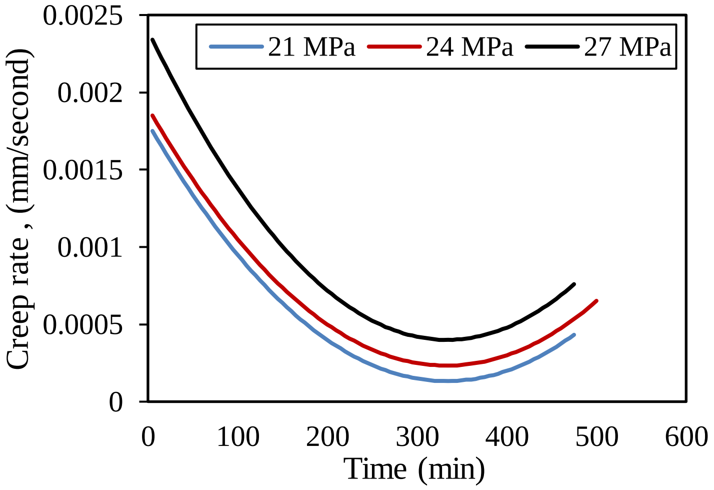

Fig. 5.7. Plot of creep rate vs time ($\frac{dh}{dt}$ vs t) of NZ at 310 °C

The basic text book information of a typical creep curve reveals that the decreasing creep rate with time during the primary creep stage has been attributed to strain hardening or reduction in the density of mobile dislocation. The secondary or steady-state region is characterized by a constant creep rate which is the result of maintaining a balance between softening and work hardening. The former is the result of recovery and the later due to dislocation generation. In the case of IC testing in addition to the applied stress, generation of dislocation, dynamic recovery and dynamic recrystallization, the other factors to be considered are the frictional resistance at the indenter-work piece interface and the constraint of metal beneath the indenter to move sideways during the advancement of the indenter. Evolutions of sub-grains occur due to the higher strains at the beginning of the IC experiments and at steady-state creep stage the sub-grains became saturated (Blum, 1991). The time dependent strain (ε) was measured during the experiments at different temperatures and stresses from which the steady-state creep rate ($\dot{\varepsilon}$) or the minimum creep rates were evaluated. From Table-5.2, the $\dot{\varepsilon}$ value was found to be the least in BM and the maximum at NZ indicating the highest creep resistance at BM region and low resistance at NZ. In TMAZ, $\dot{\varepsilon}$ was higher than that of HAZ. The different values for $\dot{\varepsilon}$ observed in different weld zones is due to the variation in the grain structure and size formed during the FSW process.

5.4.1 Factors Governing Steady-State Creep Rate

Investigation of the grain size effect on the high temperature creep rate in various materials reveal that coarse grain size decreases the steady state creep rate, i.e., coarse grain increases the creep resistance. Fleck et al. (1970) stated that the increased number of sub-grain boundaries at the secondary stage of high temperature creep deformation process leads to a decrease in the creep resistance and weakens the material. The authors reported that at temperatures above $0.4T_m$ and at low strain rates and stresses, fine grain sized materials show poor creep resistance since the mechanism of creep deformation is by grain boundary sliding. Al-Ganainy and Mostafa (2000) observed that when grain size increases, the total grain boundary energy is reduced thereby reducing the precipitation of the intermetallic compounds at grain boundary regions. Thus, the precipitation of intermetallic phases is mainly confined to inside the grain and restricts the dislocation motion which decreases the $\dot{\varepsilon}$. The NZ of the FSWed material possesses an equiaxed and finer grain structure than the BM. In the present examination, the grain size of the NZ is 23 µm and BM is 93 µm. This may be one of the reasons for the lower creep resistance at the NZ of the FSWed sample compared to the BM as shown in Fig. 5.2. Another reason may be generation of high dislocation density resulting in dislocation tangles at the weld zone as well as dissolution of the second phase precipitates as a result of the high frictional heat developed during the stirring process. TEM micrographs of Fig. 5.8 show the presence of precipitated particles and dislocation tangles. During the load application, the dislocations are pinned by the second phase ($CuAl_2$) precipitations (Sahu et al., 2016) resulting in an increase in the rate of creep deformation (Al-Ganainy and Mostafa, 2000).

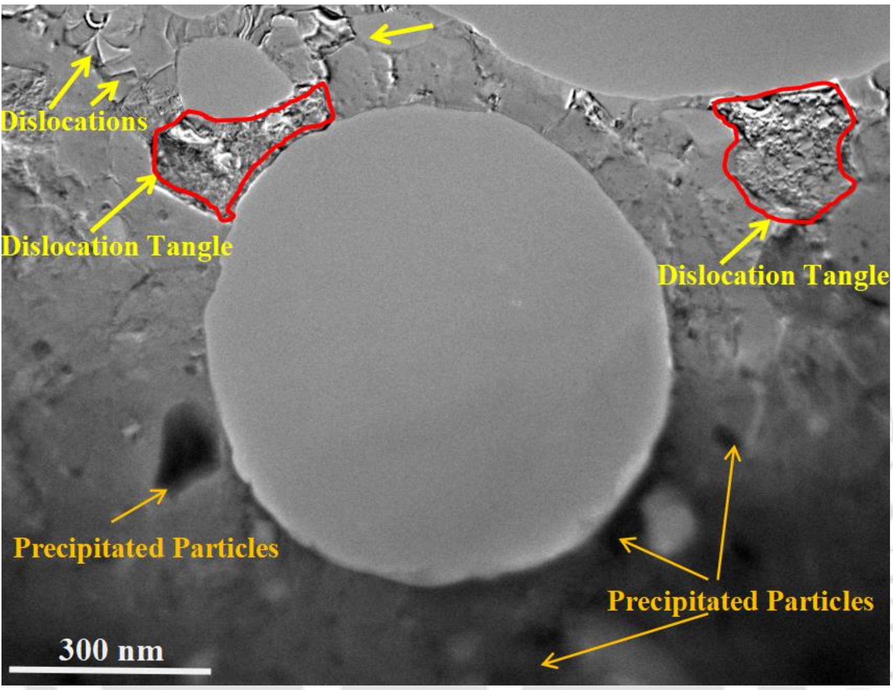

Fig. 5.8. Dislocation structures at FSWed area captured by TEM (Das et al. 2021)

FESEM micrographs of Fig 5.9(a-d) reveal presence of $CuAl_2$ second phase precipitates at the NZ, TMAZ, HAZ and BM respectively. The volume fraction of precipitates is higher in the NZ compared to the other zones as shown in Fig 5.9(a). This is due to high rate of nucleation of the $CuAl_2$ precipitates in the matrix due to the high heat generated at the NZ during the FSW process. These larger precipitates decrease the creep strength by facilitating the dislocation glide during the deformation process. The region with high precipitate density is the NZ and is presented in Fig. 5.10(a). The figure depicts the precipitations along the grain boundaries as well as inside the grain. The precipitates inside the grains were mainly rod-shaped as shown in Fig. 5.10(b) since their growth at the IC tested temperatures were along certain crystallographic planes. In contrast, very fine sized spherical precipitates are found at the grain boundary regions as well as inside the grains as evident from Fig. 5.10(c-d). These precipitates speed up the creep deformation process due to stress concentration and also due the particle-matrix interfacial energy.

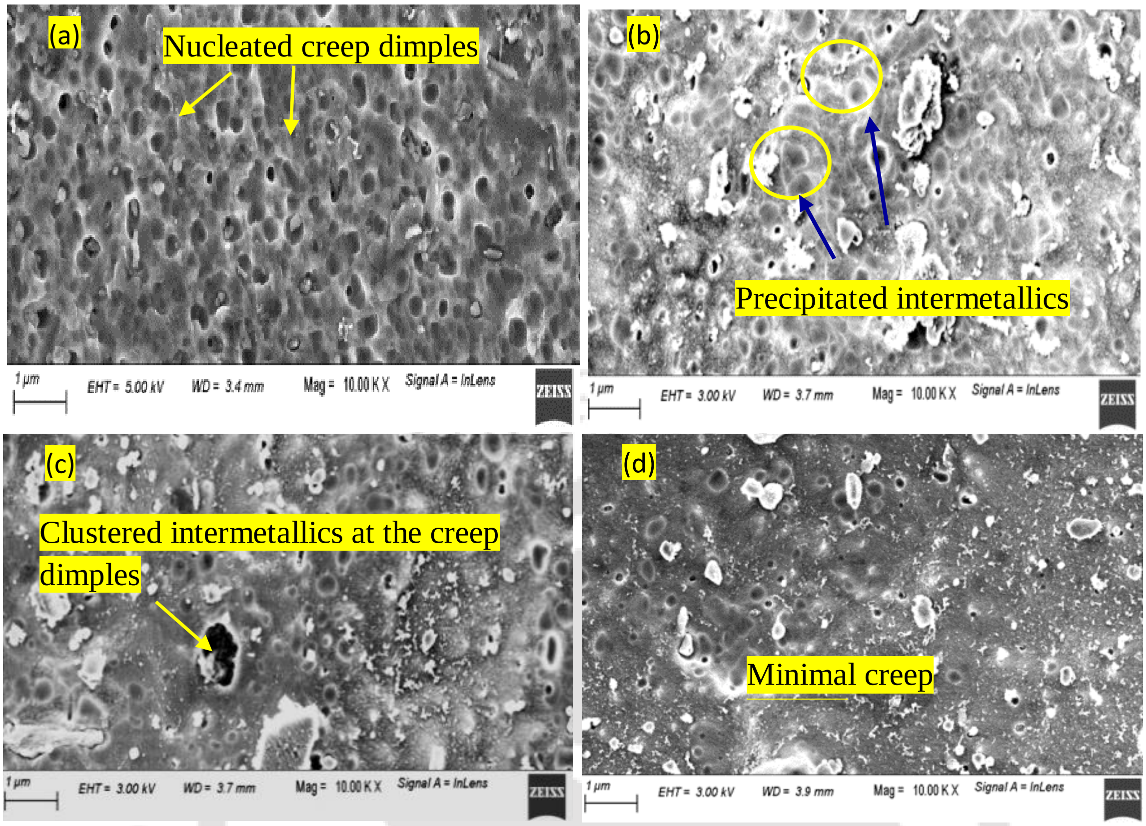

Fig. 5.9. FESEM image of IC tested surface with precipitations at (a) NZ, (b) TMAZ, (c) HAZ and (d) BM.

Microstructure of TMAZ revealed coarse grains deformed along the flow direction due to the tool rotation. As mentioned earlier, the average grain size was coarser than that of the NZ. The precipitation accumulation at the grain and grain boundaries at TMAZ are less than the NZ as shown in Fig 5.9(b). The calculated value of the $(\dot{\varepsilon})$ at TMAZ was found lower than the NZ and higher than the BM at the same experimental conditions. This indicates higher creep strength for the TMAZ compared to the NZ. The grain structure of HAZ is nearly similar to the BM as it does not undergo any recrystallization process and conducts only a portion of frictional heat during the FSW process (Sahu et al., 2016). A comparatively finer and less no of precipitation accumulation is seen as in Fig.5.9 (c). Whereas, this type of structure is only marginal in case of BM (Fig. 5.9(d)). Hence the $\dot{\varepsilon}$ value obtained at HAZ is nearly equal to the BM. Observation under FESEM reveals many micro-creep dimples on the surface for all the cases. The creep cavities nucleated and grew only up to certain limits since the experiment was prematurely stopped as the steady-state creep rate was achieved. No evidence of the growth and coalescence of the creep dimples were observed as the sample did not enter into the tertiary creep stage.

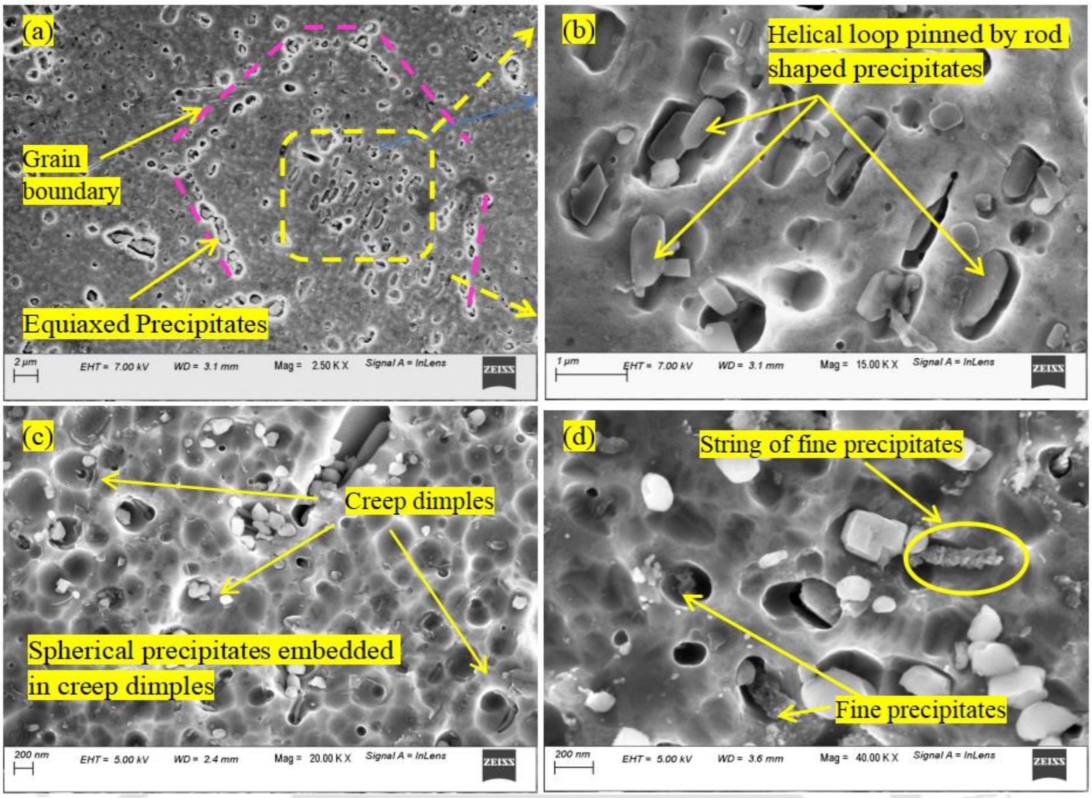

Fig.5.10. FESEM images of precipitations after IC test (a) at grain boundary, (b) magnified image of (a) rod shaped precipitations within the grain, (c) spherical precipitates and (d) magnified image of (c)

Different models exist for correlating the creep strain rates with the applied stress and temperatures. Out of these the power-law relationship is found to be the most suitable for metallic alloys especially at temperatures > $0.5T_m$. The power law expression for creep deformation is of the Arrhenius rate type of equation expressed by (Das et al., 2018).

$$\dot{\varepsilon} = A\,\sigma^n\, Exp\,(-Q/RT) \qquad (5.1)$$

Where $\dot{\varepsilon}$ = steady-state creep rate (SSCR), n = stress exponent, A = a constant, Q = activation energy for creep deformation, R = the universal gas constant and T = temperature in K.

For impression tests, the strain rate ($\dot{\varepsilon}$) and stress can be expressed in terms of minimum impression velocity (V_{imp}) and punching stress (σ) by using conversion factors.

$$\sigma_{imp} = 4L/\pi d^2 = C_1\,\sigma \qquad (5.2)$$

$$\dot{\varepsilon} = V_{imp}/C_2 d \qquad (5.3)$$

Where, L is the applied load, d is the indenter diameter (1 mm for this case). The constants or conversion factor C_1 varies from 2 to 4 and C_2 varies from 0.5 to 1.5. For most materials, $C_1 \approx 3$ *and* $C_2 \approx 1$

For the present case C_2 =1, Hence, $\dot{\varepsilon} = V_{imp}$ (5.4)

The value of stress exponent (*n*) can be determined from the IC tests. At temperatures above $0.5T_m$ (where power law creep is effective), the creep deformation of polycrystalline materials is controlled by the mechanisms associated with the stress exponent values. Mahmudi et al. (2004) found that with *n* values around 1 the deformation is by diffusional creep, for *n* values almost 2 the deformation is by grain boundary sliding, and with *n* values in the range 4–6 the deformation mechanism is by dislocation climb. The *n* value was determined from the slope of the $log\, \dot{\varepsilon}\ vs\ log\, \sigma$ plot. where $\dot{\varepsilon}$ and σ are the SSCR and applied stress $\dot{\varepsilon}$ is determined as the value of the lowest creep rate obtained from a strain rate vs. time plot for each experimental condition. The *n* values for the present IC tests were determined at three different testing temperatures viz; 310, 330 and 350º C. The plots are shown in Fig.5.11(a-d) for BM, NZ, TMAZ and HAZ respectively.

For the present investigation, the stresses are 21, 24, and 27 MPa. $\dot{\varepsilon}$ was calculated as the lowest creep rate value found from the strain rate ($\dot{\varepsilon}$) vs. time curve for each experimental condition. The plot represented a linear relationship of log σ with log $\dot{\varepsilon}$. The stress exponent values at three considered temperatures of 310, 330 and 350˚C and loads are calculated for each zone individually and are presented in Table-5.3. The stress exponent decreases with an increase in temperature. Plot of *n* vs. *T* revealed that the *n* value was decreased with test temperature. The *n* could be correlated to *T* with a polynomial of order 2 with a coefficient of correlation $R^2 = 1$. The equations for $n = F(T)$ are:

For BM, $n = -(0.00007\, T^2 + 0.081\, T + 22.482)$ (5.5)

for NZ, $n = -(0.0003\, T^2 + 0.1875\, T + 26.505)$ (5.6)

for TMAZ, $n = -(0.0004\, T^2 + 0.2785\, T + 51.645)$ (5.7)

for HAZ, $n = -(0.0004\, T^2 + 0.228\, T + 32.114)$ (5.8)

The values of *n* at BM are 4.58, 3.92 and 3.32 when tested at 310, 330 and 350 ˚C respectively. The respective values for NZ at these temperatures are 2.79, 2.70 and 2.37, for TMAZ are 3.75, 3.29 and 3.17 and 3.73, 3.65 and 3.28 are for the HAZ.

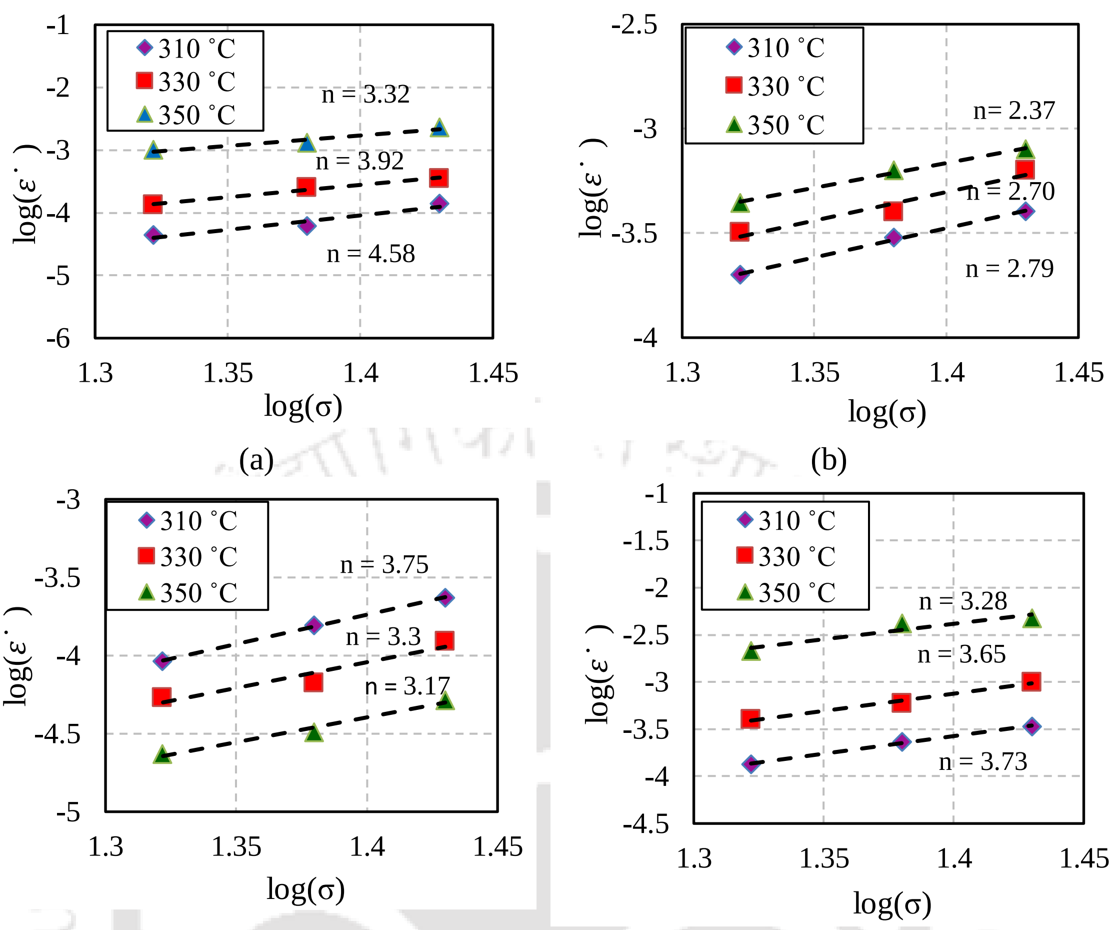

(a) (b)

(c) (d)

Fig. 5.11. Plots of *log ($\dot{\varepsilon}$)* vs. *log(σ)* for (a) BM, (b) NZ, (c) TMAZ and (d) HAZ for the IC test

Table 5.3 Stress exponent values at various zones at considered temperatures

Zone	Temperature (˚C)	*n* Value
BM	310	4.58
	330	3.92
	350	3.32
NZ	310	2.79
	330	2.70
	350	2.37
TMAZ	310	3.75
	330	3.30
	350	3.17
HAZ	310	3.73
	330	3.65
	350	3.28

Sharma et al. (2000) reported that during IC, due to the applied stress, accumulation of dislocations occurs in the elastic-plastic region leading to increase in dislocation density at high temperature. The elastic-plastic zone beneath the indenter is subjected to stress at elevated temperature, thereby resulting in material flow from these elastic-plastic region to the surface. The process leads to the dislocation glide which is facilitated only by vacancy diffusion. The results of the IC test reveal that, in each zone, the value of stress exponent decreases with increase in temperature. This is attributed to the generation of excess vacancies at the high IC test temperatures. The high concentration of vacancies at higher temperatures promotes dislocation climb process and aids in softening of the material. The low *n* values indicate creep by dislocation climb at high temperatures.

The apparent activation energy for the IC deformation processes (Q_{ic}) was estimated by plotting the $log\ \dot{\varepsilon}$ *vs. 1000/T* at constant stresses. The slope of the plot gives the value of $Qic/2.3R$ (Yadav et al., 2019). Fig. 5.12(a-d) depicts the $log\ \dot{\varepsilon}$ *vs. 1000/T* plots for the BM and welded samples at NZ, TMAZ and HAZ respectively from which the apparent activation energy values were determined. The values of Q_{ic} presented are the average of the three values.

The calculated average value of Q_{ic} for the IC process for BM was estimated as 226.34 kJ/mol. The activation energy of HAZ was 221.45 kJ/mol and is near to that of the BM. Q_{ic} for the TMAZ was 118.5 kJ/mol and depends on the level of the stress applied during the test. In the case of welded samples, NZ has the lowest activation energy which was 53 kJ/mol and was characterized by very fast creep deformation process. The values of Q_{ic} for the IC test for the BM and HAZ are higher than the activation energy for self-diffusion in pure aluminium (~142 kJ/mol). Sharma et al. (2000) considered the role of temperature on elastic modulus during the calculation of the activation energy (Q_{ic}) for IC process by the relationship given by:

$$Q_{ic} = Q_d + R\left(\frac{d\ (\ln E)}{d\ (1/T)}\right) \tag{5.9}$$

where, Q_d is the activation energy for self-diffusion and *E* is the elastic modulus.

As the term $d\ (\ln E)/d(1/T)$ is positive, the above equation predicts that $Q_{ic} > Q_d$. The quantity of the above term increases with temperature at temperature > $0.5T_m$. The values of *n* and activation energy presented in Table 5.4 reveals dislocation glide ($n \approx 3$) as the deformation mechanism at BM, TMAZ and HAZ. From the stress exponent and also since the calculated activation energy for the creep deformation is lower than the value of the lattice energy for self-diffusion, it appears that grain boundary sliding is the deformation mechanism at the NZ (Kutty et al., 2010). Different activation energy at different zones is mainly due to the change in vacancy concentration (McKamey et al., 1992). The creep strength at different localized zones was found to be in the order of BM > HAZ > TMAZ > NZ and depends on the grain size as discussed earlier. As this creep deformation process is under low stress regime (n<5) (Sharma et al., 2000) the creep strength increases as the grain size is increased.

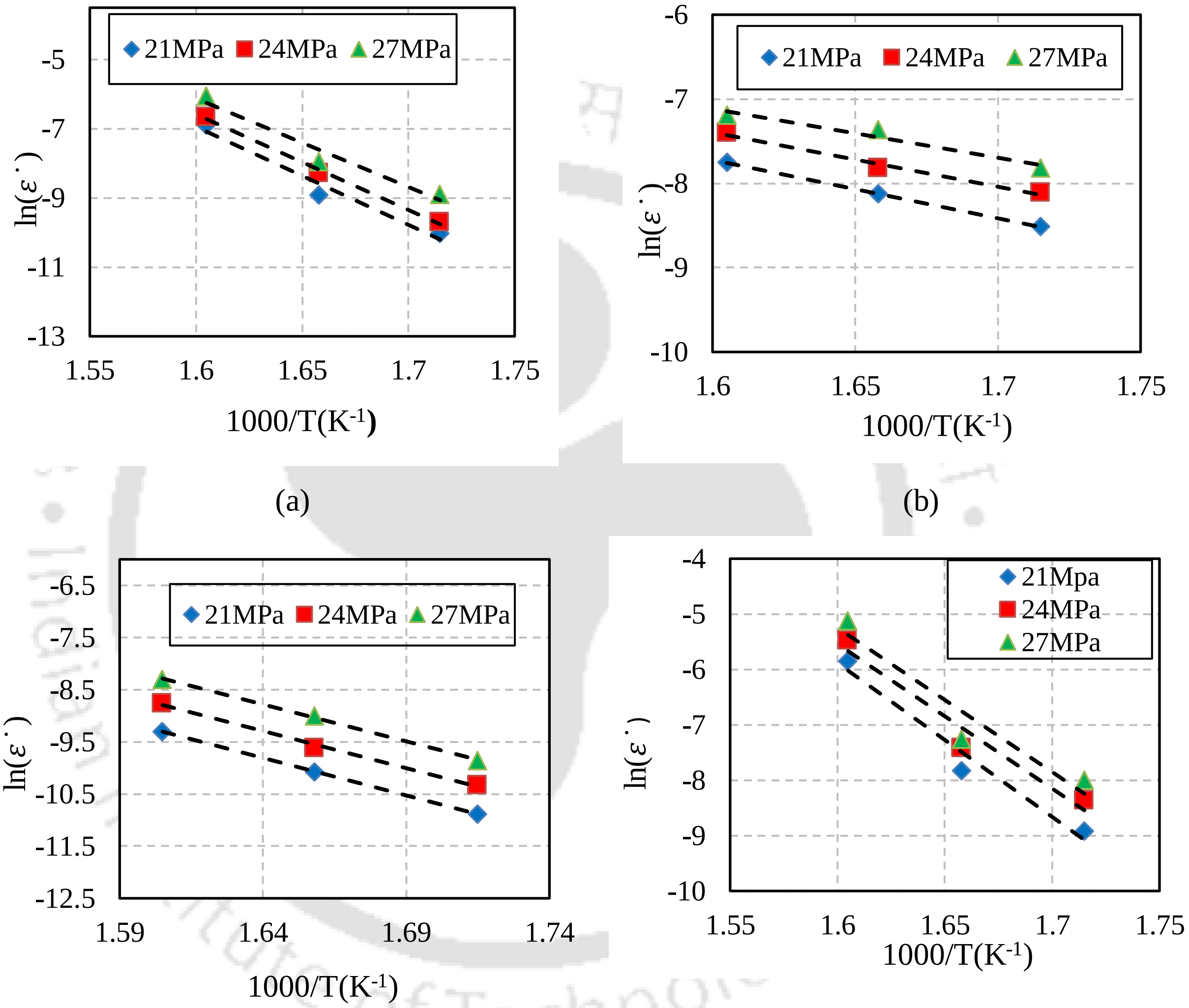

(a) (b)

(c) (d)

Fig. 5.12. Plots of ln ($\dot{\varepsilon}$) vs 1000/T(K^{-1}) at (a) BM, (b) NZ, (c) TMAZ and (d) HAZ

Table 5.4 Activation energy Q_{ic} at different IC tested zones.

Zones	**Q_{ic} value$_{(avg)}$ (KJ/mol)**
BM	226.34
NZ	53.04
TMAZ	118.51
HAZ	221.45

5.4.2 Hardness and Microstructure during Creep

The effects of high temperature IC deformation process on hardness and microstructural properties in FSWed AA2014 are presented and discussed in this section. Owing to the combined effects of the plastic deformation caused by the tool pin due to the stirring process and the frictional heat generated during the tool rotation, recrystallization occurs at the NZ resulting in fine grained structures. The average hardness of the welded area was more than the BM after FSW due to the finer grains as discussed earlier. The hardness of welded specimen after IC test was determined at locations as shown in Fig. 5.13 at 0.5 mm interval between two consecutive points and 1mm between two lines. Table 5.5 shows the microhardness values of the BM as well as different weld zones after IC tests. It is observed that the hardness of the BM as well as that of the welded samples increased after IC. The reason for this is attributed to the fine grain size due to recrystallization and precipitation of intermetallics at the grain boundaries during the IC test (Gupta, 2020). The presence of precipitated particles is seen at the grain periphery and also inside the grain. At NZ, the concentration of these particles is more compared to that in other zones as discussed earlier. Further recrystallization due to IC testing phenomena decreases the grain size which increases the compactness and hence the hardness.

Fig. 5.13. Hardness tested sample after IC test

Table 5.5 Average micro-hardness values at different IC tested zones

Zones	Avg. microhardness after IC test
BM	117
NZ	190
TMAZ	180
HAZ	165

During IC test, with the advancement of the indenter, the material gets deformed with three noticed zones viz: zone I, zone II and zone III as shown in Fig. 5.14 (a) in the specimen cut transverse to the impression mark. Zone-I comprises of a dead metal zone just below the indenter which does not deform during the IC test. The bulk metal in the dead metal zone acts as a constraint for the metal flow during the creep deformation process and hence the metal flows along the lateral sides of the indenter. The optical micrographs of the zone I below the indenter is shown in Fig. 5.14 (b) which represents the undeformed grain structure with fine agglomerated Al_2Cu second phase particles. This non-deformed hemispherical core incorporates a hydrostatic pressure within (Butt et al., 1996) this region. This zone is surrounded by an elastic-plastic hemispherical zone represented as zone II shown in Fig.5.14(c). In zone II grains are plastically deformed due to shear force (Vijayanand et al., 2014). This region is characterized by the flow lines emerging from the indenter lateral side surface. The zone accommodates the punch displacement and deformation occurs heavily and the metal flows radially as is evident from the flow lines in the figure. In addition, very fine grains due to dynamic recrystallization are also evident in this region.

From the optical micrographs, it was noticed that the grains get deformed heavily due to the IC testing conditions. The deformation occurs due to the punching force applied during the testing. Agglomerated second phase particles at the grain boundary were found to be more at this zone. The figure also reveals fine grains with average diameter of 12 µm at NZ i.e., the grain diameter is around 50% that of the diameter of NZ before IC test. This is the result of dynamic recrystallization and accelerated aging during IC test (Gupta et al., 2020). The microstructure study also reveals a fine grain size at other creep tested zones. Zone III (Fig. 5.14(d)) indicates that not much metal flow has taken place since the distance of this zone is far from the indenter tip. The secondary precipitation process discussed above occurs during the IC process of the FSWed as well as the BM (Rajak et al., 2020).

The area below the indenter at each localized zones of NZ, TMAZ, HAZ as well as BM were viewed under optical microscope from the top surface after IC test. The photo micrographs of these regions are shown in Fig. 5.15(a-d) respectively. The features indicate that, below the indenter, neither the grains are deformed not recrystallization has taken place and the microstructure is similar to that observed before the IC test. The grains in NZ are finer than that of BM (Fig. 5.15a). The TMAZ retains the usual pulled out grains shown in Fig.5.15b and are finer than HAZ (Fig.5.15c) and BM (Fig.5.15d). The unchanged grain size below the indenter indicates the presence of hydrostatic pressure (Butt et al., 1996). Intermetallics at the grain boundaries and embedded inside the grain as shown in Fig.5.9. was also observed in Fig. 5.15. in the respective zones. From the EDX analysis, the composition of the intermetallics before and after the IC test of the welded sample were identified as the compounds of Al with the Cu, Fe, Si, Mn and Mg from the EDX study shown in Fig. 5.16(a-b) respectively.

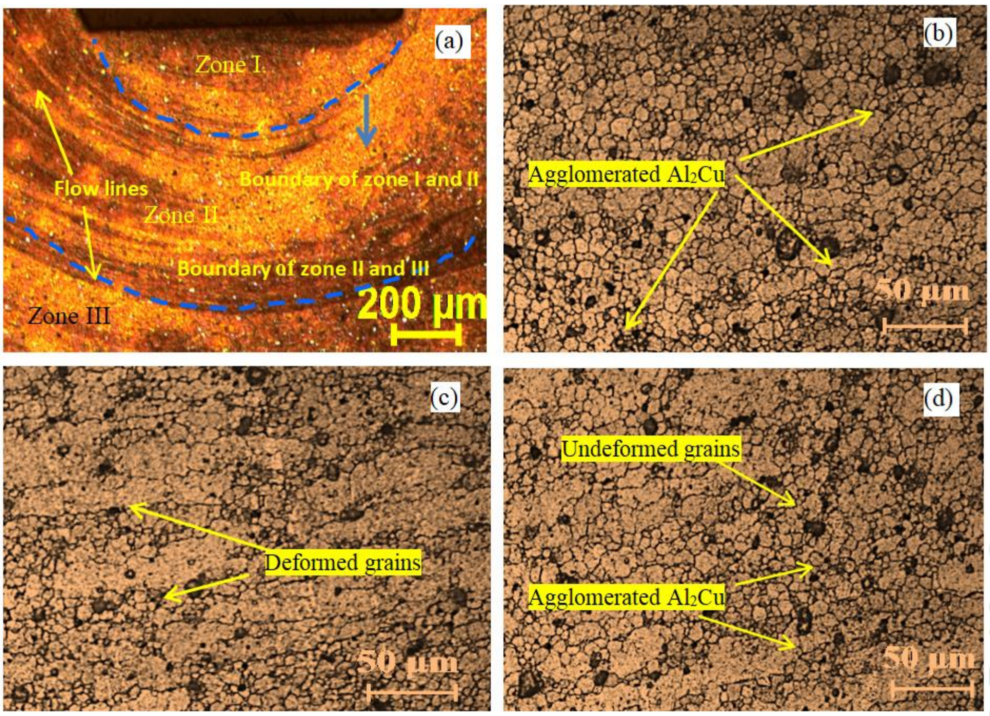

Fig. 5.14 (a) Optical micrograph of different zones below the indenter after IC test, detail microstructure at (b) zone I, (c) zone II and (d) zone III.

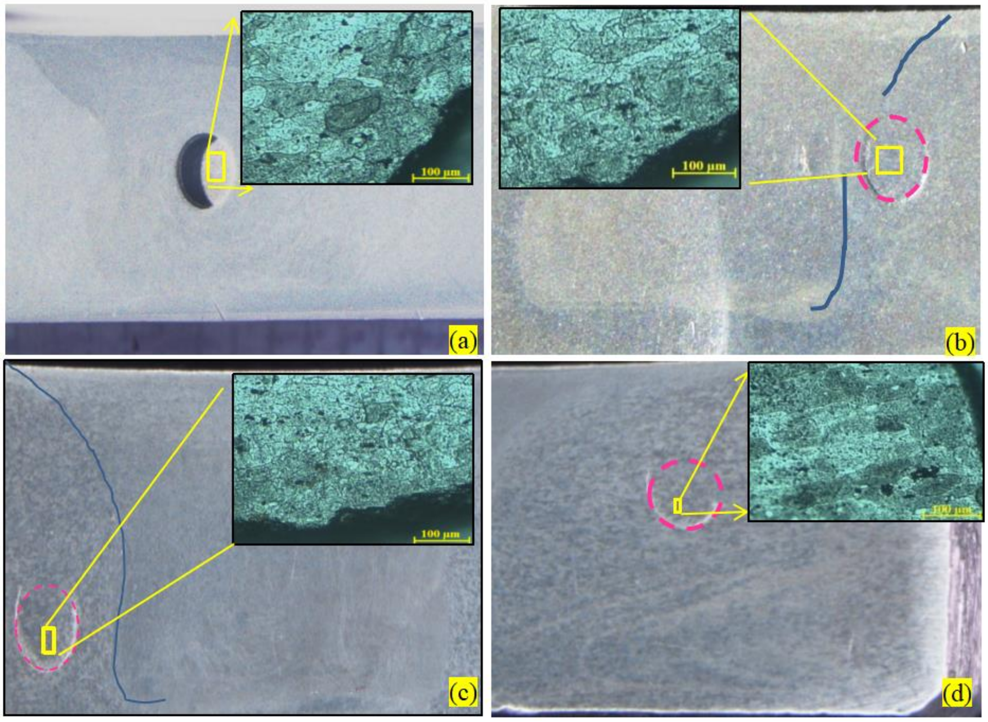

Fig. 5.15 Optical micrographs of top view of IC tested surface at (a) NZ (b) TMAZ (c) HAZ and (d) BM

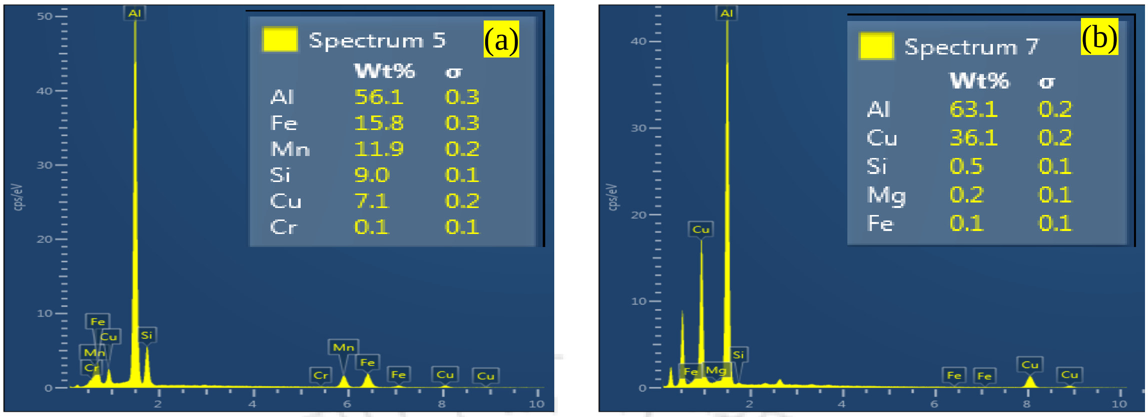

Fig. 5.16 EDX image of intermetallic (a) before and (b) after the IC test of FSWed samples

5.5 Summary

The IC behaviour of FSWed AA2014 was analyzed at different localized area and remarkable differences in the creep behaviour of FSWed and BM material was observed and the following conclusions are extracted.

- Plastic deformation occurred on account of intense material flow in FSW process, finer equiaxed grain structures were obtained in the NZ.
- The creep strength of AA2014 was declined considerably after FSW and was incorporated with the lower activation energy which is dependent on the temperature and grain size.
- NZ shows the least value of creep rate, stress exponent and apparent activation energy for the IC process in compared to the TMAZ and HAZ. For the coarse grain structure, creep strength is equivalent to the BM at the HAZ.
- Hardness of the creep tested sample was increased due to further decrease in the grain structure of the localized area for the recrystallization during IC test and agglomeration of precipitates.
- The intermetallic compounds of Al + Fe + Cu as ascertained by the EDX analysis were clustered at the grain boundaries.
- The precipitated intermetallic at the NZ surface is more than the BM and shows the highest among all the zones.

Chapter 6

Fatigue Crack Growth Rate Studies at Different Weld Zones of FSWed AA2014

6.1 Introduction

Aluminium alloys find wide applications in aerospace and locomotive industries as structural materials due to their high strength to weight ratio. FSW is employed as the best metal joining process in these materials for its numerous advantages over the conventional fusion welding process. These structural components are always subjected to reversed / repeated and / or random stress cycle conditions for longer period. For having higher service life of these components, a better fatigue performance of the materials is required. Better fatigue property of these components can be achieved by controlling the microstructure of the weld area. The microstructure changes that can be achieved by varying the process parameters of the FSW process for AA2014 was investigated and the results have been presented in Chapter 4. Due to the inherent nature of the FSW process, the microstructure of the weld region is heterogeneous and hence the mechanical properties will be different for different zones (Mishra and Ma 2005). The fatigue failure during the application will therefore be along the weakest zone of the weldments. The weakest zone during the FSW process therefore is required to be identified and the necessary thermos-mechanical treatment may be carried out to eliminate or reduce this effect.

In this chapter the FCG characteristics are studied at the selected zones of FSWed AA2014 Aluminium alloy. The FCGR of FSWed AA2014 plate through various weld zones was studied with initial notches located parallel to the welding direction. The effects of microstructures on the FCGR at NZ, TMAZ and HAZ have been examined and compared with that of the BM. The result of heat treatment (HT) carried out in this case on the mechanical properties (hardness and tensile strength) is studied in this section. The results of the studies are presented in the subsequent sections followed by discussion and finally, the chapter ends by summarizing the findings.

6.2 Tensile Properties and Hardness of FSWed Specimen After Heat Treatment

The tensile stress vs. strain curve of FSWed sample without and with heat treatment are shown in Fig 6.1. The mechanical properties of both samples are presented in Table 6.1. During the PWHT, release of internal stresses (that are induced during the FSW process) results in enhancement of the mechanical properties. The UTS and YS were 102% and 103 % of the as-welded samples respectively. The reduced tensile strength of the welded joint was recovered up to a certain extent after the PWHT. Though the tensile properties like UTS and YS were improved, % elongation was decreased after PWHT and is 93% of the as-welded sample. The tensile fracture features as in Fig 6.2 show dimple features indicating ductile failure. Figure 6.2(a) represents complete ductile tensile fractured surface before HT process. Figure 6.2(b) depicts finer and shallow dimples all over the fractured surface of the HTed sample indicating a slight decrease in the ductility.

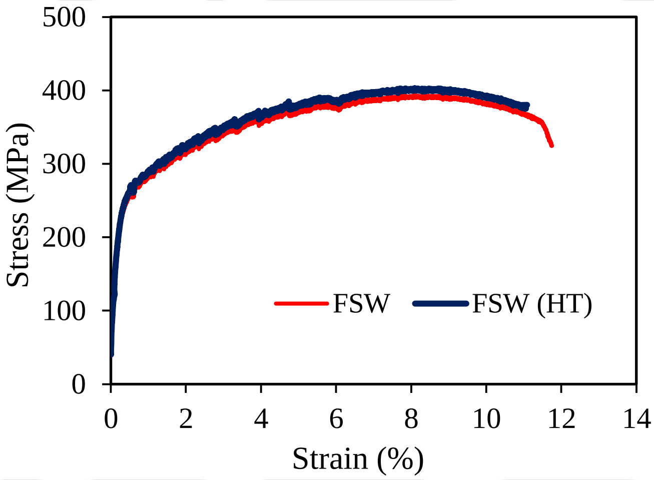

Fig. 6.1. Stress vs. strain curve of specimen after FSW and FSWed specimen after HT

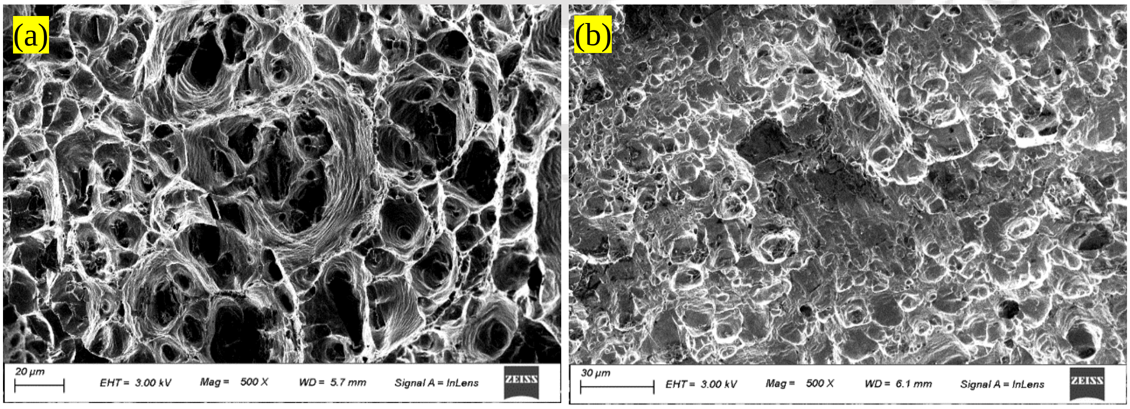

Fig. 6.2. Tensile fractography of FSWed sample (a) before and (b) after the HT process

Table 6.1: Tensile properties after HT

Properties	UTS (MPa)	YS (MPa)	%E	Hardness (average) at		
				NZ	TMAZ	HAZ
FSW HT	403	293	11	168	153	147
FSW	393	282	11.75	165	150	132

The hardness of the FSWed samples after HT were analyzed and compared with the FSWed sample without HT. Figure.6.3 shows the location of the hardness testing points along the weld area. Fig. 6.4 shows the variation of hardness across various weld zones in the FSWed sample before and after PWHT. The hardness distribution across different weld zones of the FSWed sample is uneven in addition to the fact that the difference in hardness from HAZ to the NZ is large. It is also evident that the variation in hardness from HAZ to NZ has reduced and the distribution of hardness across the weld zones are almost even after heat treatment. Due to the post weld heat treatment of solutionizing followed by ageing the strength of the FSWed joint is restored. From the figure it is found that there is only a marginal increase in the hardness value at NZ and at TMAZ (both almost ~ 2%), whereas, the hardness at the HAZ increases by 10% after the PWHT. This may be due to the dynamic recovery and recrystallization process. It is probable that a higher dislocation density in this zone repairs the precipitation hardening during aging by adding the nucleation sites (Wei et al., 2000). Ageing following quenching caused the homogeneous precipitation of strengthening phases resulting in even distribution of the hardness across all weld zones (Krishna and Ramanaiah 2011). Since the role of hardness in fatigue crack propagation is insignificant (Tra et al., 2012) the effect of hardness is ignored in this study.

Fig. 6.3. Vickers microhardness tested sample along the weld area after HT

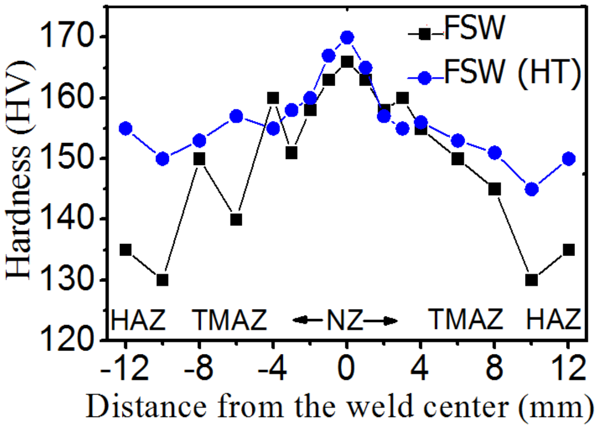

Fig. 6.4. Hardness at different weld zones of FSWed sample before and after HT

6.3 Microstructure at Nugget Zone Before and After the HT

The microstructure at NZ of the welded sample before and after the HT was studied under OM and illustrated in Fig 6.5 (a) and (b) respectively. During the FSW process the weld zone is subjected to stirring and plastic deformation process resulting in the presence of large amount of residual stress in the weld zone. This residual stress degrades the mechanical attributes of the friction stir welded structures. NZ is exposed to maximum temperature during FSW thereby altering the distribution of strengthening precipitate with associated change in the Mechanical properties. During FSW fine equiaxed grains are formed at the NZ due to recrystallization. OM micrographs of FSWed zones shown Fig. 6.5 (a) reveals sub-grains which are indicative of recrystallization during the joining process. The grain size measured by line intercept method was 23 μm. After the solutionising HT, it is observed that the sub-grains are absent and structure shows fine and almost equi-axed grains as shown in Fig. 6.5 (b). No change in the grainsize was observed after heat treatment.

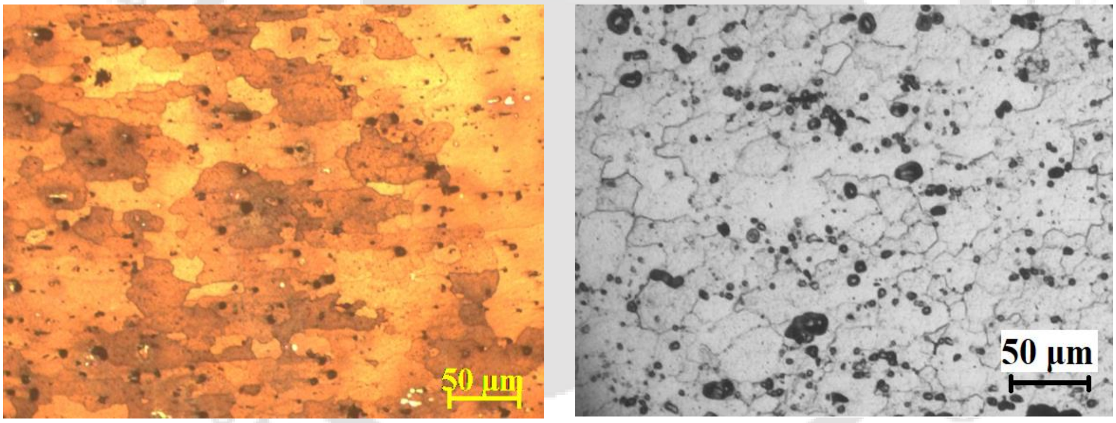

(a) (b)

Fig. 6.5. Microstructure at NZ (a) before and (b) after the Heat Treatment process

It was reported from a number of studies that the finer the grain size, the greater the fatigue crack propagation (FCP) rate (Hanlon et al. 2003, Vasudevan et al. 1997). This is valid from nanocrystalline metallic materials to the conventional microcrystalline alloys. In FSWed materials, the NZ experienced an intense plastic deformation as a result of which a huge number of dislocations would be generated. The dislocations are aligned and pinned at sub-grain boundaries or near second phase precipitations resulting in a deformed region around these sites. The fraction of the energy possessed by the NZ is called partial deformation energy. Since existence of the partial deformation energy adds to the total energy, the energy barrier is lowered thereby making the crack propagation faster at the

NZ compared to other zones. Study regarding the effect of dislocations on the FCG rate substantiated the fact that the FCP behavior was affected by dislocations (Nishimura and Miyazaki 2004), i.e., during the loading cycle, the vacancy generation, the emission and absorption of the dislocations at the crack tip and subsequent coalescence of cracks favors the crack propagation.

For the dynamic recovery and recrystallization in FSW process, the potential forces were the resultant of the deformation energy (Su et al. 2005). However, due to the rapid cooling of the weldments to room temperature the recrystallization process could not be fully accomplished. Hence some amount of energy is stored in NZ. Dai et al. 2013 evaluated this residual stored energy by the DSC analysis and studied its effect on the FCP rate at NZ as well. They concluded that this stored energy in the NZ contributes to the crack propagation. It was suggested that the stored energy provided additional driving force when crack propagated in NZ, thus made the crack propagation easier and faster. In the present work, a post weld heat treatment was performed to release the stored energy at NZ to validate its role in crack propagation. As the FCG property is affected by the grain structure (Vasudevan et al. 1997), the main aim of the HT is to just release the extra energy without altering the grain size. Grainsize analysis of the microstructure shown in Fig. 6.5 revealed that the grain size of the NZ was not altered by the PWHT and the grains were distinct with well-defined boundaries. The sub grain boundaries were not evident in the heat-treated samples indicating annihilation of dislocations thereby lowering the residual energy during HT (Dai et al. 2013). The hardness of the sample was increased as discussed earlier due to the re-precipitations of the strengthening precipitates. But according to the study carried out the effect of hardness on the FCG property was negligible and was not considered in this study (Bussu and Irving 2003, and Tra et al. 2012).

6.4 Fatigue Crack Growth Characteristics of FSWed AA 2014Alloy

Figures 6.6 (a), (b) and (c) present the crack length vs. no. of cycles (*a* vs. *N*) plots for the various FSW zones (NZ, TMAZ, HAZ and BM) at load ratios of 0.1, 0.33 and 0.6 respectively. The figure reveals same nature of plots along all the four zones. However, the crack growth rate was different along the different zones. It is also evident that the FCGR depended on the *R* ratio. The crack growth along all the four zones increased at a slow rate at the initial stages of the fatigue loading. After reaching around 10^4 cycles, the crack growth was faster through the NZ and TMAZ indicating the transition from second stage to the third stage of crack propagation.

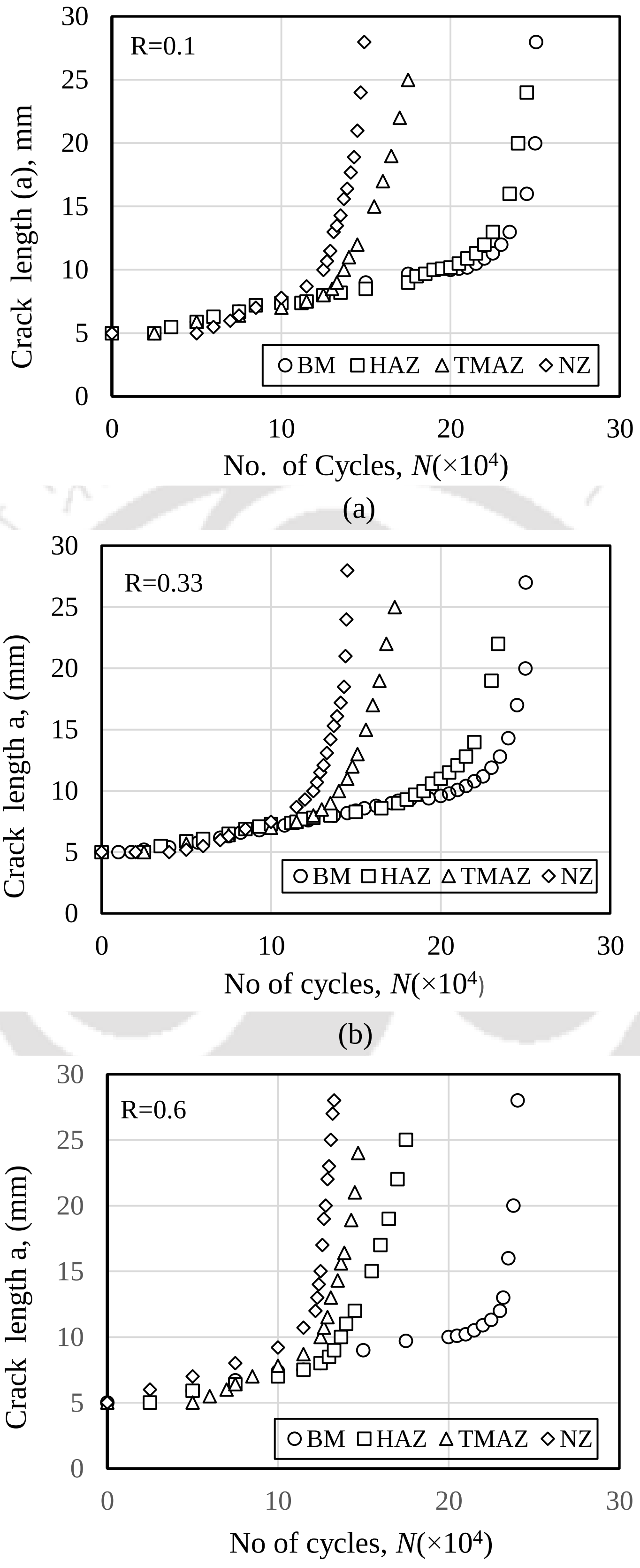

(a)

(b)

(c)

Fig. 6.6. Crack length vs. no. of cycles for stress ratios (a) 0.1, (b) 0.33 and (c) 0.6

As shown in Fig. 6.6 (a) at stress ratio 0.1, NZ shows a rapid crack growth after 1.20×10^5 no of cycles and TMAZ after 1.30×10^5 no. of cycles. The cracks in the HAZ and BM show linear growth in crack length for a greater number of cycles followed by a sudden increase with increase in the N. Rapid FCG occurs after a higher no. of cycles of 2.25×10^5 for HAZ and 2.35×10^5 for BM. The samples failed after 1.49×10^5 and 1.75×10^5 cycles when propagated along the NZ and TMAZ, respectively. In contrast to the above, the transition from second stage to the third stage crack growth occurred only after around 18×10^4 fatigue cycles when the crack growth was along the HAZ and BM. The failure of the samples occurred after 2.45×10^5 and 2.5×10^5 cycles for the crack propagation taking place along the HAZ and BM, respectively. With increase in the stress ratios as in Fig. 6.6 (b) and Fig. 6.6 (c), the no. of cycles required to enter third stage rack growth was less. The sample failed at less no. cycles also. For all the stress ratios BM shows the highest resistance to the FCG followed by HAZ and TMAZ. NZ represents the lowest resistance to FCG. However, differences in crack length are observed between the zones of the weld with a change in stress ratio with respect to N.

The critical crack size, a_c, is the crack length at which it enters the third stage of crack growth i.e., the crack length at which the crack has a tendency to propagate faster thereby catastrophic failure is about to happen and depends on the R value. The a_c value for each zone for all the three R ratios are determined from the da/dN vs. a plot shown in Fig. 6.7 (a) (b) and (c) for load ratios of *0.1*, *0.33* and *0.6* respectively. For all R values, maximum a_c was observed for the BM samples followed by HAZ, TMAZ and NZ in decreasing order. The critical crack length evaluated is presented in Table 6.2. At stress ratio of 0.1, BM specimens exhibit the maximum a_c of 32.01mm whereas HAZ exhibits 30.44 mm followed by TMAZ of 27.44 mm. NZ represents the least a_c of 25.77 mm that is 80.5% of the BM. There is a noticeable percentage decrease in the a_c of 19.5% in compared to the BM. For all the stress ratios the critical crack length for the BM is the highest and for the NZ is the least. For stress ratio *0.33* the a_c for BM, HAZ, TMAZ and NZ are 30.17 mm, 28.0 mm, 27.22 mm and 22.45 mm respectively. The a_c for NZ is 74.4% of the BM. For the stress ratio of *0.6*, the a_c for BM, HAZ, TMAZ and NZ are 29.13 mm, 26.52 mm, 25.46 mm and 18.31 mm respectively. The a_c for NZ is 62.8% of the BM. BM requires the highest and NZ the lowest no. of cycles for the respective a_c to achieve. This behaviour may be due to the decrease in the ductility of the welded metal compared to the BM due to the coarsening of the strengthening precipitates of the alloy during FSW.

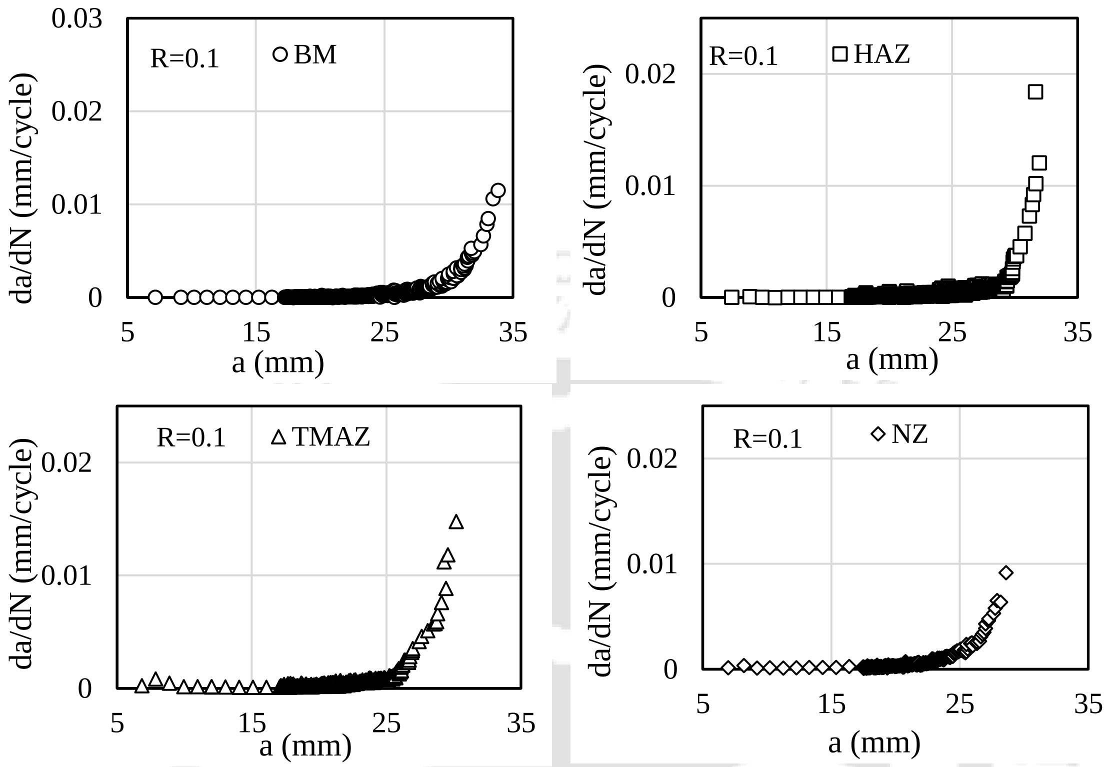

Fig. 6.7 (a). *da/dN vs.* crack length at R=0.1 for the four weld zones.

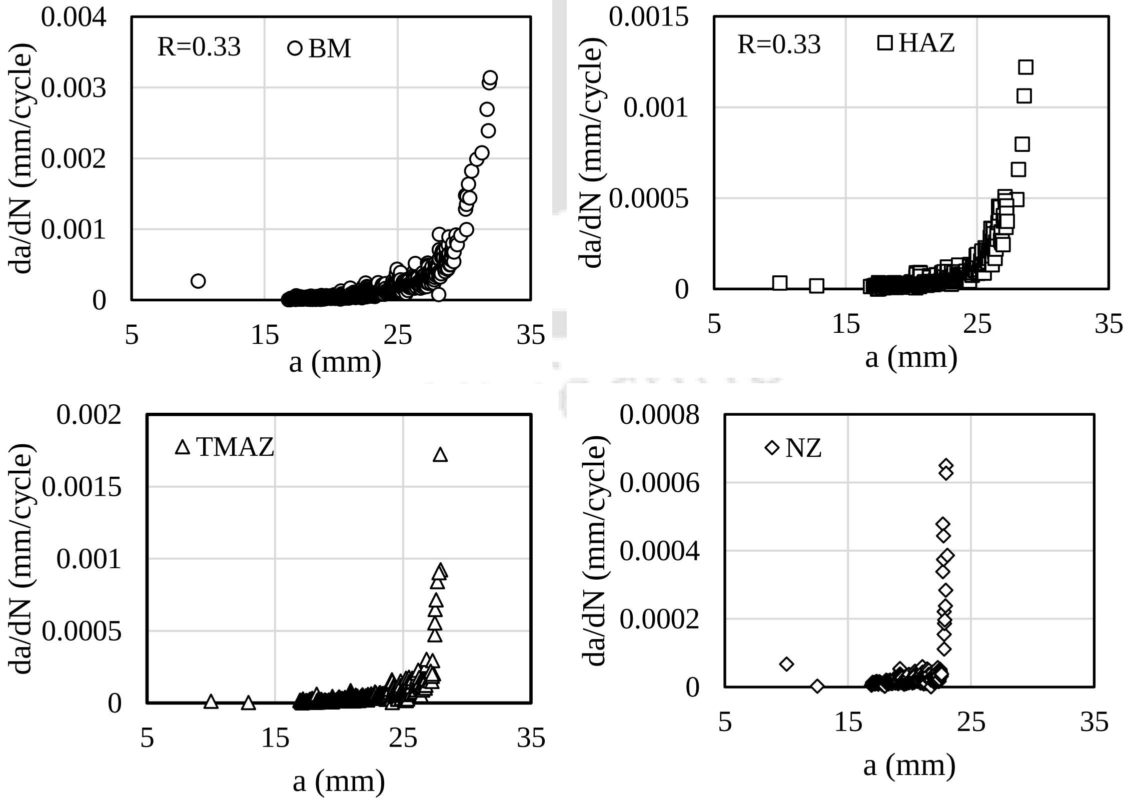

Fig. 6.7 (b). *da/dN vs.* crack length at R=0.33 for the four weld zones.

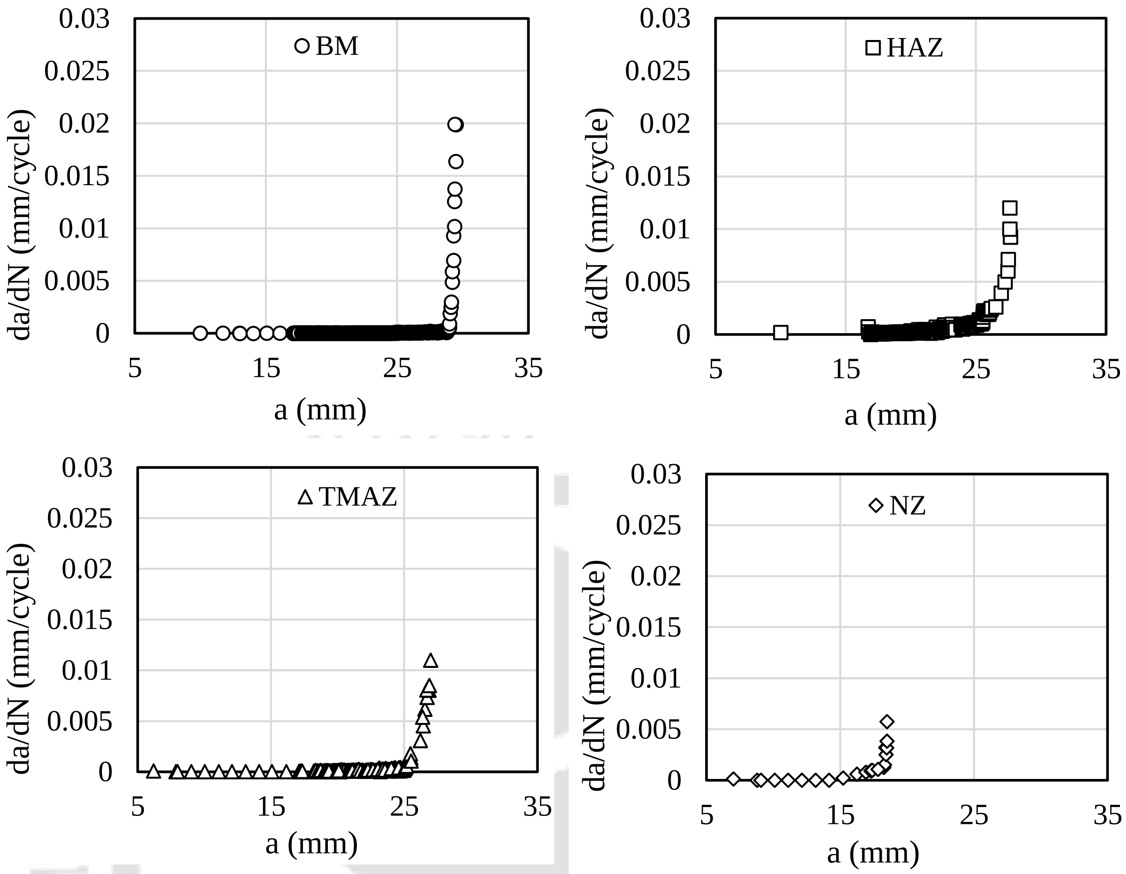

Fig. 6.7 (c). *da/dN vs.* crack length at R= 0.6 for the four weld zones.

Table 6.2 Critical crack length at different stress ratios

Stress Ratio	Critical crack length, a_c (mm) at different zones			
(*R*)	BM	HAZ	TMAZ	NZ
0.1	32.01	30.44	27.44	25.77
0.33	30.17	28.0	27.22	22.45
0.6	29.13	26.52	25.46	18.31

Fatigue behaviour of the BM as well as welded sample are studied at stress ratios of *0.1*, *0.33* and *0.6*. The crack growth rate phenomena in this study satisfies the following equations according to ASTM E647 as follows

$$(W - a) \geq \frac{4}{\pi}\frac{K_{max}}{\sigma_y} \tag{6.1}$$

Where (*W*- *a*) is specimen's uncracked length, K_{max} is the maximum stress intensity, σ_y is the yield strength (Sharma and Mishra, 2008). A typical curve for the FCG is a sigmoidal curve with three different regions viz: crack initiation region or stage I, stable crack growth region or stage II and unstable fracture region or stage III. The fatigue performance of the specimens at NZ, TMAZ, HAZ and BM were estimated and analyzed at region II according to Paris formula (Suresh, 1985) as given below.

$$\frac{da}{dN} = C(\Delta K)^m \quad \text{for} \quad \Delta K > \Delta K_{th} \tag{6.2}$$

Where, da/dN is the FCGR, *C* and *m* are material constants (intercept and slope of the log-log plot respectively), *m* is Paris index, *ΔK* is stress intensity factor range, ΔK_{th} is the FCP threshold. The fatigue crack growth rates *da/dN* as a function of *ΔK* applied for the respective *R* ratios of *0.1*, *0.33* and *0.6* at different weld zones along with the BM are presented in Fig.6.8 (a), (b) and (c) respectively. The double logarithmic plot represents a linear relationship between the FCG and *ΔK* applied. From the best fit result at Paris region or region II, *Paris* constants are estimated and presented in Table 6.3.

Table 6.3 Parameters from Paris equation at different weld zones

Sample	Stress ratio R= 0.1		Stress ratio R=0.33		Stress ratio R=0.6	
	C	m	*C*	m	*C*	m
NZ	4.85×10^{-11}	4.22	6.33×10^{-10}	6.24	9.2×10^{-9}	6.94
TMAZ	6.63×10^{-10}	3.43	4.8×10^{-11}	5.11	3.1×10^{-10}	5.81
HAZ	8.79×10^{-11}	2.69	6.4×10^{-10}	4.16	4.7×10^{-9}	4.36
BM	1.38×10^{-10}	2.42	1.9×10^{-9}	3.87	7.1×10^{-10}	3.95

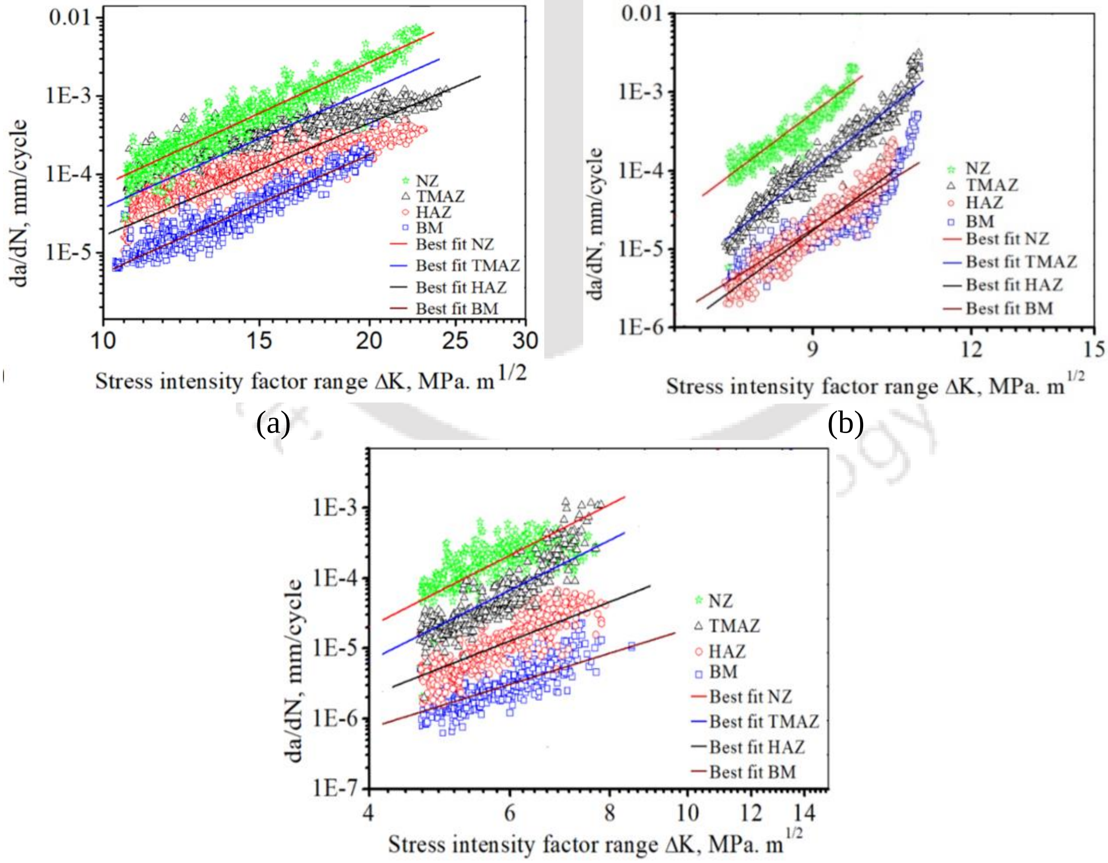

(a)

(b)

(c)

Fig. 6.8. Plots of *da/dN* vs. *ΔK* at different weld zones with stress ratios *R* values of (a) 0.1, (b) 0.33 and (c) 0.6

Figure 6.8 (a) represents the relationships between the FCP rates *da/dN* at each zone at constant load ratio of *0.1* and within a particular range of *ΔK.* As from the figure, the FCGR of welded metal at NZ is the maximum and resistance to FCGR is the lowest at the same range of *ΔK* in compared to the other zones. Paris equation is employed to fit the experimental data of FCGR at different zones of the FSWed specimen along with the BM to find out the rates as follows:

$$\frac{da}{dN} = 4.85 \times 10^{-11}(\Delta K)^{4.22} \quad (6.3)$$

$$\frac{da}{dN} = 6.63 \times 10^{-10}(\Delta K)^{3.43} \quad (6.4)$$

$$\frac{da}{dN} = 8.79 \times 10^{-11}(\Delta K)^{2.69} \quad (6.5)$$

$$\frac{da}{dN} = 1.38 \times 10^{-10}(\Delta K)^{2.42} \quad (6.6)$$

The equations (6.3), (6.4), (6.5) and (6.6) expressed above are for the FCGR *Da/dN* of NZ, TMAZ, HAZ and BM respectively. NZ represent the maximum Paris constant and the highest rate of FCGR followed by TMAZ, HAZ and BM respectively. Figure 6.8 (b) represents the relationships between the FCP rates *da/dN* at each zone at constant load ratio of 0.33. The Paris equations fitted are as follows:

$$\frac{da}{dN} = 6.33 \times 10^{-10}(\Delta K)^{6.24} \quad (6.7)$$

$$\frac{da}{dN} = 4.80 \times 10^{-11}(\Delta K)^{5.11} \quad (6.8)$$

$$\frac{da}{dN} = 6.40 \times 10^{-10}(\Delta K)^{4.16} \quad (6.9)$$

$$\frac{da}{dN} = 1.90 \times 10^{-9}(\Delta K)^{3.87} \quad (6.10)$$

The equations (6.7), (6.8), (6.9) and (6.10) expressed above are for the FCGR *Da/dN* of NZ, TMAZ, HAZ and BM respectively. The resistance to FCGR is the lowest for the NZ as assured from the highest Paris index. At the lower range of stress intensity factor, the FCGR of HAZ is equivalent to the BM and the trend coincides at a particular range. With increase in the stress intensity range the FCGR of HAZ is marginally increased than BM as found from the plot. The expressions for the FCGR *da/dN* at higher load ratio of 0.6 for the selected zones are presented in Fig. 6.8 (c) as follows:

$$\frac{da}{dN} = 9.20 \times 10^{-9}(\Delta K)^{6.94} \quad (6.11)$$

$$\frac{da}{dN} = 3.10 \times 10^{-10}(\Delta K)^{5.81} \quad (6.12)$$

$$\frac{da}{dN} = 4.70 \times 10^{-9}(\Delta K)^{4.36} \qquad (6.13)$$

$$\frac{da}{dN} = 7.1 \times 10^{-10}(\Delta K)^{3.95} \qquad (6.14)$$

The equations (6.11), (6.12), (6.13) and (6.14) expressed above are for the FCGR *Da/dN* of NZ, TMAZ, HAZ and BM respectively. With the increase in the load ratio there is a decrease in the fatigue life observed for all the selected zones. For all the three cases as mentioned above, the fatigue life of BM is superior with the lowest FCGR. At the lower *ΔK* regions, the FCG for NZ is the fastest due to the finer grain structure and higher strain hardening resulting in lower crack blunting effects for all the loading conditions. For The superior tensile properties of the BM as ascertained from the tensile test, fatigue crack growth resistance increases due to the decrease in the plastic strain per load cycle. Pao et al. 2009 reported that residual stresses had comparatively more significant effect on FCG rate than the microstructure effect, except at low threshold regimes where the impact of the microstructure was more dominant. In the present work, the residual stress was not evaluated but compared with the FCG behaviours of the as-welded and PWHTed specimen. The heat treatment of the weldment results in better homogeneity in the microstructure and reduces the residual stresses at the weld zones. The compressive residual stress had a positive effect on increasing the resistance to fatigue failure (S.J. Hong et al. 2006).

The high scatter in the FCG test results is the consequence of non-homogeneity in the microstructure in the region of crack propagation (D. Taylor 1992). In the upper II region, cracks propagated very quickly in FSWed samples than the BM due to the lower threshold. At NZ, crack propagated with maximum rate followed by the TMAZ. The crack growth rate in HAZ region was identical to the base which defines that the range of threshold stress intensity factor ΔK_{th} for FCG at NZ was the lowest than the TMAZ. The value of ΔK_{th} for HAZ was similar to the BM and the variation in the crack propagation history was more prominent at lower *ΔK* value (Muzvidziwa et al. 2016).

Near threshold characteristics of the fatigue cracks can be understood by the closure mechanism associated with the sample during the fatigue loading which in turn depends on the microstructure. Crack deflection is a phenomenon which is generally observed at the initial stages of crack propagation, i.e., at the near threshold regime. Crack deflection is also influenced by the grain size. Coarser the grain size, higher is the crack deflection. In case of the BM, the grain size is 97 µm whereas for the HAZ, it is 63 µm. Due to the coarse grains, the roughness is more and the actual crack path in the BM is large due to the zig zag path which crack propagates along the grain boundary. The increased crack length along with the presence of precipitated intermetallic or second phase particles at the grain boundary region results in higher number of fatigue cycles for the initiation of threshold region for the BM as well as HAZ compared to the other zones (Fig.6.9(a,b). In the case of NZ, since the grains are fine (~15 µm), the crack is almost smooth and follows a straight path as shown in Fig.6.9(c,d). The elongated grain structure of the TMAZ (35 µm) which is a characteristic feature of the FSWed joint, yielded a moderately rough fracture surface as shown in Fig.6.9(e,f) due to a comparatively more average grain size than the NZ (Gavras et al. 2010) in the initial stages of crack propagation.

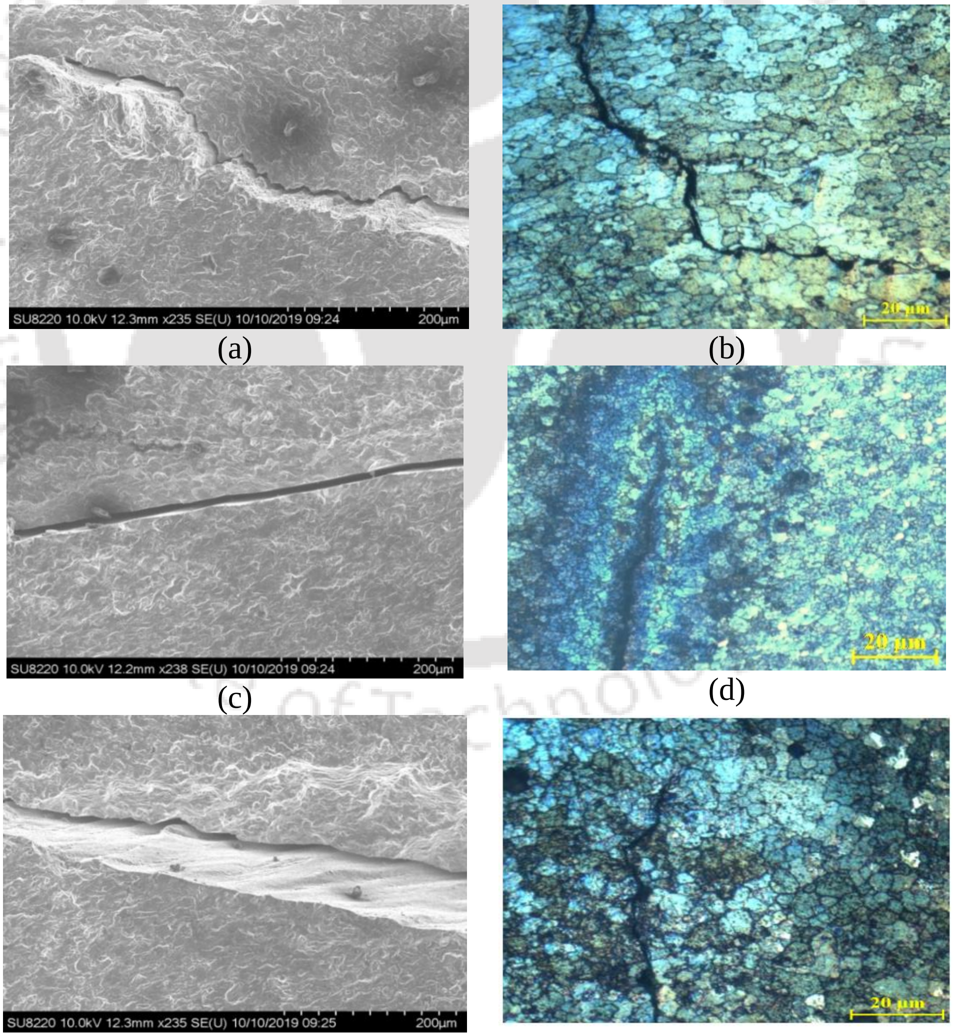

(a) (b)

(c) (d)

(e) (f)

Fig. 6.9. FESEM and OM image of the fatigue cracks at near threshold/region I at (a, b) HAZ, (c, d) NZ and (e, f) TMAZ respectively.

In regions II and III of the FCP, the crack path is different from region I. The crack closure due to microstructure has a less effect on the crack growth rate. With the increase in the crack driving force *ΔK* at this region, the interference between the two fracture surfaces is decreased, as a result of which, the shielding of the crack at the crack tip is reduced. In the upper II and lower III regions of the sample, the crack propagation rate was higher in the FSWed sample than the BM. The FCG mechanism in this region, to a great extent, depends on the size of the plastically deformed zone in front of the crack tip (Gavras et al. 2010). In region II the deformed material zone size is less and covers more grain boundary area to allow for the intergranular cracks as shown in Fig. 6.10(a). In region III, the plastic zone size is large and the cracks propagated through grain boundaries at very high Δ*K*. Fractograph shown in Fig. 6.10(b) reveals a mixed mode of failure as evidenced from brittle as well as ductile features along with features of secondary crack propagation (crack branching) though grain boundaries.

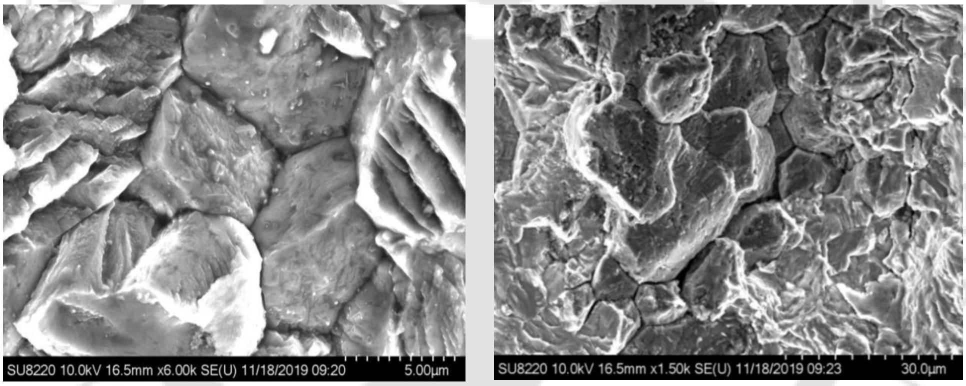

(a) (b)

Fig. 6.10. Fatigue cracks (a) through grain boundary (b) Mixed mode with crack branching

6.5 Fatigue Crack Growth After Heat Treatment

FCG tests were carried out on the HTed samples. Figure 6.11 shows the *da/dN* vs. *ΔK* plots for the weldment at NZ after HT tested with an *R* value of 0.1. Analysis of the plot revealed the Paris constants as $c = 2.9 \times 10^{-10}$ and $m = 2.60$. These values are very close to the values of the BM ($c = 1.38 \times 10^{-10}$ and $m = 2.42$) (discussed earlier in section 6.4) indicating that the heat treatment has improved the fatigue properties of the weldment. The release of the stored internal energy from the weld zones during the heat treatment results in the improvement of the fatigue properties.

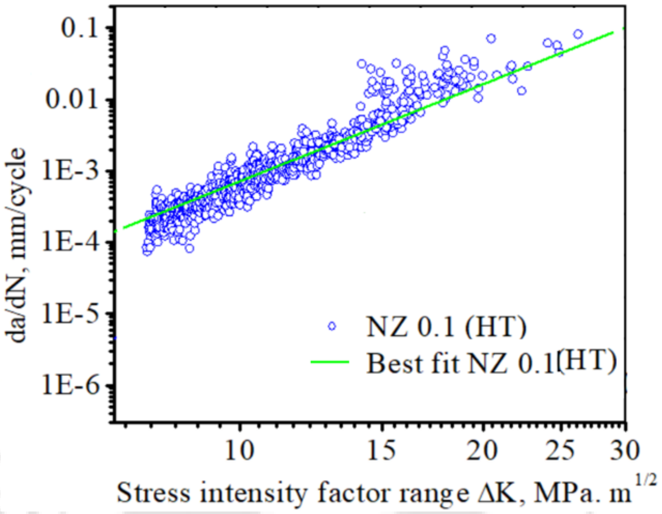

Fig. 6.11. Plots of *da/dN* vs. *ΔK* at NZ for load ratio *R* = 0.1

6.6 Fractographic study

Photograph of a typical fractured surface of the sample failed during the FCGR test is shown in Fig 6.12. The middle portion of three regions: left region is near the pre-crack which is the crack initiation region; the middle region representing- the steady state crack growth region and the right side the unstable crack growth region, demarcated by the lines shown in the figure were observed under FESEM. The samples in which crack propagation through the three zones NZ, TMAZ and HAZ were investigated.

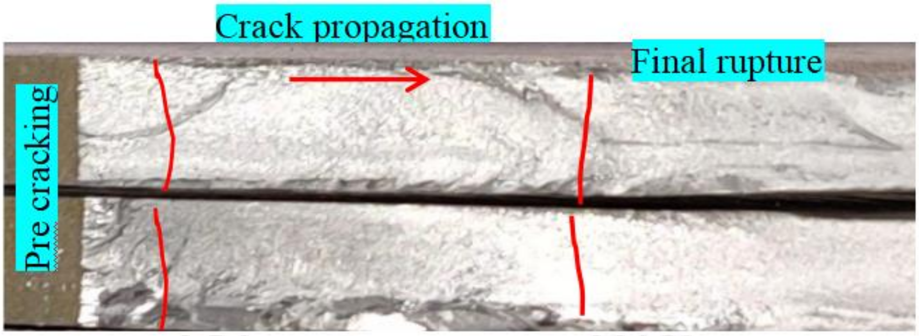

Fig. 6.12. Photograph showing a typical fracture surface after FCGR test

Fractograph of crack initiation regions in the samples of TMAZ, HAZ and NZ are shown in Fig 6.13 (a)-(d). The dominant features are second phase particle cracking, and debonding at the particle-matrix interface. Similar features are observed in all the four weld zones at the crack initiation regions. In general, the features represent a quasi-brittle fracture. More or less similar features are seen for all the four zones. In addition, few porosities evident at the heat affected zone, which might have formed during the FSW process. During the fatigue loading stage, the crack initiation in all the weld zones occurs either by particle cracking or by particle-matrix interface debonding. Lugo et al. 2011 and

Balasundaram et al. 2003 reported that during tensile loading, cracks initiated at sites of particle fracture or interface debonding since these are regions of high stress concentrations. In the present study, since the features are almost same for all the weld zones it is established that the crack intuition is by either particle fracturing or interface debonding especially during the tensile loading stage of the fatigue cycle.

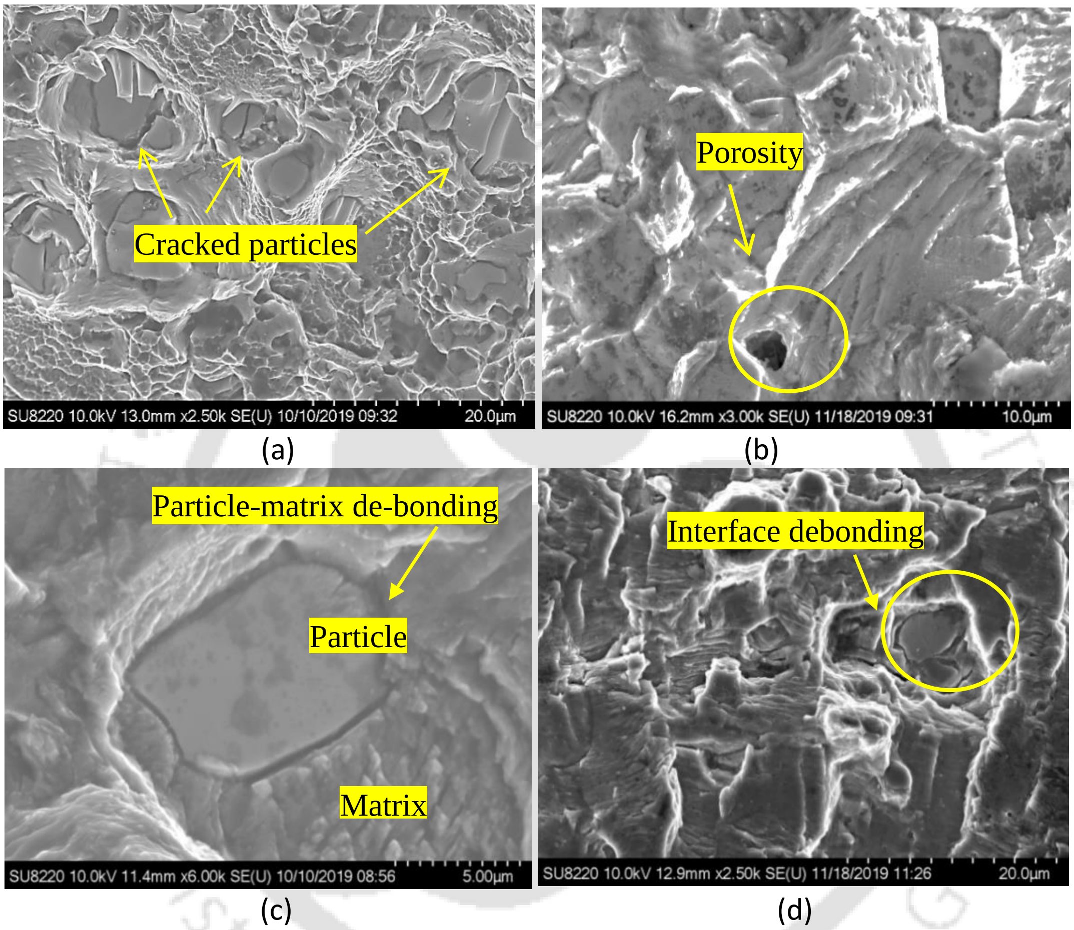

(a) (b)

(c) (d)

Fig. 6.13 Crack initiation sites in (a) TMAZ, (b) HAZ (c) NZ and (d) BM

Figure 6.14 shows the fractorgraphs at the three regions in Fig. 6.12 for the NZ and BM for comparison. Due to the severe plastic deformation associated with the FSW process the fracturing of the intermetallic particles occur. Since micro-cracks are associated with particle fracturing a large number of micro cracks will be uniformly distributed in the matrix prior to the FCGR test. The fractured intermetallic particles mainly in the TMAZ, which are the source of crack initiation and growth are evident in Fig. 6.13(a). During the fatigue loading stage, these intermetallics acts as stress concentration site and generates crack in the adjoining matrix (Payne J et al. 2010) and eventually leads to final failure. It is generally known that the Young's modulus of the intermetallic particles are higher than that of the metallic matrices by one or more orders of magnitude. During the FSW process, plastic deformation is not experienced at the HAZ. However, during the loading stage, due to the large difference in Young's modulus values between the matrix and the intermetallic particles results in shear stresses at the particle-matrix interface. During the cyclic loading, as the shear stress at the interface reaches a level higher than the interface bond strength, debonding of the particle-matrix occurs resulting in nucleation of micro cracks. In addition, micro-porosities present in the HAZ, as shown in Fig. 6.13(b) also act as crack nucleation sites at the HAZ.

In NZ, due to the severe plastic deformation and simultaneous recrystallization, the grains are refined. The fragmented fine particles during the FSW process are dispersed uniformly in the matrix due to the high plasticity developed during the intense stirring action. This along with the recrystallization, results in elimination of the micro-cracks associated with the particle fracture. Under these conditions, the crack initiation sites are debonding at particle matrix interface as evident in Fig. 6.13(c) and similar to the BM in as in Fig.6.13 (d).

Features of fine striations, crack branching due to nucleation of fine micro-cracks ahead of the growing crack and evidence of quasi ductile features at the stable crack propagation stage (stage II region) are evident in Fig. 6.14 (a) & (b). The fracture features during the stable crack propagation stage were similar in all the weld zones. Stage III crack propagation, i.e., the region of unstable crack growth leading to final rupture are characterized by dimple features, as shown in Fig. 6.14 (c) & (d), indicating that the material failed in a ductile manner. This is expected since due to the typical loading nature, the final failure of ductile material during FCGR testing is by ductile shearing and is characterized by dimple features.

After heat treatment (HT), the fatigue property of the weldment was improved appreciably and almost equivalent to the BM. In the steady crack growth regions (Stage II, crack growth), fatigue striation type features are evident as shown in Fig. 6.15 indicating crack closure mechanism which are typical for ductile materials. The restoration of the fatigue properties of the weldment due to PWHT is mainly due to the improvement in the mechanical properties especially the ductility by release of the residual energy stored in the weldment during the welding process (Lakshminarayanan and Balasubramanian 2012). This resulted in almost similar fatigue crack growth behaviour for the weldment after HT compared to the BM.

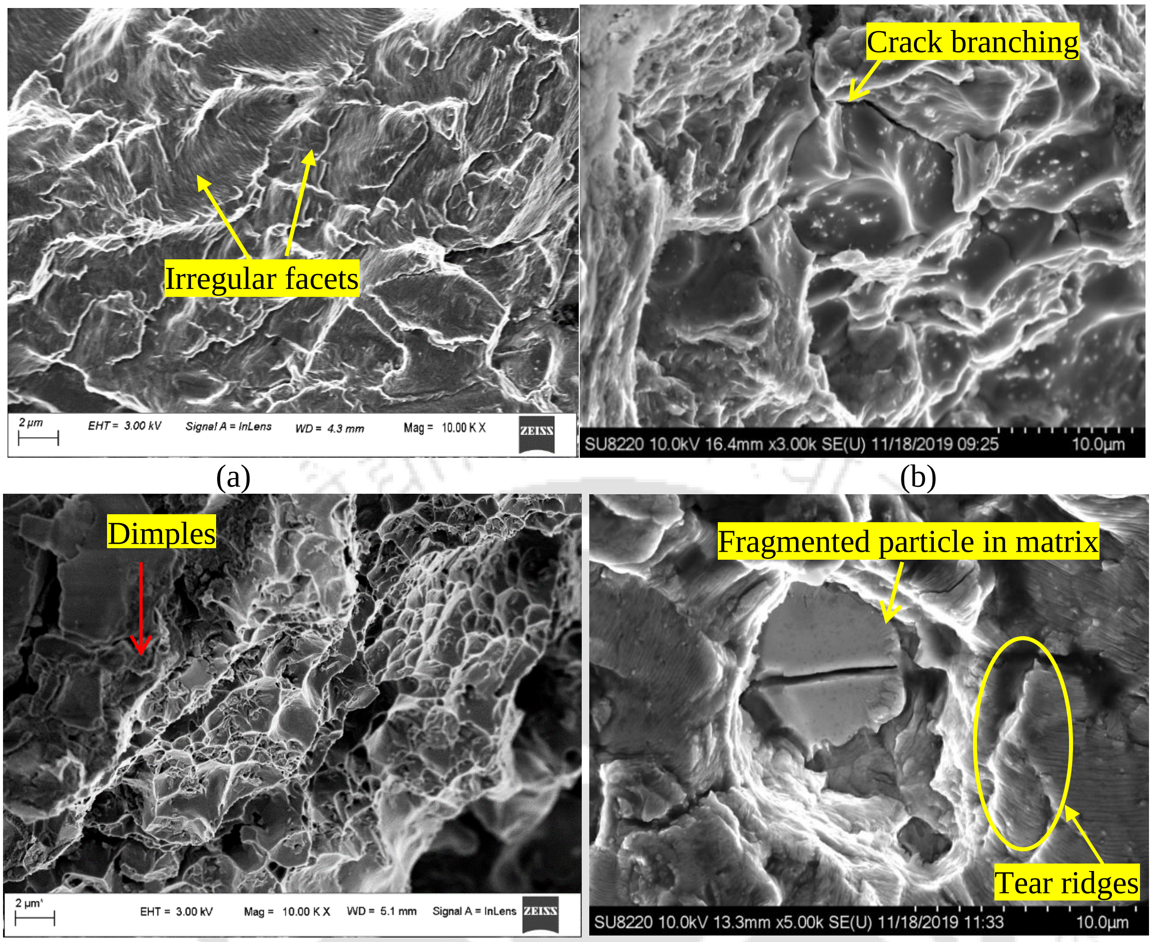

(a) (b)

(c) (d)

Fig.6.14. FESEM images of fatigue propagation at (a) BM, (b) NZ and final failure at (c) BM and (d) NZ respectively.

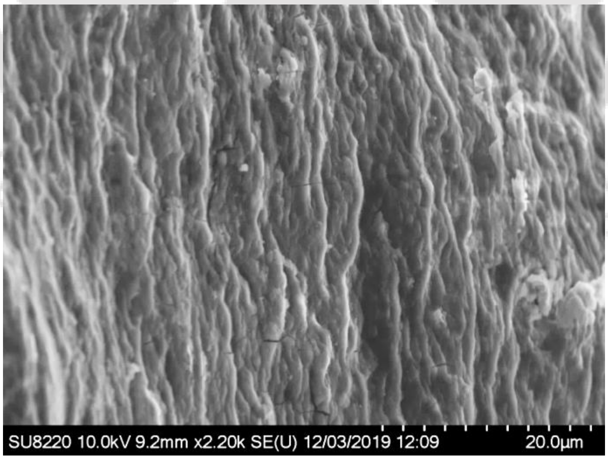

Fig. 6.15. Fatigue fractured surface of HT sample at NZ.

6.7 Summary

FCGR of FSWed AA2014 at different load ratios and weld zones has been estimated and the following conclusions are derived.

- Fatigue crack grows faster in fine grained NZ as compared to the strained grains of TMAZ and coarser grained HAZ/BM.
- The number of cycles to attain a_c was the highest for the BM and lowest for the NZ at all R values. With the increase in R value the no. of cycles required to attain the respective a_c decreases.
- NZ represents the highest FCG rates with the highest Paris index m for all the load ratios.
- FCGR at NZ was equivalent to the BM and tensile properties are also improved after the HT.
- The fragmented intermetallic generated during the FSW process was the main point of stress concentration and fatigue crack initiation at TMAZ. At NZ, the cause of FCGR was mainly for the particle-matrix detachment.
- The crack profile of the BM was more torturous than the FSWed sample.

Chapter 7

Microstructure and Mechanical Properties of FSWed AA6061-T6 Joints

7.1 Introduction

The experimental details of this chapter are explained in Chapter 3. The results of FSW on AA6061-T6 alloy are examined and correlated to the effect of process parameters. The chapter starts with the analysis of mechanical properties of the FSWed joints under various processing conditions. The influence of the parameters like tool shoulder diameter (SD), plunge depth, tool tilt angle, tool pin geometry etc. on the weld qualities are discussed in detail. The discussion is continued with flexural properties and bending angle study, micro-hardness at weld zones, fatigue strength analysis followed by a brief discussion on the microstructure study of the welded parts. Discussion on the impact of process parameters on the grain size are included thereafter. The investigation carried out on the fracture surface under FESEM is discussed. The findings of the study are summarized at the end. The process parameters table presented in Chapter 3 is reproduced here for the easy recapitulation.

7.2. Mechanical Properties of AA6061-T6 Al Alloy Weldments

7.2.1 Tensile Properties

Tensile properties like UTS, YS and elongation percentage of the weld samples are evaluated and compared with the BM properties as shown in Table 7.1. For all the experimental conditions, the BM attributes are more than the welded sample. The stress vs. strain plots of few weldments along with the BM is presented in Fig.7.1. BM shows the highest UTS, YS and % elongation. The UTS and YS of the best specimen (E9) are 302 MPa and 266 MPa and correspond to 96% and 98% of the BM respectively. The welded specimen shows less work hardening. During the tensile straining, the stress increased continuously with strain up to fracture exhibiting a wide work hardening region for the BM whereas, for the welded sample (E9) the stress increases and remained constant afterwards with further deformation till failure.

Table 3.5 Considered process parameters for the present work

Exp. No	Shoulder Diameter of Tool (mm)	Plunge Depth (mm)	Tool Tilt Angle (°)	Tool Pin Profile
E1	18	0.03	1	Straight Cylindrical (STC)
E2	**21**			
E3	24			
E4	21	**0.06**	1	Straight Cylindrical (STC)
E5		0.09		
E6	21	0.06	**2**	Straight Cylindrical (STC)
E7			3	
E8	21	0.06	2	Tapered Cylindrical (TAC)
E9				**Square (SQ)**
E10				Threaded Cylindrical (THC)
* Tool rotational speed 875 rev/min and welding speed 60 mm/min is kept fixed for all experiments				

Table 7.1 Mechanical properties of joints with various process parameters

Exp. No	E 1	E 2	E 3	E 4	E 5	E 6	E 7	E 8	E 9	E 10	**BM**
UTS (MPa)	180	246	220	256	250	271	255	283	302	291	**310**
YS (MPa)	140	201	180	205	203	210	204	219	266	227	**270**
Elong. (%)	7.22	8.28	7.78	9.30	9.07	10.32	10.11	10.87	12.00	11.48	**11.00**

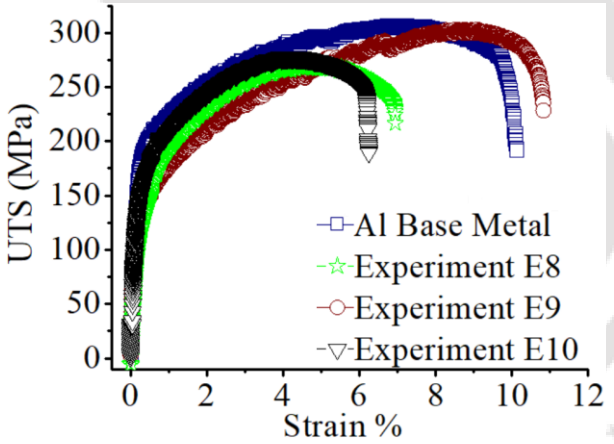

Fig.7.1. Stress vs. strain curve of E8, E9 and E10 obtained from experiment with BM

The tensile properties like the UTS, YS and elongation percentage are co-related with the change of shoulder diameter (SD) for the cases E1, E2, E3 as represented in Fig.7.2. During the trial experiments, suitable joints were not obtained by using tools with shoulder diameters lower than 18 mm. The best quality joints were achieved with shoulder diameter 21mm with UTS, YS, and % elongation values of 246 MPa, 201MPa and 8.28 that are 36%, 43.6% and 14.6% increase in value at 18 mm SD respectively. With further increase in the SD to 24 mm, mechanical attributes show a decreasing trend. As the shoulder diameter increases from 21 mm to 24 mm, the UTS, YS, and % elongation decreased by around 10.72%, 10.44% and 6.0%, respectively.

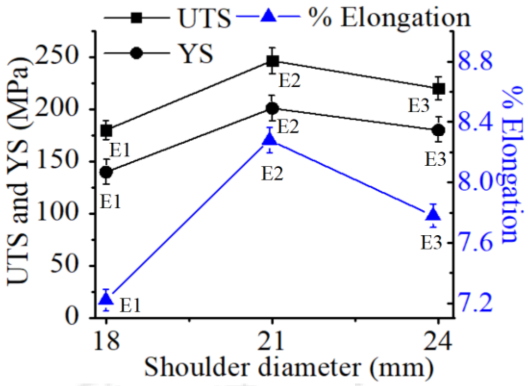

Fig.7.2. Plot of UTS, YS and % Elongation vs. tool shoulder diameter

UTS, YS and % elongation variation of with respect to plunge depth for E2, E4 and E5 are shown in Fig 7.3. UTS and YS increased marginally (< 3.6 %) with increase in plunge depth up to 0.06 mm and decreased with further increase in plunge depth. Elongation % increased by 12% from 0.03 to 0.06 mm plunge depth and with further increase in the plunge depth decrease the tensile properties marginally.

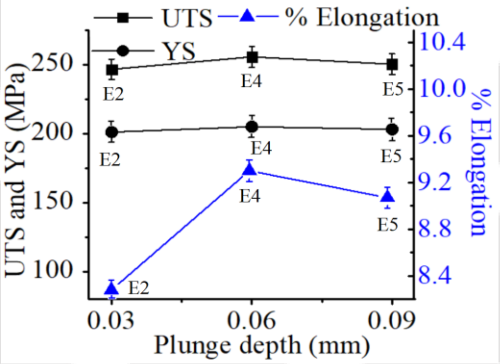

Fig.7.3. Plot of UTS, YS and % Elongation vs. plunge depth

The effect of tool tilt angle on UTS, YS and % elongation for the cases E4, E6 and E7 are shown in Fig.7.4. In this case the tool with 2° tilt angle gave more strength compared to 1° tilt angle. With increase in the tilt angle from 1 ° to 2 ° the properties improved but by 6%. With further increase in the tilt angle the plot represents a marginal (<6%) decline in the mechanical attributes.

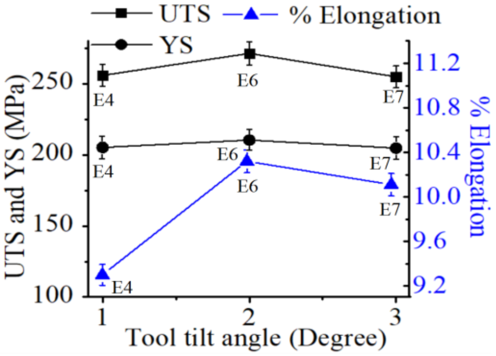

Fig.7. 4. Plot of UTS, YS and % Elongation vs. tool tilt angle

The effect of 4 types of tool pin geometry considered namely straight cylindrical (STC), taper cylindrical (TAC), threaded cylindrical (THC) and square pin for the cases E6, E8, E9 and E10 respectively and their effects on mechanical properties of the weld are represented in Fig.7.5. Out of the considered pin profiles, square (SQ) pin gave the best tensile properties in compared to the others. The UTS achieved in case of SQ pin is 11% more than STC tool and 6.3% more than TAC tool pin. The properties deteriorate at THC tool pin profile.

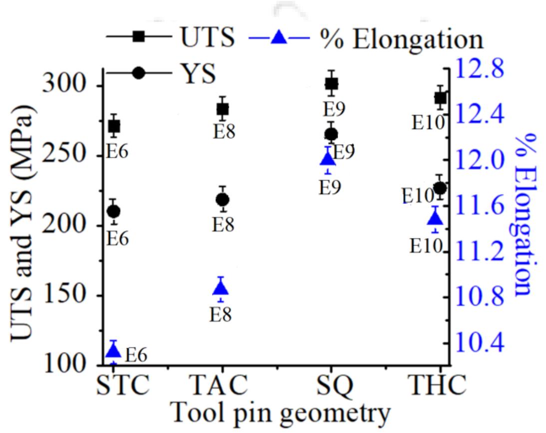

Fig.7. 5. Plot of UTS, YS and % Elongation vs. tool pin geometry

7.2.2 Flexural and Bend Test

The flexural stress (FS) and bending angle of each test are directly proportional to each other. Some of the bend tested specimens without any fracture are shown in Fig.7.6. The FS trend of the measured values is quite similar to the variation in the tensile strength. The variation in FS and bend angle of the weldments w.r.t process parameters are presented in Table 7.2. The variation in FS and bend angle with respect to shoulder diameter for the cases of E1, E2 and E3 is shown in Fig. 7.7. As the shoulder diameter increases from 18 to 21 mm, FS increases from 284 MPa to 300 MPa indicating an increase in value of 5.6%. With further increase in the tool SD to 24 mm, the FS obtained is 288 MPa that is 4% less than the maximum value at 21 mm SD.

Fig. 7.6. Specimens after bend test

Table 7.2 Bending properties of joints with various process parameters

Exp. No	E1	E2	E3	E4	E5	E6	E7	E8	E9	E10	**BM**
FS (MPa)	284	300	288	311	301	329	321	357	496	381	**505**
Bend angle (°)	95	110	105	115	110	120	115	130	140	135	**140**

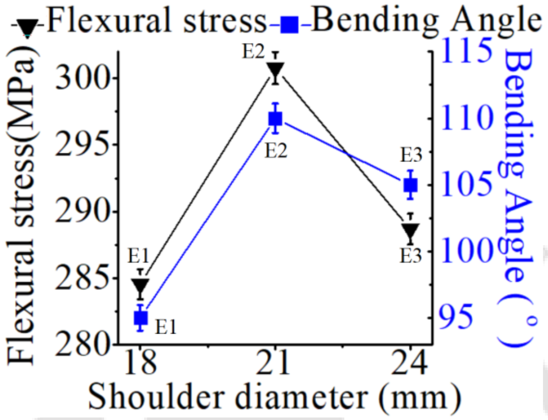

Fig.7. 7. Plot of Flexural Stress and bend angle vs. Shoulder diameter

Variation of FS and bend angle vs. plunge depth (E2, E4 and E5) is shown in Fig.7.8. Flexural stress increases from 300 MPa to 310 MPa (3.3%) and bend angle from 110 to 115° with increase in the plunge depth from 0.03 to 0.06 mm respectively. With further increase in the plunge depth to 0.09 the FS and bend angle decreases as observed in the trends.

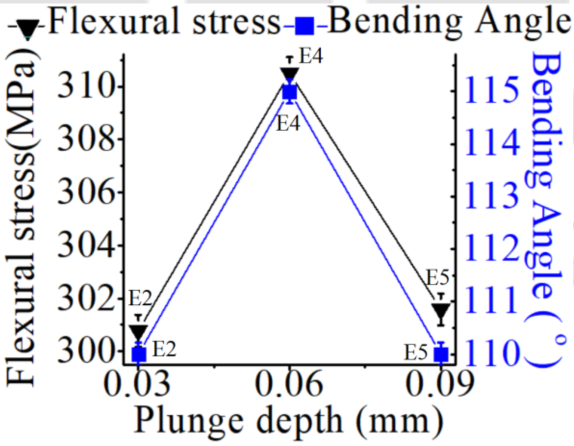

Fig.7. 8. Plot of Flexural Stress and bend angle vs. plunge depth

When considering the tool tilt angle (E4, E6 and E7) it was found that 2° tool tilt angle gave the maximum flexural stress of 329 MPa and bend angle of 120° compared to 1° and 3° as shown in Fig.7.9. The % increase in the FS is 6.1%. With further increase in the tilt angle a nominal decrease in the value is observed from the graph.

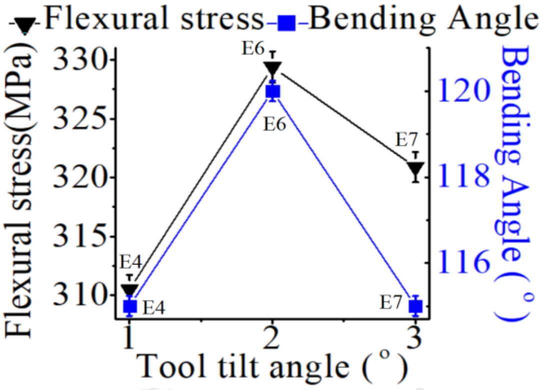

Fig.7. 9. Plot of Flexural Stress and bend angle vs. tool tilt angle

Figure 7.10 illustrates the variation of flexural stress and bend angle obtained for weld with respect to various tool pin geometry for the cases E6, E8, E9 and E10. From the graph it is observed that the maximum FS (495 MPa) and bend angle (140 °) is achieved in case of SQ pin tool. The FS of 329 MPa and bend angle 120° are obtained in case of STC tool pin. For TAC pin the values are 356 MPa and 130° respectively. The THC profile shows a decrease in FS value of 380 MPa and bend angle of 135°.

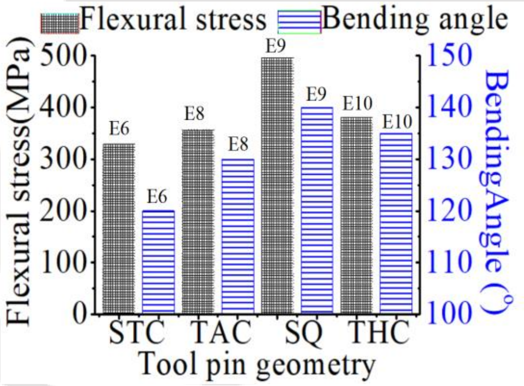

Fig.7. 10. Plot of Flexural Stress and bend angle vs tool pin geometry

7.2.3 Micro-hardness

Welds obtained from E9 exhibited the maximum Vickers microhardness (HV) of 138 at NZ in compared to others as shown in Table 7.3. Hardness was measured at a gap of 1 mm distance at NZ and at 2 mm apart in other zones and at the top, middle and bottom of the cross section of sample E9 as shown in Fig.7.11(a). The microhardness profile of the specimen E9 (welded with tool shoulder diameter of 21mm, plunge depth of 0.06 mm, tool tilt angle of 2°, and welding speed of 63 mm/min) is shown in Fig.7.11(b). Vickers microhardness of the FSWed sample is superior to the BM. NZ represents the maximum hardness in compared to the other zones. This hardness is 33% higher than the hardness of the BM (105). Average HV at TMAZ is 118 and increased by 12.4%, whereas at HAZ the

HV is 108 and a nominal increase of 3% is achieved. The hardness at the upper part of the weldment is higher than both middle and lower sections. From the graph it is also observed that the highest value of hardness is obtained for the NZ followed by TMAZ, HAZ and BM.

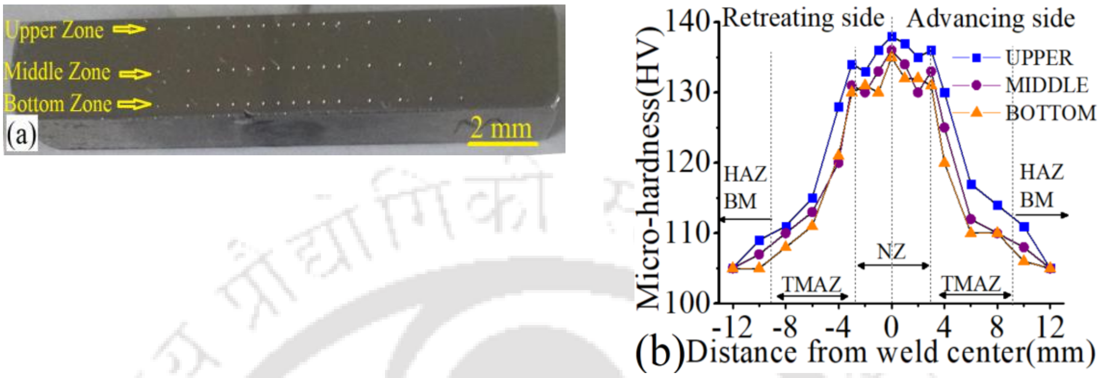

Fig.7.11. (a) Hardness indentation of the tested specimen, (b) Hardness value at the upper, middle and lower zones in thickness direction

The variation of microhardness vs. shoulder diameter is shown in Fig.7.12(a). The plot depicts an increase in the HV value from 103 to 113 when SD increase from 18 mm to 21mm and that is the maximum hardness achieved. With further increase in the SD to 24 mm HV decreases to 110. There is a marginal increase in the HV (7.6% of BM) is observed for 21mm SD. The variation in HV value with respect to the plunge depth is illustrated in Fig.7.12(b). A marginal increase in the hardness value (< 2%) is observed with increase in the plunge depth from 0.03 mm to 0.06 mm. As the plunge depth was further increased to 0.09 mm, the hardness decreases nominally. The maximum HV is attained at 0.06 mm plunge depth and is 115. The plots of HV vs. tool tilt angle is shown in Fig.7.12(c). The plot represents an increase in the trend as the tool tilt angle is increased from 1 to 2^o. At 2^o tilt angle the maximum HV of 120 that is 14.3% of BM is achieved. Hardness decreases marginally at 2^o tilt angle. Figure 7.12(d) shows the trend in HV with respect to various tool pin geometry. The maximum HV value at the weld NZ is achieved with SQ pin tool profile. The hardness value achieved for the weldment using the SQ pin profile is 138 and is 31.4 % higher than that of the BM.

Table:7.3 Vickers microhardness at NZ for each experimental condition

Exp. No	E1	E2	E3	E4	E5	E6	E7	E8	E9	E10	BM
Hardness at NZ (HV)	103	113	111	115	114	120	118	127	138	133	105

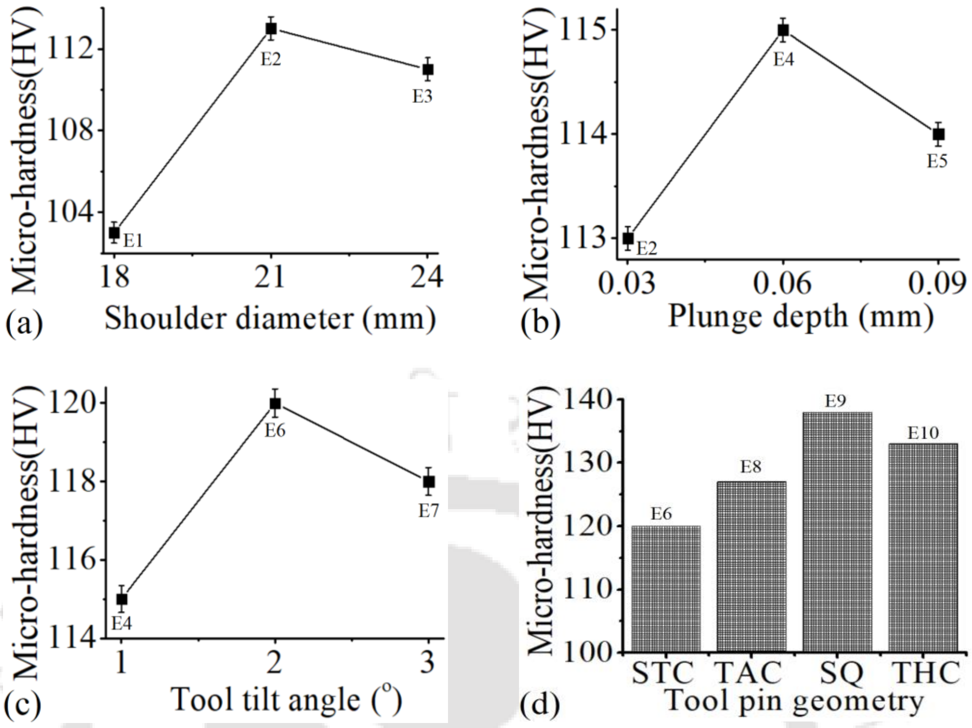

Fig.7.12. Plot of HV vs. (a) shoulder diameter, (b) plunge depth, (c) tool tilt angle, (d) tool pin profile

7.2.4 Fatigue Test

Photographs of few fatigue tested samples of E9 at different stress levels with respect to the maximum stress of the BM are represented in Fig.7 .13a. The considered stress levels for E9 are in the range 40% to 80% of the BM UTS at 10% step interval. In each test the considered stress ratio R is -1. At this stress intervals, the stress amplitude vs no of cylces to failure (S_a *vs N*) plot obtained is shown in Fig.7.13b. The failure zones of the tested sample provide information regarding the fracture at different zones of the weld. At the stress amplitudes of 120 MPa and 150 MPa which corresponds to 40% and 50% of UTS, fracture occurred in TMAZ. However, at stress amplitude from 180 MPa to 240 MPa corresponding to 60%, 70% and 80% of UTS, fracture occurred at NZ after completing a higher number of fatigue cycles as shown the plot. The plot also represents that at the lowest stress amplitude of 120 MPa which is 40% of UTS, the number of cycles to failure in both E9 and base metal sample are nearly same. However, at higher amplitude there are some more differences in the number of cycles due to the higher impact of the strength of the weld zone. The fatigue strength of experiment E9 sample is higher than the BM.

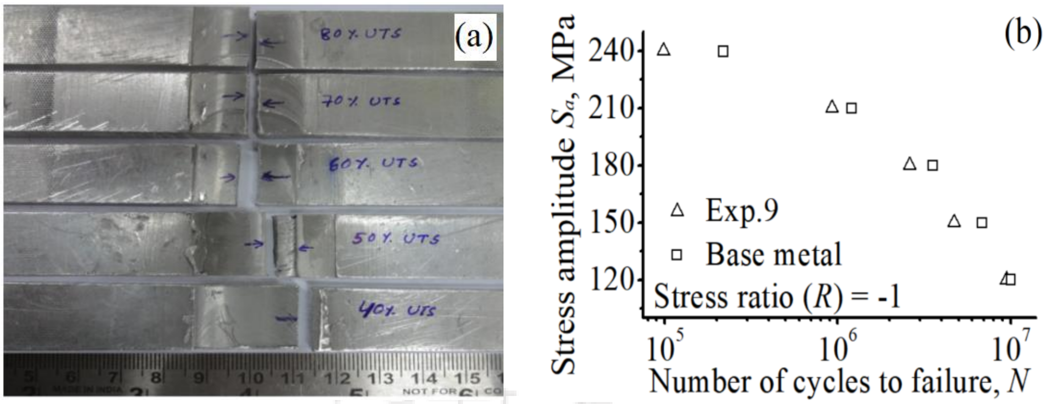

Fig.7.13 (a) Some of the fatigue tested specimen showing failure zones at different stress levels, (b) S-N analysis of the sample extracted from experiment E9 and base metal.

7.3 Metallographic Study

7.3.1 Weld Microstructure

The weld bead in case of FSW consists of three regions, namely NZ or stir zone (SZ), TMAZ and HAZ. The weld bead of the best experimental sample E9 (based on mechanical properties) is shown in Fig.7.14. The macro-view (Fig.7.14(a)) shows different zones at advancing and retreating sides of the weld. It is observed that the weld bead is uniform in advancing as well as retreating side, however the TMAZ area on advancing side is somehow more than the retreating side.

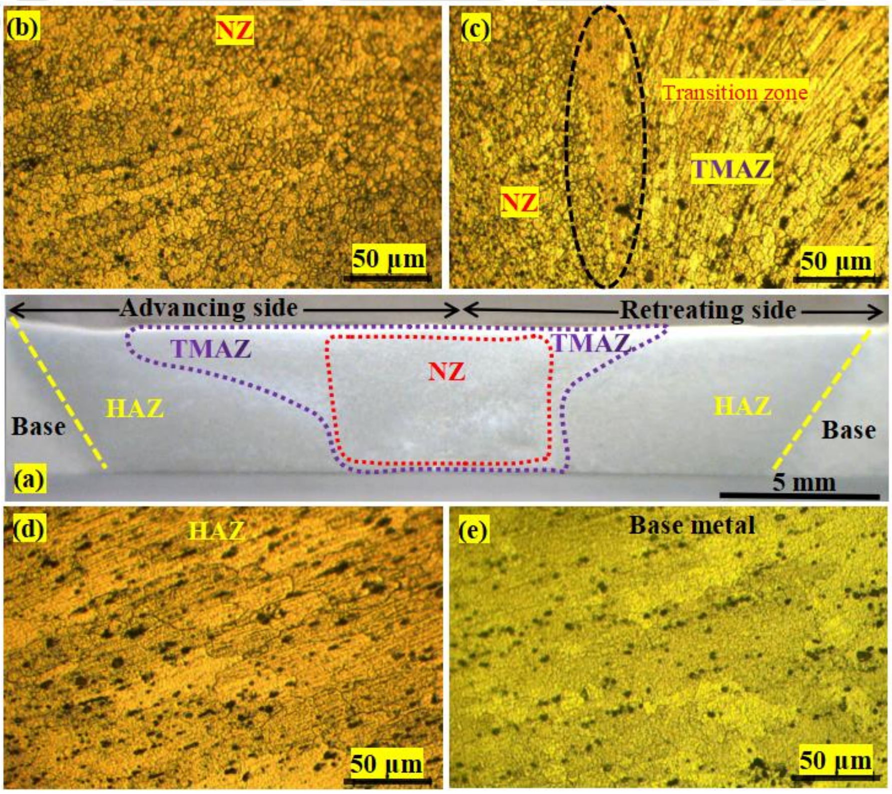

Fig.7.14 Weld bead of the sample and optical microstructure at different zone.

Similar observations were reported by others (Sahu et al., 2018). The microstructure specifies the variation of grain size at different zones. The NZ grains are equiaxed, finer with average diameter of 24 μm (that is 28 % of base metal grain 85 μm) as shown in Fig.7.14b. A distinct boundary present between the NZ and TMAZ is called the transition line as observed in the TMAZ region and represented in Fig.7.14c. Elongated and deformed grains of 45 μm are visible in TMAZ region. Flow lines in the tool pin movement direction are also visible in this region. However, there was a negligible effect of heat on the grain of HAZ as shown in Fig.7.14d. HAZ shows similar grain of 78 μm size and similar to the BM. The base metal grain is around 85 μm as shown in Fig.7.14e.

7.3.2 Grain Size Variation at NZ with respect to Process Parameters

The effect of process parameters used for the FSW process on the grain size at NZ is studied and presented in Table-7.4. With the increase in shoulder diameter the grains became finer as shown in Fig.7.15a-c. The grains become finer from 62 to 46 μm with increase in the shoulder diameter from 18 to 21mm. Further increase in the shoulder diameter up to 24 mm results in coarser grains with an average diameter of 50 μm. The grain size varies according to the plunge depth as shown in Fig.7.15 b, d and e. Finer grains of 40 μm are obtained in case of 0.06 mm plunge depth in compared to 46 and 42 μm average grain size at 0.03mm and 0.09mm plunge depth respectively. Tool tilt angle variation also plays an important role in grain size as shown in the Fig.7.15 d f and g. Fine grain size of average diameter of 36 μm is achieved with tilt angle 2° as compared to 40 and 38 μm average grain size at 1° and 3 ° tool tilt angle. Out of all the considered process parameters, tool pin profiles have a vital role in grain refinement as the grain refinement mostly occurs during stirring action by the tool pin. Out of four considered tool pin profiles, SQ exhibits the finest grain as shown in the Fig.8i (E9, 24μm which is 72% finer than base metal grain size). So, the best weld output of experiment E9 is achieved with the selected process parameters of SQ tool with 21 mm shoulder diameter, 0.06 mm plunge depth and tool tilt angle of 2° with the other combinations of process parameters like tool rotational speed and welding speed which are already kept constant for this research work.

Table 7. 4 Variation of grain size with different experimental conditions

Exp. No	E1	E2	E3	E4	E5	E6	E7	E8	E9	E10	**BM**
Grain Size of NZ (μm)	62	46	50	40	42	36	38	30	24	27	**85**

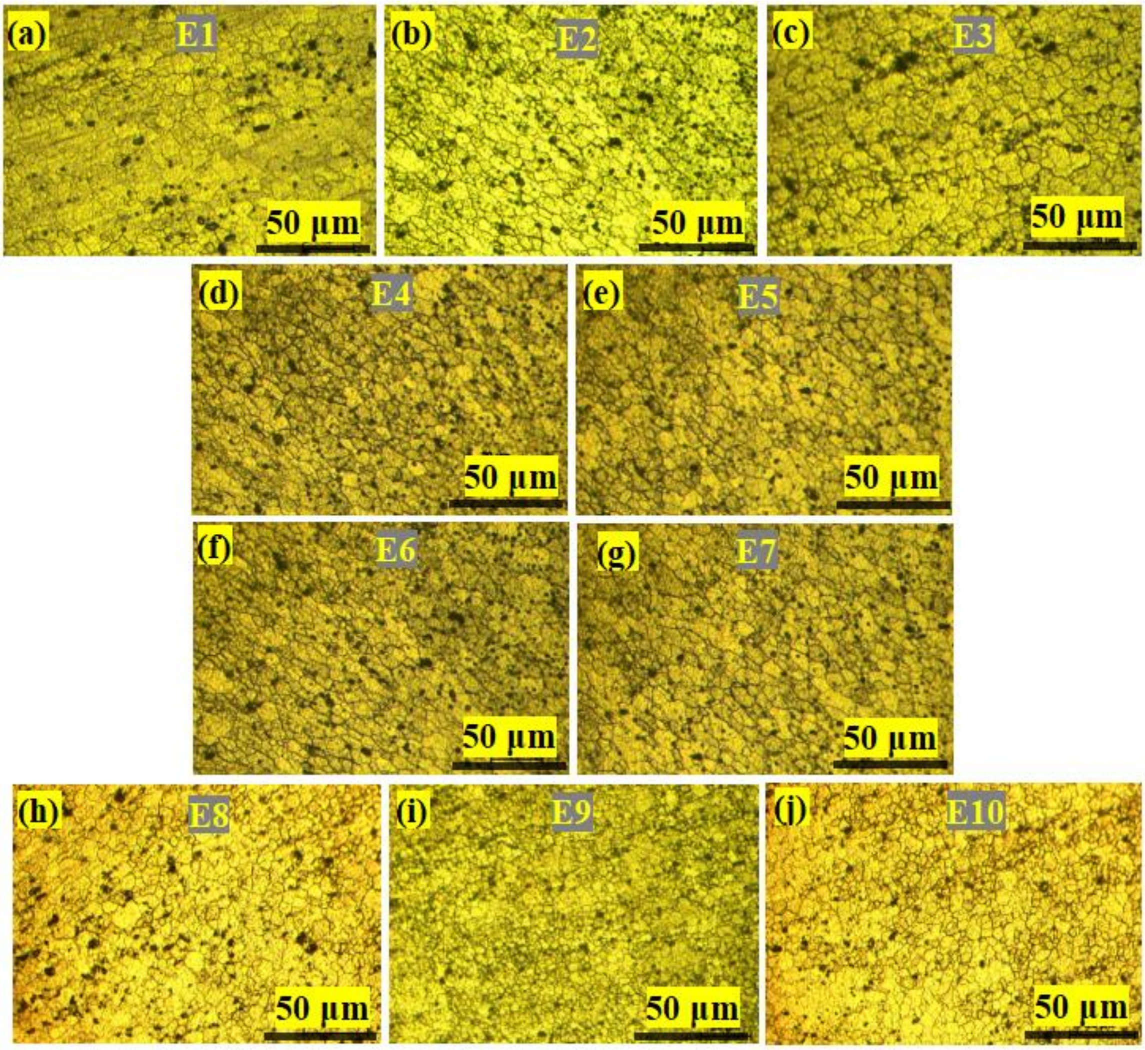

Fig.7.15 Optical photographs of variation of grain size at NZ with variation of shoulder diameter (a) E1, (b) E2, (c) E3, plunge depth (b) E2, (d) E4, (e) E5, tool tilt angle (d) E4, (f) E6, (g) E7 and tool pin profile (f) E6 (h) E8 (i) E9 (j) E10

7.4 Fractography

7.4.1 Tensile Fractograph

Tensile fractography revealed two dissimilar fracture mode in the specimens failed at and before the joint based on the quality of the joint. The specimens, failed before the FSWed zone (E6, E9,) represent ductile fracture behaviour with dimples features as shown in Fig.7.16a and 7.16b. On the contrary, features of brittle fracture are also evident in fracture surface of specimens failed at the weld zone (E1, E2). The variation in weld softening during the FSW process leads to different fracture modes during the tensile testing. Due to the material hardening process during the FSW leading to brittle joints, poor joint strength was achieved in compared to the BM. Hence, brittle fracture pattern is seen in FSWed samples (TMAZ region, E1) as shown in Fig.7.16c. In addition, some secondary cracks are also visible in sample E2 as shown in Fig.7.16d. In spite of the brittle fracture mode in the welded region, the NZ of E10 is characterized by dimples features indicative of ductile failure. Since the microstructure at top and bottom portions in each zone of the weldments is different, the size of the dimples also varies across these regions. In the top area of the weld NZ, larger dimples are found and shown in Fig.7.16e, indicative of good plasticity and toughness at this zone. The fracture surfaces on the bottom area of the NZ represents comparatively smaller and shallow dimples uniformly distributed shown in Fig.7.16f. This change in microstructure is mainly due to less frictional heat input and poor metal plasticization in the lowest region of the tool pin.

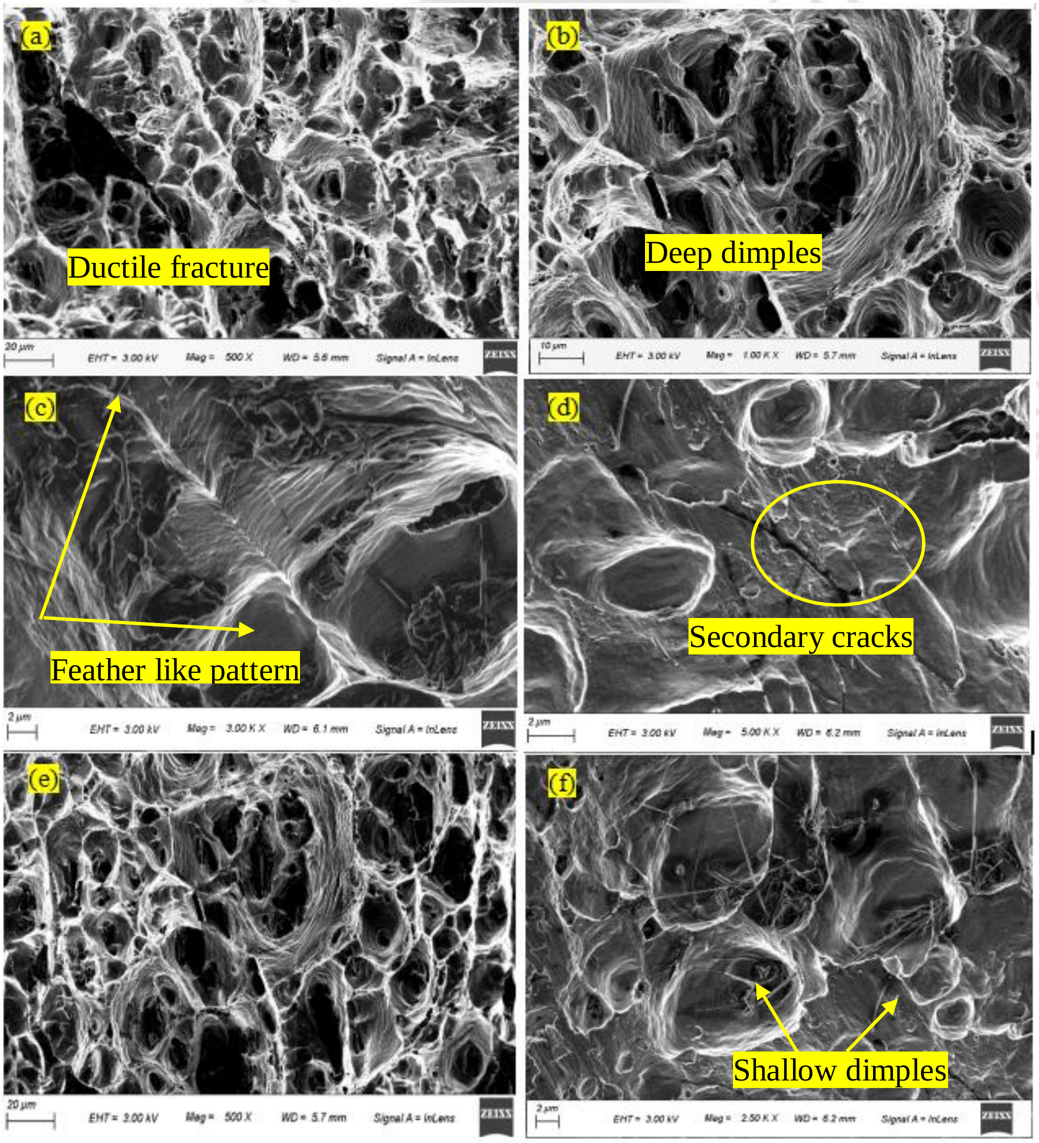

Fig.7.16 FESEM images of tensile fractured surface of (a) specimen E6, (b) specimen E9, (c) specimen E1, (d) specimen E2, (e) specimen E10 upper NZ and (f) specimen E10 bottom of NZ

7.4.2 Fatigue Fractograph

The FESEM images of the fractured surfaces after fatigue test are represented in Fig.7.17. The fractured surface of the micro-crystalline ductile AA6061-T6 FSWed metal can be divided into three main regions namely (1) crack initiation region (2) stage I and stage II of crack propagation region, followed by (3) void nucleation, coalescence and growth. The crack initiates at regions of stress concentrations like surfaces (both internal or external surfaces) and discontinuities like voids, inclusions, second phase particles, grain boundaries, etc. Figure 7.17 a shows a single crack on the surface with Stage I crack propagation. The stage II crack propagation regions (Fig 7.17b & c) show striations which is typical of steady state crack propagation in ductile materials. Grain size plays a vital role in the fatigue life mainly in high cycle regime and dominates the stage I crack propagation.

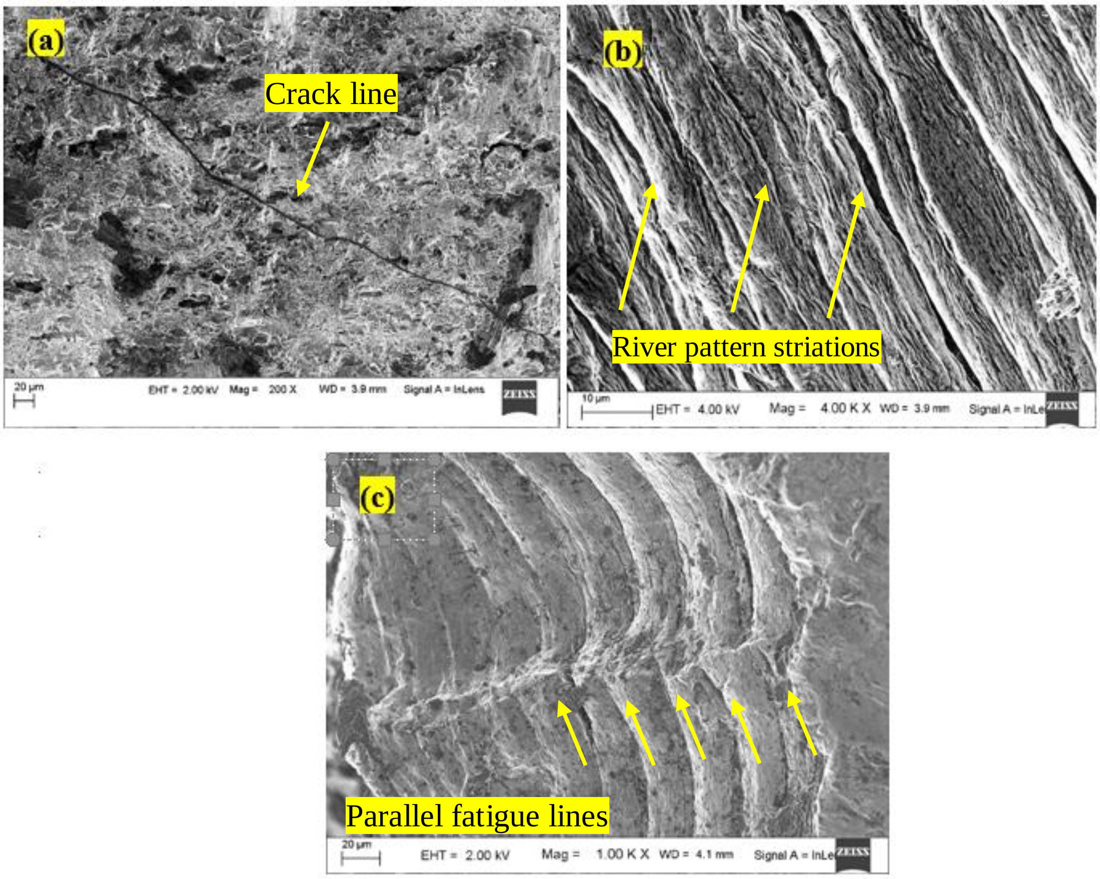

Fig.7.17. FESEM fractography and fatigue crack growth at different regions

The fatigue fracture at different zones was attributed to the stress concentration, the grain refinement and the dynamic loading due to the cyclic loading. The fatigue tested sample indicates that during the testing the crack initiated from the specimen edge and propagated towards the center. As the considered sample (E9) for the fatigue test was weld defect free, the fracture occurred only due to the repeated cyclic loading rather than any other cause. The striation observed in fatigue tested sample is shown in Fig.7.18a. Across the entire fracture surfaces, varying sizes of dimples features are seen. In addition to these features, particle cracking, voids at grain boundaries and brittle features are also evident as shown in Fig.7.18b.

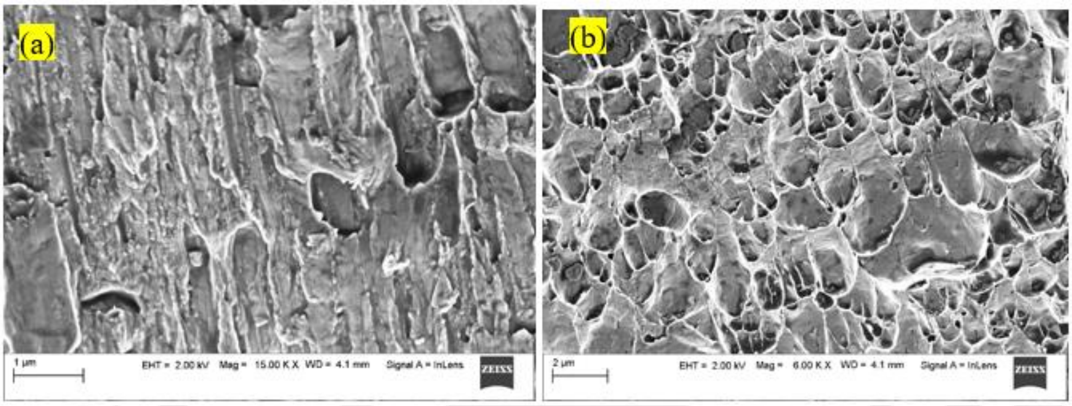

Fig.7.18. SEM detected fatigue fractograph and different crack feature of Exp.9 and BM.

7.5 Discussions

The mechanical properties of the welded joint decreased after the FSW process. The stress strain diagram as shown in Fig.7.1 represents that the UTS, YS and % elongations are decreased after the welding. This may be due the following reasons (i) softening due to the recrystallization of the alloy due to plastic deformation and high heat generation during the FSW process (ii) dissolution of the second phase strengthening precipitates at the high temperature condition during the FSW process (iii) formation of heterogeneous weld zones with nonuniform mechanical properties resulting in failure during mechanical loading (iv) degradation in mechanical properties due to weld defects if present any. The best joint quality is attained with the SQ pin tool with shoulder diameter 22 mm, plunge depth 0.06 mm and tool tilt angle of 2^o. The tool rotational speed and welding speed are kept to be constant as 875 rev/min and 60 mm/min respectively for all sets of experiments that are optimized from the previous experiments.

The effect of SD on the weld quality as illustrated in Fig.7.2. Tool with 21 mm SD indicates the highest tensile strength. With increases in SD the contact surface between the work piece and tool increases and leads to more frictional heat generation. In case of 18 mm shoulder diameter, the tensile strength is less due to insufficient frictional heat generation for less contact area. However, in case of 24 mm shoulder diameter the tensile properties again deteriorate due to more heat generation that leads to coarser grain structure thereby reducing the strength.

The effect of plunge depth on mechanical properties shown in Fig.7.3. indicates that with an increase in plunge depth the tensile properties are enhanced up to a certain level and beyond which it decreases with further increase in the plunge depth. As the plunge depth creates the downward pressure and proper contact to generate frictional heat. So, in this case of 0.06 mm plunge depth, a proper contact is established and the tensile strength increases compared to 0.03 mm. However, at 0.09 mm plunge depth due to extreme pressure more heat is generated that leads to coarsening of the grain and deteriorate the tensile properties. Also, at higher plunge depth more downward pressure creates high volume of flash and excessive local thinning occurred at the shoulder and work piece contact area that leads to decrease in tensile strength of the joint.

The variation of mechanical properties of the FSWed joint with tool tilt angle illustrated in Fig.7.4 reveals that at a constant plunge depth, if tool tilt angle is considered than the pressure at the front side of the tool is more and yield higher plasticization compared to the back side of the tilted tool. Hence, tilting effect can eliminate the tear line and root defect of the FSWed sample. Defect free welds are obtained with considered tool tilt angles. The tool with 2^o tilt angle exhibited higher strength compared to 1^o. At 1^o tilt angle the pressure at the front of the tool is negligible compared to the 2^o. At 2^o tilt angle the exerted pressure at the front of the shoulder is increased favoring proper stirring resulting in defect free joint. However, as the tool tilt angle is increased to 3^o, excess ploughing occurred at front region and loss of some plasticized extra material deteriorate the overall strength of the joint. In this study 4 types of tool pin geometry are considered namely straight cylindrical, taper cylindrical, threaded and squire pin and their effects are represented in Fig.7.5.

Flexural stress or bend strength can represent the highest stress of the tested material during the moment of yield. Flexural stress and the bending angle of the test are directly proportional to each other. The flexural stress trend of the measured values is quite similar to the tensile strength. When considering the flexural stress variation due to the shoulder diameter, it was observed that flexural stress increases up to certain limits and then decreases as shown in the Fig.7.7. The experiment at 21 mm shoulder diameter gives more flexural stress because of proper heat generation which leads to better weld qualities compared to 18 mm and 24 mm shoulder diameter. Also, at 21 mm shoulder a better bending angle is achieved. Similar observation is found in case of the experiment with 0.06 mm plunge depth as shown in Fig.7. 8. The flexural stress and bending angle are more in this case because of the proper contact of shoulder with work piece fraying surface and generation of better heat to plasticize the material. However, at 0.09 mm plunge depth more amount of heat generation leads to maximum flush generation and weakens the strength of the joint with less flexural strength and bending angle. 2^{o} tool tilt angle gives better flexural stress and bending angle compared to 1^{o} and 3^{o} as shown in Fig.7.9. During tool tilt it was observed that the plasticized material entered from front and stirs more at backside of the traversed tool due to more amount of tool face plough into the plate. In this case the weld defects are eliminated due to the highest pressure of shoulder plough and restriction of the soft material beneath the shoulder without flare out. Out of all the considered process parameters, tool pin geometry has more effects on flexural stress and bending angle as shown in Fig.7.10. It is clear from the figure that the highest flexural stress is achieved with SQ tools because of the highest strength achieved due to the pulsating effect of the tool pin that leads to the highest strength compared to other tool pin geometry. The above results show that the weld with 21 mm shoulder diameter of the SQ tool at a 2^{o} tool tilt angle and 0.06 mm plunge depth gives the highest flexural stress of 495.93 MPa that is around 98% of the BM. The highest bending angle at this condition is 140^{o}.

7.6 Summary

From the experimental results the summary of the conclusions is extracted as follows

- FSW process can be fruitfully implemented to join 6 mm thick AA6061-T6 plate without any weld defect by a 21 mm shoulder diameter SQ tool with tilt angle 2^{o}, 0.06 mm plunge depth and at 815 rev/min tool rotational speed and 60 mm/min welding speed.
- Weldments with very good joint quality with UTS and FS values 97% and 98% of the BM respectively was achieved. The best joint obtained for the case where the grain size was 72% of the grain size of BM.

- The maximum hardness value is obtained at NZ and the lowest at HAZ. The hardness measured at the upper zone of the joint in the cross-section direction is the highest than the middle and lower zone.
- At stress amplitude of 120 MPa which is 40% of UTS the number of cycles to failure in E9 is same as the base metal.
- The properties of the weldment are influenced by the grain size at NZ
- The specimens, failed before the FSWed zone represent ductile fracture behaviour with dimples features whereas features of brittle fracture are evident in specimens failed at the weld zone.
- As the considered sample (E9) for the fatigue test was weld defect free, the fracture occurred only due to the repeated cyclic loading rather than any other cause.

Chapter 8

Impression Creep Deformation Behaviour of FSWed AA6061-T6 at Various Weld Zone

8.1 Introduction

Creep properties of materials are very important for various applications especially in areas of aviation and energy sectors like power plants. A quick method of studying the creep behavior is by impression creep testing. FSW is a process of welding the materials below its melting point temperature. However, the weld region of a FSWed component has mainly three zones: (i) NZ, (ii) TMAZ and (iii) HAZ. The nature of the material at these zones is highly heterogeneous due to the heterogeneity in the microstructure (Sahu and Pal 2017). The mechanical properties and deformation behavior at high temperatures of these three zones are different and the final failure of the material is decided by the properties of the weakest zone. Hence the creep properties of various zones are needed to be estimated for the safe application of the components. Through the IC method, the in-service deformation phenomena under high temperature of the material can be estimated through a small volume of the material.

The process parameters for getting the best weldments of FSWed AA6062-T6 are obtained on the basis of mechanical property attributes and was presented in Chapter 7. In this chapter the IC deformation behavior at selected weld zones of the best weldments in FSWed AA6061 alloy is studied at temperatures in the range 326, 359 and 378 °C and at stresses 24, 28, and 32 MPa. IC tests are carried out at three different weld zones of NZ, TMAZ and HAZ along with the BM and compared. The microstructure of the creep tested samples is observed under OM and FESEM. The composition of the intermetallic particles has been analysed using EDX study. This is followed by discussion of the results and finally the chapter ends by summarizing the findings.

8.2 Mechanical Properties

The mechanical properties: tensile tests, flexural and bend tests of the best quality weldment is presented in Table 8.1. The UTS and YS of the best specimen (E9) are 302 MPa and 266 MPa and correspond to 96% and 98% of the BM respectively. The bending angle obtained for the best weldment is same as that obtained for the BM. Vickers microhardness at NZ was the maximum followed by TMAZ and HAZ.

Table 8.1 Mechanical properties of the best FSWed sample (sample No. E15)

UTS (MPa)	YS (MPa)	% Elong.	Flexural stress (MPa)	Bending angle (°)	Hardness at NZ (HV)	Hardness at TMAZ (HV)	Hardness at HAZ (HV)
302	266	12	496	140	138	118	108

8.3 Microstructural Features of the FSWed Joint before IC Test

During FSW, the plasticized material from the two plates is intensely mixed up and form the joint. Due to the peculiar nature of FSW, the weld bead yielded a heterogeneous microstructure consisting of NZ or the stirred zone, TMAZ and HAZ along with BM and is shown in Fig. 8.1a. NZ consists of equiaxed fine grains as compared to the other zones as shown in Fig. 8.1b. This fine size at the NZ is due to the dynamic recrystallization as a result of the frictional heat developed and plastic deformation.

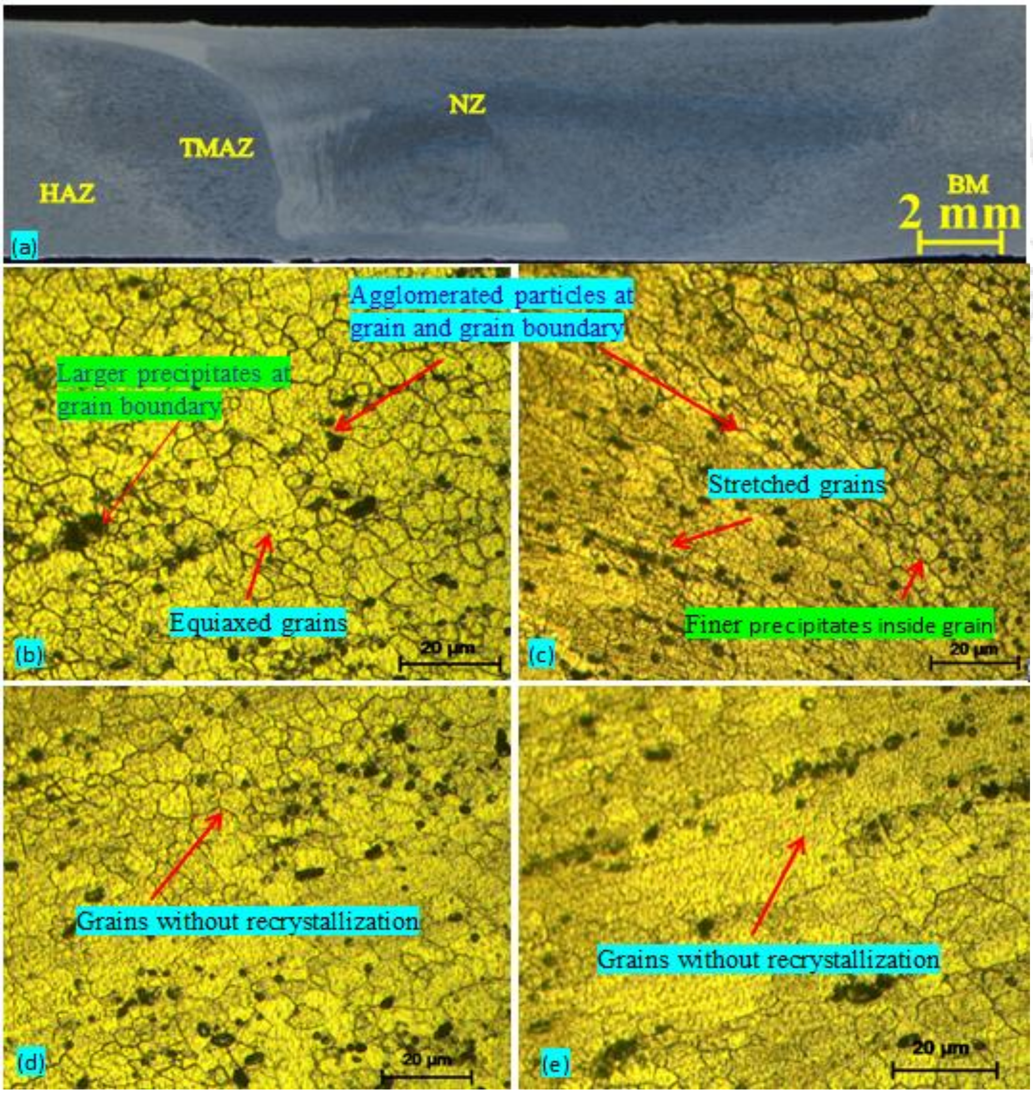

Fig. 8.1. (a) FSWed bead with detailed microstructure at (b) NZ, (b) TMAZ, (c) HAZ, (e) BM

The grains at the TMAZ are heavily deformed in the direction of the tool pin motion. Due to this the grains are coarse grains and elongated along the metal flow direction as is evident from Fig. 8.1c. HAZ is far away from any influence of the FSW process and has nearly unaltered grain structure (Sahu et al., 2017) and is shown in Fig. 8.1d. The grain structure of BM is similar to HAZ and is shown in Fig. 8.1e. The average grain size at each zone was measured by line intercept method. The average grain size at NZ is 24 µm. TMAZ is comprised of elongated grains of 45 µm and HAZ is 78 µm which is close to the BM grains of 85 µm. The grains at NZ are 73% finer than the BM. The optical micrographs also evidenced the agglomerated particles clustered inside the grain and at the grain boundaries due to the thermo-mechanical action during the FSW process (Wang et al., 2014).

8.4 Impression Creep Results Analysis

Results of the IC test at temperature greater than $0.5T_m$ (T_m is absolute melting point temperature) can be explained by various models. Among these the power law creep equation of the Arrhenius rate type (Das et al., 2018) is widely accepted model. In power law creep equation, the strain rate is co-related to the applied stress and temperature by the expression:

$$\dot{\varepsilon} = A\sigma^n \, Exp\,(-Q/RT) \qquad (8.1)$$

where, $\dot{\varepsilon}$ is the SSCR or minimum strain rate, A is a material constant, n is stress exponent, σ is equivalent stress, Q is activation energy for creep, R is universal gas constant and T is the temperature in K. For the impression creep test, the strain rate ($\dot{\varepsilon}$) and stress can be expressed in terms of minimum impression velocity (V_{imp}) and punching stress (σ) by using the conversion factors.

$$\sigma_{imp} = 4L/\pi d^2 = C_1\sigma \qquad (8.2)$$

$$\dot{\varepsilon} = V_{imp}/C_2 d \qquad (8.3)$$

Where, L = applied load, d = indenter diameter (1 mm for this case). C_1 and C_2 are constants. The constants or conversion factor C_1 varies from 2 to 4, and C_2 varies from 0.5 to 1.5. For most materials, $C_1 \approx 3$ and $C_2 \approx 1$

For the present case C_2 is considered as 1, Hence, $\dot{\varepsilon} = V_{imp}$ (8.4)

The impression depth vs. time plots for the IC test represents an increase in the impression depth with increase in time. The plot is similar to the primary and secondary stages of creep deformation of a general creep curve. The third stage of the curve is not possible to obtain. This is since beyond a certain stage of the indenter advancement in to the specimen, the frictional forces at the lateral surfaces of the indenter will be dominating and impede the penetration (Yadav et al., 2019). The creep curve represents the two stages viz; (i) the primary creep stage, where the impression depth increases with a sudden application of load increases at a decreasing rate. This is due to the evolution of the sub grains with increased number of sub grain boundaries which hinder the movement of the dislocations and lower the creep deformation rate. (ii) In the second stage, the rate of creep deformation becomes minimum or nearly constant is called SSCR due to the balanced effects of the processes i.e., strain hardening and recovery. The second part of the graph represents a steady state at constant stress. It represents a minimum change in strain value.

The impression depth vs. time plots for each selected zones viz: BM, NZ, TMAZ and HAZ at a temperature of 326 ˚C and stresses of 24, 28 and 32 MPa are presented in Fig.8.2(a-d) respectively. For the case of BM (Fig. 8.2(a)), the impression depth *h* increases up to 0.20 mm at a stress of 32 MPa and remains constant with further increase in time. The impression depth is 0.19 mm for the stress of 28 MPa and 0.15 mm at 24 MPa and remains almost constant with further increase in impression time.

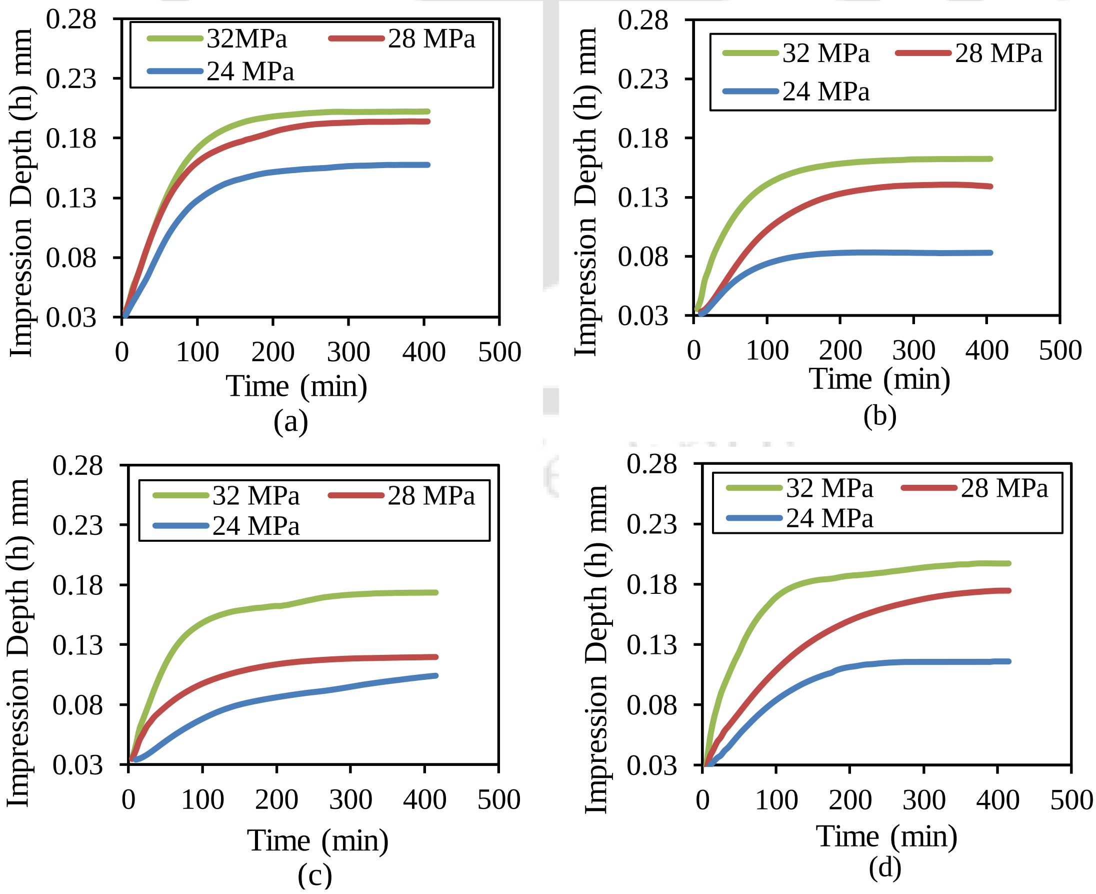

(a) (b) (c) (d)

Fig. 8.2. Impression depth vs. time of (a) BM, (b) NZ, (c) TMAZ and (d) HAZ at 326 ˚C.

The change in strain is negligible here. At HAZ as shown in Fig. 8.2(b), the impression depth *h* increases, with all conditions of applied load, up to a certain time. With further increase in time, no change in the *h* observed. The maximum strain achieved for HAZ is less than that for the BM. For TMAZ (Fig. 8.2(c)) the plot is similar to the HAZ and the maximum *h* obtained was less than HAZ for the same loading conditions. For the NZ as shown in Fig. 8.2(d) the least value of *h* is obtained in compared to all the four zones and the time required to achieve is also the least. The specimen entered into the steady state creep stage earlier than the other cases. The plots of *h* vs. time at 359 and 378 ºC for the selected zones are presented in Fig. 8.3 and Fig. 8.4 respectively.

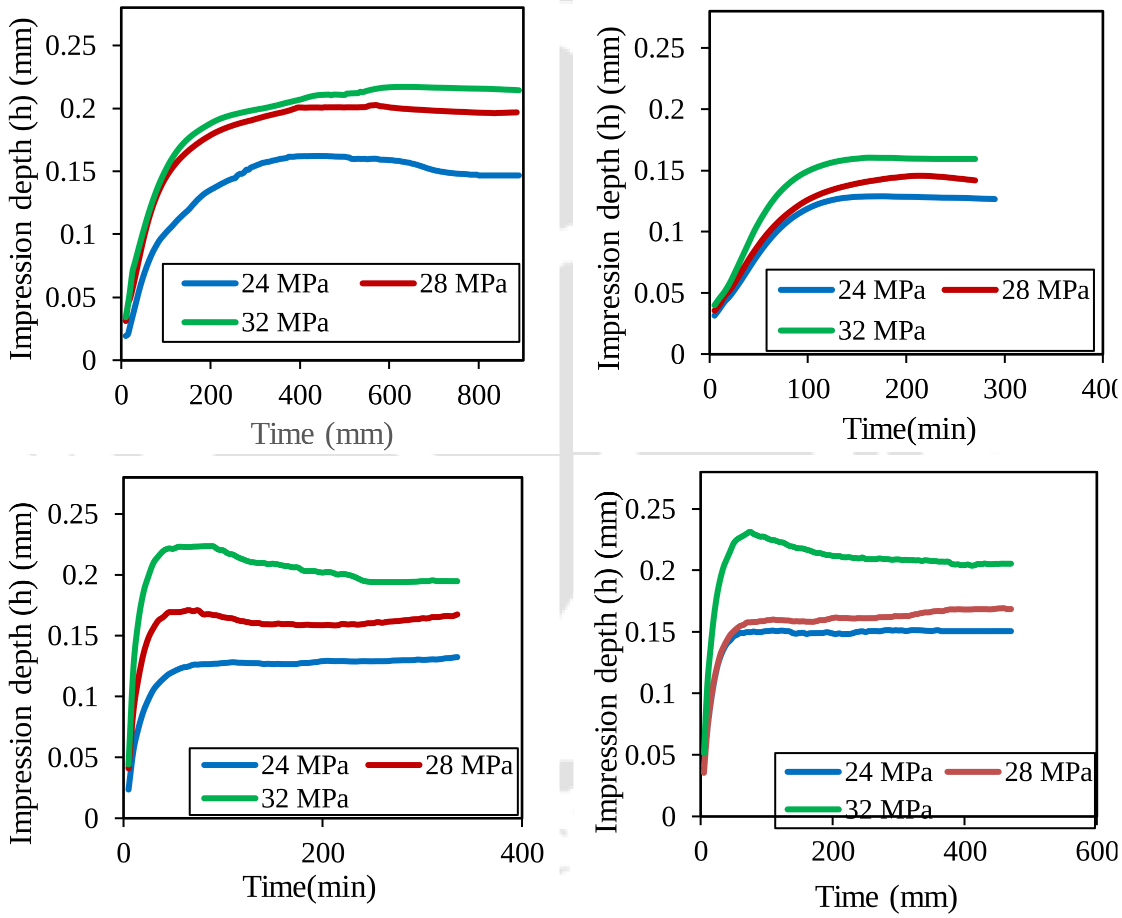

Fig. 8.3. Impression depth vs time for (a) BM, (b) NZ, (c) TMAZ and (d) HAZ at 359 ˚C

Following are the observations found from the plots: (i) the maximum impression depth (h_m) increases with increase in applied stress at a constant temperature (ii) at a constant applied stress, h_m increases as the test temperature increases from 326 to 378 ℃. The h_m decreases with further increase in test temperature (Fig. 8.5) and (iii) as is evident from Fig. 8.6, the rate of change of h_m w.r.t the stress applied $\frac{d}{d\sigma}(h_m)$, increases linearly with increase in temperature. The minimum creep rate (SSCR) value determined for all the experimental conditions at various weld zones are presented in Table 8.2. The SSCR was minimum for NZ and maximum for the BM.

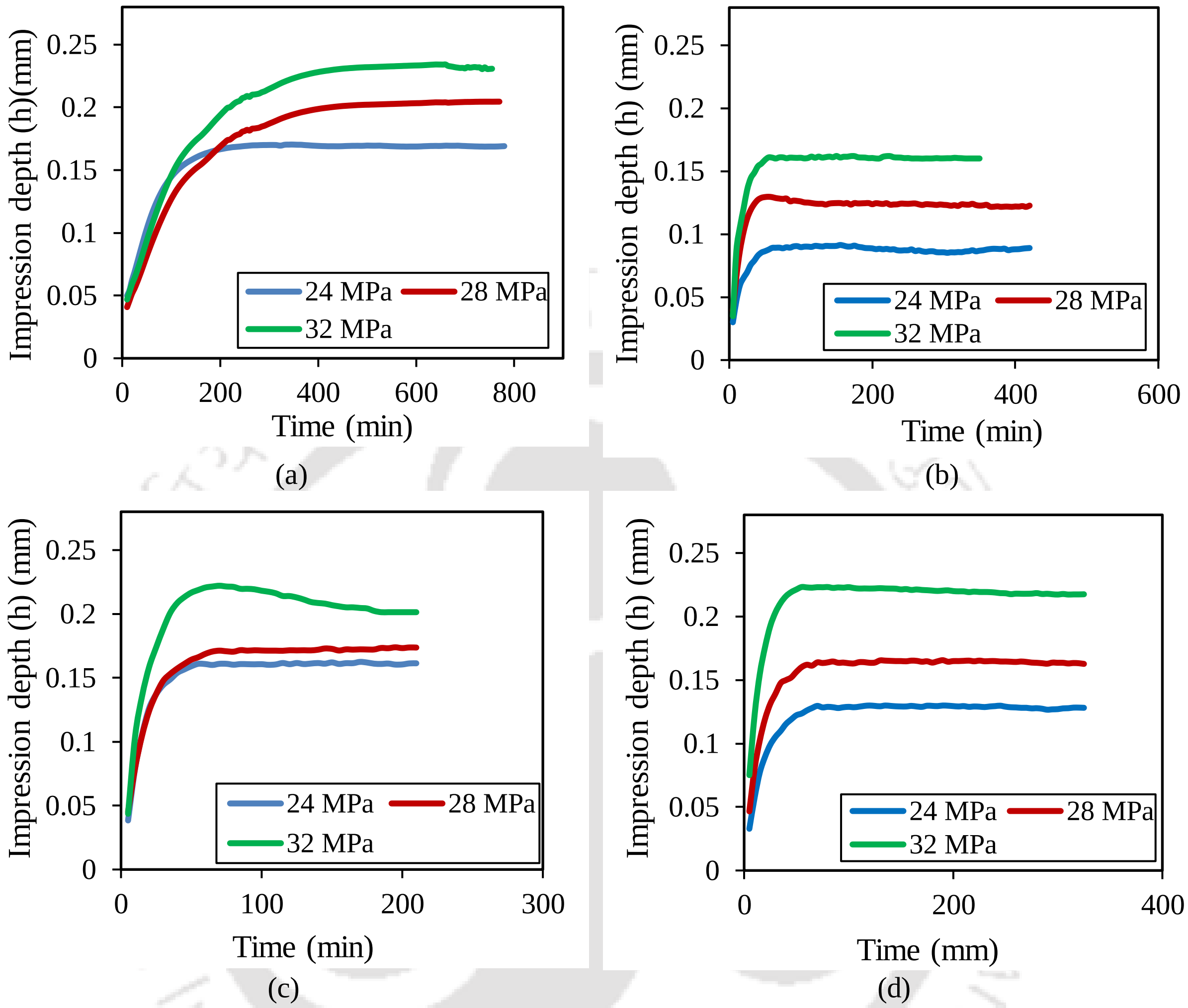

(a) (b) (c) (d)

Fig. 8.4. Impression depth vs. time for (a) BM, (b) NZ, (c) TMAZ and (d) HAZ at 378˚C

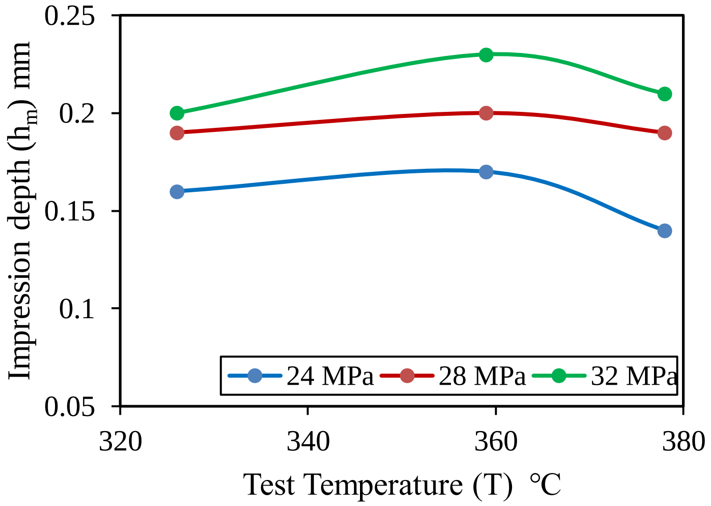

Fig 8.5. Plot of impression depth h_m, vs. test temperature T

Table 8.2 SSCR at various weld zones with different stress and temperature

Zone	Stress (MPa)	SSCR, $\dot{\varepsilon}$ (mm / sec)		
		326 ℃	359 ℃	378 ℃
BM	24	1.3×10^{-5}	3.1×10^{-5}	6.3×10^{-5}
	28	2.3×10^{-5}	5.1×10^{-5}	8.3×10^{-5}
	32	3.5×10^{-5}	7.9×10^{-5}	1.4×10^{-4}
NZ	24	1.0×10^{-3}	2.3×10^{-3}	3.7×10^{-3}
	28	1.7×10^{-3}	4.1×10^{-3}	6.7×10^{-3}
	32	2.3×10^{-3}	4.9×10^{-3}	7.6×10^{-3}
TMAZ	24	8.2×10^{-5}	4.1×10^{-4}	5.3×10^{-4}
	28	1.9×10^{-4}	6.1×10^{-4}	7.2×10^{-4}
	32	3.1×10^{-4}	7.0×10^{-4}	8.1×10^{-4}
HAZ	24	1.4×10^{-5}	2.2×10^{-4}	4.3×10^{-4}
	28	1.2×10^{-4}	4.0×10^{-4}	6.1×10^{-4}
	32	2.8×10^{-4}	5.6×10^{-4}	9.2×10^{-4}

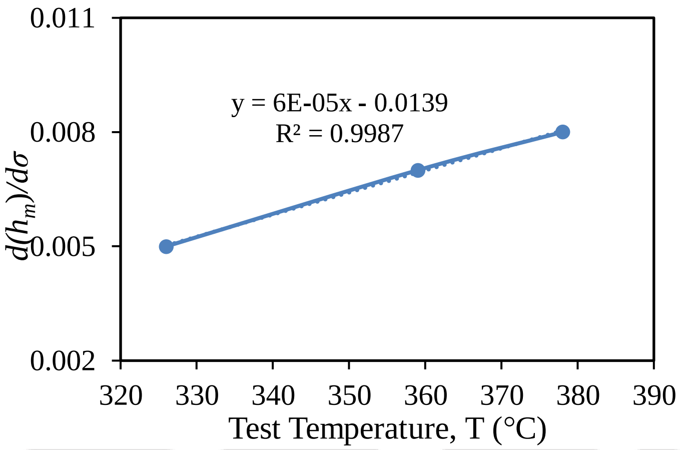

Fig 8.6. Plot of rate of change of penetration depth w.r.t stress applied $\frac{d}{d\sigma}(h_m)$ vs. T

The stress exponent values of the power law creep equation at different considered weld zones can be determined from the IC experiments and the deformation mechanism at these zones can be understood (Mahmudi et al., 2004). Numerous mechanisms have been proposed regarding the deformation of the material during the IC process due to their ordered atomic structures. Under these conditions the stress exponent value *n* of the power law equation can identify the controlling factor for the deformation process. For $n = 1$ the deformation is by diffusional creep; for grain boundary sliding n = 2 and for dislocation glide n = 3. When 4 < n < 5, the deformation is by dislocation climb and when n=6, it is particle strengthening (Jung et al., 1987 and Sharma et al., 2000). For the present investigation, the plots of ($\dot{\varepsilon}$) (as estimated from the experimental curve) as a function of equivalent stresses are presented in Fig. 8.7. The $\dot{\varepsilon}$ vs. σ plot on a log-log scale for the three different temperatures indicate straight line relationships for all the weld zones. Since the slope of these lines represents *n*, the values of *n* at each temperature for the BM, NZ, TMAZ and HAZ were determined from Fig. 8 and is presented in Table 8.3. With the rise in the testing temperature from 326 ° C to 378 ° C at each selected zone, the stress exponent *n* decreases which is an IC phenomenon. This is because as the temperature increases, the material deforms easily due to the dislocation intersection as well as generation of new dislocations with high mobility showing a declining value of *n* at each zone and constant stress conditions. The stress exponent decreases with an increase in temperature. Plot of *n* vs. *T* revealed that the *n* value was decreased with test temperature.

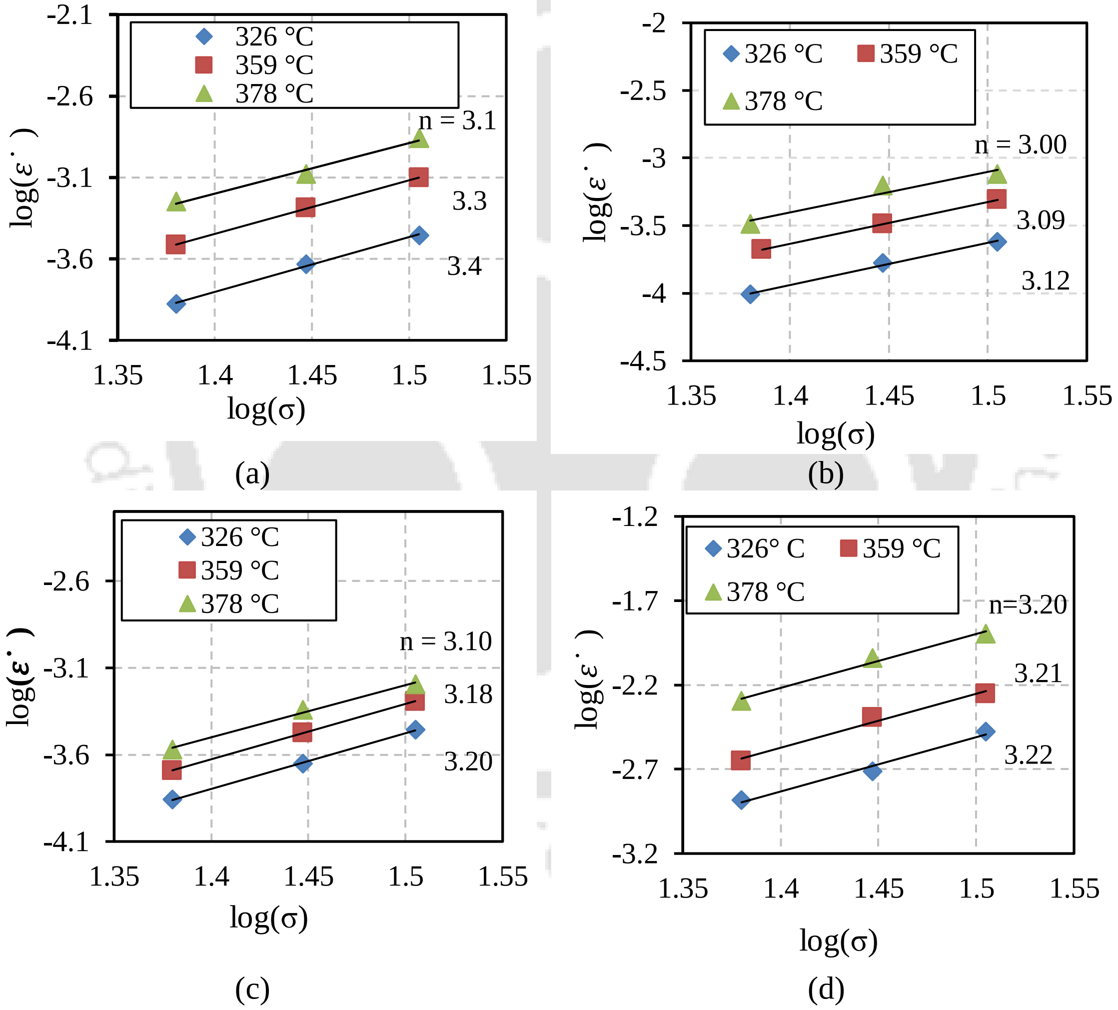

(a) (b)

(c) (d)

Fig. 8.7. Function of ($\dot{\varepsilon}$) with respect to (σ) at different temperatures for (a) BM, (b) NZ, (c) TMAZ and (d) HAZ

The *n* could be correlated to *T* with a polynomial of order 2 with a coefficient of correlation R^2=1. The relationships *n=F(T)* for the 4 weld zones is shown by equation (8.5) to equation (8.8).

for BM, $$n = -(0.0001 \times T^2 - 0.0957 \times T + 12.483) \tag{8.5}$$

for NZ $$n = -(0.0007 \times T^2 - 0.0495 \times T + 5.1986) \tag{8.5}$$

for TMAZ $$n = -(0.0007 \times T^2 - 0.0469 \times T + 4.7148) \tag{8.5}$$

for Haz $$n = -(0.0004 \times T^2 - 0.0026 \times T + 2.8162) \tag{8.5}$$

Table 8.3 The stress exponent values n at various weld zones at considered temperatures

Zone	Temperature (˚C)	n Value
BM	326	3.40
	359	3.30
	378	3.10
NZ	326	3.12
	359	3.09
	378	3.00
TMAZ	326	3.20
	359	3.18
	378	3.10
HAZ	326	3.22
	359	3.21
	378	3.20

The value of $\dot{\varepsilon}$ is dependent on the applied stress and temperatures as seen from the graphs and is different for the base and the welded samples. The welded samples exhibit higher creep rate and deform easily as compared to the BM at the same experimental conditions due coarsening of the strain hardening particle during FSW process. In FSWed samples, the creep rate was different for each selected zones at the same experimental conditions. The variation in the creep properties was due to the complexity and variation in the microstructure of the individual weld zone. Due to the complex phenomenon of the FSW process, weld area develops a heterogeneous structure at different weld zones due arising from the uneven temperature distribution resulting in non-uniform, recrystallization. It was observed that NZ creeps faster than any other zones. This may be due to several reasons: i) The finer grain size - at temperature greater than $0.5T_{m.}$, the smaller grain size increases the creep rates and hence the phenomenon of impression creep becomes easy (Fleck et al., 1970). The grain size has a significant effect on the SSCR in the low stress regimes ($n \leq 5$). In the present IC test conditions, the average grain size of NZ is the smallest followed by TMAZ, HAZ and BM as discussed earlier. There is an increase in the number of sub grain boundaries when the IC process enters in to the secondary stage. These sub grain boundaries accelerate the creep deformation process. ii) generation of new dislocations at the grain boundaries along with the dislocations already generated during the FSW process. These dislocations deteriorate the strengthening effect of the alloy by creating the sites for the precipitation process of the second phase particles. Also, the second phase particles act as the stress concentration factors. The precipitates at sub-boundaries of smaller grains accelerate the dislocation motion (Al-Ganainy and Mostafa 2000) and hence the creep deformation occurs with a higher creep rate. With the increase in the grain size, the grain boundary width increases which therefore constrain the motion of the dislocation and at the same time, greater number of second phase precipitations remain embedded inside the grain rather than at the boundaries. Figures 8.8 (a-c) depict the micrographs of the indented surface at NZ revealing precipitated phases at sub-grain boundaries and inside the grains.

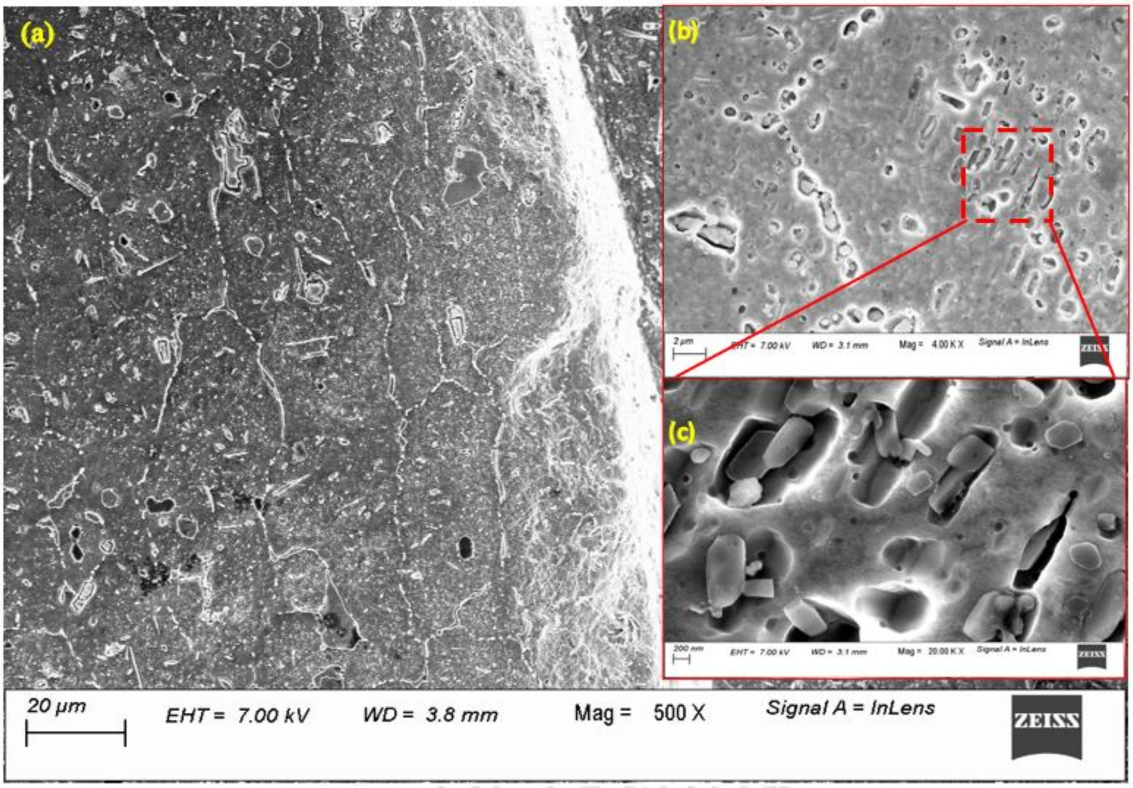

Fig.8.8 (a) Indented surface at NZ, and its (b) precipitates accumulation at sub-grain boundary and inside grain, (c) magnified rod-shaped precipitates embedded in the grain

Figure 8.9 shows the OM and FESEM micrographs at different IC tested areas revealing the distribution of the intermetallic particles. At NZ, large number of irregular shaped intermetallic particles can be seen (Fig. 8.9 (a-b)) and in several sites these particles appear to be agglomerated. These intermetallic facilitate the creep deformation process in NZ. Semi equiaxed precipitates with lesser in number are evident at TMAZ as seen from Fig. 8.9 (c-d). Figure 8.9 (g-h) indicates that at the BM area, a smaller number of finer precipitates are found dispersed inside the grains.

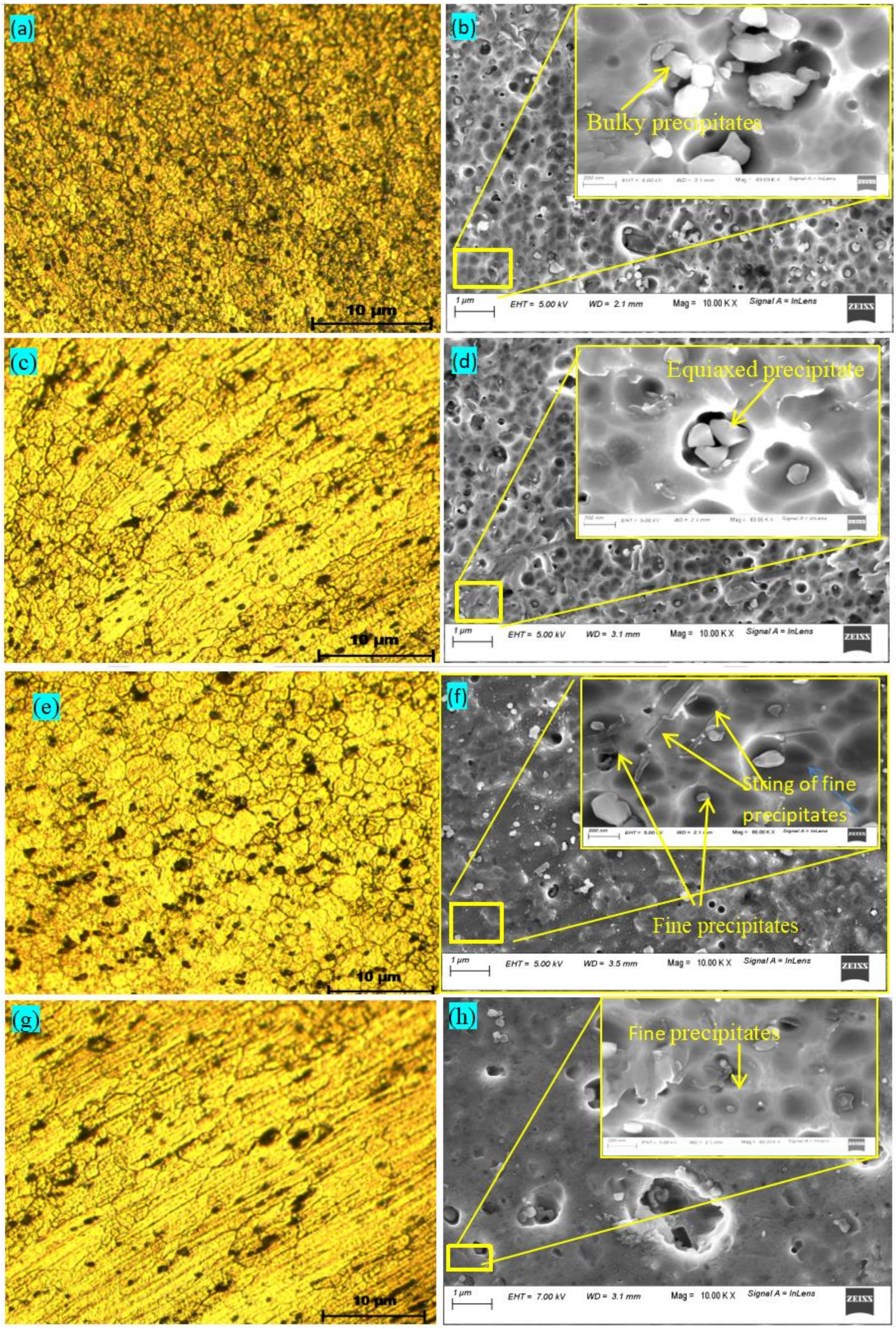

Fig.8.9. Precipitation revealed through OM and correlated with FESEM analysis at (a-b) NZ, (c-d) TMAZ, (e-f) HAZ and (g-h) BM after IC test

The higher number and bigger size of the agglomerated intermetallic at NZ may be due to the prior agglomeration of the strengthening precipitates due to the thermo-mechanical process of FSW. During IC test condition, these precipitates grow in size due the exposure to applied temperature and stress. The more no. of intermetallics reflect that NZ creeps at the highest rate than TMAZ followed by HAZ and BM at the same IC test condition.

The results of the EDX study performed on the agglomerated particles on the FSWed samples before and after the IC test are shown in Fig.8.10(a-b) respectively. The most common strengthening precipitate which is Mg_2Si of the AA6061 was not found in the FSWed component. The high heat generated during FSW process results in the rise in the temperature of the weldment. Dawood et. al 2015 reported that at temperatures above 200 °C, Mg_2Si precipitates dissolve in the matrix. However, after the IC test, second phase particles of Al_3Mg_2, (AlMg), and possibly compound of Al–Mg–Si–Cu–Fe were found in the microstructure which was similar to the reported findings (Sahu et al., 2020)

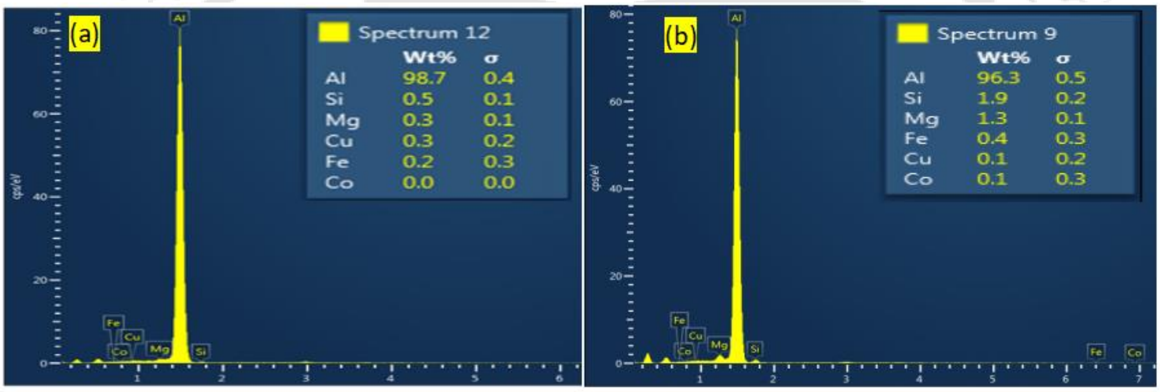

Spectrum 12

	Wt%	σ
Al	98.7	0.4
Si	0.5	0.1
Mg	0.3	0.1
Cu	0.3	0.2
Fe	0.2	0.3
Co	0.0	0.0

Spectrum 9

	Wt%	σ
Al	96.3	0.5
Si	1.9	0.2
Mg	1.3	0.1
Fe	0.4	0.3
Cu	0.1	0.2
Co	0.1	0.3

Fig.8.10. EDX spectra of intermetallic particles before and after IC

The apparent activation energy values also help in understanding the deformation mechanism of the IC process. The average activation energies for the IC process (Q_{IC}) were estimated from the slope of the log ($\dot{\varepsilon}$) vs. $\frac{1000}{T}$, where T is the test temperature in Kelvin. The plots of log ($\dot{\varepsilon}$) vs. $\frac{1000}{T}$ for the BM and FSWed samples at NZ, TMAZ and HAZ were presented in Fig.8.11(a-d) respectively. It is evident that activation energy for the IC test decreases with the increase in the applied stress. The experimental value of Q_{IC} for the BM and FSWed sample showed different values at different weld zones which is due to the in-homogeneous microstructure, as discussed earlier. The calculated average activation energies determined for the graphs for the NZ, TMAZ and HAZ are shown in

Table 8.4. The values of activation energies of the IC process were found to be higher than the activation energy for self-diffusion of pure Al which is ~142 kJ/mol (Sherby and Burke, 1968). This is due to the fact that while calculating the activation energies as per the relationship given below the correction for elastic modulus was not performed.

$$Q_{IC} = Q_d + R\left(\frac{d\,(\ln E)}{d\,(1/T)}\right) \tag{8.9}$$

Where, Q_{IC} is the activation energy for the IC process Q_d is the self-diffusion activation energy and E is the elastic modulus.

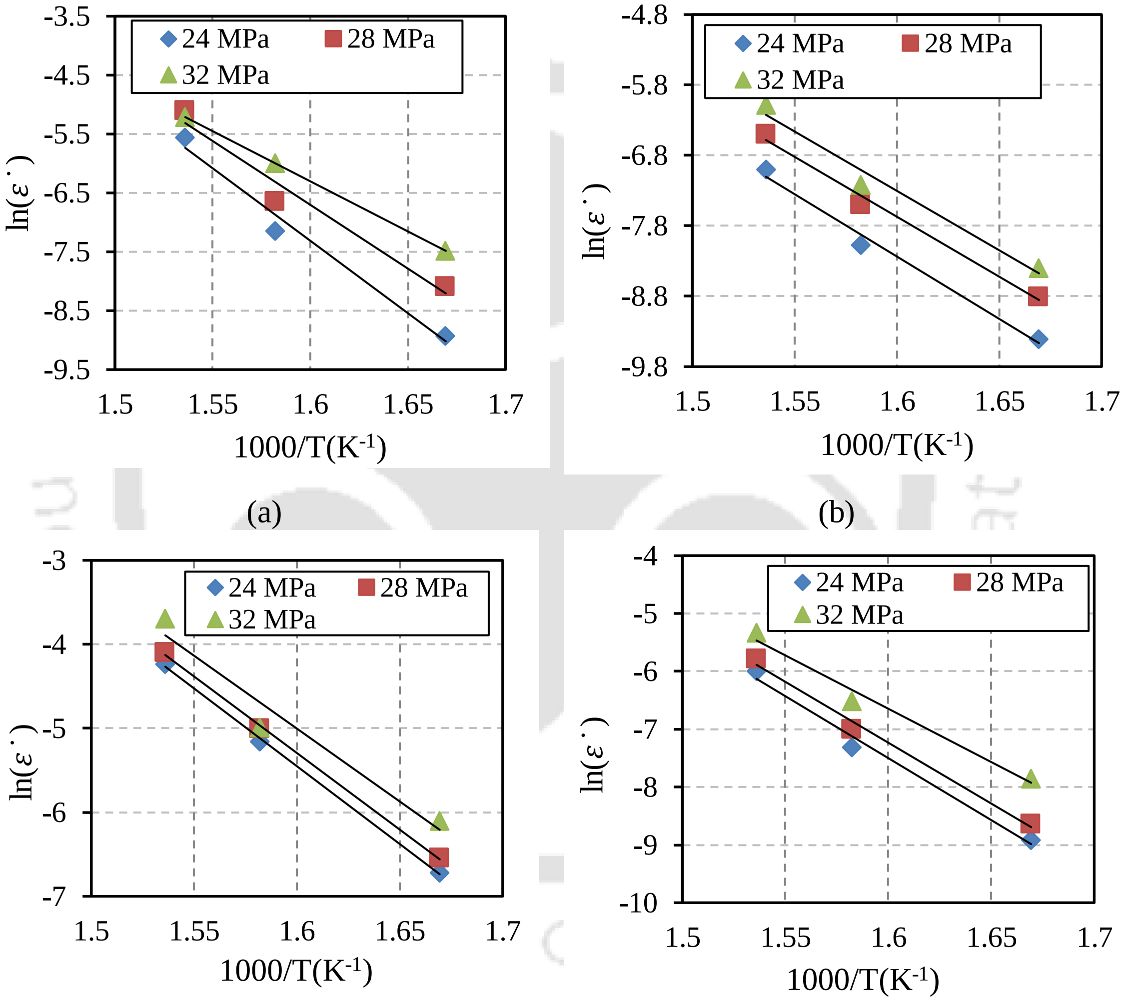

(a) (b)

(c) (d)

Fig. 8.11. Plots of ln $(\dot{\varepsilon})$ vs 1000/T for (a) BM, (b) NZ, (c) TMAZ and (d) HAZ

As $\left(\frac{d\,(\ln E)}{d\,(1/T)}\right)$ has a positive value, Q_{IC} should be greater than Q_d i.e $Q_{IC} > Q_d$. At low temperature the term $\left(\frac{d\,(\ln E)}{d\,(1/T)}\right)$ has negligible value, but as the experiments were carried out at temperatures higher than $0.5T_{m,}$ the term increases with increase in temperature. Hence the values of Q_{IC} are more than the value of Q_d. From the above investigation, it was realized that NZ of FSWed sample showed the lowest value of activation energy and stress exponent whereas BM has the highest. As the IC process in the present case was in a low stress regime (n<5), the creep strength is directly proportional to the grain size i.e., creep strength is more when grain size is more (Sharma et al., 2000). From the metallographic study, the average grain size of the NZ is found to be 9 µm and the TMAZ, HAZ and BM are 16 µm, 31 µm and 35 µm, respectively, after IC test. Though there was a variation in the grain size within the welded area, the transition in the *n* value is not very sharp. From the observed values of the stress exponent and activation energy, the deformation is observed to be homogeneous and predicted to be through dislocation glide in all the selected zones.

Table 8.4 Average activation energy values at different IC tested samples.

Zones	**Q_{IC} value$_{(avg)}$ (KJ/mol)**
BM	175
NZ	143
TMAZ	150
HAZ	169

8.5 Microstructure after Impression Creep

In IC process, the flat end cylindrical indenter penetrated into the test material due to the applied load at elevated temperatures. The material beneath the indenter gets deformed in different distinct zones named zone-i, zone-ii and zone-iii which are demarcated by the curved lines in Fig.8.12a. Zone (i) is the volume of the hemispherical shaped dead metal zone just below the indenter which remained unaffected during the IC deformation process. A magnified view of the microstructure of zone-I is shown in Fig.8.12b. In this region the nature of the stress is hydrostatic in nature as reported by Butt et al (Butt et al., 1996). The micrographs at this region shows undeformed grain structure with precipitations of second phase particles at the grain boundaries. Zone-ii is the elastic plastic hemispherical region surrounding zone-i. As evident from Fig.12c, plastic flow occurs resulting in deformation of the grains during the creep (Vijayanand et al., 2014). The deformation near the bottom edge of the indenter was severe and alternate dark and faint curved lines are seen which was due to the unaffected volume of metal at zone-i. Zone-i releases the stress applied on the indenter in radial direction to its nearby zone. The metal in this zone restricts the flow during the movement of the indenter and remained unaffected. So, the indenter movement was supported by zone-ii where heavy plastic deformation occurs for which the flow lines are visible. Zone-iii is the far field region where the effect of indenter was not felt as can be seem from Fig.8.12d due to the absence of plastic deformation. From the metallographic investigation carried out at the BM, as well as at NZ, TMAZ and HAZ of FSWed material it was found that there was a refinement in grain size after the IC test due to recrystallization and aging process (Chu et al., 1979). The precipitation of intermetallic compounds occurred inside the grain and at the grain boundaries during the creep tests both in BM and in welded samples (Regev et al., 2018). The grains at just below the indenter remained unaffected during the IC test. Metallographic study was carried out at each selected zone.

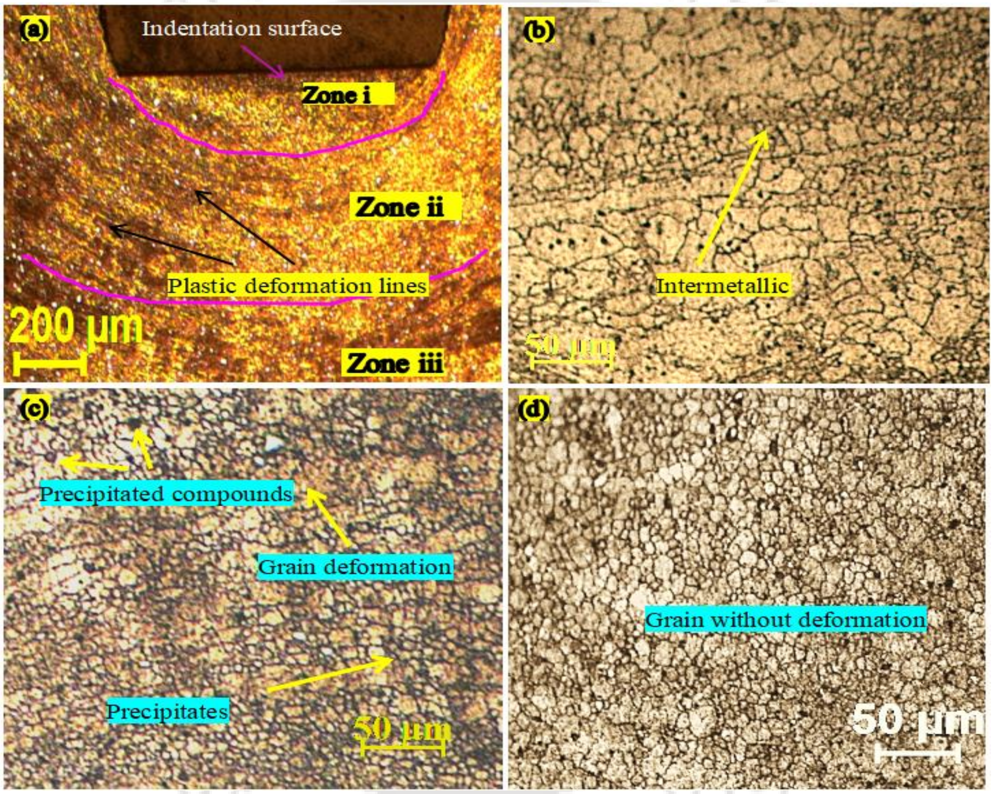

Fig. 8.12(a) Microstructural features of IC tested surface cut transverse to the impression mark cross-sectional view of (b) zone i (c) zone ii (d) zone iii

The impression mark after the IC test at BM, NZ, TMAZ and HAZ is presented in Fig.8.13(a-d). As the grain experiences hydrostatic stress, it retained its structure unaffected throughout the IC test. The original grain size of BM before and after the IC are found to be the same Fig.8.14a. The border line shown in figures depicts the indenter outer edge inside which the grains experiences creep during IC test. The structural features inside and out the border was found to be similar at each welded zone. The dynamically recrystallized NZ also reflects the same grain morphology after the creep test. Precipitated particles were also found all dispersed inside the grain but the size was visible to be more as discussed earlier and shown in Fig.8.14b. The usual elongated grain in TMAZ was also found same as shown in Fig.8.14c.

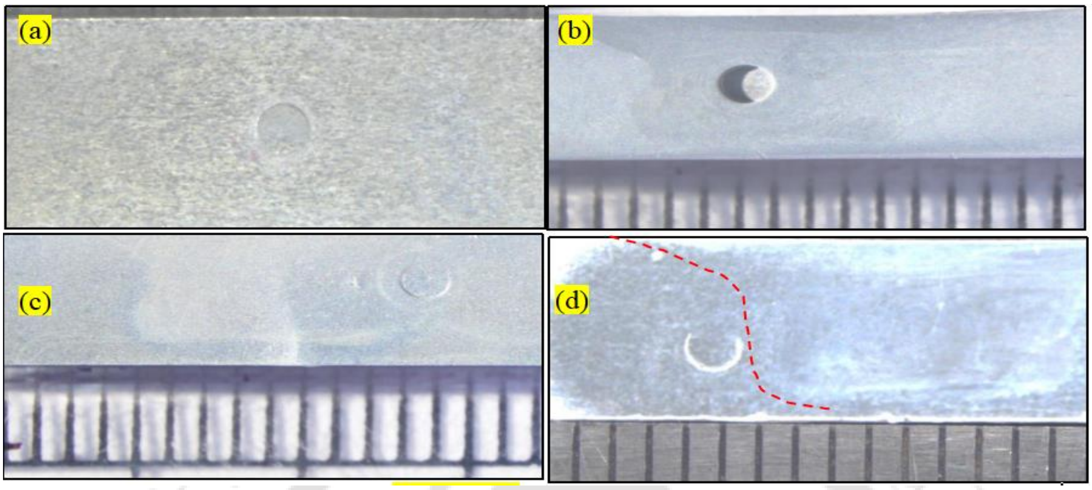

Fig.8.13. IC tested samples with impression mark at (a) BM, (b) NZ, (c), TMAZ, (d) HAZ

The microstructural features of HAZ shown in Fig 8.14d depicts similar features before and after IC test. From the metallographic analysis it was realized that the grain structure just below the indenter remained unaffected throughout the IC test due to the hydrostatic stress. Though the size remained unaffected, the structure and morphology of the grains changed owing to the applied stress and temperature of the test. Second phase particles were formed inside the grain boundary due to the IC test conditions.

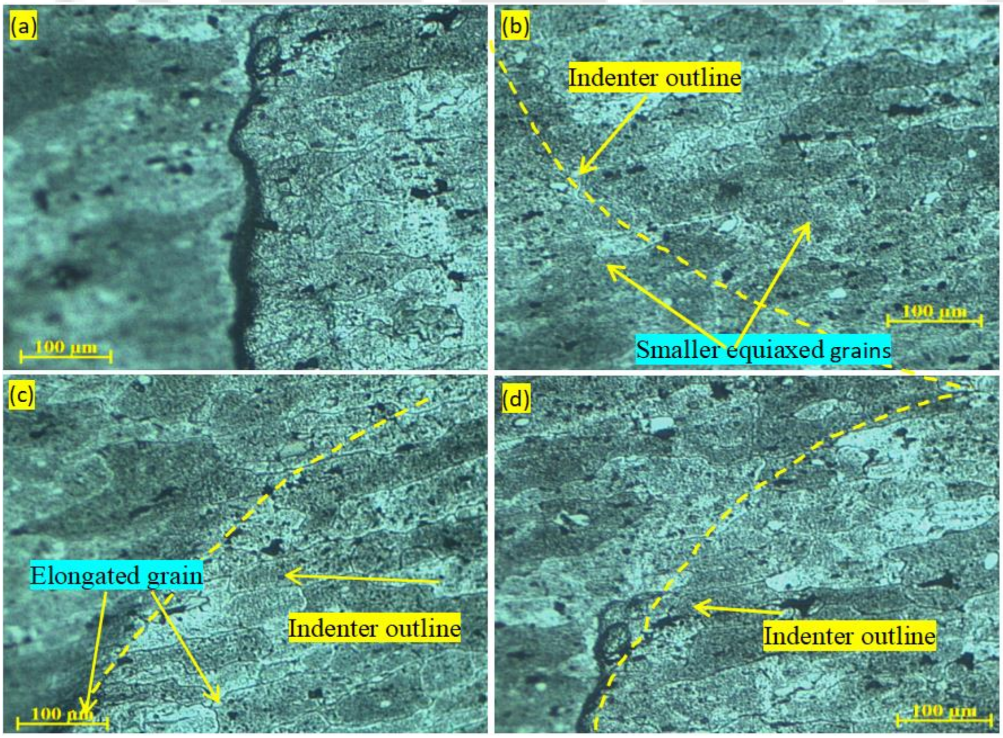

Fig.8.14. Microstructure at the indented area of IC tested samples shown in (Fig.12.) at (a) BM, (b) NZ, (c) TMAZ, (d) HAZ

8.6 Summary

The present analysis on the IC testing of FSWed AA6061 at individual weld zones along with the BM was concluded with the following results

- The creep rate of AA6061 decreases after FSW process with highest creep rate at NZ than TMAZ followed by HAZ.
- Creep strength of the FSWed material was declined due to the smaller grain structure resulted during the FSW process as a result of dynamic recrystallization as well as for the dislocations pinned with precipitation evolved during the creep phenomenon.
- The stress exponent and activation energies for the IC process were highest for the BM and lowest for the NZ.
- Microstructural investigation of the creep tested sample confirms the recrystallization process with reduced grain size.
- The deformation is observed to be homogeneous and through dislocation type for all the cases.
- The grain size below the indenter after IC test was remained unaffected due to hydrostatic pressure.

Chapter 9

Fatigue Crack Growth Rate Behaviour of Friction Stir Welded AA6061-T6 Aluminium Alloy

9.1 Introduction

Aluminium 6xxx series find extensive use in transportation industries due to their excellent mechanical properties obtained by solution heat treatment followed by artificial aging. This alloy being a wrought alloy, many times, it becomes necessary of joining various parts of a component. For safe design of the component subjected to varying stresses, information regarding fatigue crack propagation (FCP) phenomenon is required especially at the joints. Since FSW process introduces different weld zone, each having their own characteristic microstructure, the FCP rate along these zones will be different. The present work is aimed at understanding the fatigue crack growth rate (FCGR) along the different weld zones of FSWed AA6061-T6 alloy and compared. FCGR tests were carried out for different load ratios (*R* values). Compact tension (CT) specimens were prepared such that the crack propagation under mode-I conditions is along the specific weld zones viz. NZ, TMAZ, HAZ and BM. The results obtained are presented and discussed in the subsequent paragraphs.

9.2 Tensile Properties and Hardness of FSWed Specimen after Heat Treatment

The tensile properties of the heat treated (HTed) sample after FSW were analyzed and compared with the sample without heat treatment (HT) as shown in Fig.9.1. The tensile properties of the FSWed sample after the HT is presented in Table-9.1. The strength is restored by the HT process after welding. The reduction of the strength of FSWed joint is because the precipitates are dissolved due to the stirring action of the rotating tool which generates approximately 400°C–500°C temperatures during weld thermal cycle (Bussu and Irving 2003). In the HT process, the internal stresses induced during the thermos-mechanical process of FSW were released and re-precipitation of the hardening precipitates occurs as a result of which the tensile properties were enhanced. The UTS and YS are 304 MPa and 268 MPa and are 98 % and 99% of the BM respectively. Though the tensile properties like UTS and YS were improved, a marginal decease in the % elongation was observed after HT. The tensile specimen most often breaks between the NZ and TMAZ of the weld. Figure 9.2 shows the fractograph of the sample failed at the NZ before and after heat treatment. The tensile fracture feature shows dimples indicting ductile failure in both samples and is shown in Fig. 9.2. However, the heat-treated samples reveal bi-modal dimple features. The re-precipitated strengthening particles after the HT are all seen in the fractured surfaces also.

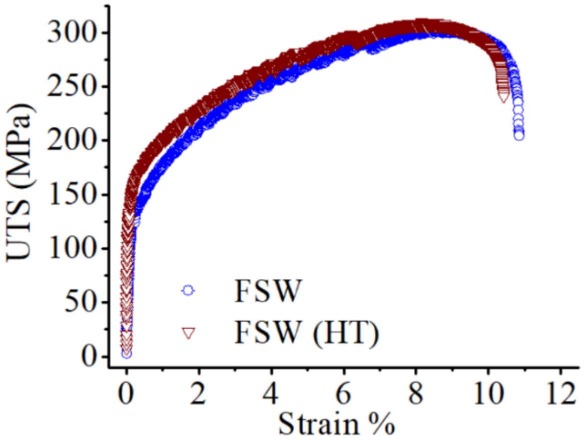

Fig. 9.1. Stress vs. strain curve of specimen after FSW and FSWed specimen after HT

Table 9.1: Tensile properties after HT

Sample	UTS (MPa)	YS (MPa)	%E	Hardness (average) at		
				NZ	TMAZ	HAZ
FSW HT	304	268	11	141	131	126
FSW	302	266	12	138	118	108

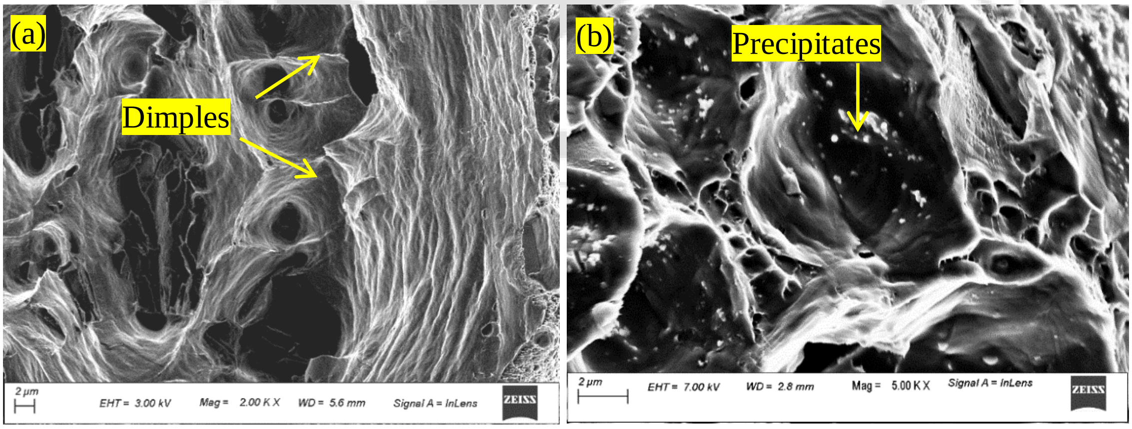

Fig. 9.2. Tensile Fractograph of NZ (a) before and (b) after the HT process

The results of Vickers micro hardness and tensile properties of the FSWed sample after HT were compared with the results without HT. Figure 9.3 compares the microhardness values of the FSWed specimen before and after the HT. The figure shows an increase in the Vickers microhardness values for each weld zones after the HT. NZ represents a nominal increase of 2.2% in the hardness value. At TMAZ the increase in the value is 11% whereas at HAZ the value is the maximum and is about 17%. The softening problem due to the FSW is solved and the hardness is improved. After HT, the differences in the hardness value at each weld zone are decreased. During the high temperature conditions of FSW, the strengthening phases of the alloy were dissolved. Ageing following quenching caused the homogeneous precipitation of these strengthening phases. Due to re-precipitation process, the characteristics compounds of Al-Mg-Si in 6xxx alloy system i.e Mg2Si and Al2CuMg are all distributed uniformly along the welded area. The evenly distributed hardened second phase compounds have an outcome of homogeneously distributed hardness as found from the graph. The average microhardness values before and after the HT is presented in Table-9.1.

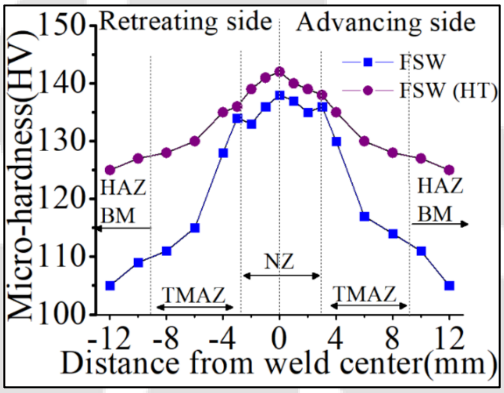

Fig. 9.3. Vickers microhardness at different weld zones as FSW and HT FSW sample

9.3 Microstructure before and after Heat Treatment at Nugget Zone

The microstructural study at nugget zone before and after the HT of FSWed AA6061-T6 was performed and the OM image is presented in Fig. 9.4. Due to FSW, severe material flow occurs at the NZ since the metal becomes more plastic due to the high heat generated at this region compared to other zones. At this high temperature, dynamic recrystallization occurs resulting in finer grains of average size 24 µm (Fig 9.4a). As can be seen from Fig. 9.4b, no noticeable change in the grain size has occurred during the heat treatment. This was expected since the heat treatment temperatures was decided such that no grain growth occurs and rather only the residual stresses are removed or reduced. As a result of the solutionising HT, re-precipitation of strengthening particles occurs in the Al–Mg alloy and was found uniformly distributed throughout the weld section thereby improving the strength of the FSW joints (Cavaliere et al. 2009).

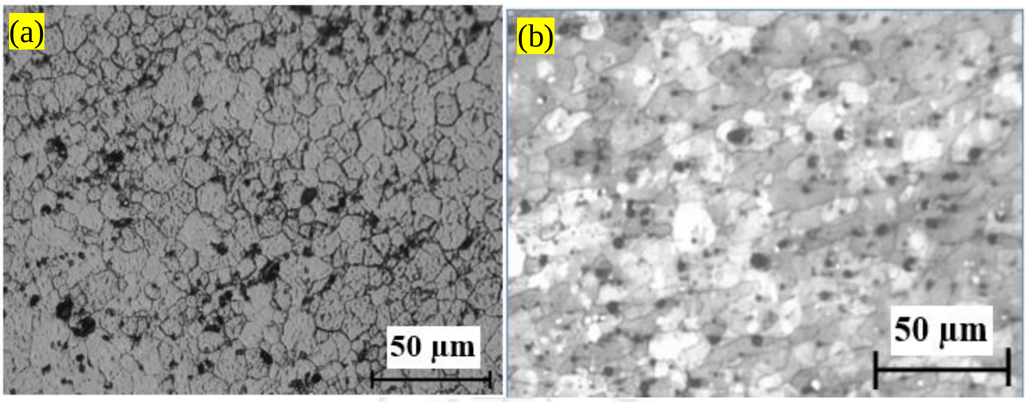

Fig.9.4. OM micrograph showing grain structures at NZ (a) before and (b) after the HT

9.4 Fatigue Crack Growth Rate Phenomena

The crack length vs. no of cycles (a vs N) at various weld zones for stress ratios of 0.1, 0.33 and 0.6 respectively are presented in Fig. 9.5 a, b, c respectively. Irrespective of the load ratios the plots depict the same trend. The crack growth rate along four zones is almost similar in the first stage of crack propagation region. However, the beginning of stage 2 crack growth is different for all the four zones. Along the NZ and TMAZ the crack enters stage-II region after almost 1.20 $\times 10^5$ cycles and 1.40 $\times 10^5$ cycles respectively. However, it took around 2.2×10^5 and 2.35×10^5 no. of cycles to enter in to stage –II crack growth region in the HAZ and BM, respectively i.e., crack growth resistance was higher in the case of HAZ and BM. These observations are attributed to the following reason. Severe plastic deformation occurs during FSW in the NZ and TMAZ followed by sudden cooling that results in loss in ductility and induces residual stress. Whereas, in the HAZ and BM zone, plastic deformation is almost absent and is not much affected by heat input. The fine-grained structure and loss of ductility in the NZ and TMAZ results in less resistance to crack propagation through these regions compared to that through the HAZ and BM. Same trend was observed when experiments were conducted for stress ratios of 0.33 and 0.6 also Fig. 9.5(b-c). The plots of *da/dN* with respect to *a* at three different load ratios of 0.1, 0.33 and 0.6 for each selected zones are illustrated in Fig. 9.6 a, b, c respectively.

The critical crack length (a_c) determined from the plots are presented in Table 9.2. At R = 0.1, the critical crack length a_c determined for the BM was 30.1 mm and was the maximum. The a_c for HAZ, TMAZ and NZ determined were 28.8 mm, 27.1mm and 23.6 mm respectively. NZ exhibits the least a_c and is 78% of BM and hence fracture of the sample occurs at lower no. of cycles. There is only a marginal difference in the a_c (1.7 mm) between HAZ and TMAZ. At *R=0.33*, the critical crack length for BM was 29.6 mm. With the increase in load ratio, the critical crack length decreases and the cycle to achieve the critical crack length is also decreased. The maximum a_c is observed in the HAZ (a_c=28.0 mm) whereas it was minimum (a_c=20.4 mm) in the NZ. The a_c in the TMAZ is 27.0 mm.

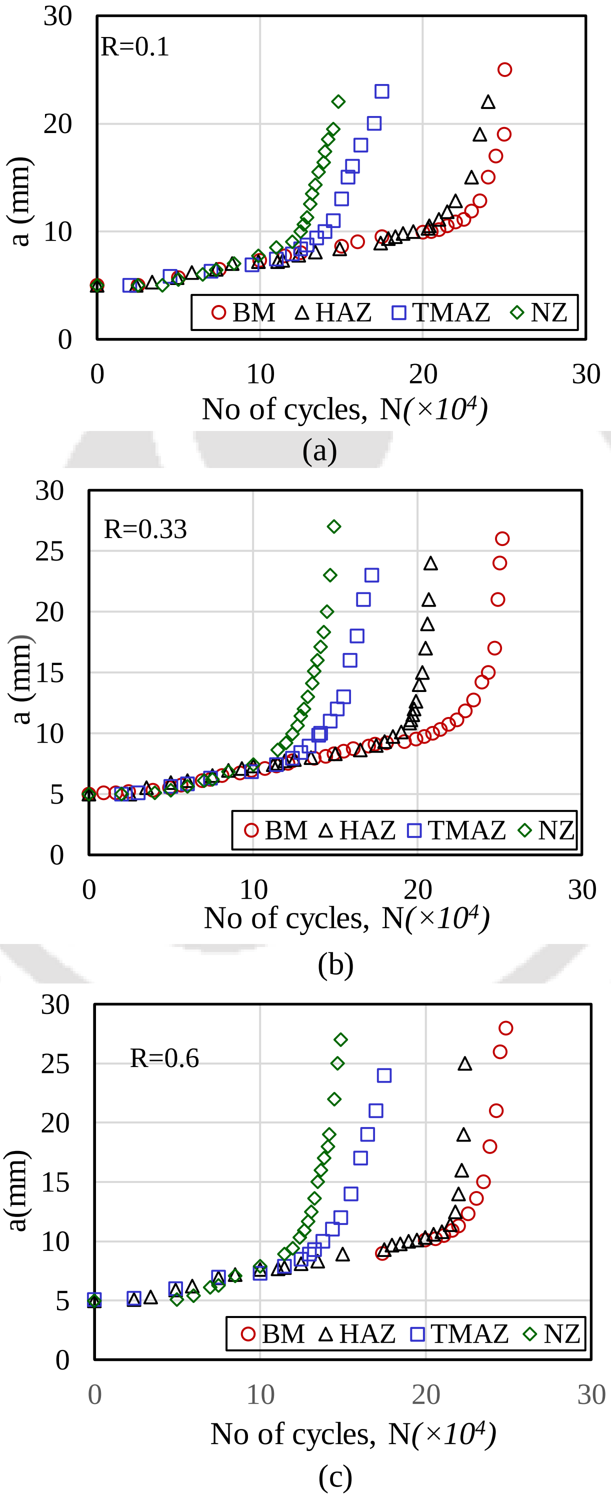

(a)

(b)

(c)

Fig.9.5. Crack length vs. no. of cycles for stress ratios (a) 0.1, (b) 0.33 and (c) 0.6

Table 9.2 Critical crack length at various stress ratios

Load Ratio	Critical crack length, a_c (mm) at different Zones			
	BM	HAZ	TMAZ	NZ
0.1	30.1	28.8	27.1	23.6
0.33	29.6	28.0	27.0	20.4
0.6	28.1	26.5	25.5	19.6

As the R value increases from 0.1 to 0.22, the value of a_c decreases by 13% in the NZ. Percentage % decrease in the a_c with increase in R from 0.1 to 0.33 for NZ is 13%. With further increase in the R value, the a_c decreases further. For load ratio 0.6 the a_c value in the BM, HAZ, TMAZ and NZ are 28.1mm, 26.5mm, 25.5mm and 19.6mm, respectively. BM needs the highest and NZ the lowest cycles to achieve the respective critical crack length. This is due to the decreased ductility of the FSWed material due to the coarsening of the strengthening precipitates during the FSW process. Critical crack length a_c for NZ at this condition is 69.6% of BM. In the NZ a_c decreases by 4% where, the R is increased from 0.33 to 0.6. Plots of da/dN vs. crack length are shown in Figs 9.6:

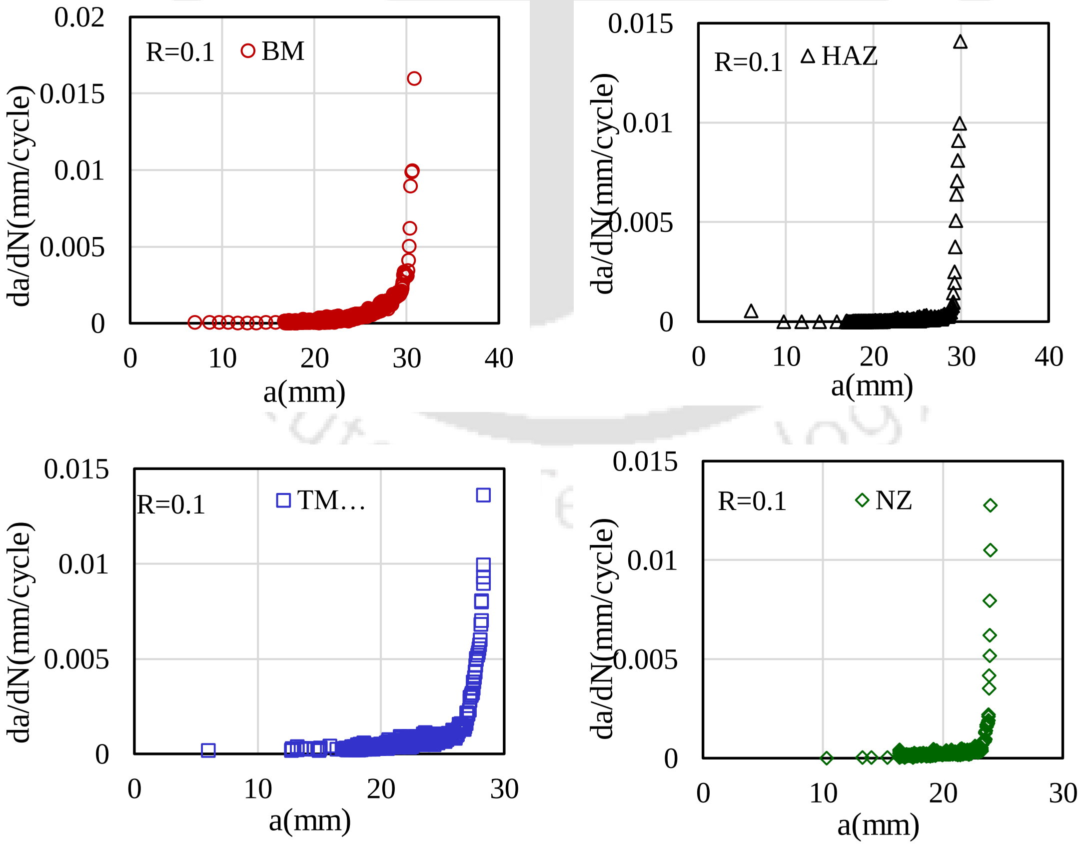

Fig. 9.6. (a) Crack length (*a*) vs. *da/dN* for stress ratios of 0.1

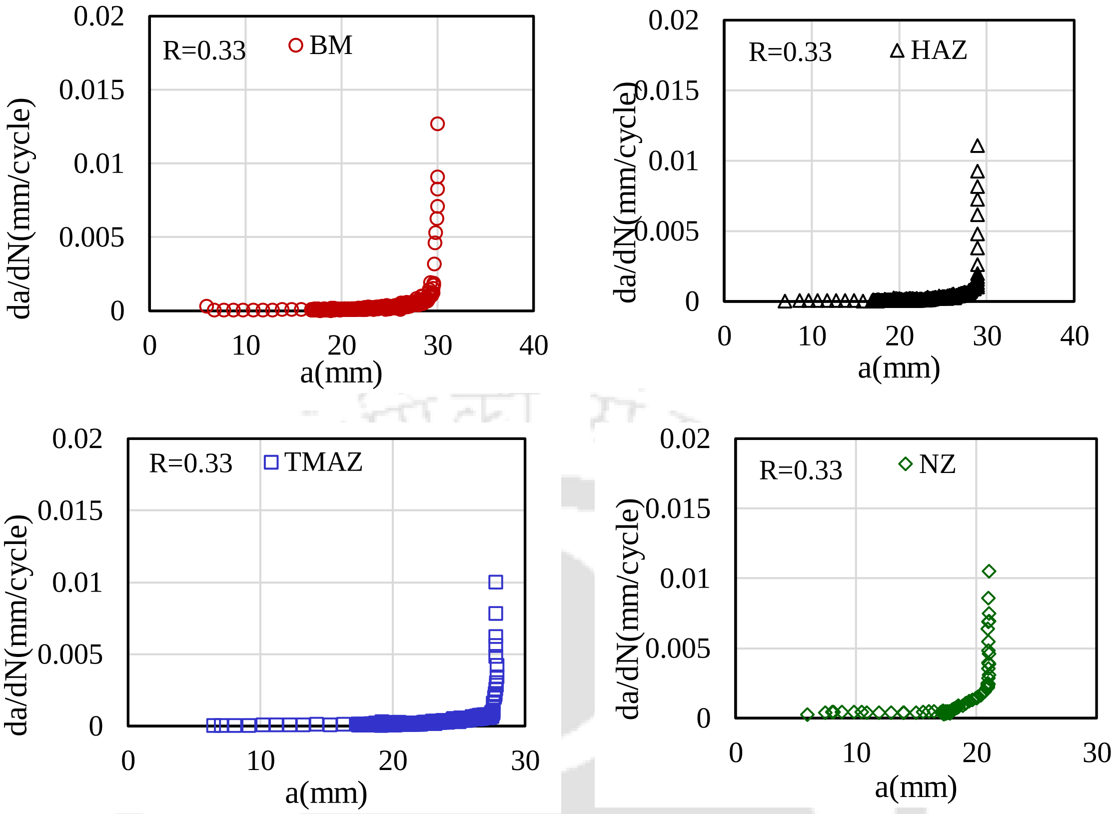

Fig. 9.6 (b). Crack length (*a*) vs. *da/dN* for stress ratios of 0.33

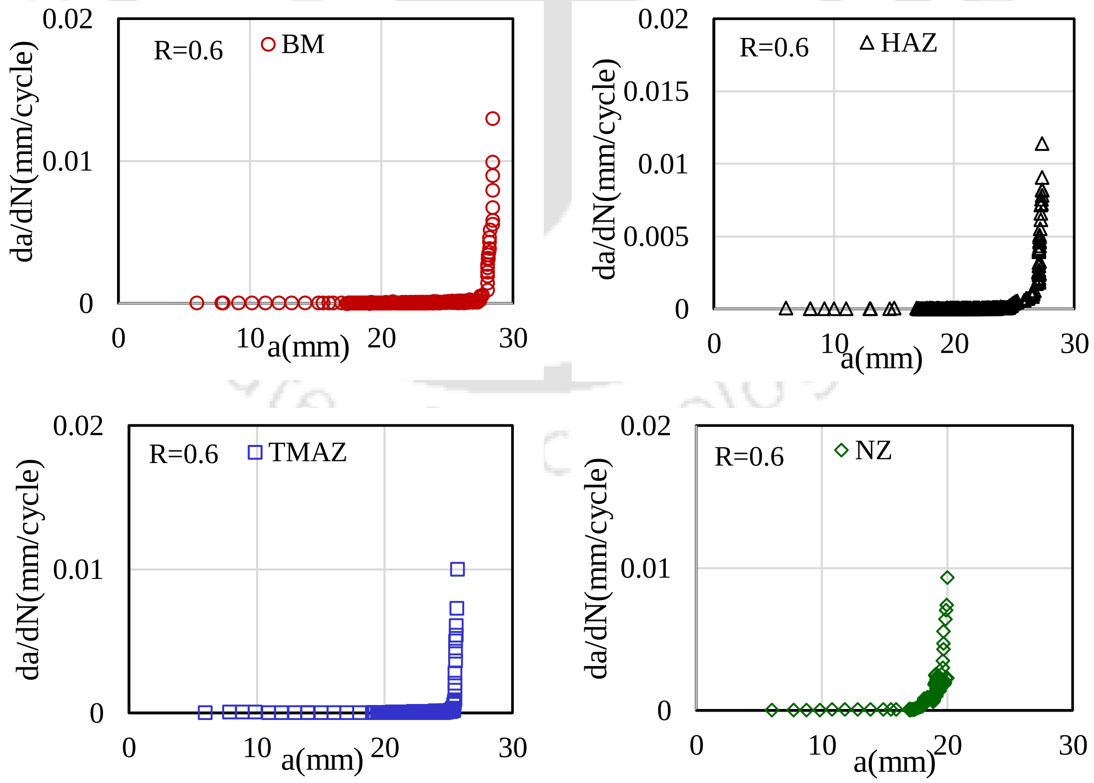

(c)

Fig. 9.6. (c) Crack length (*a*) vs. *da/dN* for stress ratios of 0.6

From the a vs. N data plots of da/dN vs. ΔK were obtained. The $\frac{da}{dN}$ $vs. \Delta K$ plots for the three R values along the different weld zones are shown in Fig. 9.7. The data in the figure corresponds to *region II* i.e., stable crack propagation region. A linear relationship was found in the stable crack growth region. For a particular value of ΔK, the FCG rate through the BM was lower compared to other weld zones. The highest crack growth rate was observed for the NZ and decreased in the order TMAZ, HAZ and BM. Figure 9.7(a), (b) and (c) show similar trend for the experiments carried out with three R values. The exponent 'm' and 'C' determined from the data are presented in Table 9.3. It was observed that the crack growth rate was sensitive to the particular weld zone. FCG rate in the weld zone was significantly higher than that in the BM. With the increase in the stress ratio R, the threshold value for the fatigue crack initiation was decreased and also the cracks propagated very fast as compared to the BM. The value of ΔK_{th} for the BM was the maximum whereas for NZ it was the lowest which is attributed to the fine grain size and more residual stresses in NZ.

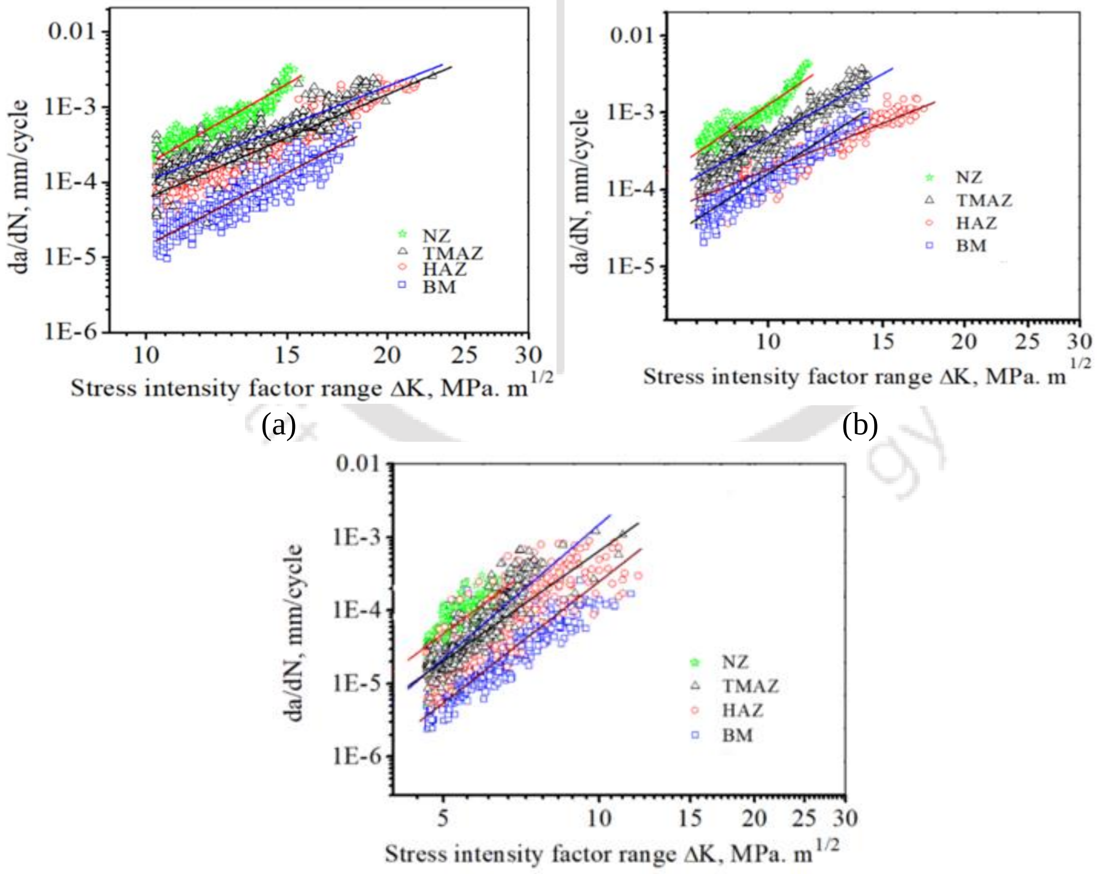

(a) (b)

(c)

Fig. 9.7 Plots of (*da/dN*) vs. *ΔK* at (a) R= 0.1, (b) R= 0.33 and (c) R= 0.6 along different zones of weldments

Table 9.3 Constants of Paris equation for various weld zones

Sample	Stress ratio *R*= 0.1		Stress ratio *R*=0.33		Stress ratio *R*=0.6	
	C	*m*	*C*	*m*	*C*	*m*
NZ	2.81×10^{-9}	4.8	6.5×10^{-12}	6.9	1.2×10^{-14}	7.8
TMAZ	5.34×10^{-9}	4.2	4.7×10^{-10}	6.0	3.1×10^{-12}	6.8
HAZ	8.89×10^{-8}	4.0	7.3×10^{-9}	4.8	5.2×10^{-10}	5.1
BM	1.38×10^{-6}	3.7	1.2×10^{-8}	5.7	7.1×10^{-9}	4.2

From Table 9.3, the Paris equations for the different weld zones are as follows:

(a) at R = 0.1;

For NZ, $$\frac{da}{dN}=2.81\times10^{-9}(\Delta K)^{4.8} \quad (9.1)$$

For TMAZ, $$\frac{da}{dN}=5.34\times10^{-9}\ (\Delta K)^{4.2} \quad (9.2)$$

For HAZ, $$\frac{da}{dN}=8.89\times10^{-8}\ (\Delta K)^{4.0} \quad (9.3)$$

For BM, $$\frac{da}{dN}=1.38\times10^{-6}\ (\Delta K)^{3.7} \quad (9.4)$$

(b) at *R* = 0.33;

For NZ, $$\frac{da}{dN}=6.5\times10^{-12}\ (\Delta K)^{6.9} \quad (9.5)$$

For TMAZ, $$\frac{da}{dN}=4.7\times10^{-10}\ (\Delta K)^{6.0} \quad (9.6)$$

For HAZ, $$\frac{da}{dN}=7.3\times10^{-9}\ (\Delta K)^{4.8} \quad (9.7)$$

For BM, $$\frac{da}{dN}=1.2\times10^{-8}\ (\Delta K)\ 5.7 \quad (9.8)$$

(c) at *R* = 0.6;

For NZ, $$\frac{da}{dN}=1.2\times10^{-14}\ (\Delta K)^{7.8} \quad (9.9)$$

For TMAZ, $$\frac{da}{dN}=3.1\times10^{-12}\ (\Delta K)^{6.8} \quad (9.10)$$

For HAZ, $$\frac{da}{dN}=5.2\times10^{-10}\ (\Delta K)^{5.1} \quad (9.11)$$

For BM, $$\frac{da}{dN}=7.1\times10^{-9}\ (\Delta K)^{4.2} \quad (9.12)$$

9.4.1 Effect of Microstructure on Fatigue Crack Propagation Path

Several researchers have reported that the FCP rate is sensitive to the grain structure (Tra et al. 2012, Hanlon et al. 2003, Vasudevan et al. 1997). The nature of the FSW alloys that makes it unique from the other structural materials is the microstructural difference. The ultra-fine grains have the effect of lowering the threshold value for the FCP rate (Gavras et al. 2010). During testing at low stress ratio, the effects were more prevalent. Basically, at near threshold or at region I, the FCP rate depends the grain size. Finer the grain size, lower the threshold for the FCP. The grain boundaries are regions of higher energy and hence are potential sites for crack nucleation and propagation. The grain boundary area in finer grained structure is higher as compared to coarse grained structure. Any crack which has nucleated propagates through the grain and when it reaches the grain boundary region gets deflected through the grain boundary. Crack deflection leads to longer crack path and hence retards the crack propagation. The crack path in coarser grains is higher compared to finer grains and at the same time the orientation angle of the crystallographic planes also increases. Hence in fine grained structure, the crack nucleation occurs early and crack propagation rate is faster as compared to coarse grained structure (Lutjering and Williams 2009, Attanasio et al. 2013). For the finer grain size at NZ and TMAZ the crack deflection is less in compared to the zones such as HAZ and base material. The paths through which the crack has propagated along various weld zones are shown in Fig. 9.8. The crack path through NZ shown in Fig. 9.8a. is smoother while is rough for the case of BM (Fig. 9.8b). The crack path along TMAZ and HAZ shows a moderately rough fractured surface shown in Fig. 9.8(c, d) respectively. Since the grain size increases in the order of NZ-TMAZ-HAZ-BM, the threshold values also increase in the same order. Similar observation was also reported by other investigator (Hanlon et al. 2003).

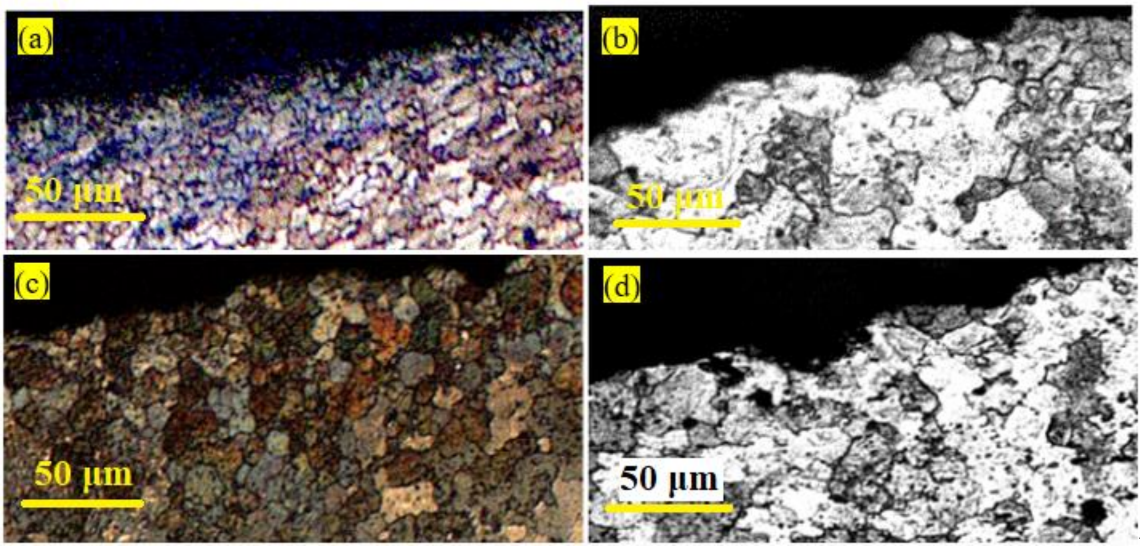

Fig. 9.8. Crack propagation path in region I at (a) NZ, (b) BM, (c) TMAZ and (d) HAZ

The properties of various constituent phases in the matrix influence the crack growth phenomenon in regions II and III. Figure 9.9 a shows grain boundary failure indicating that the crack propagated through the grain boundary region during stage II crack growth in NZ. Similar features were also observed for TMAZ samples. Figure 9.9b shows the typical fracture feature of HAZ and BM. Brittle features typical of trans-granular facture and micro-cracks along the grain boundary regions are evident. The plastic zone size ahead of the crack is large as the crack enters stage III crack growth region (Pilchak and Williams 2011). Presence of dimple features in regions of Stage III crack growth indicates that the final failure is by shear deformation.

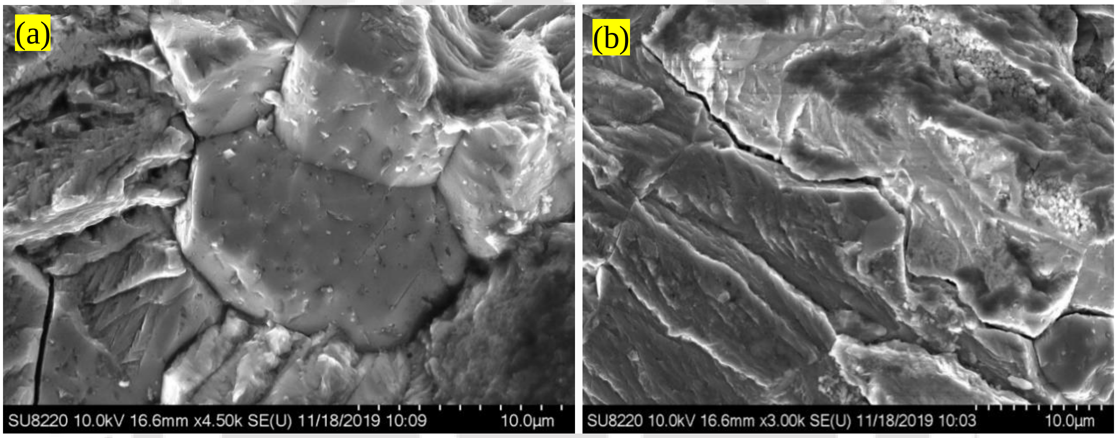

Fig. 9.9. Crack propagation path in region II at (a) NZ and (b) HAZ

9.4.2 FCP Behaviour at NZ After HT

In FSW process, severe plastic deformation occurs at NZ and an excess number of dislocations would be generated during this deformation process (Sahu et. al). The energy possessed by the dislocations represents partial deformation energy. Recovery and recrystallization process occurs during the FSW process (Tra et al. 2012). But due to the faster cooling rate all the deformation energy was not utilized and the unused energy remains stored as residual internal energy thereby raising the total energy at these locations. Since these occurs at the NZ, the FCP rate along this region in the FSWed weldments is high. It was expected that PWHT will release the residual energy during the welding stage and thereby decrease the FCGR.

Figure 9.10 shows the *da/dN* vs. *ΔK* plot for R = 0.1 for the crack growth along NZ after PWHT. Comparing this figure with Fig 9.7 for the same case but without heat treatment indicates that the FCP rate after HT reduced considerably. The PWHT resulted in an improved strength as well as the fatigue crack growth resistance. Analysis of the plot for the PWHTed sample reveals that the constants in the Paris equation are $c = 2.22 \times 10^{-6}$ and $m = 4.0$. The results are comparable to the BM ($c = 1.38 \times 10^{-6}$, and $m = 3.7$). The PWHT has improved the crack growth resistance at the NZ, which was the weakest weld zone, by release of stored residual energy.

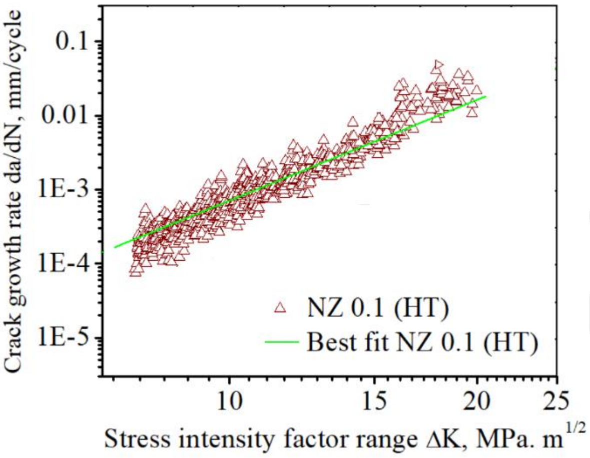

Fig. 9.10 Plots of *da/dN* vs. *ΔK* at NZ for load ratio $R = 0.1$

9.5 Fractography of FCG Tested Sample

The fractured surfaces of the fatigue failed samples were observed under FESEM. A typical photograph of the failed sample surfaces at very low magnification is shown in Fig. 9.11. In general, three distinct regions are visible; the region of crack initiation, steady state crack propagation regions and the final unsteady crack propagation region. The fracture surfaces are not identical for all the specimens and all the regions. Three visually distinct fractured regions are noticed viz: fatigue pre-cracking, crack propagation and final failure parts corresponding to the three stages of fatigue crack propagation.

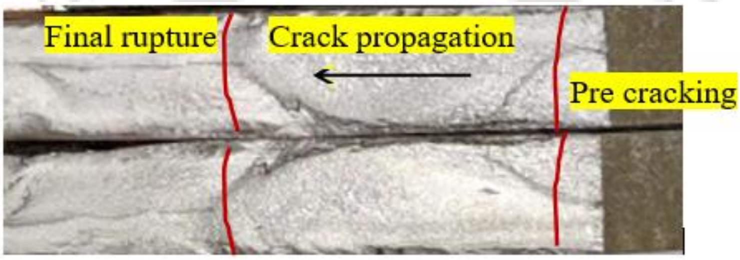

Fig. 9.11. Fatigue crack propagation at different distances from the initial notch tip

Figure 9.12 shows the fractograph of the sample where the crack propagated through the NZ. The fractograph taken at the crack initiation region (Fig.9.12a) reveals brittle features, striations, short micro cracks and intergranular failure. At the stable crack propagation region, quasi-cleavage features (Fig.9.12b) are evident characterized by second phase particle fracture and debonding at the particle matrix interface. The final failure region is characterized by ductile failure (Fig.9.12c).

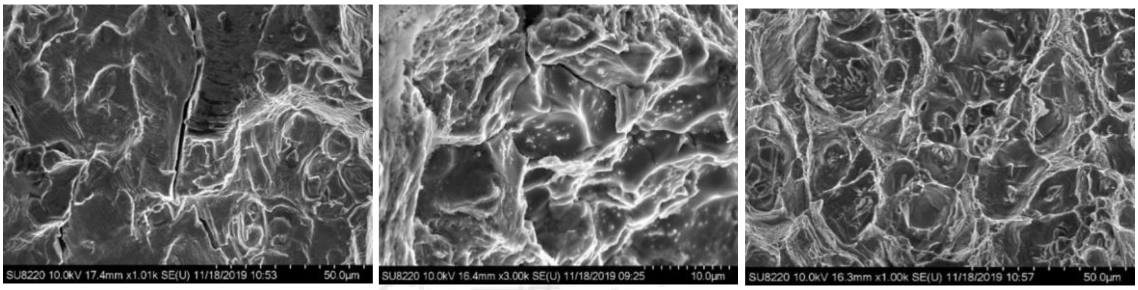

(a) (b) (c)

Fig. 9.12. Fracture surfaces of NZ at regions of (a) crack initiation, (b) steady state propagation and (c) unstable crack growth region

The crack propagation region of the TMAZ shown in Fig.9.13(a) depicts features of cleavage fracture. The stable crack propagation region, as evident from Fig.9.13(b), is characterized by inter-granular fracture and micro-cracks indicating that the crack path was through the grain-boundaries. Features in the stage-II crack growth region (Figure 9.13(c)) indicates that the final failure is by ductile failure.

(a) (b) (c)

Fig. 9.13. (a). Fracture surfaces at (a) pre-cracking, (b) propagation and (c) final fracture regions at TMAZ

The crack growth region of the HAZ indicates (Fig 9.14a) brittle failure. The feature of steady state region of FCG shows fish bone type of features (Fig.9.14b) indicating transgranular cleavage failure whereas the final failure (Stage-III) is by ductile failure, as reveled from Fig 9.14c.

Fractograph of the fatigue failed surfaces of the BM is shown in Fig.9.15. The stage I region of the crack propagation reveals brittle features as is evident from Fig.9.15a. However, striations are seen at the steady state crack growth region (Fig. 9.15b) indicating fatigue crack growth of ductile materials. The mechanism of the formation of the striations in ductile materials during cyclic loading are well documented in the literature. The stage-

III crack region shown in Fig 9.15c reveals bi-modal dimple features, i.e., mixture of fine and coarse dimples indicating that the final failure was by ductile shearing.

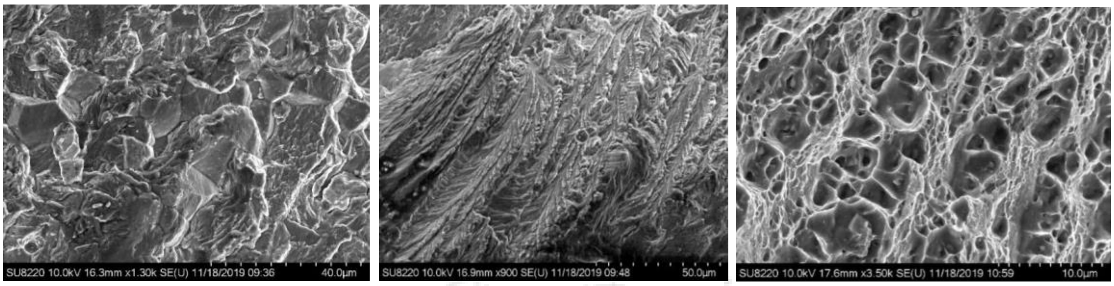

(a) (b) (c)

Fig. 9.14. Fracture surfaces at (a) pre-cracking, (b) propagation and (c) final fracture regions at HAZ

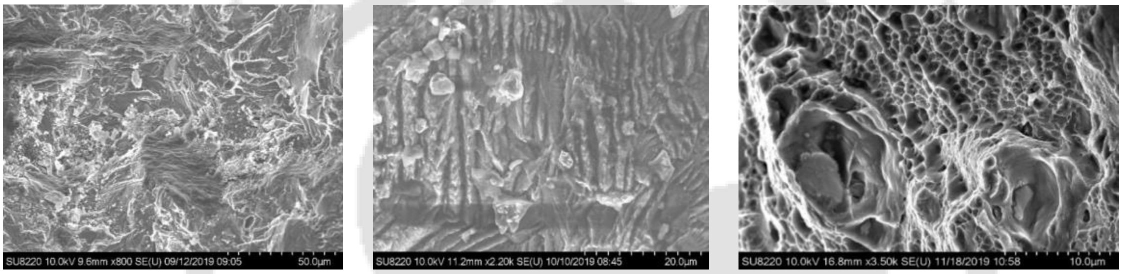

(a) (b) (c)

Fig. 9.15 Fracture surfaces at (a) pre-cracking, (b) propagation and (c) final fracture regions at BM

9.6 Fatigue Fractograph at NZ after HT

Figure 9.16 depicts the FESEM image of the fractured surface of the post weld heat treated sample. Though at low magnification it appears as brittle failure, observation at high magnification reveal fine dimples distributed over the entire fracture surface, characteristics of ductile failure.

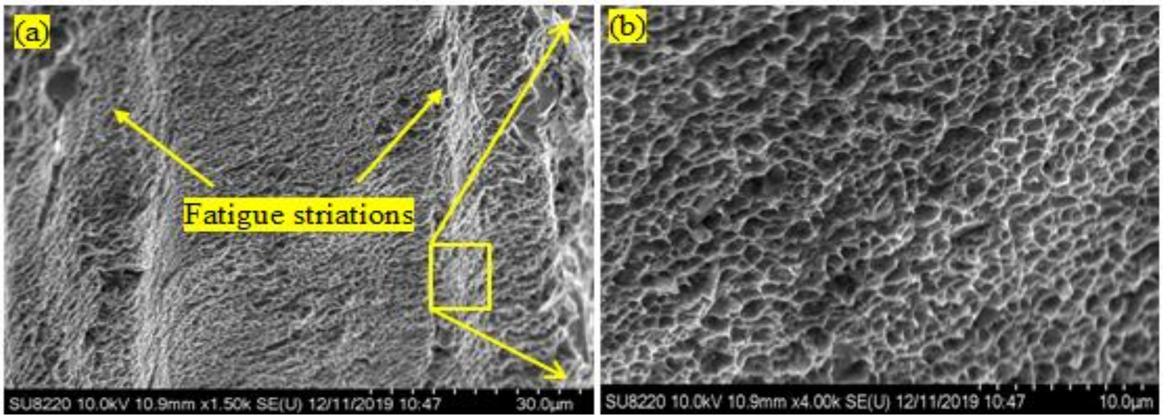

Fig. 9.16. Fractograph of NZ after HT at (a) low magnification and (b) high magnification.

9.7 Conclusion

In this research FCGR before and after the HT of FSWed AA6061-T6 alloy at low, intermediate and high load ratios and at different weld zones with notch placed parallel to the welding direction has been estimated and the following conclusions are derived.

- FSW of AA6061-T6 alloy reduced the fatigue crack resistance of the material. The weakest part of the weldment w.r.t. FCGR was the NZ.
- The critical crack length a_c for the NZ was the lowest compared to other weld zones and was 78% of the BM.
- The critical crack length a_c decreased with increase in R value.
- NZ enters into *stage III* of FCGR with less no. of fatigue cycles compared to the other zones.
- The loss of strength, uneven hardness throughout the weld zones and FCG resistance of the weldment was restored by post weld heat treatment. No significant grain growth was observed after post-weld heat treatment in the NZ and was characterized by fine equi-axed grains and re-precipitation of hardening second phase particles.
- The initiation of fatigue crack was by cleavage and nucleation of micro-cracks ahead of the crack. The steady state crack growth region was in a ductile manner. The unstable crack growth region was characterized by ductile failure.
- The crack propagation and failure in post weld Heat treated sample was by ductile mode of fracture.

Chapter 10

Conclusions and Future Scope of the Work

10.1 Conclusions of the Present Work

In the present work, similar metal friction stir welded joints are produced from AA2014 as well as AA6061-T6 Aluminium alloys by optimization of process parameters. The quality of the weldments is established based on the output characteristics viz., UTS, YS, %E, bending angle, flexural strength, average micro-hardness and microstructure. The best welded specimen, with respect to the microstructure and mechanical properties, are IC tested to study the creep deformation behavior of different weld zones. The constitutive parameters viz, n and Q_{ic} of the power law creep equation for the individual weld zones were determined and compared with the BM. The FCGR tests in mode-I loading were performed on the best welded specimen in such a manner that the crack propagation was parallel to the welding direction and through the individual weld zones. From analysis of the steady state crack growth region, the Paris constants (C and m), were determined. The FCG behaviour for the individual weld zones were compared with the BM.

The detailed results and findings of the present work has been highlighted at the end of Chapters 4 to 9. However, the main conclusions of the thesis are as follows:

1. The experimental investigation on similar metal FSW of AA2014 Al and AA6061-T6 alloys revealed that joints obtained with moderate shoulder diameter, square pin tool with lower plunge depth, moderate tool rotational speed and lower welding speed yielded the best joint qualities.
2. The maximum UTS, YS and FS of the optimum sample obtained from the weld of AA2014 were 86%, 90% and 92% of the BM sample respectively. For AA6061-T6 Alloy, the corresponding values were 97%, 98%, 978% of the base metal. Vickers micro-hardness at the top layer of the welded plate was the highest and is independent of all parameter’s settings. Hardness was the highest at NZ and the grain size at this region reduced by 84% and 72% respectively for the AA2014 and AA6061-T6 alloy, after FSW.

3. Failure in the best weld joint occurred outside the weldment region indicating good weld quality. The failure of the weldment was by ductile failure which is similar to that of the base metal
4. The resistance to creep deformation of AA2014 Al alloy reduced after FSW. The creep resistance was least at the NZ and increased in the order of TMAZ-HAZ-BM.
5. The creep deformation is due to the grain deformation / flow of metal in zone-ii below the indenter whereas, zone-i and zone-ii above and below zone-ii do not contribute to the creep process.
6. Increase in the overall hardness of AA2014 alloy weldment after IC testing is attributed to the precipitation and coarsening of strengthening phases.
7. The high re-precipitation of strengthening phases at the NZ for both alloys weldments is due to the low activation energy for creep deformation as a result of the high stored internal energy during the FSW compared to other zones.
8. The resistance to FCGR of FSWed AA2014 Al alloy was lower than the BM. The highest FCGR was found to be at the NZ and decreased in the order TMAZ-HAZ-BM. This is attributed to the high deformation energy stored in the NZ due to partial recrystallization resulting from the faster cooling rate during FSW.
9. Post weld heat treatment improved the FCGR along the NZ area and was comparable to the BM.
10. The creep deformation resistance of AA6061-T6 alloy plates decreased due to FSW process. The NZ is the region of early creep deformation and failure in the FSWed AA6061-T6 joint during the high temperature deformation process of IC test. Creep deformation behavior in AA6061-T6 alloy was similar to the AA2014 alloy weldment.
11. The fatigue crack propagation resistance was decreased after FSW in AA6061-T6. NZ was the weakest point during the fatigue loading. Post weld heat treatment resulted in homogeneous distribution of hardness across the weld region. The FCGR of the NZ improved due to HT and was comparable to BM.
12. Initiation of fatigue crack in both alloys weldments was by fracturing of second phase particles and/or particle-matrix interface debonding. Steady state fatigue crack growth was quasi-ductile in nature favouring nucleation of fine micro-cracks and branching ahead of the growing crack. Fine striations like features were also observed. The final failure in all weld zones of both alloys were by ductile shearing.

10.2 Future Scope

A few of the future scope of investigations which are to be addressed are enumerated below:

- The effect of different pre-heat treatment like homogenous anneal or solutionize anneal on the quality of friction stir weldments is to be performed.
- An in-depth TEM study is to be carried out regarding the dislocation generation and its effect on the grain refinement during the FSW.
- Study regarding the grain growth and recrystallization during IC testing and its effect on creep deformation is to be carried out.
- Study regarding the improvement of creep and FCGR properties at NZ is to extended.
- Study on the effect of plastic deformation at zone ii during the IC deformation process on the microstructural and mechanical properties of the material is required.
- Study regarding stress corrosion cracking /corrosion fatigue of FSW weldments with and without heat treatments are required.

References

Ahmed M M Z, Wynne B P, Rainforth W M, Addison A, Martin J P, Threadgill P L (2019) Effect of tool geometry and heat input on the hardness, grain structure, and crystallographic texture of thick-section friction stir-welded aluminium, Metall, Mater. Trans. A Phys. Metall. Mater. Sci, 50, 271–284. https://doi.org/10.1007/s11661-018-4996-2.

Al-Ganainy G S, Mostafa M T (2000) Grain Size Dependence of Steady State Creep Rate in Sn-1 wt% Zn Alloy, Egypt. J. Sol, 23(2), 333-340.

Ambriz R R, Chicot D, Benseddiq N, Mesmacque G (2011) local mechanical properties of the 6061-T6 aluminium weld using micro-traction and instrmented indentation, European Journal of Mechanics - A/Solids, 30:3, 307-315.

Arora K S, Pandey S, Schaper M, Kumar R.(2010) Effect of process parameters on friction stir welding of aluminum alloy 2219-T87, Int J Adv Manuf Technol, 50, 941–52.

Attanasio A, Gelfi M, Pola A, Ceretti E, Giardini C (2013) Influence of Material Microstructures in Micromilling of Ti6Al4V Alloy, Materials, 4268–4283.

Balasundaram A, Gokhale A M, Graham S, Horstemeyer M F (2003) Three-dimensional particle cracking damage development in an Al–Mg-base wrought alloy, Mater Sci Eng A, 355(1–2), 368–83.

Basel Y, Basel M, AlfaroMercado U, Kakiuchi T, Uematsu Y (2016) Influence of Joint Line Remnant on Crack Paths Under Static and Fatigue Loading in Friction Stir Welded Al-Mg-Sc Alloy, Frattura ed Integrita Strutturale, Vol. X, No. 35, Jan., pp. 295–305. doi:10.3221/IGF-ESIS.35.43.

Bertrand R, Robe H, Texier D, Zedan Y, Feulvarch E, Bocher P (2019) Analysis of AA2XXX/AA7XXX friction stir welds. Journal of Materials Processing Technology, 271, 312–324. https://doi.org/10.1016/j.jmatprotec.2019.03.027.

Blum W (1991) Creep of aluminium and aluminium alloys, Proceedings of symposium at the TMS Fall meeting.;9:181-209.

Bussu G, Irving P (2003) The role of residual stress and heat affected zone properties on fatigue crack propagation in friction stir welded 2024-T351 aluminium joints, Int. J. Fatigue 25 (1), 77–88.

Butt D P, Korzekwa D A, Maloy S A, Kung H, Petrovic J J (1996) Impression creep behavior of SiC particle–MoSi2 composites. J. Mater. Res, 11(6), 1528–1536. DOI: https://doi.org/10.1557 /JMR. 1996.0191.

Cavaliere P, Santis De A, Panella F, Squillace A (2009) Effect of welding parameters on mechanical and microstructural properties of dissimilar AA6082–AA2024 joints produced by friction stir welding, Mater. Des, 30 (3), 609–616.

Ceyhan U, Papierflieger C Z (2007) High Temperature Deformation and Fracture Assessment of Similar Steel Welds. 2007, http://www.gbv.de/dms/clausthal/E DISS/2007/db108543.

Chu S N G, Li J C M (1977) Impression Creep; a new creep test. Journal of Materials Science, 12, 2200–2208.DOI: 10.1007/ BF00552241.

Chu S N G, Li J C M (1979) Impression Creep of Tin Single Crystals. Materials Science and Engineering A, 39, 1 – 10.

Costa M, Leitão C, Rodrigues D (2017) Influence of post-welding heat-treatment on the monotonic and fatigue strength of 6082-T6 friction stir lap welds, J. Mater Process. Technol. 250, 289–296.

Cui L, Gao H, Li H, Liu Y, Wang D, Ding W (2019) Effect of precipitate evolution on creep damage of reduced activation ferritic/martensitic steel friction stir welded joint, Journal of Alloys and Compounds. 808, 151738. https://doi.org/10.1016/j.jallcom.2019.151738

Dai Q, Liang Z, Chen G, Meng L, Shi Q (2013) Explore the mechanism of high fatigue crack propagation rate in fine microstructure of friction stir welded aluminum alloy. Materials Science & Engineering A, 580, 184–19.

Das J, Robi P S, Ravi Sankar M (2018) Indentation Creep Behavior of Nugget Zone of Friction Stir Welded 2014 Aluminum Alloy, IOP Conf. Series: Materials Science and Engineering, A 346, 012-017. doi:10.1088/1757-899X/346/1/012017.

Das J, Robi P S, Sankar M R (2021) Estimation of deformation behaviour at different weld zones of FSWed AA2014 aluminium alloy through impression creep technique, Journal of adhesion science and technology (Taylor & and Francis), Vol: 35, https://doi.org/10.1080/01694243.2021. 1921498.

Das U, Toppo V, Sahoo T K, Sahoo R (2018) Microstructural and Mechanical Properties of FSW Joints Between AA6101-T6 and AA6351-T6 Dissimilar Al Alloys, Trans Indian Inst Met 71(4), 823–830, https://doi.org/10.1007/s12666-017-1213-8.

Dawood H I, Mohammed K S, Rahmat A, Uday M B (2015) The influence of the surface roughness on the microstructures and mechanical properties of 6061 aluminium alloy using friction stir welding. Surface & Coatings Technology, 270, 272–283. http://dx.doi.org/10.1016/ j.surfcoat.2015.02.045.

Durso G, Giardini C, Lorenzi S, Pastore T (2014) Fatigue crack growth in the welding nugget of FSW joints of a 6060 Aluminum alloy, Journal of Materials Processing Technology, 214, 2075–2084.

Fleck R G, Cocks G J, Taplin D M R (1970) The Influence of Polycrystal Grain size upon the creep ductility of copper, Metallurgical transaction, 1, 3415-3420. https://doi.org/10.1007/BF03037873.

Ganesh Kumar J, Laha K (2015) Small Punch Creep deformation and rupture behavior of 316L(N) stainless steel, Materials Science and Engineering: A. 641, 315-322.

Gavras A G, Chenelle B F,Lados D A (2010) Effects of microstructure on the fatigue crack growth behavior of light metals and design considerations, Revista Matéria, v. 15, n. 2, pp. 319-329.

Gupta M K (2020) Effects of tool profile on mechanical properties of aluminium alloy Al 1120 friction stir welds, Journal of Adhesion Science and Technology https://doi.org/10.1080/01694243. 2020.1749448.

Haeberle D C, John J L, Scott W C, Judy S R, Kandathil E V (2007) The use of a modified microindentation technique to evaluate enviro-mechanical changes in composite interphase properties, Journal of Adhesion Science and Technology 21(1)35-50 http://dx.doi.org/10.1163/15685610777 9976123

Haldar N, Datta S, Kumar Rajneesh (2018) Experimental studies on friction-stir welding of AA6061 using Inconel 601 tool, Journal of the Brazilian Society of Mechanical Sciences and Engineering, 40, 448 https://doi.org/10.1007/s40430-018-1378-z.

Hanlon T, Kwon Y N, Suresh S (2003) Grain size effects on the fatigue response of nanocrystalline metals, Scr. Mater. 49(8), 675–680.

Hong S J, Kim S S, Lee C G, Kim S J (2006) Fatigue crack propagation behavior of friction stir welded Al–Mg–Si alloy, Scr. Mater, 55, 1007–1010.

Hoseinlaghab S, Mirjavadi S S, Sadeghian N, Jalili I, Azarbarmas M, Givi M K B (2015) Influences of welding parameters on the quality and creep properties of friction stir welded polyethylene plates, Materials and Design, 67, 369–378. https://doi.org/10.1016/j.matdes.2014.11.039

Huang G, Cheng D, Wang H, Zhou Q, Shen Y (2019) Effect of tool probe with a disc at the top on the microstructure and mechanical properties of FSW joints for 6061-T6 aluminum alloy, Journal of adhesion science and technology. https://doi.org/10.1080/01694243.2019.1645381.

Huang Y, Xie Y, Meng X, Lv Z, Cao J (2018) Numerical design of high depth-to-width ratio friction stir welding, J. Mater. Process. Technol, 252, 233–241. https://doi.org/10.1016/j.jmatprotec.2017.09.029.

Ilangovan M, Rajendra B S, Balasubramanian V (2015) Effect of tool pin profile on microstructure and tensile properties of friction stir welded dissimilar AA 6061-AA 5086 aluminium alloy joints, Defence Technology, 11, 174-84.

Ilman M, Iswanto P (2013) Fatigue crack growth rate behaviour of friction-stiraluminium alloy AA2024-T3 welds under transient thermal tensioning, Mater. Des. 50, 235–243.

Jamalian H M, Farahani M, Givi B M K, Vafaei A M (2016) Study on the effects of friction stir welding process parameters on the microstructure and mechanical properties of 5086-H34 aluminum welded joints, Int J Adv Manuf Technol, 83, 611–621. DOI 10.1007/s00170-015-7581-5.

Jata K V, Sankaran K K, Ruschau J J (2000) Friction-stir welding effect on microstructure and fatigue of aluminum alloy 7050–T7451, Metall Mater Trans, 31A, s2181–92.

Jayabalakrishnan D, Balasubramanian M (2017) Friction stir weave welding (FSWW) of AA6061 aluminium alloy with a novel tool-path pattern, Australian Journal of Mechanical Engineering, https://doi.org/10.1080/14484846.2017.1373584.

Jung I, Rudy M, Sauthoff G, Koch C C, Liu C T, Stoloff N S, Izumi (1987) High Temperature Ordered Intermetallic AlloyII. Mater. Res. Soc. Symp. Proc. 81, Pittsburgh, PA, , p. 263.

Kadaganchi R, Gankidi M R, Gokhale H (2015) Optimization of process parameters of aluminum alloy AA 2014-T6 friction stir welds by response surface methodology, Defence Technology, 11, 209-219. http://dx.doi.org/ 10.1016/j.dt.2015.03.003

Kadian A, Biswas P (2017) Effect of tool pin profifile on the material flflow characteristics of AA6061, Journal of Manufacturing Processes, 26, 382–392, http://dx.doi.org/10.1016/j.jmapro.2017.03.005.

Kafali H, Ay N (2014) The effect of post heat treatment on the fatigue behavior of riction stir welded aluminum 6013 alloy for use in aerospace structures, Journal of International Scientific Publications, Materials, Methods and Technologies Volume 8, ISSN 1314-7269.

Kalinenko A, Kim K, Vysotskiy I, Zuiko, Malopheyev S, Mironov S, Kaibyshev R (2020) Microstructure strength relationship in friction-stir welded 6061-T6 aluminum alloy, Materials Science & Engineering A, 793,139858. https://doi.org/10.1016/j.msea.2020.139858.

Khalilabad M M, Zedan Y, Texier D, Jahazi M, Bocher P (2018) Effect of tool geometry and welding speed on mechanical properties of dissimilar AA2198–AA2024 FSWed joint, J. Manuf. Process, 34, 86–95. https://doi.org/ 10.1016/j.jmapro.2018.05.030.

Khan N Z, Siddiquee A N, Khan Z A, Mukhopadhya A K (2017) Mechanical and microstructural behavior of friction stir welded similar and dissimilar sheets of AA2219 and AA7475 aluminium alloys, Journal of Alloys and Compounds, 695, 2902-2908. http://dx.doi.org/10.1016/j.jallcom.2016.11.389.

Krishna P M, Ramanaiah N (2011) Effect of Post-Weld Heat Treatment on the Mechanical Properties of Friction Stir Welds of Dissimilar Aluminum Alloys, International Journal of Engineering Science and Technology (IJEST), 3 (7). ISSN : 0975-5462.

Kucukrendeci I (2015,) Mechanical and microstructural properties of EN AW-6060 aluminum alloy joints produced by friction stir welding, Bulletin of the polish academy of sciences technical sciences, 63, 475-78.

Kumar N, Patel V K (2020) Efect of SiC/Si3N4 micro-reinforcement on mechanical and wear properties of friction stir welded AA6061-T6 aluminum alloy, SN Applied Sciences, 2, 1572, https://doi.org/ 10.1007/s42452-020-03381-y.

Kutty T R G, Kumar A, Kamath H S (2010) Determination of activation parameters using impression creep data. Transactions of The Indian Institute of Metals, 63(2-3), 443-447.

Lakshminarayanan A K, Balasubramanian V (2012) Assessment of fatigue life and crack growth resistance of friction stir welded AISI 409M ferritic stainless-steel joints, Materials Science and Engineering A, 53(9), 143−153.

Lemmen H J K. Alderliesten R C, Benedictus R (2011) Evaluating Fatigue Crack Initiation Location in Friction Stir Welded AA2024-T3 Joints, International Journal of Fatigue, 33 (3), 466–476. doi:10.1016/j.ijfatigue.2010.10.002.

Liu H J, Fujii H, Maeda M, Nogi K (2003) Tensile properties and fracture locations of friction-stir-welded joints of 2017-T351 aluminum alloy, Journal of Materials Processing Technology, 142, 692–696. doi:10.1016/S0924-0136(03)00806.

Liu H J, Hou J C, Guo H (2013) Effect of welding speed on microstructure and mechanical properties of self-reacting friction stir welded 6061-T6 aluminum alloy, Materials and Design, 50, 872–878. http://dx.doi.org/10.1016/ j.matdes.2013.03.105.

Liu Y J, Zhao B, Xu B X, Yue Z F (2007) Experimental and numerical study of the method to determine the creep parameters from the indentation creep testing, Materials Science and Engineering A, 456, 103–108. doi:10.1016/j.msea.2006.11.098.

Lugo M, Jordon J B, Horstemeyer M F, Tschoppa M A, Harris J, Gokhale A M (2011) Quantification of damage evolution in a 7075-aluminum alloy using an acoustic emission technique, Mater Sci Eng A, 528(22–23), 6708–14.

Luo C, Li X, Song D, Zhou N, Li Y, Qi W (2016) Microstructure evolution and mechanical properties of friction stir welded dissimilar joints of Mg-Zn-Gd and Mg-Al-Zn alloys, Mater. Sci. Eng. A, 664, 103–113. https://doi.org/ 10.1016/j.msea.2016.03.117.

Lutjering G, Williams J C (2007) Titanium, Engineering Materials and Processes, Springer – Verlag, Berlin Heidelberg, 299–301.

Ma Y E, Zhao Z, Liu B, Li W (2013) Mechanical properties and fatigue crack growth rates in friction stir welded nugget of 2198-T8 Al–Li alloy joints, Mater. Sci. Eng. A, 569, 41–47.

Mahmudi R, Roumina R, Raeisinia B (2004) Investigation of stress exponent in the power-law creep of Pb–Sb alloys. Materials Science and Engineering A, 382, 15–22. doi:10.1016/j.msea.2004.05.078.

Malika V, Sanjeev N K, Hebbar H S, Kailas V S (2014) Investigations on the Effect of Various Tool Pin Profiles in Friction Stir Welding Using Finite Element Simulations, Procedia Engineering, 97, 1060–1068. doi: 10.1016/ j.proeng.2014.12.384.

Mastanaiah P, Sharma A, Reddy G M (2018) Role of hybrid tool pin profile on enhancing welding speed and mechanical properties of AA2219-T6 friction stir welds, Journal of Materials Processing Tech, 257, 257–269. https://doi.org/10.1016/j.jmatprotec.2018.03.002.

McKamey C G, Maziasz P J, Jones J W (1992) Effect of addition of molybdenum or niobium on creep-rupture properties of Fe3Al, J. Mater. Res, 7, 2089-2106. DOI: https://doi.org/10.1557/JMR.1992.2089.

Mishra R S, Ma Z (2005) Friction stir welding and processing, Material Science and Engineering R, 50 (1–2), 1–78. doi:10.1016/j.mser.2005.07.001.

Moghadam D G, Farhangdoost K (2016) Influence of welding parameters on fracture toughness and fatigue crack growth rate in friction stir welded nugget of 2024-T351 aluminum alloy joints, Trans. Nonferrous Met. Soc. China 26, 2567−2585.

Moradi M M, Aval H J, Jamaati R, Amirkhanlou S, Ji S (2018) Microstructure and texture evolution of friction stir welded dissimilaraluminum alloys: AA2024 and AA6061, Journal of Manufacturing Processes, 32, 1–10. https://doi.org/10.1016/j.jmapro.2018.01.016.

Moreira P, Jesus De A, Ribeiro A, De Castro P (2008) Fatigue crack growth in friction stir welds of 6082-t6 and 6061-t6 aluminium alloys: A comparison, Theor. Appl. Fract. Mech. 50 (2), 81–91 13.

Muzvidziwa M, Okazaki M, Suzuki K, Hirano S (2016) Role of microstructure on the fatigue crack propagation behavior of a friction stir welded Ti–6Al–4V, Materials Science & Engineering A, 652 59–68.

Nishimura K, Miyazaki N (2004) Role of microstructures on the growth of long fatigue cracks, Comput. Mater. Sci. 31, 269–278.

Okada T, Machida S, Nakamura T (2017) Fatigue Crack Growth of Friction-Stir-Welded Aluminum Alloy, JOURNAL OF AIRCRAFT, 54(2).

Okada T, Suzuki M, Miyake H, Nakamura T, Machida S, Asakawa M (2010) Evaluation of Crack Nucleation Site and Mechanical Properties for Friction Stir Welded Butt Joint in 2024-T3 Aluminum Alloy, International Journal of Advanced Manufacturing Technology, 50 (1), 127–135.

Padhy G K., Wu C S, Gao S (2018) Friction stir based welding and technologies - parameters, microstructures and applications: A review, Journal of Materials Science & Technology, 34,1–38.

Pao P S, Fonda R W, Jones H N, Feng C R, Moon D W (2009) Friction Stir Welding and Processing, in: V.R.S. Mishra, M.W. Mahoney (Eds.), TMS, pp. 29–38

Payne J, Welsh G, Robert J. Christ Jr, Nardiello J, Papazian John M (2010) Observations of fatigue crack initiation in 7075-T651, Int J Fatigue, 32(2), 247–55.

Peel M, Steuwer A, Preuss M, Withers P J (2003) Microstructure, mechanical properties and residual stresses as a function of welding speed in aluminium AA5083 friction stir welds, Acta Materialia, 51, 4791–4801. doi:10.1016/S1359-6454(03)00319-7.

Phani S, Oliver W C (2016) A direct comparison of high temperature nano indentation creep and uniaxial creep measurements for commercial purity aluminum, Acta Material, 111, 31-38. http://dx.doi.org/10.1016/j.actamat. 2016.03.032.

Pilchak A, Williams J C (2011) The Effect of Friction Stir Processing on the Mechanical Properties of Investment Cast and Hot Isostatically Pressed Ti-6Al-4V, Metall. Mater. Trans. A, 42, 1630–1645.

Pouget G, Reynolds A P (2008) Residual stress and microstructure effects on fatigue crack growth in AA 2050 friction stir welds. International Journal of Fatigue 30, 463–472.

Prasanna H U, Udupa K R (2016) Indentation creep studies to evaluate the mechanical properties of stainless steel welds, Australian Journal of Mechanical engineering, 14(1), 39–43.http://dx.doi.org/10.1080/ 14484846.2015.1093214.

Prasanna P, Penchalayya C, Anandamohana R D (2013) Effect of tool pin profiles and heat treatment process in the friction stir welding of AA 6061 aluminium alloy, American Journal of Engineering Research, 2, 7-15.

Rajak D K, Pagar D D, Menezes P L, Eyvazian A (2020) Journal of adhesion science and technology https://doi.org/10.1080/01694243.2020.1780716.

Rajakumar S, Balasubramanian V (2012) Predicting Grain Size and Tensile Strength of Friction Stir Welded Joints of AA7075-T6 Aluminium Alloy, Materials and Manufacturing Processes, 27, 78–83.

Rajesh Jesudoss Hynes N, Shenbaga Velu P (2018) Effect of rotational speed on Ti-6Al-4V-AA 6061 friction welded joints, Journal of Manufacturing Processes, 32, 288–297. https://doi.org/10.1016/j.jmapro.2018.02.014.

Rambabu G, Balaji Naik D, Venkata Rao CH, Srinivasa Rao K, Madhusudan Reddy G (2015) Optimization of friction stir welding parameters for improved corrosion resistance of AA2219 aluminum alloy joints. Def Technol,11,330-7. http://dx.doi.org/10.1016/j.dt.2015.05.003.

Rao D, Heerens J, Alves Pinheiro G, dos Santos J F, Huber N (2010) On characterisation of local stress–strain properties in friction stir welded aluminium AA 5083 sheets using micro-tensile specimen testing and instrumented indentation technique, Materials Science and Engineering A, 527, 5018–5025. https://doi.org/10.1016/j.msea.2010.04.047.

Regev M, Rashkovsky T, Cabibbo M, Spigarelli S (2018) Microstructure Stability during Creep of Friction Stir Welded AA2024-T3 Alloy. JMEPEG. 27, 5054–5063. https://doi.org/10.1007/s11665-017-3122-8.

Sahu P K, Das J, Chen G, Liu Q, Pal S, Zeng S, Shi Q (2020) Friction stir selective alloying of different Al% particulate reinforced to AZ31 Mg for enhanced mechanical and metallurgical properties, Materials Science & Engineering A, 774,138889, https://doi.org/10.1016/j.msea.2019.138889.

Sahu P K, Pal S (2017) Influence of metallic foil alloying by FSW process on mechanical properties and metallurgical characterization of AM20 Mg alloy, Materials Science & Engineering, A, 684, 442–455. http://dx.doi.org/10.1016/ j.msea.2016.12.081.

Sahu P K, Pal S (2017) Mechanical properties of dissimilar thickness aluminium alloy weld by single/double pass FSW, Journal of Materials Processing Technology, 243, 442–455, http://dx.doi.org/10.1016/ j.jmatprotec.2017.01.009.

Sahu P K, Pal S (2018) Effect of FSW parameters on microstructure and mechanical properties of AM20 welds, Materials and manufacturing processes, 33, (288–298 https://doi.org/10.1080/10426914.2017.1279295.

Sahu P K, Pal S, Pal S K, Jain R (2016) Influence of plate position, tool offset and tool rotational speed on mechanical properties and microstructures of dissimilar Al/Cu friction stir welding joints, Journal of Materials Processing Technology, 235, 55–67. http://dx.doi.org/10.1016/j.jmatprotec.2016.04.014.

Sahu P K, Vasudevan N P, Das B and Pal S, (2019) Assessment of self-reacting bobbin tool friction stir welding for joining AZ31 magnesium alloy at inert gas environment, Journal of Magnesium and Alloys, 7, 661–671.

Salari E, Jahazi M, Khodabandeh A, Ghasemi-Nanesa H (2014) Influence of tool geometry and rotational speed on mechanical properties and defect formation in friction stir lap welded 5456 aluminum alloy sheets. Materials and Design, 58, 381–389. http://dx.doi.org/10.1016/j.matdes.2014.02.005.

Santecchia E, Cabibbo M, Ghat M, Regev M, Spigarelli S (2020) Physical modeling of the creep response of an Al–Cu–Mg alloy with a fine microstructure transformed by Friction Stir Processing, Materials Science & Engineering A, 769, 138521. https://doi.org/10.1016/j.msea.2019.138521.

Saravanan V, Rajakumar S, Banerjee N, Amuthakkannan R (2016) Effect of shoulder diameter to pin diameter ratio on microstructure and mechanical properties of dissimilar friction stir welded AA2024-T6 and AA7075-T6 aluminum alloy joints, Int J Adv Manuf Technol, 87, 3637–3645. DOI 10.1007/s00170-016-8695-0.

Sharma G, Ramanujan R V, Kutty T R G, Tiwari G P (2000) Hot hardness and indentation creep studies of aFe–28Al–3Cr–0.2C alloy. Materials Science and Engineering A, 278, 106–112. https://doi.org/10.1016/S0921-5093(99)00590-0.

Sharma S R, Mishra R S (2008) Fatigue crack growth behavior of friction stir processed aluminum alloy, Scripta Materialia, 59, 395–398. doi:10.1016/j.scriptamat.2008.04.014.

Sherby O D, Burke P M (1968) Mechanical Behavior of Crystalline Solids at Elevated Temperatures. Pergamon Press, New York.

Sinhmar S, Dwivedi D K (2019) Effect of weld thermal cycle on metallurgical and corrosion behavior of friction stir weld joint of AA2014 aluminium alloy, Journal of Manufacturing Processes, 37, 305–320, https://doi.org/10.1016/ j.jmapro.2018.12.001.

Sivaraj P, Kanagarajan D, Balasubramanian V (2014) Fatigue crack growth behaviour of friction stir welded AA7075-T651 aluminium alloy joints, Trans. Nonferr. Met. Soc. China, 24 (8) 2459–2467.

Spigarelli S, Regev M, Mehtedi El M, Quercetti G, Cabibbo M (2011) Analysis of the effect of friction stir welding on the minimum creep rate of an Mg–3% Al–1% Zn alloy, Scripta Materialia, 65, 626–629. https://doi.org/10.1016/j.scriptamat.2011.06.042.

Su J Q, Nelson T W, Sterling C J (2005) Microstructure evolution during FSW/FSP of high strength aluminum alloys, Mater. Sci. Eng. A, 405, 277–286.

Sun T, Roy M J, Strong D, Withers P J, Prangnell P B (2017) Comparison of residual stress distributions in conventional and stationary shoulder high-strength aluminum alloy friction stir welds, J. Mater. Process. Technol, 242, 92–100. https://doi.org/10.1016/j.jmatprotec.2016.11.015.

Suresh S (1985) Fatigue crack deflection and fracture surface contact: Micromechanical models, Metall. Trans. A, 16A, 249–260.

Tanaka H, Asakawa M, Saito K, Okada T, Machida S, Kuwayama K (2013) Fatigue Crack Propagation Properties of Friction-Stir-Welded 2024-T3 Aluminum Alloy—Effect of Stress Ratio on Crack Growth Rate, Proceedings of the APISAT2013.

Tao W, Yong Z, Xuemei L, Matsuda K (2016) Special grain boundaries in the nugget zone of friction stir welded AA6061-T6 under various welding parameters, Materials Science & Engineering A, 671, 7–16. http://dx.doi.org/10.1016/j.msea.2016.06.050.

Taylor D (1992) On the use of *P-a* plots to model the behaviour of short fatigue cracks**,** Int. J. Fatigue**,** 14**,** 163.

Thomas W M, Nicholas E D, Needham J C (1991) Friction stir welding. International Patent Application No. PCT/GB92/02203 and Great Britain Patent Application No. 9125978.8.

Torre De La, Adeva P, Aballe M (1991) Indentation creep of lead and lead-copper alloys, Journal of Materials Science, 26, 4351- 4354. https://doi.org/10.1007/BF00543650.

Tra T H, Okazaki M, Suzuki K (2012) Fatigue crack propagation behavior in friction stir welding of AA6063-T5: Roles of residual stress and microstructure, International Journal of Fatigue, 43, 23–29.

Trimble D, Donnell O G E, Monaghan J (2015) Characterization of tool shape and rotational speed for increased speed during friction stir welding of AA2024-T3. Journal of Manufacturing Processes, 17, 141–150. http://dx.doi.org/10.1016/j.jmapro.2014.08.007.

Trueba Jr L, Heredia G, Rybicki D, Johannes Lucie B (2015) Effect of tool shoulder features on defects and tensile properties of friction stir welded aluminum 6061-T6, Journal of Materials Processing Technology, 219, 271–277. http://dx.doi.org/10.1016/j.jmatprotec.2014.12.027.

Uematsu Y, Tokaji K, Tozaki Y, Shibata H Fatigue behaviour of friction stir welded 6061-t6 aluminium alloy, BOOK 2T5, Fatigue and fracture, 287-288.

Vakili-Tahami F, Reza Adibeig M, Hassanifard S (2019) Optimizing creep lifetime of friction stir welded PMMA pipes subjected to combined loadings using rheological model, Polymer Testing. 79, 106049. https://doi.org/10.1016/j.polymertesting.2019.106049.

Vasudevan A K, Sadananda K, Rajan K (1997) Role of microstructures on the growth of long fatigue cracks, Int. J. Fatigue, 19, 151–159.

Vijayanand N V D, Ganesan V, Laha K, Mathew M D (2014) Evaluation of creep deformation behaviour of different microstuctural zones of 316LN SS weld joint using impression creep testing technique, Materials Science and Technology, 30:10, 1223-1228, DOI: 10.1179/1743284713Y.0000000438.

Vijayanand Naveena V D, Ganesan V, Laha K, Mathew M D (2014) Evaluation of creep deformation behaviour of different microstuctural zones of 316LN SS weld joint using impression creep testing technique, Materials Science and Technology, 30(10), 1223-1228, 10.1179/1743284713Y.0000000438.

Wang J, Yuan W, Mishra R S, Charit I (2014) An Evaluation of Creep Behaviour in Friction Stir Welded MA754 Alloy Journal of Materials Engineering and Performance, 23, 3159–3164. DOI: 10.1007/s11665-014-1092-7.

Wei B C, Chen C Q, Huang Z, Zhang Y G (2000) Aging behavior of Li containing Al–Zn–Mg–Cu alloys, Mater Sci Eng;A, 280, 161–167.

Wu H, Chen Y C, Strong D, Prangnell P (2015) Stationary shoulder FSW for joining high strength aluminum alloys, J. Mater. Process. Technol, 221, 187–196. https://doi.org/10.1016/j.jmatprotec.2015.02.015.

Yadav S D, Vasantharaja P, Riedlsperger F, Nagaraju S, Vasudevan M (2019) Zone-wise investigation of creep behaviour 9Cr–1Mo steel weld joints. Materials Science and Technology, 35(2), 155–172. https://doi.org/10.1080/02670836.2018.1545283.

Yadav V K, Gaur V, Singh I V (2020) Effect of post-weld heat treatment onmechanical properties and fatigue crack growth rate in welded AA-2024, Materials Science & Engineering A, 779, 139116.

Yanga B, Xuan FZ (2018) Creep behavior of subzones in a CrMoV weldment characterized by the in situ creep test with miniature specimens, Materials Science & Engineering A,723,148–156. https://doi.org/10.1016/j.msea.2018.03.051.

Zhang C, Cui L, Wang D, Liu Y, Liu C, Li H (2019) The heterogeneous microstructure of heat affect zone and its effect on creep resistance for friction stir joints on 9Cr–1.5 W heat resistant steel Scripta Materialia, 158, 6–10. https://doi.org/10.1016/j.scriptamat.2018.08.028.

Zhang L, Zhong H, Li S, Zhao H, Chen J, Qi L (2020) Microstructure, mechanical properties and fatigue crack growth behavior of friction stir welded joint of 6061-T6 aluminum alloy, International Journal of Fatigue, 135, 105556, https://doi.org/10.1016/j.ijfatigue.2020.105556.

Zhao Y, Yang Z, Zhang Z, Su G, Ma X (2013) Double-peak age strengthening of cold-worked 2024 aluminum alloy, Acta Mater, 61 (5)1624–1638.

Publications from the Thesis Work

Journal

1. **Jayashree Das,** P. Sreedharan Robi Mamilla Ravi Sankar, Estimation of deformation behaviour at different weld zones of FSWed AA2014 aluminium alloy through impression creep technique, ***Journal of adhesion science and technology (Taylor & and Francis)***, Vol: 35 (2021), https://doi.org/10.1080/01694243.2021.1921498.

2. **Jayashree Das,** P. Sreedharan Robi, Impression Creep Deformation Behaviour of FSWed AA6061 at Various Weld Zone, ***Australian Journal of Mechanical Engineering (Taylor & and Francis, 2021*)**, https://doi.org/10.1080/14484846.2021.1960620.

3. **Jayashree Das,** P. Sreedharan Robi Mamilla Ravi Sankar, Assessment of parameters windows and tool pin profile on mechanical property and microstructural morphology of FSWed AA2014 joints, ***SN Applied Sciences (Springer Nature)*,** volume 2, 123 (2020), https://doi.org/10.1007/s42452-019-1895-0.

4. **Jayashree Das**, S.R. Banik, S.R.S.K. Reddy, M.R. Sankar, P.S. Robi, Review on process parameters effect on fatigue crack growth rate in friction stir welding, ***Materials Today: Proceedings (Elsevier)***, volume-18 (2019) 3061–3070, https://doi.org/10.1016/j.matpr.2019. 07.178.

5. **Jayashree Das**, P. S. Robi and M. Ravi Sankar, Indentation Creep Behavior of Nugget Zone of Friction Stir Welded 2014 Aluminum Alloy, ***Materials Science and Engineering (IOP Science)*** volume-346 (2018) 012017, https://iopscience.iop.org/article/10.1088/1757-899X/346/1/ 012017.

6. **Jayashree Das** and P. Sreedharan Robi, Tool Pin Profile and Process Parameters Effects on Strength-Microstructure-Fatigue Fracture of Friction Stir Welded AA6061-T6 Aluminium Alloy, **(Communicated).**

7. **Jayashree Das** and P. Sreedharan Robi, Mechanism of Fatigue Crack Initiation and Propagation in Different Microstructural regions of Friction Stir Welded AA2014, **(Communicated).**

8. **Jayashree Das,** and P. Sreedharan Robi, Analysis on Fatigue Crack Growth Rate at different weld zones of Friction Stir Welded AA6061 Aluminium Alloy, **(Communicated).**